express
polymer letters

Editorial corner – a personal view

Shape memory polymers: Current state and future prospects

Balázs Tatár[1] , *László Mészáros*[1,2]*

[1]Department of Polymer Engineering, Faculty of Mechanical Engineering, Budapest University of Technology and Economics, H-1111 Budapest, Műegyetem rkp. 3., Hungary
[2]ELKH–BME Research Group for Composite Science and Technology, H-1111 Budapest, Műegyetem rkp. 3., Hungary

Shape memory polymers (SMPs) are intelligent materials capable of changing shape in response to external stimuli, such as heat, light, or a magnetic field. SMPs have attracted significant attention in recent years due to their unique properties and potential applications in various areas, *e.g.*, in the biomedical, aerospace, and the electronics industry (https://doi.org/10.3144/expresspolymlett.2022.66). The concept of shape memory was first discovered in the 1940s in metallic alloys, but it was not until the 1980s that the first SMPs were developed with the use of synthetic polymers. Early SMPs were limited in their applicability due to their high glass transition temperature and poor mechanical properties. However, new generations of SMPs with improved performance and functionality have been developed with the advancement of materials science and technology.

Currently, there are three main types of SMPs: thermoplastic, thermoset, and elastomeric SMPs. Thermoplastic SMPs are the most commonly used and are characterized by their high elasticity, processability, and excellent shape memory properties. Thermoset SMPs offer excellent mechanical properties and thermal stability. They are usually synthesized by crosslinking the polymer chains, such as in epoxy or phenolic resins. Elastomeric SMPs are highly stretchable and have excellent shape memory properties. They are typically a blend made from rubbers, *e.g.*, polyisoprene and polybutadiene, or can be thermoplastic elastomers (https://doi.org/10.1002/adma.202000713). SMPs face diverse challenges in different fields. In biomedicine, new SMP materials are needed that are non-toxic and biocompatible, as well as new activation methods that respond to the human body. In aerospace engineering, the load-bearing capacity of SMPs has to be increased so that they can replace more mechanical parts. Consistent repetition and multiple-shape and two-way shape memory polymers are now in demand in electronics. Researchers are currently exploring different methods to meet these demands, such as incorporating functional groups and nanofillers (https://doi.org/10.3144/expresspolymlett.2021.37). Another challenge is the limited range of stimuli that can trigger the shape memory effect. Most SMPs currently require a temperature change to trigger the shape memory effect. However, researchers are exploring new ways to trigger the shape memory effect, such as using light or a magnetic field. By developing SMPs that can respond to a wider range of stimuli, researchers can significantly broaden the potential applications of these materials (https://doi.org/10.3390/polym14173511).

In conclusion, SMPs have come a long way since their discovery in the 1980s. They offer unique properties and potential applications in various fields. Developing new generations of SMPs with improved performance and functionality is an active area of research. Researchers are also exploring ways to address the challenges of achieving a stable and repeatable shape memory effect and extending the range of stimuli that can trigger the effect. With continued research and development, SMPs have the potential to revolutionize materials science and engineering.

*Corresponding author, e-mail: meszaros@pt.bme.hu

express
polymer letters

Research article

Influence of vulcanization system on curing, mechanical, dynamic and morphological properties of maleated natural rubber and its thermoplastic vulcanizate with thermoplastic copolyester elastomer

Azizon Kaesaman[1] , *Suwaiyah Lamleah*[1], *Charoen Nakason*[2]

[1]Faculty of Science and Technology, Prince of Songkla University, Pattani, Thailand
[2]Faculty of Science and Industrial Technology, Prince of Songkla University, Surat Thani, Thailand

Abstract. Maleated natural rubber (MNR) was prepared and compounded with four alternative vulcanization systems: sulfur, peroxide, phenolic, and mixed sulfur-peroxide vulcanization systems. It was found that the peroxide and mixed sulfur-peroxide cured systems show a plateau curing curve, while the sulfur-cured system exhibits reversion, and the phenolic cured system gives marching cure behavior. Also, thermoplastic vulcanizates (TPVs) based on dynamically cured MNR and thermoplastic copolyester elastomer (TPC-ET) blends (*i.e.*, MNR/TPC-ET TPVs) by using these vulcanization systems were also prepared and characterized. The height and area underneath the dynamic vulcanization peaks in the mixing torque-time curves directly relate to the degree of vulcanization and strength along with the nature of crosslink structures, and these had the rank order peroxide > mixed sulfur-peroxide > phenolic > sulfur by vulcanization system. This is in good agreement with the maximum torque, tensile strength, hardness, moduli, and toughness of MNR compounds. The locations of the peaks also correspond to the scorch time (t_{s1}), and the sulfur and phenolic cured systems with scorch times of 2.31 and 2.44 min showed peaks at 3.3 and 3.4 min, respectively, offering improved process safety. The sulfur-cured TPV had sulfidic linkages and the smallest-sized vulcanized rubber domains, giving it the highest tensile strength, elongation at break, storage modulus, and rubber elasticity (*i.e.*, the lowest tension set and tan δ). However, the phenolic cured TPV had the highest stiffness, Young's modulus, and large vulcanized rubber domains, which relate to low content of Chroman ring structures in the crosslinked MNR vulcanizates, with a comparatively low interfacial area and hence weak interfacial interactions between MNR and TPC-ET phases. Furthermore, the mixed sulfur-peroxide and peroxide curing systems gave intermediate tension set, tan δ, and elongation at break.

Keywords: maleated natural rubber (MNR), thermoplastic copolyester elastomer (TPC-ET, COPE), vulcanization system, dynamic properties, morphological properties

1. Introduction

Natural rubber (NR) from *Hevea brasiliensisis* trees has been well-known as a renewable bio-based polymer that has been widely used in a wide variety of applications. NR molecules inside the latex rubber particles consist of the proteins with trans-1,4-isoprene units (*i.e.*, α-terminals) connected to a long sequence of cis-1,4-polyisoprene along with phospholipid at the ω-terminals [1–3]. Therefore, NR is an attractive renewable bio-based elastomer that is non-toxic. It has excellent physical properties, including high elasticity, mechanical strength, fatigue resistance, and tear strength, together with environmental friendliness. NR is the most used elastomer worldwide industrially,

---

in a variety of applications, due to its low price and good elastic, mechanical, and damping properties. However, NR has some limitations, including poor resistance to hydrocarbons, fats, oils, and greases and poor ozone and weathering resistance together with incompatibility with polar polymers [4]. Chemical modifications of NR molecules could be used to improve the NR properties and extend the scope of NR applications. Succinic anhydride grafted natural rubber, or maleated natural rubber (MNR), is considered to be one of the important NR derivatives that can be used to enhance blend [5, 6] and composite [7, 8] properties.

Thermoplastic elastomers (TPEs) are materials that combine the properties of thermoplastics and soft elastomers, but they can be processed and recycled as thermoplastics [9]. TPEs offer a variety of advantages over conventional thermoset (vulcanized) rubber materials, such as simpler processing with fewer steps and shorter fabrication times, which lead to lower finished part costs, little or no compounding process, reuse of scrap in the same fashion as with thermoplastics, and lower energy consumption and cost due to shorter molding cycles and simpler processing [10]. Commercially available TPEs, based on chemical composition and morphology, can be categorized into eight different groups: styrenic block copolymers (SBCs), polymer blends by dynamic vulcanization (TPVs), polyolefin-based thermoplastic elastomers (TPOs), halogen-containing polyolefins, thermoplastic polyurethane elastomers (TPUs), polyamide-based thermoplastic elastomers (COPA), polyether ester elastomers (COPE), and ionomeric thermoplastic elastomers [11]. Therefore, there are two common types of TPE materials based on blending rubber with thermoplastics: simple blends (SBs), such as polyolefin-based thermoplastic elastomers (TPOs), and thermoplastic vulcanizates (TPVs) [12]. Simple blends are typically prepared by blending the polymer pair without the addition of any curative, and the blend ends up having a co-continuous phase structure. In contrast, to prepare a TPV via dynamic vulcanization, curing agents or a vulcanization system are applied to the rubber phase while it is blended with the thermoplastic at an elevated temperature [13]. Generally, the mechanical, morphological and other useful related properties of TPVs mainly depend on various parameters, including blend composition [13–16], compatibility between the blend

components [17–20], phase morphology [21–24], and vulcanization system [14, 21, 22]. Various vulcanization systems have been exploited to vulcanize the rubber phase during dynamic vulcanization of rubber/thermoplastic blends to form TPV materials, for instance, sulfur [12, 15, 20, 21, 24], peroxide [14, 18, 21, 23, 25], phenolic [16, 19, 21, 22], bismaleimide [21, 25, 26], sulfur donor [17, 27], and coagents sulfur and bismaleimide [21]. Different vulcanization systems typically provide different crosslink structures, morphological properties, sizes of vulcanized rubber domains, and mechanical, dynamic, and other structure related properties.

Natural rubber (NR) is typically used as one possible elastomeric component in a TPE, which is then generally called thermoplastic natural rubber (TPNR) [28]. Besides the normal NR form, chemically modified NRs such as epoxidized natural rubber (ENR) and maleated natural rubber (MNR) have also been used to prepare TPNR, owing to their unique properties, high polarity, good compatibility with polar thermoplastics, and air impermeability. There are many kinds of thermoplastics that have been used to prepare TPNR based on blending with MNR, such as polypropylene [29–31], poly(lactic acid) [32, 33], sulfonated polystyrene [34, 35], high-density polyethylene [36], and poly(methyl methacrylate) [37].

The main aim of this research study was to assess the influences of alternative vulcanization systems on the curing, mechanical, rheological, and dynamic properties of MNR vulcanizates based on static vulcanization. The four different vulcanization systems used were sulfur, peroxide, phenolic, and mixed sulfur-peroxide vulcanization systems. Then, the dynamically cured TPC-ET/MNR blends were prepared with the alternative vulcanization systems, with the main aim being to prepare TPV materials with high damping and other related properties at a low hardness (*i.e.*, lower than 80 Shore A). This is because TPC-ET, with low hardness, is not appropriate for industrial applications due to its very poor damping properties. The addition of a high damping material component with some polarities and decent elastic properties, like MNR, could improve the elasticity and damping properties of TPC-ET materials. These new materials might be suitable for various industrial applications, such as appliances and automotive parts (interior and exterior), demanding both elasticity and strength.

2. Experimental
2.1. Materials
Natural rubber, Standard Thai Rubber (STR 5L) with Mooney viscosity (ML1+4, 100 °C) range 70–75, was manufactured by Tavorn Rubber Industry (1982) Company Limited (Songkla, Thailand). It was used as a raw material to prepare maleated natural rubber (MNR) by the preparation and characterization procedures described in our previous work [38, 39]. Maleic anhydride (MA) used in the preparation of maleated natural rubber (MNR) was manufactured by Fluka Chemika Co., Ltd (Buchs, Switzerland). Thermoplastic copolyester elastomer (TPC-ET), Hytrel® G3548L, was manufactured by DuPont (Wilmington, USA). It is a block copolymer consisting of a hard (crystalline) segment of polybutylene terephthalate and a soft (amorphous) segment based on polyether chemistry. Hytrel® G3548L is a low modulus grade with a nominal durometer hardness of 35D, melt flow index (MFI) of 10 g/10 min (190 °C, 2.16 kg, ISO 1133) and shear viscosity at a shear rate of 1000 s^{-1} = 135 Pa·s (190 °C). The zinc oxide used as an activator in the sulfur curing system was manufactured by Global Chemical Co., Ltd (Samut Prakarn, Thailand). The stearic acid used as an activator was manufactured by Imperial Chemical Co., Ltd (Pathum Thani, Thailand). Wingstay® L was used as a highly effective polyphenol antioxidant, supplied by Synthomer plc (London, UK). The sulfur used as a vulcanizing agent was manufactured by Siam Chemicals Co., Ltd, (Samut Prakarn, Thailand). The *N*-tert-butyl-2-benzothiazolesulphenamide (Santocure TBBS) used as an accelerator was manufactured by Flexsys Chemicals Belgium NV (Antwerp, Belgium). The Santoflex 6PPD (*N*-phenyl-*N'*-1,3-dimethylbutyl-*p*-phenylenediamine) used as an antioxidant was manufactured by Flexsys Chemicals

Belgium NV (Antwerp, Belgium). Dicumyl peroxide (DCP) used as a curing agent of MNR was manufactured by Wuzhou International Co., Ltd., (Wuxi, China). Triallyl cyanurate (TAC) was used as a coagent in the peroxide curing system and was manufactured by Fluka Chemie GmbH (Buchs, Switzerland). The dimethylol phenolic resin with active hydroxymethyl (methylol) groups, grade HRJ-10518 (made by reacting octylphenol and formaldehyde), was used as a phenolic curing agent and was manufactured by Schenectady International Inc., (New Port, USA).

2.2. Preparation of maleated natural rubber compounds with various vulcanization systems
Maleated natural rubber (MNR) was first prepared in-house, as described in our previous work [38, 39]. It was then compounded with the various vulcanization systems (*i.e.*, sulfur, peroxide, phenolic, and mixed sulfur-peroxide systems) by using chemical ingredients, as shown in Table 1. The compounding of rubber and chemicals was performed in an internal mixer, Brabender® Measuring Mixers, model 50EHT 3Z, Brabender® GmbH & Co. KG, (Duisburg,·Germany) at 40 °C, and at rotor speed 60 rpm according to the mixing schedule in Table 2. After dumping the rubber compound from the mixing chamber, it was further homogenized by passing through the 1 mm nip of a CT two-roll mill, Charoen TuT Co., Ltd. (Samut Prakarn, Thailand) with a friction ratio of 1:1.25 at ambient temperature for about 5 min. Then, cure characteristics of the MNR compound were analyzed by using a moving die rheometer (MDR), Rheo Tech MDPT, Tech Pro Inc, (Cuyuhoga Falls, USA) at 170 °C. The MNR compound was eventually fabricated to a thin sheet of about 2 mm thickness

Table 1. Compounding formulation of maleated natural rubber (MNR) with various vulcanization systems.

Chemical	Quantity [phr]			
	Sulfur	**Peroxide**	**Phenolic**	**Mixed sulfur-peroxide**
MNR	100	100	100	100
ZnO	5	5	5	5
Stearic acid	1	1	1	1
6PPD	1	1	1	1
TBBS	1	–	–	0.5
Sulfur	3.5	–	–	1.75
DCP	–	2	–	1
TAC	–	1	–	0.5
HRJ-10518	–	–	7	–

Table 2. Mixing schedule for compounding of maleated natural rubber (MNR) with various vulcanization systems.

Description	Mixing time [min]			
	Sulfur	Peroxide	Phenolic	Mixed sulfur-peroxide
Mastication	2	2	2	2
Stearic acid	1	1	1	0.5
ZnO	1	1	1	0.5
Wingstay® L	1	1	1	0.5
TBBS	1	–	–	1
Sulfur	1	–	–	1
DCP	–	1	–	1
TAC	–	1	–	1
HRJ-10518	–	–	1	–

by compression molding, using a compression molding machine model IA, Chaicharoen Karn Chang, Ltd., (Bangkok, Thailand) at 170 °C and high pressure for the respective cure time based on the MDR test.

2.3. Influence of vulcanization system on properties of dynamically cured MNR and thermoplastic copolyester elastomer blends

Dynamically cured MNR/TPC-ET blends or MNR/TPC-ET TPVs were prepared by blending MNR compounds with a different vulcanization system (sulfur, peroxide, phenolic, or mixed sulfur-peroxide system) (Table 1) and thermoplastic copolyester elastomer (TPC-ET) via dynamic vulcanization at the fixed 50/50 w/w blend proportions of MNR and TPC-ET. This blending ratio was selected due to the closed shear viscosities of MNR and TPC-ET with the viscosity ratio (η_{MNR}/η_{TPC-ET}) of 1.12 (shear viscosity at a shear rate of 1000 s^{-1} of MNR = 152 Pa·s at 190 °C)). Blending was performed in an internal mixer, Brabender® Measuring Mixers, model 50EHT 3Z, Brabender GmbH & Co. KG, (Duisburg, Germany) at 170 °C, with a rotor speed set at 60 rpm and using a fill factor of 0.85. The TPC-ET was first dried in a hot air oven at 80 °C for at least 2 h to eliminate moisture. It was then incorporated into the mixing chamber and mixed for about 2 min at 170 °C. The MNR compound was then added into the mixing chamber with continued blending until a plateau mixing torque or the total mixing time of 12 min was reached. The blended product was then dumped from the mixing chamber, conditioned at room temperature for at least 3 h, and then ground to small particles by using a plastic grinder machine, Bosco Engineering

Co., Ltd., (Bangkok, Thailand). The MNR/TPC-ET TPV was then fabricated by plastic injection molding machine with a clamping force of 90 tons, model TII-90F, Weltec Machinery Ltd., (Hongkong, China) fitted with standard tensile specimens mold in accordance with ISO 37. The temperature was set for different zones of injection molding at 160, 165, 170 and 170 °C in heating barrel zones 1, 2, 3 and injection nozzle, respectively. Also, the injection pressure was set in the common range between 90 to 110 MPa. Mechanical, morphological, and dynamic properties of the dynamically cured MNR/TPC-ET were eventually characterized.

2.4. Characterization
2.4.1. Cure characteristics
Cure characteristics of the MNR compound were determined at 160 °C by using a moving die rheometer (MDR), rheoTech MD$^+$, Tech Pro Inc., (Cuyahoga Falls, USA) at a fixed frequency of 1.67 Hz, and a strain amplitude of 1° arc at 170 °C. The optimum scorch time (t_{s1}), cure time (t_{c90}), minimum torque (M_L), maximum torque (M_H), and torque difference ($M_H - M_L$) were determined from the curing curves.

2.4.2. Mechanical properties
The 50/50 MNR/TPC-ET TPVs pellets were fabricated to dumbbell-shaped specimens by injection molding using a Weltec thermoplastic injection-molding machine, Weltec Machinery, Ltd., (Hongkong, China) with a clamping capacity of 90 tons. Tensile properties in terms of tensile strength, elongation at break, and tension set of MNR vulcanizates and MNR/TPC-ET TPVs were tested with a Hounsfield tensometer, model H 10 KS, Hounsfield Test Equipment Co., Ltd., (Raydon, UK) at a crosshead speed of 500 mm/min and at a room temperature according to ISO 37. Aging properties of the MNR/TPC-ET TPVs were also determined after accelerated aging at 100 °C for 22 h in a multi-cell aging oven, model Elastocon AB, Elastocon Inc, (Rämhult, Sweden), according to ASTM D 573. After removal from the oven, the samples were conditioned at room temperature for at least 24 h before the tensile strength and elongation at break were determined and compared to the ones before aging. The tension set was determined according to ASTM D412 by extending the dumbbell shape specimen to 100% elongation and left at this position for 10 min before releasing. The specimen was then allowed to recover for another 10 min before

measuring the length compared to the original length, where the % tension set was evaluated. The hardness of the MNR vulcanizates was determined by a durometer Shore A, model S1 Digital Durometers, An Instron Company, (Massachusetts, USA) according to ISO 48.

2.4.3. Morphological properties
Morphological studies of MNR/TPC-ET TPVs were carried out by using a scanning electron microscope (SEM), model Quanta 400, FEI company (Hillsboro, USA). Injection-molded samples of the MNR/TPC-ET TPVs were first cryogenically fractured in liquid nitrogen to create the new surfaces and to prevent any possibility of phase deformation during the fracturing process. The TPC-ET phase was then preferentially extracted by immersion of the fractured surface into boiling dimethyl sulfoxide (DMSO) for about 20 min. The samples were later dried in a vacuum oven at 40 °C for 12 h to eliminate contamination by the solvent. The dried surfaces were gold-coated before they were imaged by scanning electron microscopy (SEM). From the SEM micrographs, the size of rubber domains dispersed in a copolyester (TPC-ET) matrix was determined in terms of the number-average (D_n) domain diameters using Equation (1) [40]:

$$D_n = \frac{\sum N_i D_i}{\sum N_i} \tag{1}$$

where N_i is the number of particles with the diameter D_i.

2.4.4. Dynamic properties
Dynamic properties in terms of storage and loss moduli, along with complex viscosity, were characterized using a moving die processability tester, model RheoTech MDPT, Tech Pro Inc., (Cuyahoga Falls, USA). Frequency sweeps were conducted over the frequency range from 0.1 to 158 rad/s at 3% strain amplitude and 180 °C according to ASTM D6601.

3. Results and discussion
3.1. Influence of vulcanization system choice on properties of MNR compounds
3.1.1. Curing properties of MNR compounds
Figure 1 shows cure curves or torque-time curves of MNR compounds with various vulcanization systems. It is seen that different vulcanization systems exhibit different cure characteristics. That is, the peroxide and mixed sulfur-peroxide systems show a plateau curing curve with almost constant torque at the final vulcanization state. This indicates the optimum cure or equilibrium in rubber vulcanization. On the other hand, the sulfur-cured system exhibits slight reversion by marginally dropping torque around the testing time of 20 min. This arises from the breakdown of weak newly formed linkages, such as disulfidic (–C–S–S–C–) and polysulfidic (–C–S$_x$–C–) linkages, that a vulnerable to elevated temperature and high shear. In addition, the phenolic curing system shows different cure behavior by increasing torque as testing time increases or marching cure behavior. Table 3 summarizes the cure properties in terms of minimum and maximum torques, torque difference, scorch time, cure time, and cure rate index (CRI) for the MNR compounds with the various vulcanization systems. It can be seen that the peroxide-cured case has the highest maximum torque and torque difference
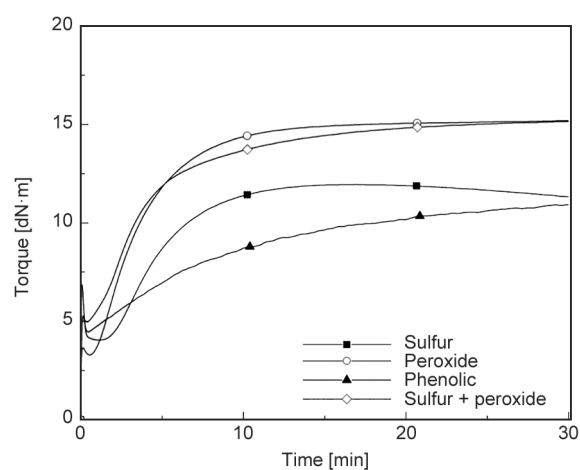

Figure 1. Torque-time curves of MNR compounds prepared with various vulcanization systems.

Table 3. Cure properties in terms of minimum and maximum torques, torque difference, scorch time, cure time, and cure rate index (CRI) for the MNR compounds prepared with various vulcanization systems.

Vulcanization system	M_L [dN·m]	M_H [dN·m]	$M_H - M_L$ [dN·m]	t_{s1} [min]	t_{c90} [min]	CRI [min^{-1}]
Sulfur	4.04	11.95	7.91	2.31	9.09	14.75
Peroxide	3.27	15.44	12.77	1.16	9.20	12.44
Phenolic	4.77	11.56	6.79	2.44	28.49	3.84
Mixed sulfur-peroxide	4.95	15.33	10.38	1.16	13.42	8.16

among the tested vulcanization systems, whose rank order was peroxide > mixed sulfur-peroxide > sulfur > phenolic cured system. This is due to peroxide curing generating comparatively stronger carbon-carbon bonds between the rubber molecules relative to the other types of new linkages induced by the other vulcanization systems. On the other hand, the phenolic system gave the least maximum torque and torque difference. This may be due to slow reactions that formed the Chroman ring structures between MNR and dimethylol phenolic resin with active hydroxymethyl (methylol) groups, and this gave rise to a low crosslink density [41]. A proposed reaction mechanism is shown in Figure 2. It can be seen that the hydroxyl and methylol groups in phenolic molecules undergo reactions with unsaturation in MNR molecules to form Chroman rings as the bridge links between rubber molecules or to form crosslinks. Therefore, the slow crosslinking reaction rate of phenolic curing is obvious due to the molecular rearrangement to form Chroman rings and also due to the low level of unsaturation in MNR molecules. This is also reflected in the lowest cure rate index (CRI) and the longest scorch and cure times with the lowest maximum torque and torque difference (Table 3).

In Table 3, it can also be seen that the MNR compounds with sulfur and phenolic vulcanization systems show longer scorch time or improved scorch safety. Therefore, these two vulcanization systems may be suitable for preparing dynamically cured MNR/TPC-ET blends due to the long enough time for transformation from the co-continuous structure of MNR/TPC-ET simple blend to large vulcanized rubber particles and eventually, the dispersed micronsized vulcanized rubber domains in the TPC-ET matrix.
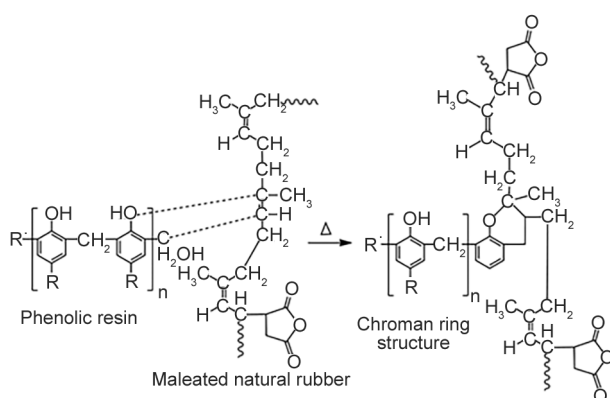
3.1.2. Mechanical properties of MNR compounds

Figure 3 shows stress-strain behaviors of the MNR vulcanizates with various vulcanization systems. It can be seen that Young's modulus (*i.e.*, the initial slope of the curve), which reflects the stiffness of the material, had the order peroxide > phenolic > mixed sulfur-peroxide > sulfur by vulcanization system. This matches the trend in 100% moduli of the MNR vulcanizates based on static vulcanization with peroxide, phenolic, mixed sulfur-peroxide, and sulfur curing systems, which are 0.84, 0.55, 0.34, and 0.32 MPa, respectively. Furthermore, the area underneath the stress-strain curve, which indicates the toughness of the material, has the same trend as Young's modulus and 100% modulus. This is attributed to the peroxide curing system generating chemical crosslinks that consist mainly of carbon-carbon bonds (–C–C– linkages) with higher bonding energy (about 347 kJ/mol) while the sulfur curing system gives weaker chemical bonds of mono-sulfidic (–C–S–C–, 301 kJ/mol), di-sulfidic (–C–S–S–C–, 271.7 kJ/mol), and poly-sulfidic types (–C–S_x–C–, < 271.7 kJ/mol) [42]. An illustration of the different types of crosslinks is shown in Figure 4. Furthermore, the phenolic curing system links rubber molecules by strong structures of phenolic resin, as indicated in Figure 2 and Figure 4d. This causes the phenolic-cured MNR vulcanizate to have slightly higher moduli than the ones prepared with mixed sulfur-peroxide and sulfur vulcanization systems.

Table 4 shows tensile properties (*i.e.*, tensile strength and elongation at break) and mechanical properties in terms of tension set and hardness (Shore A) of the MNR vulcanizates prepared with various vulcanization systems. It can be seen that tensile strength and
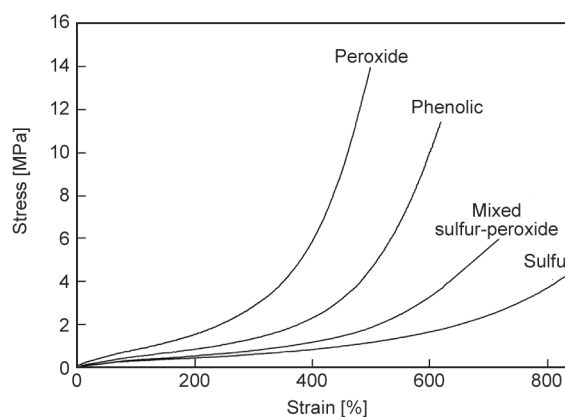

Figure 2. A proposed reaction mechanism of phenolic resin and maleated natural rubber.

Figure 3. Stress-strain behaviors of MNR vulcanizates prepared with various vulcanization systems.
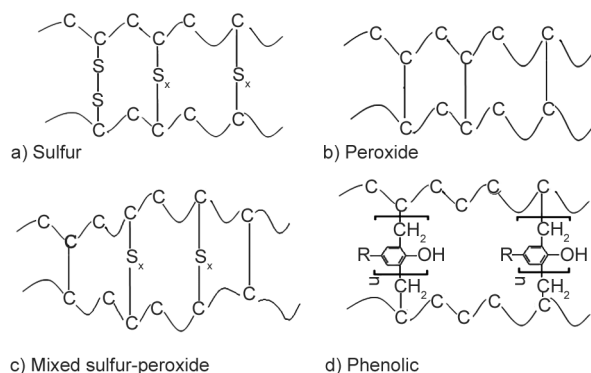
Figure 4. Representative models showing different types of crosslinks formed in a) sulfur, b) peroxide, c) mixed sulfur-peroxide, and d) phenolic cured systems.

Figure 5. Storage modulus as a function of oscillation frequency for the MNR compounds prepared with various vulcanization systems.

hardness have similar trends as moduli and toughness in Figure 3. That is, these properties ranked as peroxide > phenolic > mixed sulfur-peroxide > sulfur vulcanization systems. This is again due to different bonding energies and structures of crosslinks from the alternative vulcanization systems. In Table 4, it is also seen that the highest elongation at break (EB $\cong$ 834%) was for the MNR vulcanizate with the sulfur curing system, while the peroxide system provided the lowest EB (499%). The phenolic and mixed sulfur-peroxide systems showed intermediate elongations at the break, at 618 and 678%, respectively. This may be due to the sulfur system giving di- and poly-sulfidic linkages with high elasticity, as indicated by the lowest tension set (0.5% in Table 4). However, the peroxide system with mainly –C–C– linkages gave the lowest elastic properties, indicated by the highest tension set at 2.0% (Table 4). Furthermore, the phenolic and mixed sulfur-peroxide systems gave an intermediate tension set at 1.0%, which corresponds to the intermediate elongation at break as compared with the EBs of the MNR vulcanizates based on sulfur and peroxide curing (Table 4).

3.1.3. Dynamic mechanical properties of MNR compounds

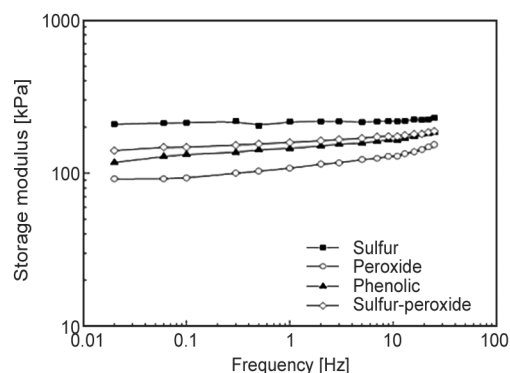Figure 5 shows the storage modulus as a function of oscillation frequency for the MNR compounds prepared with various vulcanization systems. It can be seen that the storage modulus slightly increases with frequency due to a shorter time available for molecular relaxations. The storage or elastic modulus typically represents the amount of energy stored in a tested sample. In Figure 5, it can be seen that the storage modulus at a given frequency had the order sulfur > mixed sulfur-peroxide > phenolic > peroxide by the vulcanization system. Therefore, the MNR vulcanizates with sulfur-containing curing systems (*i.e.*, sulfur or mixed sulfur-peroxide vulcanization system) showed higher elastic moduli with more energy stored than the MNR prepared with phenolic or peroxide curing system. This is again due to the higher elasticity of sulfidic linkages, which corresponds to lower tan δ at a given oscillation frequency for the MNR compounds cured with sulfur or mixed sulfur-peroxide curing system, as shown in Figure 6. It is noted that tan δ is the damping factor or loss factor defined as the ratio of the moduli (*i.e.*, loss modulus, G''/storage modulus, G'). Typically, tan δ indicates the relative degree of energy dissipation or damping by the material and hence rubber elasticity. In Figure 6, the MNR vulcanizate based on sulfur curing shows the lowest tan δ or damping factor, which indicates the highest rubber elasticity. Also, the trend of tan δ is reversed from that of the storage modulus (Figure 5): sulfur < mixed sulfur-peroxide < phenolic

Table 4. Tensile properties (*i.e.*, tensile strength and elongation at break) together with tension set and hardness (Shore A) for the MNR vulcanizates prepared with various vulcanization systems.

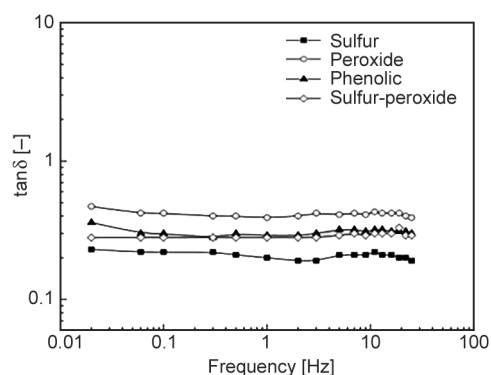| Vulcanization system	Tensile strength [MPa]	Elongation at break [%]	Tension set [%]	Hardness [Shore A]
Sulfur	4.32±0.01	834±9	0.5±0.01	22.0±1.0
Peroxide	13.98±0.03	499±8	2.0±0.03	34.0±1.0
Phenolic	11.48±0.11	618±8	1.0±0.02	29.0±1.0
Mixed sulfur-peroxide	5.26±0.02	678±6	1.0±0.03	24.0±1.0

Figure 6. Tan δ as a function of oscillation frequency for the MNR compounds prepared with various vulcanization systems.

< peroxide by vulcanization system. Therefore, the sulfur-containing systems (*i.e.*, sulfur or mixed sulfur-peroxide vulcanization system) provide the most energy storage with the highest rubber elasticity, while the MNR with peroxide curing system has the lowest elasticity with the highest energy dissipation. On the other hand, the phenolic-cured MNR vulcanizate shows intermediate moduli and loss factor.

3.2. Influence of vulcanization system choice on properties of dynamically cured MNR/TPC-ET blends

3.2.1. Time profiles of mixing torque and temperature

Figure 7 shows time profiles of torque and temperature during the mixing of the dynamically cured MNR/TPC-ET blends with various vulcanization systems. It can be seen that the mixing torque-time curve showed three peak locations, with the first one at the initial mixing when TPC-ET was added to the mixing chamber. The second peak at about the mixing time of 2 min occurs after incorporating the MNR
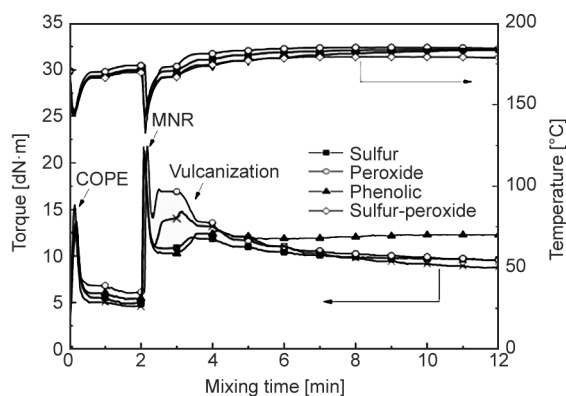

Figure 7. Mixing torque-time and mixing temperature-time curves for the dynamically cured MNR/TPC-ET blends prepared with various vulcanization systems.

compound that abruptly increased the mixing torque, which then immediately decreased. The third peak (*i.e.*, dynamic vulcanization peak) has varying heights, locations, and the area underneath the peak, due to the differences in the nature of dynamic vulcanization based on the choice of curing system. After the addition of MNR compounds, the MNR/TPC-ET blend is forced to transform from a co-continuous phase structure of a simple blend characteristic to separated vulcanizing rubber domains that are dispersed TPC-ET matrix during dynamic vulcanization [43]. The final blend morphology of the dynamically cured MNR/TPC-ET blend is a micron-sized dispersion of vulcanized MNR domains in the TPC-ET matrix. In Figure 7, it is seen that the peak height and area underneath the third peak can be ordered as peroxide > mixed sulfur-peroxide > phenolic > sulfur by the vulcanization system. We anticipate that the height and area underneath the third peak directly relate to the degree of vulcanization and the strength of crosslinks formed in the rubber phase. This is in good agreement with the maximum torque (Table 3), tensile strength, and hardness (Table 4), together with moduli and toughness (Figure 3) of the MNR compounds with different static vulcanization systems. However, the torque difference of the MNR compound based on static vulcanization has a similar trend in peak height and area under the third peak, but there is a discrepancy in delta torques of the phenolic and sulfur cured systems at 6.79 and 7.91 dN·m, respectively (Table 3). This may be attributed to the rubber phase in the dynamically cured MNR/TPC-ET blend with the sulfur curing system having a higher crosslink density than with the phenolic curing system. In Figure 7, the third peak location with different vulcanization systems corresponds to the scorch time (t_{s1}), or time till the onset of vulcanization, which is the time until one torque unit rise above the minimum torque. That is, the peroxide and mixed sulfur-peroxide curing systems gave the lowest scorch time of about 1.16 min (Table 3). It corresponds to the earliest peak location in dynamic vulcanization during mixing at about 3 min. On the other hand, the sulfur and phenolic curing systems gave scorch times of 2.31 and 2.44 min, which correspond to third peak locations in dynamic mixing at about 3.3 and 3.4 min, respectively. It is therefore concluded that the phenolic and sulfur curing systems offer improved process safety against premature vulcanization of the dynamically cured MNR/TPC-ET blends.

In Figure 7, it can be seen that the final mixing torque has a different trend than the area under the curve and the third peak location and can be ordered as phenolic > peroxide ≅ sulfur > mixed sulfur-peroxide by curing system. It is noted that the final mixing torque should have a close relation to the torque difference or the maximum torque of the statically cured MNR compounds (Table 3). However, the discrepancy may arise from the different shear and heat treatments in static (Table 3) and dynamic vulcanization (Figure 7). That is, the 12 min mixing time is optimal at 170 °C for dynamic vulcanization of the MNR/TPC-ET blends with the phenolic curing system to reach full vulcanization, as a plateau mixing torque vs. time curve is seen (Figure 7). However, in the static vulcanization of the MNR compound with the phenolic curing system (Figure 1) at the final testing time of 30 min, marching cure behavior with a steady increase in torque still exists. It means more time is needed to cure the MNR vulcanizate in static curing conditions fully. In Figure 7, other vulcanization systems (apart from the phenolic curing system) show a gradually decreasing trend of the mixing torque with time. This may be due to the destruction of some crosslinks after full vulcanization was reached. Therefore, the properties of the static and dynamic curing of MNR may be different due to different network characteristics and crosslink structures in the MNR vulcanizate and the MNR/TPC-ET blend. In Figure 7, it is also seen that the mixing temperature decreases after adding TPC-ET at the start of the mixing process and after incorporating the MNR compound at the mixing time of 2 min. After continued mixing with a rotor speed of 60 rpm, the mixing temperature is marginally increased due to shear heating and the exothermic reaction of rubber vulcanization [44].

3.2.2. Mechanical and morphological properties

Figure 8 shows stress-strain curves of dynamically cured MNR/TPC-ET blends prepared with different vulcanization systems. It is seen that Young's modulus (*i.e.*, initial slope in the linear region of the curves) of the blends can be ordered as phenolic > sulfur ≅ peroxide > mixed sulfur-peroxide by curing system. This corresponds to the trend of final mixing torques of dynamic vulcanization (Figure 7) where the blend with the phenolic system shows the highest. Still, the mixed sulfur-peroxide cured system shows the lowest final mixing torque and hence
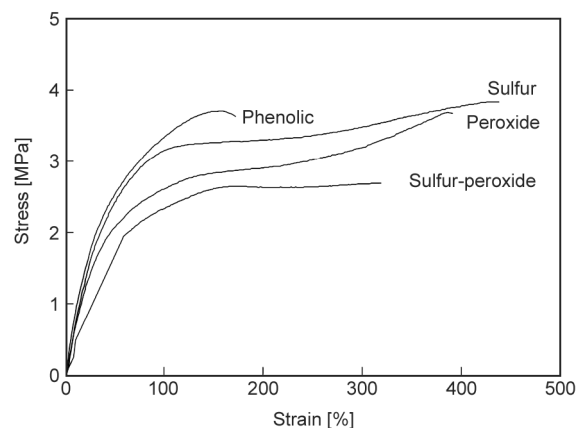

Figure 8. Stress-strain curves of dynamically cured MNR/TPC-ET blends prepared with various vulcanization systems.

lowest Young's modulus and stiffness. This also corresponds well to the morphological properties (SEM micrographs in Figure 9) and to average sizes of vulcanized MNR domains in the dynamically cured MNR/TPC-ET blends with various vulcanization systems, shown in Table 5. It can be seen that the smallest vulcanized rubber domains (about 1.8 μm) are found in the dynamically cured MNR/TPC-ET blend with the sulfur curing system (Figure 9a) and the largest domains (about 5.0 μm) are in the blend with the mixed sulfur-peroxide curing system (Figure 9d). Furthermore, the peroxide and phenolic curing systems show intermediate vulcanized rubber domain sizes at 2.5 and 3.5 μm (Figures 9b and 9c, respectively, and Table 5). It is noted that the smaller rubber domains result in less interfacial tension but, more interfacial area and interfacial adhesion, causing enhanced strength and other related properties of the dynamically cured MNR/ TPC-ET blends.

Figure 10 shows the tensile strength of dynamically cured MNR/TPC-ET blends with different vulcanization systems before and after aging. It can be seen that the tensile strength or strength at the break of the blend is in good agreement with the trend of Young's moduli (Figure 8) and with the average domain sizes of the vulcanized rubber particles (Table 5 and Figure 9). That is, the MNR/TPC-ET TPV with sulfur curing system has the highest tensile strength with the smallest vulcanized MNR domains, while the TPV with mixed sulfur-peroxide vulcanization system shows the lowest tensile strength with the largest rubber domains. The MNR/TPC-ET TPVs with peroxide and phenolic curing systems have intermediate tensile strengths and sizes of vulcanized MNR domains. In Figure 10, it is clear that the tensile
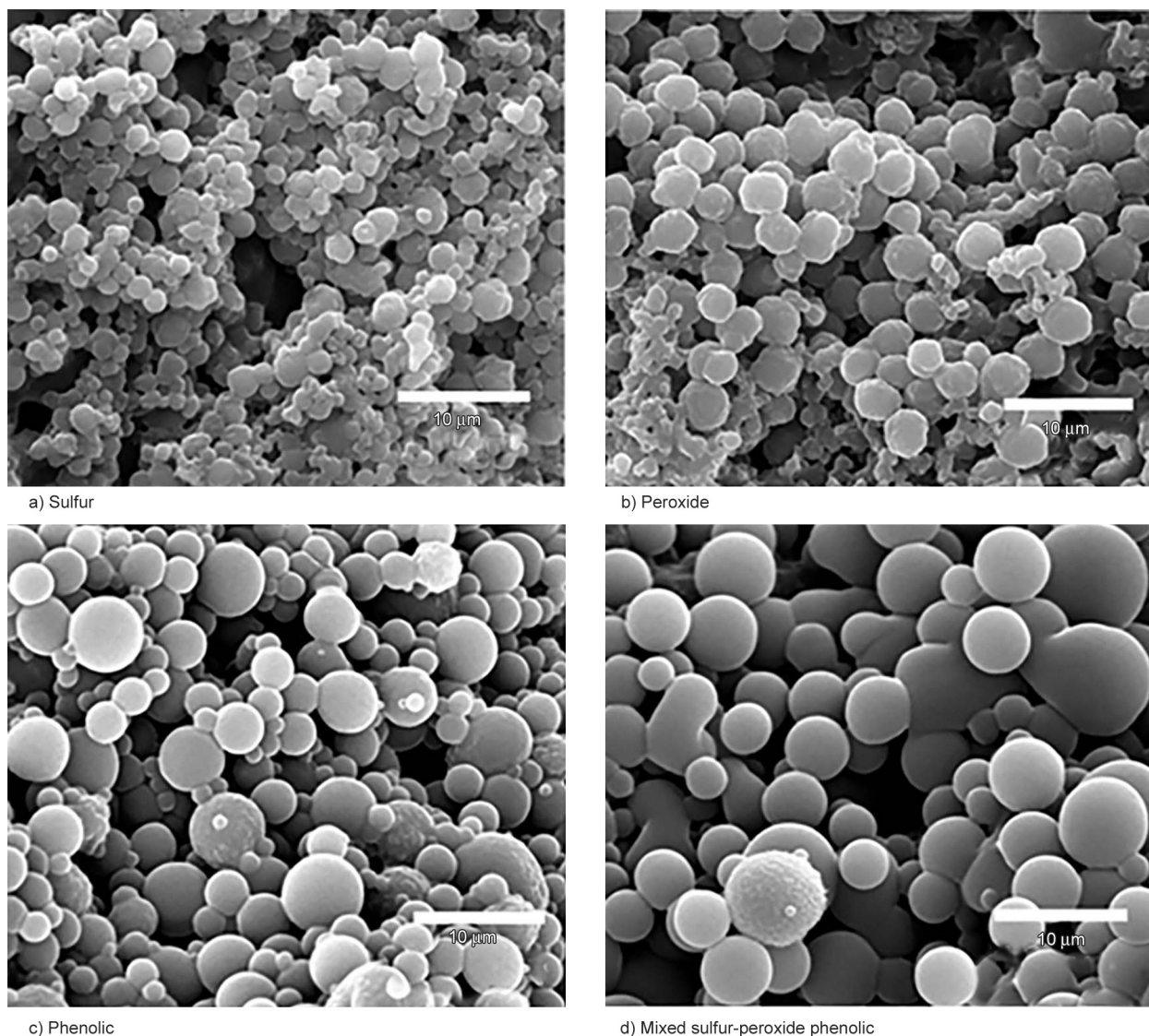
Figure 9. SEM micrographs of dynamically cured MNR/TPC-ET blends with various vulcanization systems. a) sulfur, b) peroxide, c) phenolic, and d) mixed sulfur-peroxide phenolic

strength of all TPVs increases after prolonged heat aging at 100 °C (for 22 h) tested according to ASTM D573. This may be due to an increase in newly formed crosslinks in the rubber vulcanizate, with increased crosslink density after the heat treatment. Also, the heat treatment may improve the interfacial adhesion between TPC-ET and MNR, with a proposed reaction shown in Figure 11. It is seen that a

chemical interaction between MNR with phenolic curing system and TPC-ET molecules at interfacial areas of MNR/TPC-ET TPV may occur via hydrogen
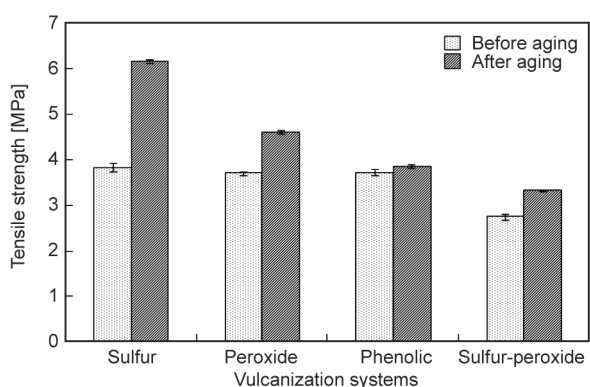
Table 5. Average particle size of vulcanized rubber domains in the dynamically cured MNR/TPC-ET blends prepared with various vulcanization systems.

Vulcanization system	Vulcanized rubber domain size [µm]
Sulfur	1.8±0.19
Peroxide	2.5±0.19
Phenolic	3.5±0.07
Mixed sulfur-peroxide	5.0±0.11

Figure 10. Tensile strength of dynamically cured MNR/TPC-ET blends prepared with various vulcanization systems, before and after aging.
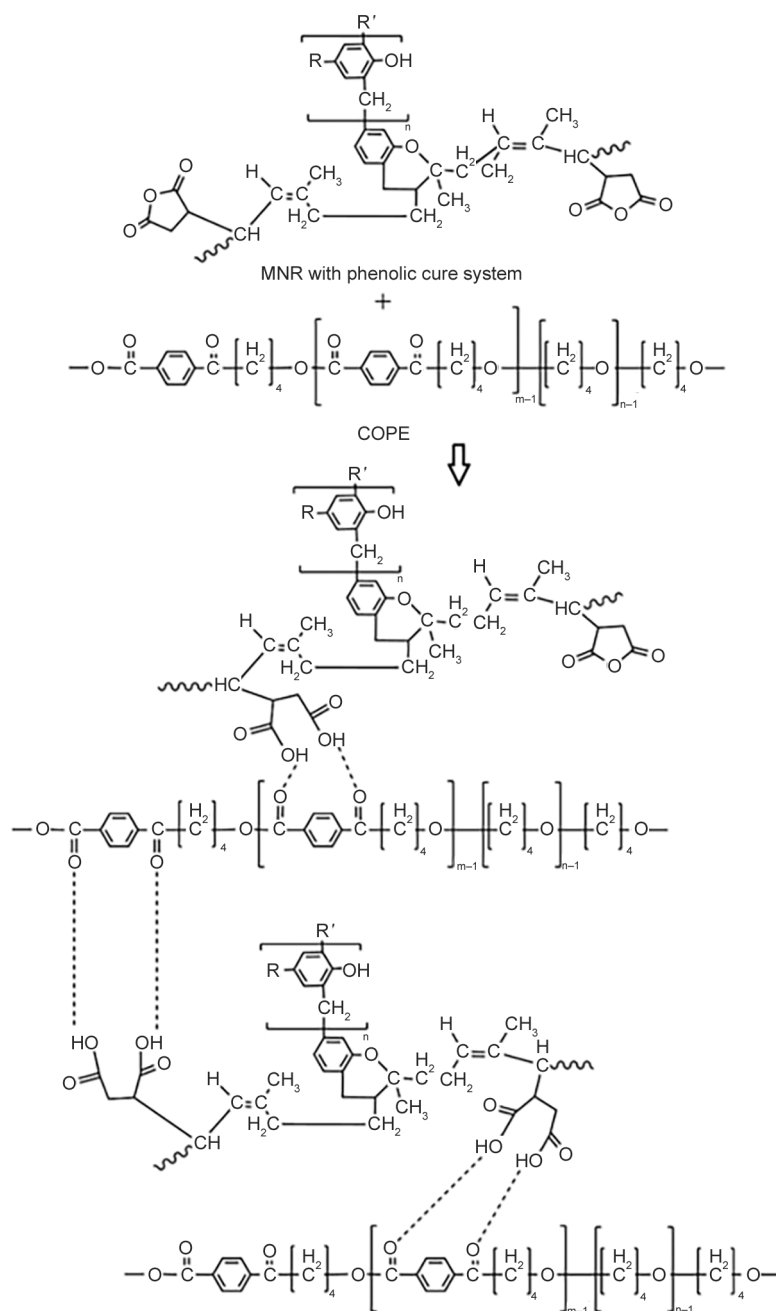
Figure 11. A possible chemical interaction via H-bonding of MNR with phenolic curing system and TPC-ET molecules at interfacial areas of MNR/TPC-ET TPV.

bonds. This is in agreement with the aging properties of NR composites with different sulfur curing systems, in which cases the overall crosslink densities increased with aging time and temperature [45]. In this work, various MNR/TPC-ET TPVs were aged by conditioning at 100 °C for 22 h in a multi-cell aging oven, Elastocon AB (Brämhult, Sweden). Likewise, under this static heat treatment, the rubber component with various vulcanization systems in the MNR/TPC-ET TPVs has the capacity to create newly formed crosslinks from the remaining curative residues and hence causes increases in the strength

properties. In a sulfur-cured case, some curatives such as free sulfur, cure accelerators, and their residues remained in the cured rubber compound. It is claimed that free sulfur is effective in increasing crosslink density during thermal aging [45].

This causes the MNR/TPC-ET TPV with a conventional sulfur curing system to have a prominent increase in crosslink density and hence in tensile strength properties after aging. Likewise, with the peroxide curing, the remaining peroxide residues are still reactive under aging and can react with MNR to form the new –C–C– crosslinks, increasing

the crosslink density and hence tensile strength, but this is at a lower level compared to the sulfur curing system. Furthermore, in TPV with phenolic curing, the least increased tensile strength is seen after heat aging. This may be due to the reaction mechanism to form Chroman rings that would need a longer time (Table 3 and Figure 7) and possibly also more energy. Also, steric hindrances to Chroman rings may retard the formation of the rubber polymer network. In Figure 10, it is also seen that the mixed sulfur-peroxide curing system also gave a higher tensile after aging due to the reactions of sulfur and peroxide curing agents.

Figure 12 shows elongation at break of the dynamically cured MNR/TPC-ET blends prepared with various vulcanization systems before and after aging. It can be seen that the elongation at break after aging of all TPVs also was slightly higher than before aging. This might be for the same reason, namely that all the vulcanization systems induced crosslinking with remnants of the crosslinking agents during static heat treatment of MNR, contributing to higher elastic properties. In addition, the elongation at break of various TPVs based on the different vulcanization systems has a similar trend with tensile strength, but the reverse trend is seen in the mixed sulfur-peroxide, and the phenolic cured system. This may be due to the constraint of Chroman rings in crosslinks of the phenolic cured TPV (Figure 2) and is in good agreement with Young's modulus and hence stiffness (Figure 8). This contributes to the rigidity of the crosslinked rubber and hence the MNR/TPC-ET TPV. Therefore, the phenolic cured material has the highest stiffness (as indicated by the highest Young's modulus in Figure 8), together with large-sized vulcanized rubber
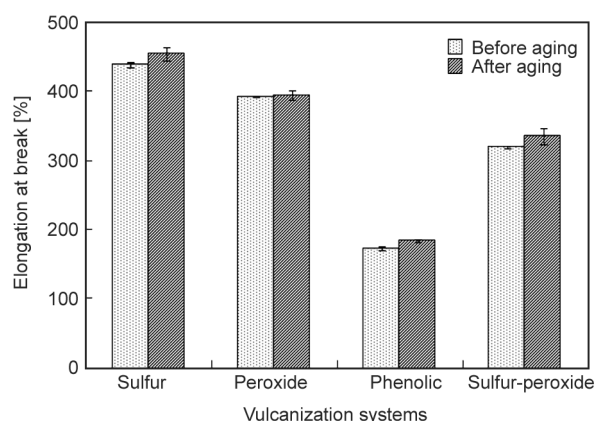
domains (Figure 9). The large vulcanized rubber particles may relate to the low content of Chroman rings in MNR during dynamic vulcanization and also to short scorch time, leading to low viscosity, shear and elongation being able to break down the vulcanizing MNR domains. This results in a lower crosslink density, as evidenced by the lowest torque difference (Table 3). Furthermore, the lower content of Chroman rings also results in a lesser interfacial surface area, weaker interfacial interactions between MNR and TPC-ET and hence larger vulcanized MNR domains (Figure 9).

Figure 13 shows the tension set and hardness (Shore A) of dynamically cured MNR/TPC-ET blends prepared with various vulcanization systems. It is noted that the tensile set (or tension set) testing of a rubber or thermoplastic elastomer evaluates the residual elongation of a test sample after being stretched and allowed to relax in a specified manner. This elongation consists of both permanent and recoverable components, thus, the tension set is used to measure the ability of a rubber sample to retain its elastic properties after extension. Therefore, a lower tension set means higher elastic properties of the material. In Figure 13, it is clear that the elastic properties in terms of tension set correspond to the trend of elongation at break as sulfur > peroxide > mixed sulfur-peroxide > phenolic by vulcanization system. Therefore, the phenolic and peroxide-cured MNR/TPC-ET TPVs with rigid crosslinks of Chroman rings and –C–C– linkages (Figure 4) have more rigidity and stiffness but less elasticity. However, the sulfidic linkages are more flexible with higher extensibility and elasticity (Figure 8). These also correspond to higher hardness of the phenolic and peroxide cured
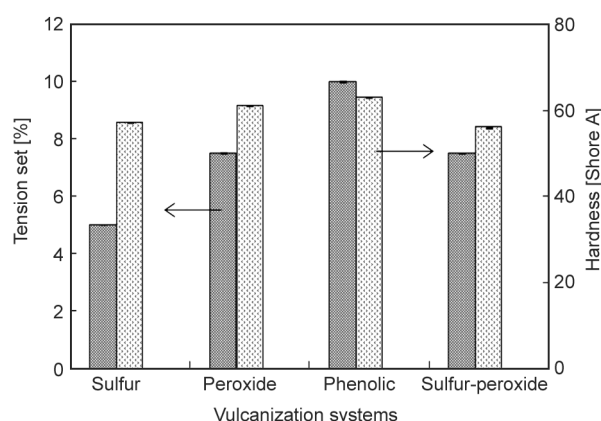

Figure 12. Elongation at break of dynamically cured MNR/TPC-ET blends prepared with various vulcanization systems, before and after aging.

Figure 13. Tension set and hardness (Shore A) of dynamically cured MNR/TPC-ET blends prepared with various vulcanization systems.

MNR/ TPC-ET TPVs than for the sulfur and mixed sulfur-peroxide cured TPVs.

4. Conclusions

Maleated natural rubber (MNR) was in-house prepared and compounded with four alternative vulcanization systems, *i.e.*, sulfur, peroxide, phenolic, and mixed sulfur-peroxide systems. We found that the peroxide and mixed sulfur-peroxide systems showed a plateau curing curve with an equilibrium state, while the sulfur system exhibited a slight reversion due to the breakdown of weak sulfidic linkages. Also, the phenolic system gives a marching cure. Dynamically cured MNR/TPC-ET blends using the four alternative MNR compounds were then prepared and characterized. It was found that the height and area underneath the third peak for dynamic vulcanization in the mixing torque *vs*. time curve relates to the degree of vulcanization and strength of crosslinks, which can be ordered as peroxide > mixed sulfur-peroxide > phenolic > sulfur by the vulcanization system. These are in good agreement with maximum torque, tensile strength, hardness, moduli, and toughness (the area underneath the stress-strain curve) for the MNR compounds prepared with static vulcanization. The location of the dynamic vulcanization peak also corresponds to the scorch time (t_{s1}) of the static vulcanization, where the peroxide and mixed sulfur-peroxide curing systems gave the shortest scorch time with the earliest peak location at a mixing time of about 3 min. The sulfur and phenolic systems had scorch times of 2.31 and 2.44 min and peak locations at 3.3 and 3.4 min, respectively. Therefore, the phenolic and sulfur systems offer more process safety against premature reactions in dynamically cured MNR/TPC-ET blends. It was also found that the TPV with sulfur curing system had mono-, di- and poly-sulfidic linkages in the rubber networks giving the smallest vulcanized rubber domains dispersed in the TPC-ET matrix, causing the highest interfacial adhesion and hence tensile strength, elongation at break, storage modulus, and rubber elasticity in terms of the lowest tension set and tan δ (in dynamic test). However, the phenolic cured TPV shows the highest stiffness, Young's modulus (*i.e.*, the highest slope at the initial part of the stress-strain curve), and large vulcanized rubber domains. This may be related to low contents of Chroman rings crosslinking the MNR networks, causing lower surface area and interfacial

interaction between MNR and TPC-ET phases. The mixed sulfur-peroxide and peroxide curing systems showed intermediate tension set, tan δ, and elongation at break. Furthermore, the tensile strength and elongation at break increased in all cases after aging by heat treatment. This is due to the continued curing reactions of MNR during heat treatment. The phenolic-cured TPV showed the least change in tensile properties from aging, due to slow reactions that form Chroman rings. Therefore, it is concluded that the sulfur-cured system offers the best overall properties of the MNR/TPC-ET TPV.

Acknowledgements

References

[1] Wei Y., Zhang H., Wu L., Jin L., Liao S.: A review on characterization of molecular structure of natural rubber. MOJ Polymer Science, **1**, 197–199 (2017).
https://doi.org/10.15406/mojps.2017.01.00032

[2] Tarachiwin L., Sakdapipanich J., Ute K., Kitayama T., Bamba T., Fukusaki E., Kobayashi A., Tanaka Y.: Structural characterization of α-terminal group of natural rubber. 1. Decomposition of branch-points by lipase and phosphatase treatments. Biomacromolecules, **6**, 1851–1857 (2005).
https://doi.org/10.1021/bm058003x

[3] Tarachiwin L., Sakdapipanich J., Ute K., Kitayama T., Tanaka Y.: Structural characterization of α-terminal group of natural rubber. 2. Decomposition of branch-points by phospholipase and chemical treatments. Biomacromolecules, **6**, 1858–1863 (2005).
https://doi.org/10.1021/bm058004p

[4] Indrajati I. N., Setyorini I.: Mechanical properties, set and rebound resilience characteristics of natural rubber/ethylene vinyl acetate blend on various ratios. Macromolecular Symposia, **391**, 1900136 (2020).
https://doi.org/10.1002/masy.201900136

[5] Lopattananon N., Kraibut A., Sangjan R., Seadan M.: Ionic elastomer blends of zinc salts of maleated natural rubber and carboxylated nitrile rubber: Effect of grafted maleic anhydride. Journal of Applied Polymer Science, **105**, 1444–1455 (2007).
https://doi.org/10.1002/app.26312

[6] Hemsri S., Thongpin C., Supatti N., Manomai P., Socharoentham A.: Bio-based blends of wheat gluten and maleated natural rubber: Morphology, mechanical properties and water absorption. Energy Procedia, **89**, 264–273 (2016).
https://doi.org/10.1016/j.egypro.2016.05.034

[7] Hayeemasae N., Sensem Z., Sahakaro K., Ismail H.: Maleated natural rubber/halloysite nanotubes composites. Processes, **8**, 286 (2020).
https://doi.org/10.3390/pr8030286

[8] Zeng Z., Ren W., Xu C., Lu W., Zhang Y., Zhang Y.: Maleated natural rubber prepared through mechanochemistry and its coupling effects on natural rubber/cotton fiber composites. Journal of Polymer Research, **17**, 213–219 (2010).
https://doi.org/10.1007/s10965-009-9307-6

[9] Karger-Kocsis J.: Thermoplastic rubbers *via* dynamic vulcanization. in 'Polymer blends and alloys' (eds.: Shonaike G. O., Simon G. P.) Marcel Dekker, New York, 125–153 (1999).

[10] Drobny J. G.: Handbook of thermoplastic elastomers. William Andrew, New York (2014).

[11] Wang W., Lu W., Kang N-G., Mays J., Hong K.: Thermoplastic elastomers based on block, graft, and star copolymers. 'Elastomers' (ed.: Cankaya N.) IntechOpen, London, 97–119 (2017).
https://doi.org/10.5772/intechopen.68586

[12] Sripornsawat B., Saiwari S., Nakason C.: Thermoplastic vulcanizates based on waste truck tire rubber and copolyester blends reinforced with carbon black. Waste Management, **79**, 638–646 (2018).
https://doi.org/10.1016/j.wasman.2018.08.038

[13] Dubinin S., Duchacek V.: Thermoplastic vulcanizates (in Czech). Chemické Listy, **102**, 166–172 (2008).

[14] Utara S., Boochathum P.: Novel dynamic vulcanization of polyethylene and ozonolysed natural rubber blends: Effect of curing system and blending ratio. Journal of Applied Polymer Science, **120**, 2606–2614 (2010).
https://doi.org/10.1002/app.33466

[15] Passador F. R., Rojas G. J. A., Pessan L. A.: Thermoplastic elastomers based on natural rubber/polypropylene blends: Effect of blend ratios and dynamic vulcanization on rheological, thermal, mechanical, and morphological properties. Journal of Macromolecular Science Part B: Physics, **52**, 1142–1157 (2013).
https://doi.org/10.1080/00222348.2012.756323

[16] Sasdipan K., Kaesaman A., Vennemann N., Nakason C.: Influence of blend ratio on properties of novel thermoplastic vulcanizates based on copolyester/epoxidized natural rubber blends. Iranian Polymer Journal, **23**, 965–977 (2014).
https://doi.org/10.1007/s13726-014-0292-1

[17] Mandal A. K., Chakraborty D., Siddhanta S. K.: Effect of the compatibilizer, on the engineering properties of TPV based on Hypalon® and PP prepared by dynamic vulcanization. Journal of Applied Polymer Science, **131**, 40312 (2014).
https://doi.org/10.1002/app.40312

[18] Xiong J., Cui R., Xu C., Ding J., Chen Y.: Silica-reinforced ethylene propylene diene monomer/polypropylene thermoplastic vulcanizates with interfacial compatibilized by methylacrylate. Polymer Composites, **42**, 701–713 (2020).
https://doi.org/10.1002/pc.25859

[19] Pichaiyut S., Nakason C., Kaesaman A., Kiatkamjornwong S.: Influences of blend compatibilizers on dynamic, mechanical, and morphological properties of dynamically cured maleated natural rubber and high-density polyethylene blends. Polymer Testing, **27**, 566–580 (2008).
https://doi.org/10.1016/j.polymertesting.2008.03.004

[20] Sun Z., Zhang Y., Shao H., He A.: *In situ* reactive compatibilization of polypropylene/trans-1,4-poly(isoprene-*co*-butadiene) rubber (TBIR) blends with balanced toughness and stiffness *via* dynamic vulcanization. Reactive and Functional Polymers, **14**, 60–68 (2019).
https://doi.org/10.1016/j.reactfunctpolym.2019.06.001

[21] Fagundes E. C. M., Jacobi M. A. M.: Influence of a crosslinked system on the morphology and properties of TPVs based on PA/NBR. Journal of Applied Polymer Science, **123**, 3072–3080 (2012).
https://doi.org/10.1002/app.34885

[22] Tanrattanakul T., Kosonmetee K., Laokijcharoen P.: Polypropylene/natural rubber thermoplastic elastomer: Effect of phenolic resin as a vulcanizing agent on mechanical properties and morphology. Journal of Applied Polymer Science, **112**, 3267–3275 (2009).
https://doi.org/10.1002/app.29816

[23] Fan J., Cao L., Huang J., Yuan D., Chen Y.: The construction and verification of toughening model and formula of binary poly(lactic acid)-based TPV with *co*-continuous structure. Materials Chemistry and Physics, **231**, 95–104 (2009).
https://doi.org/10.1016/j.matchemphys.2019.04.014

[24] Paran S. M. R., Naderi G., Ghoreishy M. H. R., Heydari A.: Enhancement of mechanical, thermal and morphological properties of compatibilized graphene reinforced dynamically vulcanized thermoplastic elastomer vulcanizates based on polyethylene and reclaimed rubber. Composites Science and Technology, **161**, 57–65 (2018).
https://doi.org/10.1016/j.compscitech.2018.04.006

[25] Leite P. R. S., Soares B. G., Sirqueira A. S.: Dynamically vulcanized polypropylene/styrene–butadiene rubber blends: The effect of a peroxide/bismaleimide curing system and composition. Journal of Applied Polymer Science, **120**, 981–990 (2011).
https://doi.org/10.1002/app.33123

[26] Sain M. M., Oravec J., Lacok J., Beniska J.: Studies on the modification of nitrile rubber–poly(vinyl chloride) blends. Effect of nonconventional vulcanization systems. Acta Polymerica, **40**, 648–652 (1989).
https://doi.org/10.1002/actp.1989.010401008

[27] Manleh C., Nakason C., Lopattananon N., Kaesaman A.: Effect of sulfur donor on properties of thermoplastic vulcanizates based on NR/PP. Advanced Materials Research, **626**, 54–57 (2012).
https://doi.org/10.4028/www.scientific.net/AMR.626.54

[28] Faibunchan P., Nakaramontri Y., Chueangchayaphan W., Pichaiyut Y., Kummerlöwe C., Vennemann N., Nakason C.: Novel biodegradable thermoplastic elastomer based on poly(butylene succinate) and epoxidized natural rubber simple blends. Journal of Polymers and the Environment, **26**, 2867–2880 (2018).
https://doi.org/10.1007/s10924-017-1173-4

[29] Nakason C., Saiwari S., Kaesaman A.: Thermoplastic vulcanizates based on maleated natural rubber/polypropylene blends: Effect of blend ratios on rheological, mechanical, and morphological properties. Polymer Engineering & Science, **46**, 594–600 (2006).
https://doi.org/10.1002/pen.20498

[30] Nakason C., Saiwari S.: Effect of grafted maleic anhydride content and recyclability of dynamically cured maleated natural rubber/polypropylene blends. Journal of Applied Polymer Science, **110**, 4071–4078 (2008).
https://doi.org/10.1002/app.29070

[31] Nakason C., Saiwari S., Kaesaman A.: Rheological properties of maleated natural rubber/polypropylene blends with phenolic modified polypropylene and polypropylene-*g*-maleic anhydride compatibilizers. Polymer Testing, **25**, 413–423 (2005).
https://doi.org/10.1016/j.polymertesting.2005.11.006

[32] Tanrattanakul V., Jaratrotkamjorn R., Juliwanlee W.: Effect of maleic anhydride on mechanical propertiesand morphology of poly(lactic acid)/natural rubber blend. Songklanakarin Journal of Science and Technology, **42**, 697–704 (2020).

[33] Mohammad N. N. B., Arsad A., Rahmat A. R., Sani N. S. A.: Effects of maleated natural rubber on mechanical properties of polylactic acid/natural rubber blends. Materials Science Forum, **819**, 284–289 (2015).
https://doi.org/10.4028/www.scientific.net/MSF.819.284

[34] Pulungan A. N., Wirjosentono B., Kurniawan E., Sihombin J. L., Hendrana S.: Polymer electrolyte membrane fuel cell from sulfonated polystyrene and maleated natural rubber blend. Rasayan Journal of Chemistry, **13**, 1112–1123 (2020).
https://doi.org/10.31788/RJC.2020.1325616

[35] Pulungan A. N., Wirjosentono B., Hendrana S.: X-ray diffraction and morphology studies of sulfonated polystyrene and maleated natural rubber blend with PE-*g*-MA as compatibilised. in 'Proceedings of the 1st International conference on chemical science and technology innovation, Medan, Indonesia, Vol 1, 324–328 (2019).
https://doi.org/10.5220/0008935003240328

[36] Kahar A. W. M., Ismail H.: High-density polyethylene/natural rubber blends filled with thermoplastic tapioca starch: Physical and isothermal crystallization kinetics study. Journal of Vinyl and Additive Technology, **22**, 191–199 (2016).
https://doi.org/10.1002/vnl.21422

[37] Nakason C., Saiwaree S., Tatun S., Kaesaman A.: Rheological, thermal and morphological properties of maleated natural rubber and its reactive blending with poly(methyl methacrylate). Polymer Testing, **25**, 656–667 (2006).
https://doi.org/10.1016/j.polymertesting.2006.03.011

[38] Nakason C., Kaesaman A., Samoh S., Homsin S., Kiatkamjornwong S.: Rheological properties of maleated natural rubber and natural rubber blends. Polymer Testing, **21**, 449–455 (2002).
https://doi.org/10.1016/S0142-9418(01)00109-X

[39] Nakason C., Kaesaman A., Supasanthitikul P.: The grafting of maleic anhydride onto natural rubber. Polymer Testing, **23**, 35–41 (2004).
https://doi.org/10.1016/S0142-9418(03)00059-X

[40] Grestenberger G., Potter G., Grein C.: Polypropylene/ethylene-propylene rubber (PP/EPR) blends for the automotive industry: Basic correlations between EPR-design and shrinkage. Express Polymer Letters, **8**, 282–292 (2014).
https://doi.org/10.3144/expresspolymlett.2014.31

[41] Nakason C., Nuansomsri K., Kaesaman A., Kiatkamjonwong S.: Dynamic vulcanization of natural rubber/high density polyethylene blends: Effect of compatibilization, blend ratio and curing system. Polymer Testing, **25**, 782–796 (2006).
https://doi.org/10.1016/j.polymertesting.2006.05.001

[42] Kleps T., Piaskiewicz M., Parasiewicz W.: The use of thermogravimetry in the study of rubber devulcanization. Journal of Thermal Analysis and Calorimetry, **60**, 271–277 (2000).
https://doi.org/10.1023/A:1010134315762

[43] Faibunchan P., Pichaiyut S., Kummerlöwe C., Vennemann N., Nakason C.: Green biodegradable thermoplastic natural rubber based on epoxidized natural rubber and poly(butylene succinate) blends: Influence of blend proportions. Journal of Polymers and the Environment, **28**, 1050–1067 (2020).
https://doi.org/10.1007/s10924-020-01655-5

[44] Hada K., Nakajima T.: Studies on the thermochemistry of the vulcanization of rubber. VII. Heating curves for the vulcanization of the system: Raw rubber–sulfur (2). Rubber Chemistry and Technology, **6**, 56–63 (1933).
https://doi.org/10.5254/1.3547537

[45] Choi S-S., Kim J-C., Lee S. G., Joo Y. L.: Influence of the cure systems on long time thermal aging behaviors of NR composites. Macromolecular Research, **16**, 561–556 (2008).
https://doi.org/10.1007/BF03218560

express
polymer letters

Research article

The effect of crosslink density on the cold crystallization behavior of polybutadiene elastomers

Arpan Datta Sarma[1,2]*, Erathimmanna Bhoje Gowd*[3], Amit Das[1], Gert Heinrich[1,4]

[1]Leibniz-Institut für Polymerforschung Dresden e.V, D-01069 Dresden, Germany
[2]Luxembourg Institute of Science and Technology, 4362 Esch-sur-Alzette, Luxembourg
[3]Materials Science and Technology Division, CSIR-National Institute for Interdisciplinary Science and Technology, Trivandrum, 695019 Kerala, India
[4]Technische Universität Dresden, 01062 Dresden, Germany

Abstract. This report presents an insightful investigation of the cold crystallization behavior of sulfur-crosslinked polybutadiene elastomers. The influence of crosslink density on the cold crystallization activities of sulfur-crosslinked polybutadiene rubber (BR) is investigated using differential scanning calorimetry, dynamic mechanical analysis, and X-ray techniques. A significant increase in storage modulus (E') is observed at a temperature just above the glass transition temperature (T_g). This behavior was found to be highly dependent on the crosslink density of the rubber. The dynamic mechanical behavior of the sulfur crosslinked BR is supported by further studies using differential scanning calorimetry and low-temperature X-ray diffraction. This study could contribute to a better understanding of the behavior of BR-containing tire tread rubbers at lower temperatures.

Keywords: *butadiene rubber, cold crystallization, low-temperature modulus, low-temperature X-ray diffraction, dynamic mechanical analysis*

1. Introduction

Crystallization is a process by which molecular building blocks spontaneously organize into an orderly three-dimensional structure to form a solid substance. The crystallization behavior and crystallinity of polymers are different from low-molecular-weight materials [1]. Long-chain polymeric molecules can consist of both a 'crystallizable part' and a 'non-crystallizable part' (amorphous part). The non-crystallizable, amorphous part consists of chain ends, branching points, twisting points, entanglements, and tie molecules [2]. If it is possible to maintain equilibrium throughout the crystallization process and if the initial distribution of the crystallizable-amorphous fraction is known, the equilibrium distribution of crystallites as a function of temperature can be described by Flory's theory [2]. Despite its popularity in polymer physics, the clear and complete concept of the polymer crystallization process has not yet been well established [3–5]. The main reason for this fact is that the process of crystallization depends on both equilibrium (thermodynamically controlled) and non-equilibrium (kinetically controlled) factors which are very complex for polymeric materials [6].

Extensive works have been done to understand the crystallization behavior of semicrystalline polymers. A semicrystalline polymer is capable of crystallizing not only from the molten state (known as melt crystallization) but also from the glassy phase (known as cold crystallization). Limited studies have been reported on the cold crystallization behavior of polymers compared to the melt crystallization behavior.

Cold crystallization can influence the mechanical properties of the products during their usage in real environments. Above the glass transition temperature, cold crystallization can occur by the formation of folded lamellar morphology and results in semicrystalline morphology at the nanometer level [7]. According to Wunderlich *et al*. [2], this is a random type of crystallization that occurs without any redistribution of molecules but allows only the neighboring amorphous state to crystallize. Due to the high molecular weight and randomness, rubber molecules are generally amorphous [8]. However, a few rubbery materials with high *cis* content show some exceptional behaviors regarding specific orientation and crystallization induced by strain and/or low temperature. Rubbery materials, namely polyisoprene (natural and synthetic), polybutadiene (BR), hydrogenated acrylonitrile butadiene rubber (HNBR), and polychloroprene fall in that category [9–12]. In a recent paper by Schawe *et al*. [13], the structural relaxation of HNBR in the glass temperature range is discussed, where the tetramethylene unit (produced by the hydrogenation of the butadiene unit of the HNBR copolymer) offers the crystalline tendency at glassy region. It is emphasized that a rigid amorphous fraction around the small crystallites limits the further growth of the crystals [13].

It has been reported already that the rate of crystallization of polybutadiene depends on the microstructural purity [14]. Polybutadienes with ~97% *cis* content show an almost ten times faster rate of crystallization than the same material with ~90% cis content [15]. The rate of the crystallization can be denoted as crystallization half-time, the time required for the crystallization of half of the crystallizable segments. The value of crystallization half-time is calculated to be infinite at glass transition temperature and equilibrium melting temperature. In addition, the heating/cooling rate has been identified as a key parameter in controlling the crystallization/cold crystallization behaviors of elastomeric systems [12].

Several techniques have been developed to study the crystallization of semicrystalline polymers. Out of them, differential scanning calorimetry (DSC) [16–18], wide-angle X-ray scattering [7, 19], transmission electron microscopy (TEM) [20], atomic force microscopy (AFM) [21], fluorescence spectroscopy [22], infrared (IR) spectroscopy [16, 23] and vibrational circular dichroism [24] are well-practiced. There are very limited reports regarding the cold crystallization of rubbery materials. Besides, the possibility of using mechanical characterization methods (*e.g.*, dynamic mechanical analysis, DMA) to understand the cold crystallization behaviors has been neglected throughout. The lack of a detailed report on cold crystallization behaviors of rubbery materials and its dependency on the crosslink density of the system have inspired the authors to investigate the current domain.

The main aim of the current topic was to understand the cold crystallization behavior of polybutadiene rubber networks having different crosslink densities. To follow the mentioned aim, butadiene rubber was compounded with different amounts of crosslinking chemicals and vulcanized. The compounds were designed to show different crosslink densities. In order to understand the effect of crosslink density on the cold crystallization behavior of the system, the vulcanized rubber compounds were characterized by DSC, low-temperature X-ray diffraction, and DMA.

2. Experimental
2.1. Materials
Neodymium-catalyzed polybutadiene rubber (Buna CB 24) with 96% cis content and Mooney viscosity of 44 (ML (1+4) at 100 °C) was procured from LANXESS Deutschland GmbH (Köln, Germany). ZnO was procured from ACS reagent, while stearic acid was purchased from Fisher Scientific GmbH (Schwerte, Germany). *N*-cyclohexyl-2-benzothiazole sulfenamide (CBS; Vulkacit CZ/ EG-C) was purchased from Lanxess. Sulfur (S), and toluene (95%) both were purchased from Thermo Fisher Scientific (Geel, Belgium). All the rubber chemicals used for the present study were of technical grade.

2.2. Mixing
All the mixing experiments were carried out in a laboratory-scale two-roll mill (Polymix 110 L, size: 203×102 mm, Servitech GmbH, Wustermark, Germany) at 40 °C. First, the rubber was masticated (~1 min) and a uniform band was produced on the front roll. The nip gap was adjusted (~1 mm) to obtain a suitable bank on top of the mill. ZnO and stearic acid (St. A.) were added and mixed with the rubber for another two minutes. The curatives (CBS and S) were then added to the bank and mixed for further two more minutes until a uniform rubber compound is formed. After complete mixing, the compounded rubber was sheeted out and cooled. The

Table 1. Formulation of a series of polybutadiene compounds formulated with different amounts of curatives; the formulations are given in parts per hundred parts of rubber [phr] unit.

Sample name	Polybutadiene	ZnO	St A	CBS	S
Sample 1	100	3	2	0.75	1
Sample 2	100	3	2	1.50	2
Sample 3	100	3	2	2.25	3

samples were then matured for 3–4 hours and subjected to a rheological analysis using a rotorless vulcameter, Elastograph (Germany), at 150 °C. The optimum cure time was calculated from the respective cure curves obtained from the vulcameter. The optimum cure time was defined by the time required to achieve 90% of the maximum-observed cure torque as obtained from the vulcameter. The rubber compounds were then cured with respect to their cure times using a hot press (Fontijne Holland, Model TP400, Delft, The Netherlands), operating at a temperature of 150 °C temperature and a pressure of 15 MPa. A square shape picture frame mold was used to shape the materials. Depending on the specific gravity of the material and the geometry of the mold an appropriate amount of material was placed inside the mold, resulting in a 1.9–2.1 mm thick rubber sheet. The recipes for all the rubber samples are shown in Table 1. It is worth noting that the ratio between the curing agents (CBS and S) remained the same throughout the formulation of the different rubber compounds.

2.3. Crosslink density
A small piece (0.10±0.02 g) of a square-shaped cured rubber sample was kept in toluene (~20 ml) in a stopped bottle. The solvent was changed after every 24 hours, and the swollen weight of the sample was noted. After the equilibrium swelling was reached (which was confirmed by the same weight of the rubber samples for two consecutive days), the samples were taken out, the excess solvent was wept by blotting paper, and the swollen weight was noted. The sample was then dried (at 60 °C in an oven for 6–8 hours) and weighed again. The crosslink density was estimated by the Flory-Rehner equation [25–27], as described in Equation (1):

$$\nu_e = \frac{-\ln(1-V_r) + V_r + \chi V_r^2}{V_1\left(V_r^{1/3} - \frac{V_r}{2}\right)} = \frac{\rho_p}{M_c} \tag{1}$$

where ν_e is the effective number of chains in a real network/unit volume, V_r is the polymer volume fraction in a swollen network in equilibrium with pure solvent and can be calculated using Equation (2). χ is designated as polymer-solvent interaction parameter and V_1 is the solvent's molar volume. The molecular weight of the polymer segment between two successive crosslinks (M_c) can be expressed as a ratio of the density of the polymer ($\rho_p = 0.91$ g/cm^3) and the crosslink density of the composite [28]:

$$V_r = \frac{\frac{\text{Weight of dry rubber}}{\text{Density of rubber}}}{\frac{\text{Weight of dry rubber}}{\text{Density of rubber}} + \frac{\text{Weight of absorbed solvent}}{\text{Density of solvent}}} \tag{2}$$

2.4. Differential scanning calorimetry
The cured rubber samples were subjected to a calorimetric study using a differential scanning calorimeter (DSC), Q2000 V24.11 (TA Instruments, USA). The studies were performed with ~10±2 mg of cured samples using standard aluminum pans in an inert atmosphere of nitrogen. The experiments were conducted in a temperature range of –90 to 100 °C with a heating/cooling rate of 3 °C per minute. The samples were first cooled from room temperature to –90 °C, then successive heating, cooling, and heating cycle were performed for all the samples.

2.5. Low-temperature X-ray scattering
Low-temperature X-ray scattering experiments were carried out using a XEUSS X-ray scattering system from Xenocs (operated at 50 kV and 0.60 mA) in transmission geometry using Cu K$_\alpha$ radiation (wavelength, $\lambda = 1.54$ Å). The distance between the sample and detector was calibrated using a silver behenate. The scanning was carried out at different temperatures using a hot stage fitted with liquid nitrogen-flowing equipment. The degrees of crystallinity, χ_c, of different samples were calculated using Equation (3) [29]. The size of the crystallites were estimated using the Scherrer equation [30], with a value of the Scherrer constant of 0.9 [31]:

$$\chi_c = \frac{A_c}{A_a + A_c} \tag{3}$$

A_c and A_a are the areas of the crystalline peak and the amorphous signal, respectively, from the deconvoluted X-ray plots.

2.6. Dynamic mechanical analysis

The samples for dynamic mechanical analysis were punched out from the cured rubber sheet with a dimension of $10 \times 5 \pm 0.1 \times 2 \pm 0.1$ cm ($L \times B \times T$) using an internally customized die. The samples were then conditioned for 16–20 hours at $23 \pm 3\,°C$ before the experiment. Temperature sweep experiments were performed in tensile mode using a dynamic mechanical analyzer GABO EPLEXOR® (Netzsch, Germany) with a 2000 N load cell. The measurements were carried out within the temperature range of -120 to $+80\,°C$ with a heating rate of $2\,°C/min$ at a frequency of 10 Hz under 1% static and 0.2% dynamic strain (strain-controlled mode). The samples were first cooled from room temperature to $-120\,°C$, then the experiments were carried out. A soaking time of 60 s was provided to allow the sample to equilibrate with the starting temperature before the start of each cycle.

2.7. Plotting and data interpretation

OriginPro 2019b was used to plot all the results. The inbuild 'Gaussian' function in that software was used to perform the deconvolution of low-temperature X-ray scattering plots. The deconvoluted plots were then used for the calculation of the degree of crystallinity and size of crystallites.

3. Results and discussion

3.1. Crosslink densities of different rubber samples

All the cured rubber samples were subjected to crosslink density measurement via the equilibrium swelling method taking toluene as the solvent (molar volume $V_1 = 106.3$ cm^3/mol). The value of the polymer-solvent interaction parameter ($\chi = 0.34$) was used in the calculation as referred in previous reports [32, 33]. The values of the estimated crosslink densities and the values of the molecular weights between the successive crosslinks of all the samples are collected and tabulated in Table 2. From Table 2, a change in the order of magnitude of crosslink densities can be observed. As expected, the values of

crosslink densities of the samples are proportional to the content of curatives in the formulation.

3.2. Differential scanning calorimetric analysis of different cured rubber samples

The cooling and the second heating curves as obtained from DSC measurements are shown in Figure 1, where the cooling cycles are denoted by dotted lines, and the heating cycles are denoted by solid ones. During the cooling cycle, exothermic peaks (around -60 to $-45\,°C$) associated with melt crystallization were observed for Samples 1 and 2. Sample 1 showed a sharp crystallization peak (FWHM = 11.3), while the crystallization peak for Sample 2 was found to be broad (FWHM = 17.9). The sharpness of the exothermic peak may indicate the homogeneity of the crystal structure. During the second heating cycle, exothermic peaks associated with cold crystallization were observed (around -66 to $-55\,°C$) for Samples 2 and 3. The width of the cold crystallization peak for Sample 2 and Sample 3 were found to be comparable (FWHM for Sample 2 = 11.3 *vs.* Sample 3 = 11.6). The exothermic peak of cold crystallization was found to be followed by an endothermic peak (around -30 to $-15\,°C$) for all the samples,
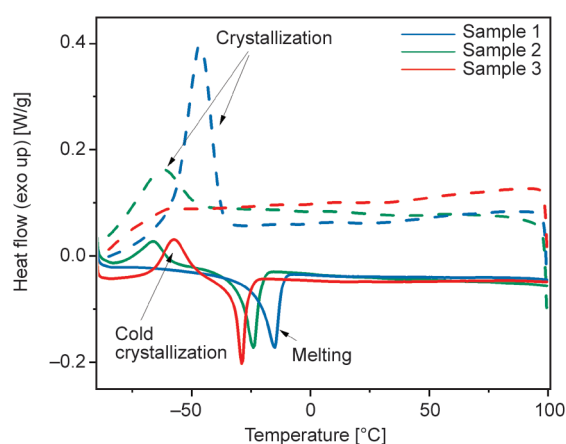

Figure 1. Cooling and second heating cycles of polybutadiene rubber samples with different crosslink densities as obtained from DSC studies. The cooling curves are shown by the dotted lines where the heating curves are designated by solid lines.

Table 2. Crosslink densities of cured polybutadiene samples containing different amounts of curatives.

Sample name	Crosslink density [mol/cm^3]	Average molecular weight between two successive crosslinks [g/mol]
Sample 1	$8.8 \cdot 10^{-5} \pm 2 \cdot 10^{-6}$	$10\,300 \pm 350$
Sample 2	$19.0 \cdot 10^{-5} \pm 1 \cdot 10^{-6}$	$4\,800 \pm 48$
Sample 3	$22.6 \cdot 10^{-5} \pm 1 \cdot 10^{-6}$	$4\,000 \pm 30$

which might denote the melting of the crystals. Associating the exothermic peak intensities with the percentage of crystallinity, a decreasing tendency of the percentage of crystallinity was observed from the figure as a function of crosslink density. It can be argued that due to the increased crosslink density, it was difficult for the rubber chains to organize themselves to attain regular structures. The argument can be supported by the almost negligible peak intensity of crystallization for Sample 3 during the cooling cycle. On the other hand, with the lowest crosslink density, it was most favorable for the molecules of Sample 1 to form the crystalline domains, which was reflected by the highest exothermic peak intensity during the cooling cycle.

Due to the constraints imposed by the crosslinked structure, the molecules of the highly crosslinked samples (Sample 2 and Sample 3) were unable to align during the cooling cycle. Because of this inability, the molecules tend to orient themselves during the heating cycle. It is possible that due to the low degree of crosslinking, the molecules of Sample 1 crystallized during cooling and no cold crystallization was observed during the heating cycle. The molecular mobility caused by the thermal energy has contributed to the more crosslinked molecules arranging themselves in regular order and achieving a kind of crystallinity. This phenomenon can be related to cold crystallization. As the process is kinetically limited for Sample 3, the cold crystallization peak appears at a higher temperature for this sample. It should also be noted that a higher chance of crystallization during the cooling cycle is associated with a lower chance of cold crystallization during the heating cycle.

This statement can be supported by the values of enthalpies tabulated in Table 3, where it is shown that the sum of the enthalpy of melt crystallization (ΔH_{cry}) and the enthalpy of cold crystallization (ΔH_{cold}) is equal to the melting enthalpy (ΔH_{melt}). The melting enthalpy can be regarded as a measure of the overall

percentage of crystallinity. With the lowest crosslink density, Sample 1 shows the highest percentage of crystallinity as shown in Table 3.

3.3. Low-temperature X-ray diffraction studies of different cured rubber samples

Low-temperature X-ray diffraction studies were conducted to understand the effect of crosslink density on the cold crystallization behavior of polybutadiene elastomer. The study was conducted within the temperature range of –100 and 20 °C. The diffraction patterns were recorded at a regular interval of 20 °C while heating the melt-cooled samples and are reported in Figure 2. Two distinct peaks corresponding to the crystalline domains of the crosslinked polybutadiene elastomer at 2θ of 19° and 22.7° can be seen in the diffraction patterns of the individual samples, which is consistent with the previous report [33]. The peak at 2θ of 19° corresponds to the crystal plane of (020), while the other one (22.7°) corresponds to the (110) plane. Among the studied samples, Sample 1 was found to be the most crystalline, while the percentage of crystallinity was observed to decrease as a function of the crosslink density of the elastomeric samples. As observed in DSC thermograms, the melt-cooled samples crystallized upon cooling, and no cold crystallization was observed during heating in the case of Sample 1. It was found that the peaks corresponding to the crystalline domains of Sample 1 decrease with increasing temperature and disappear beyond the temperature of 0 °C. The disappearance of the characteristic peaks may correspond to the melting of the crystalline domains of Sample 1. Sample 3, on the other hand, was found to show no crystalline peaks at the beginning; however, the characteristic peaks of crystalline polybutadiene domains appeared upon heating. The two distinct peaks at 2θ of 19.0 and 22.7° were clearly observed when the temperature was raised to –60 °C (from –80 °C). The appearance of the mentioned peaks may correspond to the cold crystallization of

Table 3. Enthalpy values for crystallization, cold crystallization, and melting for the crystalline domains, along with the respective transition temperatures for a series of cured rubber samples of different crosslink densities.

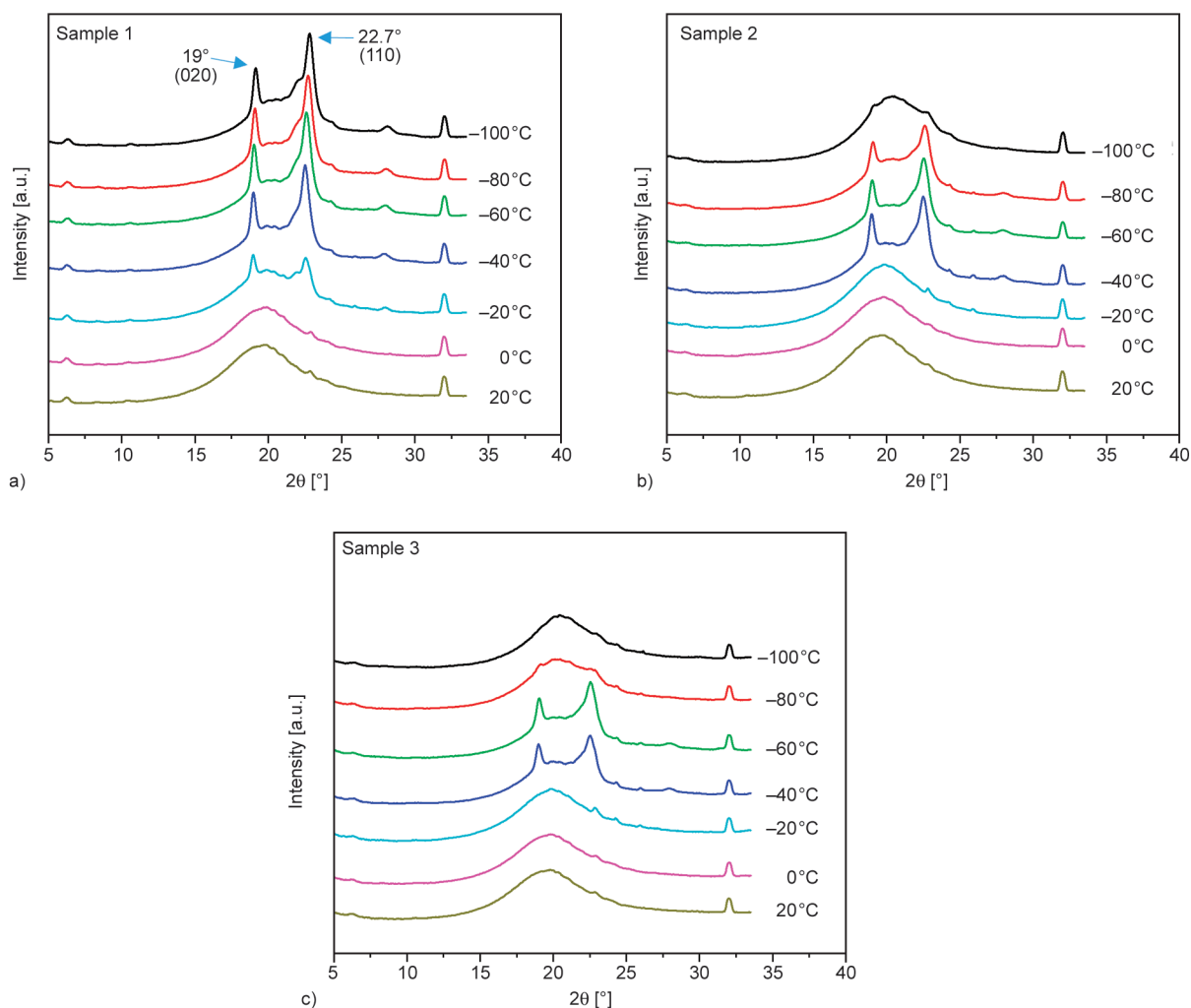| Sample name	Enthalpy of crystallization (during the cooling cycle), ΔH_{cry} [J/g]	Enthalpy of cold crystallization, ΔH_{cold} [J/g]	T_{melt} [°C]	T_{cryst} [°C]	$T_{coldcryst}$ [°C]	$\Delta H_{cry} + \Delta H_{cold}$ [J/g]	Melting enthalpy, ΔH_{melt} [J/g]
Sample 1	29.02	0.38	–31	–32	–68	29.40	26.03
Sample 2	13.54	8.50	–36	–44	–78	22.04	22.53
Sample 3	0	16.80	–40	N.A.	–70	16.80	17.65

Figure 2. Low-temperature X-ray analysis of a series of cured polybutadiene rubber samples with different crosslink densities, showing different cold crystallization behaviors: a) Sample 1, b) Sample 2, c) Sample 3.

the crosslinked polybutadiene elastomer. The crystalline peaks were found to disappear beyond –20 °C for Sample 3. These observations are in good agreement with the DSC data. The cold crystallization behavior was also observed for Sample 2; the crystalline peaks appeared upon heating (at –80 °C) and disappeared beyond –20 °C. The order of disappearance of the crystalline peaks follows the same trend of melting endotherms as observed during the DSC analysis, Sample 3 the first and Sample 1 at a higher temperature. As discussed previously, the higher the crosslink density, the higher the chance of cold crystallization for elastomeric samples, which can be observed during low-temperature X-ray diffraction studies. At the same time, with the highest crosslink density, Sample 3 was found to require a higher amount of thermal energy to orient the polymer segments, which is in line with the previous observations.

The low-temperature X-ray plots were further deconvoluted to isolate the crystalline peaks and the amorphous signal. As an example, the deconvoluted plot of Sample 2 at –60 °C is shown in Figure 3. The full width at half maxima (FWHM) and area of the deconvoluted plots were extracted from each deconvoluted X-ray image and used to calculate degree of crystallinity (χ_c) and the size of crystallites. The Scherrer equation was used to estimate the size of the crystalline domains. The estimated results are gathered and shown in Table 4. From Table 4, the largest crystallite sizes can be observed for Sample 1 (~18 nm crystals with (020) plane and ~11–12 nm crystals with (110) plane), while the smallest crystallite sizes were observed for Sample 3 (~15 nm crystals with (020) plane and ~8–9 nm crystals with (110) plane). The largest size of the crystalline domain can support the DSC observation of the highest melting temperature along with the broadest melting

Table 4. Degree of crystallinity and size of the crystalline domains for a series of cured rubber samples of different crosslink densities.

Temperature [°C]	Sample 1			Sample 2			Sample 3		
	χ_c	Crystal size (020) [nm]	Crystal size (110) [nm]	χ_c	Crystal size (020) [nm]	Crystal size (110) [nm]	χ_c	Crystal size (020) [nm]	Crystal size (110) [nm]
−100	0.27	18.52	13.32	0	N.A.	N.A.	0	N.A.	N.A.
−80	0.28	18.10	12.88	0.19	14.74	9.70	0	N.A.	N.A.
−60	0.29	17.69	12.47	0.26	15.61	9.47	0.26	14.74	8.83
−40	0.25	18.96	10.62	0.24	16.25	9.47	0.22	15.31	9.14
−20	0.11	18.10	11.39	0	N.A.	N.A.	0	N.A.	N.A.
0	0	N.A.	N.A.	0	N.A.	N.A.	0	N.A.	N.A.
20	0	N.A.	N.A.	0	N.A.	N.A.	0	N.A.	N.A.

endotherm for Sample 1. A linear proportionality can be observed for the crystal size and the melting temperature as observed by DSC. The degree of crystallinity for all the samples, regardless of the crosslink density, was found to be maximum at –60 °C. This can be due to the cumulative effect of the crystallinity and cold crystallinity of the sample at this temperature. For Sample 1, the degree of crystallinity was found to decrease above a specific temperature (–40 °C) and disappeared after 0 °C. On the contrary, for other samples, the degree of crystallinity increased upon heating due to cold crystallization, and disappeared after –40 °C. The results are in line with the observations of the DSC analysis.

3.4. Dynamic mechanical analysis of different cure rubber samples

All samples with different crosslink densities were subjected to dynamic mechanical analysis (DMA).

The experiments were carried out in a strain-controlled mode of DMA [9]. The temperature response diagrams are shown in Figure 4. A glass-rubber transition for the crosslinked rubber samples can be observed at about –90 °C. With the highest percentage of crystallinity, Sample 1 showed a minimal decrease in storage modulus during the glass-rubber transition, while Sample 3 showed the largest decrease. The decrease in storage modulus was then followed by an increase in storage modulus for Samples 2 and 3 (at –70 to –60 °C). This unusual increase in storage modulus after the glass transition temperature may be associated with the formation of crystalline domains during the process of cold crystallization. With the highest number of crosslinks, Sample 3 shows the highest degree of cold crystallization, as previously observed (DSC and low-temperature X-ray studies). Followed by the increase of the modulus for Sample 2 and 3, another drop of
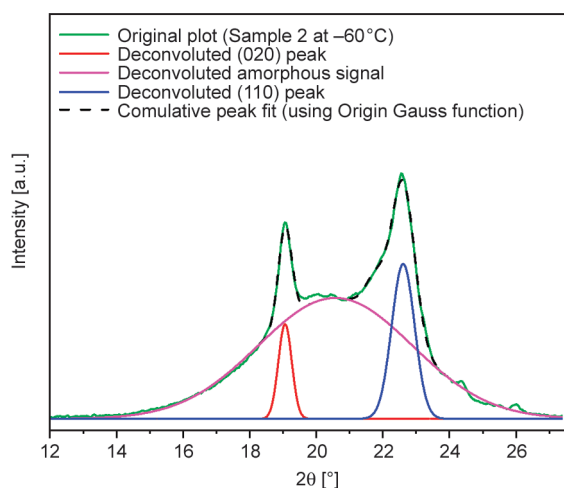
Figure 3. Deconvoluted peaks and cumulative peak fit for Sample 2 at –60 °C as an example for a series of polybutadiene rubber samples with different crosslink densities.
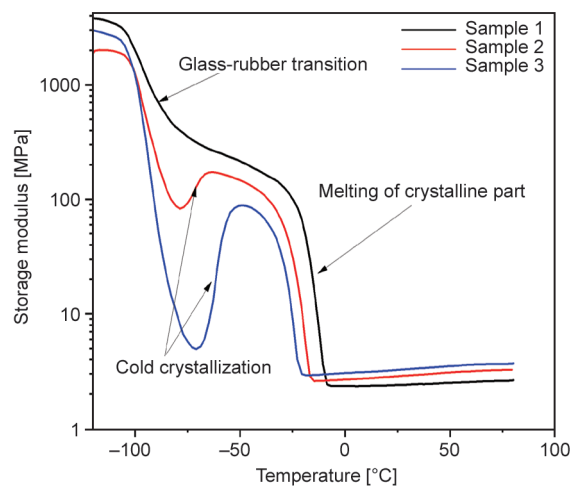
Figure 4. Dynamic mechanical analysis of a series of cured polybutadiene rubber samples with different crosslink densities, showing different cold crystallization behaviors during the glass-rubber transition.

storage modulus (at –27 to –15 °C) was observed for all the samples. The second drop can be associated with the melting of the crystalline domains. It is worth noting that the sample with the lowest crosslink density showed the highest modulus at low temperatures (<–10 °C). Crystallinity may be the leading factor behind the high modulus of the low crosslinked samples at low temperatures. The order of storage modulus of the samples was found to be reversed at a higher temperature. The highest modulus was found for the sample with the highest crosslink density at room temperature, as expected.

4. Conclusions

Polybutadiene rubber with high cis content was compounded with sulfur crosslinking agents to form rubber composites with different crosslink densities. The samples were then subjected to DSC, low-temperature X-ray diffraction, and DMA analysis. In the studies, a characteristic and interesting behavior during cold crystallization, influenced by the crosslink density, was observed. The rubber compound with the lowest crosslink density showed the highest amount of crystallinity and the lowest degree of cold crystallizability, and vice versa. The sudden increase in stiffness of highly crosslinked rubber samples when heated from sub-ambient temperatures to room temperature can be attributed to the cold crystallization of the BR chains. In addition, the samples with low crosslink density were found to have a high modulus below –10 °C, as an effect of a sufficient number of crystalline domains but a low modulus at room temperature. The incorporation of reinforcing fillers and the introduction of different curing systems (peroxide, different S-curing systems with different S to accelerator ratio) may alter the cold crystallization behavior of polybutadiene. A separate study can be envisaged to understand all these effects.

Acknowledgements

References

[1] Gedde U. W., Hedenqvist M. S.: Crystallization kinetics. in 'Fundamental polymer science' (eds.: Gedde U. W., Hedenqvist M. S.) Springer, Heidelberg, 327–386 (2019).
https://doi.org/10.1007/978-3-030-29794-7_8

[2] Wunderlich B.: Theory of cold crystallization of high polymers. The Journal of Chemical Physics, **29**, 1395–1404 (1958).
https://doi.org/10.1063/1.1744729

[3] Reiter G., Sommer J-U.: Polymer crystallization: Observations, concepts and interpretations. Springer, Heidelberg (2003).
https://doi.org/10.1007/3-540-45851-4

[4] Allegra G., Meille S. V.: Pre-crystalline, high-entropy aggregates: A role in polymer crystallization? in 'Interphases and mesophases in polymer crystallization III' (ed.: Allegra G.) Springer, Heidelberg, 87–135 (2005).
https://doi.org/10.1007/12_009

[5] Strobl G.: Crystallization and melting of bulk polymers: New observations, conclusions and a thermodynamic scheme. Progress in Polymer Science, **31**, 398–442 (2006).
https://doi.org/10.1016/j.progpolymsci.2006.01.001

[6] Lund R., Alegría A., Goitandía L., Colmenero J., González M. A., Lindner P.: Dynamical and structural aspects of the cold crystallization of poly(dimethylsiloxane) (PDMS). Macromolecules, **41**, 1364–1376 (2008).
https://doi.org/10.1021/ma702055b

[7] Šics I., Ezquerra T. A., Nogales A., Denchev Z., Alvarez C., Funari S. S.: Cold crystallization of poly(ethylene naphthalene-2,6-dicarboxylate) by simultaneous measurements of X-ray scattering and dielectric spectroscopy. Polymer (Guildf), **44**, 1045–1049 (2003).
https://doi.org/10.1016/S0032-3861(02)00742-5

[8] Gent A. N.: Rubber elasticity: Basic concepts and behavior. in 'The science and technology of rubber' (eds.: Mark J. E., Erman B., Roland C. M.) Academic Press, Boston, 1–26 (2013).
https://doi.org/10.1016/B978-0-12-394584-6.00001-7

[9] Wunde M., Klüppel M.: Effect of filler and blending with SBR and NR on thermally induced crystallization of high-cis BR as evaluated by dynamic mechanical analysis. Express Polymer Letters, **14**, 261–271 (2020).
https://doi.org/10.3144/expresspolymlett.2020.22

[10] Bukhina K.: Crystallization of elastomers at low temperatures. in 'Low-temperature behaviour of elastomers' (ed.: Bukhina K.) CRC Press, Boca Raton, 59–94 (2007).
https://doi.org/10.1201/b12239

[11] Chenal J. M., Chazeau L., Bomal Y., Gauthier C.: New insights into the cold crystallization of filled natural rubber. Journal of Polymer Science Part B: Polymer Physics, **45**, 955–962 (2007).
https://doi.org/10.1002/polb.21105

[12] Bertini F., Canetti M., Ricci G.: Crystallization and melting behavior of 1,2-syndiotactic polybutadiene. Journal of Applied Polymer Science, **92**, 1680–1687 (2004).
https://doi.org/10.1002/app.20115

[13] Schawe J. E. K., Wrana C.: Competition between structural relaxation and crystallization in the glass transition range of random copolymers. Polymers (Basel), **12**, 1778 (2020).
https://doi.org/10.3390/polym12081778

[14] Bruzzone M., Sorta E.: Elastomer structures and 'cold crystallization'. Rubber Chemistry and Technology, **52**, 207–212 (1979).
https://doi.org/10.5254/1.3535204

[15] Bekkedahl N., Wood L. A.: Crystallization of vulcanized rubber. Rubber Chemistry and Technology, **14**, 347–355 (1941).
https://doi.org/10.5254/1.3540030

[16] Vasanthan N., Manne N. J., Krishnama A.: Effect of molecular orientation on the cold crystallization of amorphous–crystallizable polymers: The case of poly(trimethylene terephthalate). Industrial & Engineering Chemistry Research, **52**, 17920–17926 (2013).
https://doi.org/10.1021/ie402860t

[17] Supaphol P., Apiwanthanakorn N.: Nonisothermal cold-crystallization kinetics of poly(trimethylene terephthalate). Journal of Polymer Science Part B: Polymer Physics, **42**, 4151–4163 (2004).
https://doi.org/10.1002/polb.20276

[18] Apiwanthanakorn N., Supaphol P., Nithitanakul M.: Non-isothermal melt-crystallization kinetics of poly(trimethylene terephthalate). Polymer Testing, **23**, 817–826 (2004).
https://doi.org/10.1016/j.polymertesting.2004.03.001

[19] Mano J. F., Wang Y., Viana J. C., Denchev Z., Oliveira M. J.: Cold crystallization of PLLA studied by simultaneous SAXS and WAXS. Macromolecular Materials and Engineering, **289**, 910–915 (2004).
https://doi.org/10.1002/mame.200400097

[20] Ivanov D. A., Pop T., Yoon D. Y., Jonas A. M.: Direct observation of crystal–amorphous interphase in lamellar semicrystalline poly(ethylene terephthalate). Macromolecules, **35**, 9813–9818 (2002).
https://doi.org/10.1021/ma011784j

[21] Ivanov D. A., Amalou Z., Magonov S. N.: Real-time evolution of the lamellar organization of poly(ethylene terephthalate) during crystallization from the melt: High-temperature atomic force microscopy study. Macromolecules, **34**, 8944–8952 (2001).
https://doi.org/10.1021/ma010809b

[22] Luo W-A., Liao Z., Yan J., Li Y., Chen X., Mai K., Zhang M.: Cold-crystallization of poly(trimethylene terephthalate) studied by photoluminescence of its amorphous portion. Macromolecules, **41**, 7513–7518 (2008).
https://doi.org/10.1021/ma801119n

[23] Yoshii T., Yoshida H., Kawai T.: Effect of structural relaxation of glassy PET on crystallization process observed by the simultaneous DSC–XRD and DSC–FTIR. Thermochimica Acta, **431**, 177–181 (2005).
https://doi.org/10.1016/j.tca.2005.01.070

[24] Chao Y-K., Praveena N. M., Yang K-C., Gowd E. B., Ho R-M.: Crystallization of polylactides examined by vibrational circular dichroism of intra- and inter-chain chiral interactions. Soft Matter, **18**, 2722–2725 (2022).
https://doi.org/10.1039/D2SM00060A

[25] Rooj S., Das A., Thakur V., Mahaling R. N., Bhowmick A. K., Heinrich G.: Preparation and properties of natural nanocomposites based on natural rubber and naturally occurring halloysite nanotubes. Materials & Design, **31**, 2151–2156 (2010).
https://doi.org/10.1016/j.matdes.2009.11.009

[26] Flory P. J., Rehner J.: Statistical mechanics of cross-linked polymer networks I. Rubberlike elasticity. The Journal of Chemical Physics, **11**, 512–520 (1943).
https://doi.org/10.1063/1.1723791

[27] Vijayabaskar V., Stephan M., Kalaivani S., Volke S., Heinrich G., Dorschner H., Bhowmick A. K., Wagenknecht U.: Influence of radiation temperature on the crosslinking of nitrile rubber by electron beam irradiation. Radiation Physics and Chemistry, **77**, 511–521 (2008).
https://doi.org/10.1016/j.radphyschem.2007.09.011

[28] Hoti G., Caldera F., Cecone C., Pedrazzo A. R., Anceschi A., Appleton S. L., Monfared Y. K., Trotta F.: Effect of the cross-linking density on the swelling and rheological behavior of ester-bridged β-cyclodextrin nanosponges. Materials (Basel), **14**, 1–20 (2021).
https://doi.org/10.3390/ma14030478

[29] Aziz S. B., Abdullah O. G., Rasheed M. A., Ahmed H. M.: Effect of high salt concentration (HSC) on structural, morphological, and electrical characteristics of chitosan based solid polymer electrolytes. Polymers, **9**, 187 (2017).
https://doi.org/10.3390/polym9060187

[30] Kurajica S., Mužina K., Keser S., Dražić G., Munda I. K.: Assessment of cell toxicity and oxidation catalytic activity of nanosized zinc-doped ceria UV filter. Chemical and Biochemical Engineering Quarterly, **35**, 157–164 (2021).
https://doi.org/10.15255/CABEQ.2020.1905

[31] Vinila V. S., Isac J.: Synthesis and structural studies of superconducting perovskite $GdBa_2Ca_3Cu_4O_{10.5+\delta}$ nanosystems. in 'Design, fabrication, and characterization of multifunctional nanomaterials' (eds.: Thomas S., Kalarikkal N., Abraham A. R.) Elsevier, Amsterdam, 319–341 (2022).
https://doi.org/10.1016/B978-0-12-820558-7.00022-4

[32] Hergenrother W. L.: Characterization of networks from the peroxide cure of polybutadiene. Journal of Applied Polymer Science, **16**, 2611–2622 (1972).
https://doi.org/10.1002/app.1972.070161014

[33] Parker W. O., Ferrando A., Ferri D., Canepari V.: Cross-link density of a dispersed rubber measured by ^{129}Xe chemical shift. Macromolecules, **40**, 5787–5790 (2007).
https://doi.org/10.1021/ma070793a

express
polymer letters

Research article

The electrospinning of less common polyamides via direct and alternating current

Pavel Holec[1]*, Radek Jirkovec*[2], *Tomáš Kalous*[1], *Václava Benešová*[2], *Jiří Brožek*[2],
Jiří Chvojka[1]

[1]Department of Nonwovens and Nanofibrous Materials, Technical University of Liberec, CZ-461 17, Czech Republic
[2]Department of Polymers, University of Chemistry and Technology, Prague, CZ-166 28, Czech Republic

Abstract. This paper presents a method for direct and alternating current electrospinning of polymeric solutions of three less common polyamides (nylons). Homopolyamide PA 8, heteropolyamide PA 6|9 and semi-aromatic amide (phthalamide) PA 6(3)T were dissolved in the formic acid and dichloromethane mixture, which have proved to be a suitable solvent for various other linear polyamides. The dependence of the viscosity, electrical conductivity, and spinnability via the direct (DC) and alternating current (AC) technology on the solution concentration was observed. Scanning electron microscope images of the prepared nanofibers were acquired and consequently analyzed for fiber defects, followed by measuring the fiber diameters. The differences in the nanofiber quality of DC layers and AC plumes were discussed. Finally, the optimal concentrations for the electrospinning of the examined solutions were determined. The communication follows our previous work and extends the number of electrospinnable polyamides, thus facilitating future research in this area.

1. Introduction

Synthetic linear polyamides (nylons) are a group of chemically related polymers containing amide groups (–CONH–) and aliphatic chains or aromatic cores. The increasing length of the chain (or the number of cores) alters the properties of polyamides, such as polarity, tensile strength, glass transition temperature, melting point, solubility, wettability, or gas permeability [1]. A number of PA types allow for sorting them into logical groups (homopolyamides, heteropolyamides, aromatic polyamides) with defined and gradually changing properties. It can be harnessed for choosing the most suitable polyamide for a particular application. The polyamide nanofibers evince good thermal, mechanical, and chemical resistance, thus allowing for their application in demanding sectors [2]. Polar polyamides (*e.g.* PA 6 and

PA 6|6 [3, 4]) are usually soluted in formic acid or a formic and acetic acid mixture. However, less polar PAs require more expensive solvents, thus limiting their industrial potential. Behler *et al*. [5] found that the formic acid and dichloromethane mixture can be used as a universal solvent for PAs. Our previous work showed that it is possible to electrospin the PA 4, PA 6, PA 11, PA 4|6, PA 6|6, PA 6|10, and PA 6|12 from the solvent using direct (DC) or alternating current (AC) technology [6]. The advantage of the method is the possibility of producing different nanofibrous materials without needing solvent or set-up alteration. It also allows DC and AC electrospinning. While both technologies produce polymeric nanofibers [7, 8], the differences are evident in terms of the final structure of the material, thus impacting its application [8]. This paper extends the range of DC
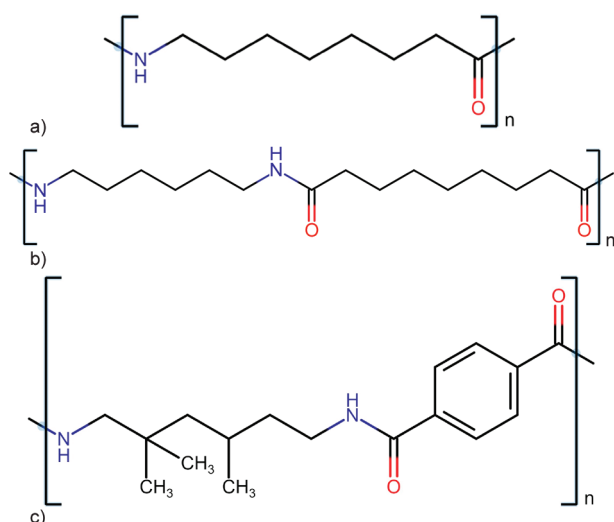
Figure 1. Chemical structures of repeating units – PA 8 (a), PA 6|9 (b), and PA 6(3)T (c) made in online software Chem-Space.

and AC electrospinnable polyamides by three less common types: PA 8, PA 6|9 [9], and PA 6(3)T [10] (Figure 1). The described method is suitable for producing PA nanofibers for filtration [11] or solid-phase extraction sorbents [12].

2. Experimental section
2.1. Materials and preparation of the solution
PA 8 was synthesized at the Department of Polymers – UCT Prague. Monomer η-capryllactam (Fluka AG – Buchs, Switzerland) was distilled under reduced pressure before use. The η-capryllactam was polymerized in a sealed ampoule in 1 mol% of ε-aminocaproic acid at 250 °C for 96 hours. The yield of polymer: 99,7%; viscosity average molar mass M_v = 24500 g/mol; melting temperature (differential scanning calorimetry, DSC) 194 °C.

The PA 6|9 (CAS 27136-65-8) and PA 6(3)T (CAS 25497-66-9) were purchased from Scientific Polymer Production Inc. (New York, NY, USA), the formic acid (CAS 64-18-6) and dichloromethane (CAS 75-09-2) from Penta s.r.o. (Prague, Czech Republic). Sets of 6, 8, 10, 12, 14, and 16 wt% solutions were prepared by dissolving the polyamides in a mixture of formic acid and dichloromethane at a weight ratio of 1:1. They were stirred for 24 hours on a magnetic stirrer at standard laboratory conditions.

2.2. Methods
Viscosity and electrical conductivity
A HAAKE Rotovisco (Thermo Fisher Scientific, Prague, Czech Republic) rheometer with a C35/1°Ti L cone was used to assess dynamic viscosity. Each measurement lasted 30 s in continuous mode, and the shear rate was increased linearly from 300 to 3000 1/s. A Eutech Instruments CON 510 (Eutech Instruments – Thermo Fisher Scientific Inc., Landsmeer, The Netherlands) with a K10/6MM8 was used for the determination of the conductivity of the solutions. The measurements were repeated three times at a temperature of 21 °C.

Electrospinning system
An AU-60P0.5-L (Matsusada Precision, Ōtsu, Japan) positive voltage source was used for the DC electrospinning, and a KGUG 36 transformer (ABB, Prague, Czech Republic) with an ESS 104 regulator (Thalheimer-Trafowerke, Ostrava, Czech Republic) at a frequency of 50 Hz (sinusoidal wave) was used for the AC electrospinning. The setups for both methods were identical: a steel rod (diameter 10 mm) was used as the positive electrode, upon which a droplet of the polymeric solutions was deposited and subsequently electrospun. A steel plate was used as the fiber collector (grounded for the DC, electrically neutral for the AC system) at a distance of 100 mm from the electrode top. The paper [6] describes the electrospinning setup in more detail. The supplied voltage was 30 kV for the DC and effective 30 kV for the AC methods. The electrospinning process took 30 s for each sample. The relative humidity during electrospinning was 40%, and the temperature was 21 °C.

Scanning electron microscopy
A Q150R ES rotary-pumped coater (Quorum, Lewes, UK) was used to coat the nanofibers with a 10 nm thick deposit of gold. A Vega 3 scanning electron microscope (TESCAN, Brno, Czech Republic) was employed at a 10 kV accelerating voltage. ImageJ freeware (version 1.52a, Bethesda, MD, USA) was used to measure the fiber diameters (200 for each sample).

3. Results and discussion
3.1. Viscosity and electrical conductivity
All tested solutions' dynamic viscosities and conductivities increased with the concentrations (Figure 2). The dynamic viscosity of the PA 8 was higher due to its higher molecular weight. The lower conductivity of PA 6(3)T was caused by lower moisture content in the PA 6(3)T compared to more polar
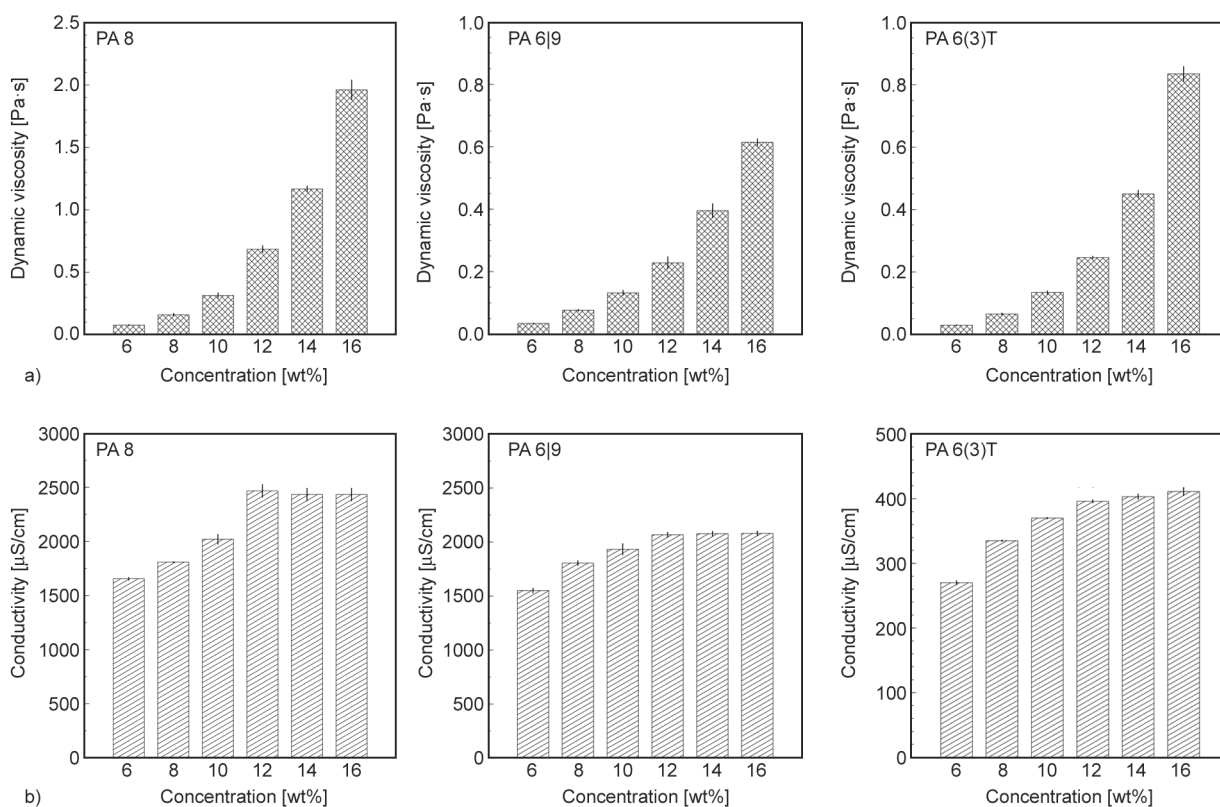
Figure 2. Dynamic viscosity at a shear rate of 500/s (a) and conductivity (b) of the solutions.

PA 8 or PA 6|9. The decreased formic acid dissociation rate led to the solution's lower conductivity.

3.2. DC and AC electrospinning
Prepared polyamide solutions were spinnable via both the DC and AC technologies. The collector's surface covered with fibers of the DC electrospun layers was highest for the 8% PA 8 and 10% PA 6|9 and PA 6(3)T solutions (Figure 3). Above or below these concentrations, the layers covered a smaller area and were less homogeneous. The lower concentration determined for the PA 8 was caused by the higher molecular weight, which corresponded to the viscosity measurements.

3.3. Fiber diameters and defects
The SEM images showed that the quality of the DC- and AC-fabricated fibers was standard for all the samples except the fibers produced from the 12, 14, and 16 % PA 8 solutions via the DC electrospinning. A fibers and ribbons mixture was observed for the 12% PA 8. At 14 and 16%, samples consisted entirely of ribbons (Figure 4a and Figure 4b). This phenomenon was not observed for the samples of the same solutions produced via the AC method. While the isolated occurrence of ribbons in AC samples

was observed, they were sporadic and never formed a compact structure (Figure 4c). It was caused by the lower momentum of AC fibers, which flight to the collector was accelerated by lower energy via the ionic wind. In contrast, the DC fibers were accelerated by stronger electrostatic force and were flattened by impact with the collector. This phenomenon was observed only for solutions of higher concentrations, where the initial polymeric streams from Tylor cones were thicker due to the higher viscosity of solutions.

The fiber diameters and the standard deviations of all three polyamide layers increased with the increasing concentration of the solutions (see Table 1). Concerning the deviations, the estimation of the differences between the fibers prepared via the DC and AC approaches from identical solutions was inconclusive. The significant increase in the fiber diameters of the 14 and 16% PA 8 solutions was caused by the creation of ribbons (only major diameters were measured).

4. Conclusions
The paper presents a method for the DC and AC electrospinning of PA 8, PA 6|9, and PA 6(3)T solutions. The dynamic viscosity and conductivity of the solutions were measured to support observed facts.
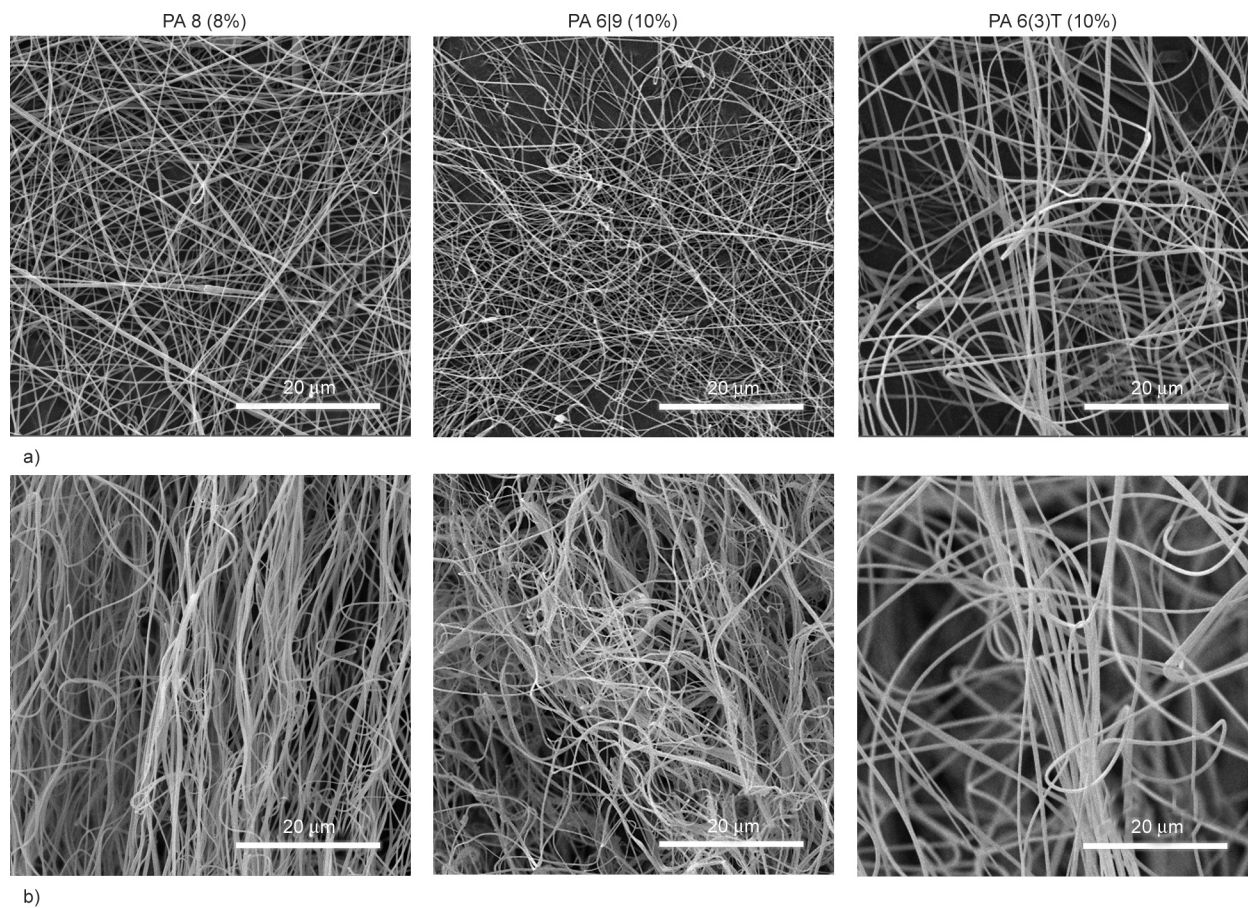
Figure 3. SEM images of the DC (a) and AC (b) electrospun PA 8, PA 6|9, and PA 6(3)T nanofibers.
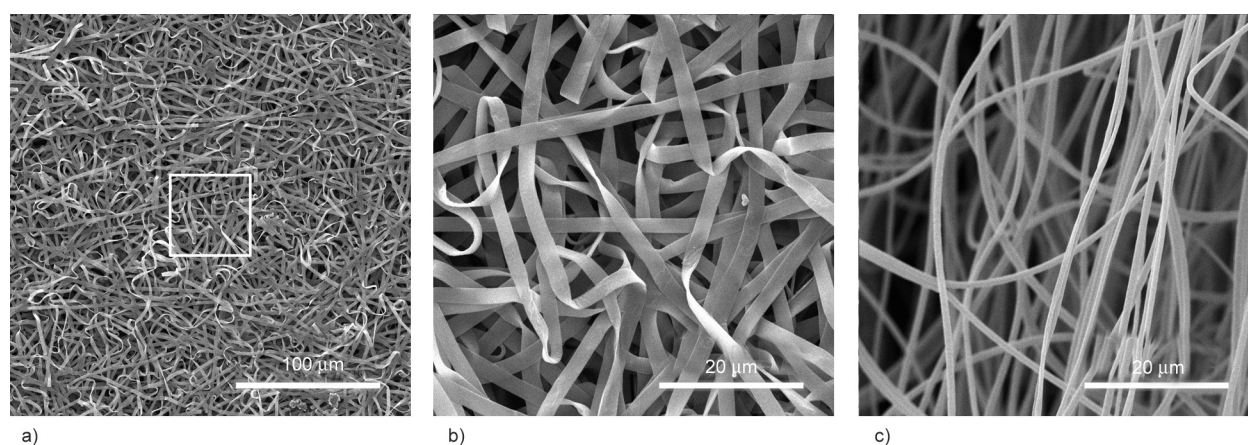

Figure 4. The DC electrospun PA 8 (16%) consisted of ribbons (a); the white square specifies the location of the detail shown in the (b), whereas the AC electrospun structure of the PA 8 (16%) showed no ribbon content (c).

Table 1. The dependence of the average fiber diameters on the polymeric solutions concentration (± standard deviation).

Concentration [wt%]	PA 8		PA 6|9		PA 6(3)T	
	DC [nm]	AC [nm]	DC [nm]	AC [nm]	DC [nm]	AC [nm]
6%	185±43	176±59	126±24	140±39	176±39	194±45
8%	213±41	250±75	149±26	214±56	239±47	244±46
10%	340±66	286±59	207±44	245±71	359±97	484±90
12%	413±79	359±55	277±43	263±81	834±168	532±117
14%	2077±250	674±142	315±47	413±178	977±250	789±278
16%	2273±186	951±308	670±169	486±176	1217±143	984±401

The most suitable of the tested solutions were 8% PA 8, 10% PA 6|9, and 10% PA 6(3)T, of which the DC-produced nanofiber layers and the AC-produced nanofiber plumes were observed to be the most voluminous and homogeneous. The SEM images showed no defects in the fibers at the same time. The lower concentration for PA 8 was caused by its higher molecular weight, which corresponded with the viscosity measurements. The DC spinning of the 14 and 16% PA 8 solutions resulted in the production of exclusively ribbon structures, which was not observed for the AC spun samples because the carrying speed of AC fibers to the collector was lower than for the DC spun fibers. Considering the previous results of PA electrospinning, it was confirmed that the used solvent system is suitable for the DC and AC electrospinning of synthetic linear polyamides.

Acknowledgements

References

[1] Mark J. E.: The polymer data handbook. Oxford University Press, Oxford (2009).

[2] Gui L., Cui Y., Zhu Y., An X., Lan H., Jin J.: *g*-C$_3$N$_4$ nanofibers network reinforced polyamide nanofiltration membrane for fast desalination. Separation and Purification Technology, **293**, 121125 (2022).
https://doi.org/10.1016/j.seppur.2022.121125

[3] Heikkilä P., Harlin A.: Parameter study of electrospinning of polyamide-6. European Polymer Journal, **44**, 3067–3079 (2008).
https://doi.org/10.1016/j.eurpolymj.2008.06.032

[4] Guerrini L. M., Branciforti M. C., Canova T., Bretas R. E. S.: Electrospinning and characterisation of polyamide 66 nanofibers with different molecular weights. Materials Research, **12**, 181–190 (2009).
https://doi.org/10.1590/S1516-14392009000200012

[5] Behler K., Havel M., Gogotsi Y.: New solvent for polyamides and its application to the electrospinning of polyamides 11 and 12. Polymer, **48**, 6617–6621 (2007).
https://doi.org/10.1016/j.polymer.2007.08.058

[6] Holec P., Jirkovec R., Kalous T., Baťka O., Brožek J., Chvojka J.: The potential for the direct and alternating current-driven electrospinning of polyamides. Nanomaterials, **12**, 665 (2022).
https://doi.org/10.3390/nano12040665

[7] Kenry, Lim C. T.: Nanofiber technology: Current status and emerging developments. Progress in Polymer Science, **70**, 1–17 (2017).
https://doi.org/10.1016/j.progpolymsci.2017.03.002

[8] Balogh A., Farkas B., Verreck G., Mensch J., Borbás E., Nagy B., Marosi G., Nagy Zs. K.: AC and DC electrospinning of hydroxypropylmethylcellulose with polyethylene oxides as secondary polymer for improved drug dissolution. International Journal of Pharmaceutics, **505**, 159–166 (2016).
https://doi.org/10.1016/j.ijpharm.2016.03.024

[9] Steyaert I., Delplancke M. P., van Assche G., Rahier H., de Clerck K.: Fast-scanning calorimetry of electrospun polyamide nanofibres: Melting behaviour and crystal structure. Polymer, **54**, 6809–6817 (2013).
https://doi.org/10.1016/j.polymer.2013.10.032

[10] Pai C-L., Boyce M. C., Rutledge G. C.: Mechanical properties of individual electrospun PA–6(3)T fibers and their variation with fiber diameter. Polymer, **52**, 2295-2301 (2011).
https://doi.org/10.1016/j.polymer.2011.03.041

[11] Heikkilä P., Taipale A., Lehtimäki M., Harlin A.: Electrospinning of polyamides with different chain compositions for filtration application. Polymer Engineering & Science, **48**, 1168–1176 (2008).
https://doi.org/10.1002/pen.21070

[12] Erben J., Klíčová M., Klapstova A., Háková M., Lhotská I., Zatrochová S., Šatínský D., Chvojka J.: New polyamide 6 nanofibrous sorbents produced via alternating current electrospinning for the on-line solid phase extraction of small molecules in chromatography systems. Microchemical Journal, **174**, 107084 (2022).
https://doi.org/10.1016/j.microc.2021.107084

express
polymer letters

Research article

Self-healing behaviour of lignin-containing epoxidized natural rubber compounds

Bedriye Nur Yeşil[1] iD *, Tuba Ünügül*[1] iD *, Bağdagül Karaağaç*[1,2*] iD

[1]Department of Chemical Engineering, Kocaeli University, Umuttepe Campus, 41380 Kocaeli, Turkey
[2]Department of Polymer Science & Technology, Kocaeli University, Umuttepe Campus, 41380 Kocaeli, Turkey

Abstract. Epoxidized natural rubber (ENR) is a relatively new raw material that can be used in many applications, such as rubber-based adhesives, self-crosslinking, and compatibilization of rubber and filler matrices in favor of reactive epoxy groups. However, as almost all types of polymeric materials do, ENR is exposed to mechanical, chemical, and thermo-oxidative degradation during service life, resulting in micro- and macro-cracks in the material body as well as on the surface. The self-healing approach is considered a good solution to provide longer service life by instantaneous repairing these cracks by means of internal and external stimulants. In literature, most attempts at self-healing of ENR focus on irreversible covalent bond based systems. In this study, lignin and a common anti-reversion agent 1,3-bis(citraconimido-methyl) benzene (CIMB) have been evaluated for carrying out self-healing through reversible covalent bonds via Diels-Alder interaction between ENR and CIMB. In addition, lignin could significantly improve self-healing by promoting an epoxy ring-opening reaction on the ENR backbone. The best healing conditions were selected as 180 °C and 15 minutes, and 83% self-healing was achieved by incorporating 6 phr lignin and 15 phr CIMB into the reference compound. Satisfactory self-healing performance has been attributed to the synergistic effect of lignin and CIMB.

Keywords: material testing, lignin, mechanical properties, rubber, self-healing

1. Introduction

Because of irreversible cross-links, rubber-based materials may undergo a structural deformation at either the micro- or the macro-level when exposed to external effects such as chemical, radiative, oxidative, and/or UV-based effects. Since those deformations or fractures continue to build up during the service life of rubber material, its performance gradually decreases over time. It is crucial in most applications not only to avoid the visible effects of those deformations over the material, at least temporarily during the material's service life, but also to ensure a long-lasting performance to be similar or comparable to its initial value. Thus, the 'self-healing' approach for rubber materials has been studied extensively for the last couple of years [1–3]. Self-healing is the ability of a material to repair the micro- and macro-failures in its structure with or without the help of an external stimulant. External and internal self-healing are the two main approaches suggested [4, 5]. The external self-healing approach suggests self-healing by using healing agents. The internal self-healing approach, on the other hand, suggests a healing process without the need for healing agents, instead depends on the functional groups on the chemical structure of the material and their ability to create reversible non-covalent interactions such as H-bonds, metallic interactions as well as metal-ligand interactions [6–8].

Epoxidized natural rubber (ENR) is synthesized by chemically controlled modification of the natural rubber (NR) with formic peroxy acid. This novel raw

material is commercially available depending on its molar epoxy content. Thanks to its rigidity, ENR is widely used in the automotive and aviation industries for the manufacture of joints, bumpers, gaskets, sealants, sponges, cross-linked pipes, and pressure-sensitive adhesives. It is also used for the manufacture of medical tapes, plasters, and carpet backings [1, 9–11]. In the presence of reactive epoxy groups, ENR can further be used in self-crosslinking applications as a compatibilizer for polar fillers and as an adhesion enhancer between rubber and metal structures [12–15]. In addition to the above, ENR can undergo a dual cross-linking process via its C=C double bonds and reactive epoxy sites. Sulfur cross-linking can occur over allylic H atom on C=C double bond, whereas secondary cross-links are initiated by the essential compound additives containing amino, chlorine, and carboxyl functional groups as a result of epoxy chain opening reaction [16–18].

The existence of reactive epoxy groups on ENR may lead to the regeneration of already broken polymer chains where appropriate conditions exist. There are a few studies met in the literature on the self-healing of ENR [7, 19–22]. Imbernon *et al*. [19] investigated the self-healing behavior of ENR-based rubber compounds containing dithiobutyric acid with reactive disulfide groups (DTDB). In this study, they reported ENR to exhibit standard natural rubber characteristics up to 100 °C, whereas self-healing could occur as a result of cross-linking disulfide groups after rearrangement between polymer chains above 150 °C. In another study, Xu *et al*. [21] investigated the self-healing mechanism of carboxymethyl chitosan incorporated ENR latex, where they achieved 90% self-healing by means of reversible H-bonds between ENR and carboxymethyl chitosan molecules. Liu *et al*. [20] investigated the self-healing characteristics of two different types of zinc methyl acrylate incorporated ENR (ENR-25 and ENR-40) at various time and temperature conditions, where they considered the tensile properties as the criteria for success. They achieved 80% self-healing for ENR-40 conditioned at 80 °C for 1 h and 70% for ENR-25 conditioned at 30 °C for 50 min. Self-healing by Diels-Alder reaction is an easier and much more practical method than the other self-healing methods as it can be performed by using solely heat rather than using a catalyst or pre-treatment on the monomer or fractured surface [23, 24]. Self-healing of cross-linked materials can be achieved as a result of the formation of

the thermally reversible covalent bonds in the Diels-Alder mechanism. In self-healing applications of rubber, which are assisted by the Diels-Alder mechanism, materials containing highly electronegative and reactive furan/maleimide groups are used for the formation of a dien-dienophyl couple [25–27]. Bismaleimides are reactive products where maleimide units exist on dianhydride or diamine terminal groups. The carbonyl groups linked to the terminal site of maleimides act as dienophiles in order to undergo a Diels-Alder reaction with the double bond conjugated dienes of bismaleimides. In rubber technology, bismaleimides are mainly as co-agents in peroxide vulcanization and anti-reversion agent in sulfur vulcanization of highly unsaturated rubbers [28, 29]. 1,3-bis(citraconimidomethyl)benzene (CIMB) is used as an anti-reversion agent used in sulfur vulcanization, and it acts by altering the reaction mechanism to avoid reversion. CIMB can undergo cyclo-addition reactions by the Diels-Alder mechanism to re-combine diene and triene structures which formed as a result of chain scission due to various deteriorating external factors [30]. In this study, unlike its accustomed use, the use of CIMB in the Diels-Alders addition reaction was investigated to identify its effect on the self-healing process over the rubber materials.

Lignin is a worldwide available biopolymer that can be extracted from plant cell walls. More than 50 million tonnes of lignin is produced as a by-product of craft and bio-ethanol manufacturing processes. Lignin, an amorphous biopolymer, exhibits various properties depending on its monomeric composition and substituents. This monomer has reactive functional groups such as aliphatic hydroxy, phenolic hydroxy, methoxy, carbonyl, and carboxyl, allowing the preparation of graft copolymers with a wide range of industrial chemicals [31–38]. The reactivity of lignin mainly depends on its functional groups as well as molecular weight distribution and solubility properties [39–42]. Lignin is an abundant and low-cost additive that provides stability and good mechanical properties to the compositions thanks to the presence of aromatic structures. It can undergo a broad range of chemical transformations and provide hydrophilic or hydrophobic characteristics depending on its origin. Furthermore, lignin can be used to protect the materials against oxidative degradations, and it is more resistant to most biological attacks than cellulose and other structural polysaccharides [39, 43, 44]. The chemical functionalities in lignin are

able to react with the epoxy sites of ENR, making lignin the cross-linking center of the lignin/ENR composites [45]. –OH functionality, which induces self-healing via the formation of hydrogen bonding with ENR [4].

Lignin is categorized into two major methods of isolation: sulfur and sulfur-free lignin extraction processes. Sulfur lignin comprises kraft lignin and lignosulphonate lignin, which are primarily produced by paper and pulp industries. Kraft lignin is hydrophobic and contains a high level of condensed structures, phenolic hydroxyl groups, and aliphatic thiol groups [46–48]. Lignosulphonates are water soluble, contain sulfur in the form of sulfonate groups present on their aliphatic side chains, and are produced of waste liquid from softwood [49]. They have a higher average molar mass than kraft lignin with a broad polydispersity [49, 50]. Sulfur-free lignin generally is a low molecular weight product of high purity.

In recent years, many studies related to the use of lignin in rubber compound formulations have been reported. Most of those studies have focused on the use of lignin as a reinforcing filler, anti-aging agent, adhesion enhancer, and additive to improve the thermal and mechanical properties of rubber compounds [38, 43, 45, 51]. Some other studies focused on cross-linking reactions in the presence of lignin. Jiang *et al*. [45] investigated lignosulphonate lignin (0–40 phr)/ ENR blends, which were prepared at 180 °C and in the absence of traditional rubber cross-linking agents such as sulfur and peroxide. They measured cross-linking degree, glass transition temperature, mechanical and dynamic-mechanical properties. The results showed lignin to provide higher cross-link density by inducing the epoxy ring-opening reaction of ENR. However, a relatively higher amount of lignin caused poor rubber-filler interaction and lower tensile modulus due to insufficient compound homogeneity. Besides, lignin may undergo a Diels-Alders cyclo-addition reaction if already functionalized with furan and/or maleic anhydride groups incorporated furan functionality to lignin by the reaction between furfuryl glycidyl ether and phenolic OH groups of lignin [52]. Lignin's phenolic and aliphatic groups have also reacted with maleimidohexonic acid to provide maleimide groups onto lignin. These functionalized lignins were then combined to form a gel structure via a Diels-Alder reaction at 70 °C. The gel structure could be reversed into a liquid state at 120 °C, where the reaction was called retro-Diels-Alder.

Despite several studies about both self-healing of rubber compounds and cross-linking rubber by means of lignin, there is not any study met in the literature on the self-healing of lignin-containing regular rubber compounds. In this study, the self-healing behavior of ENR-based rubber compounds in the presence of lignin and CIMB has been investigated. The rheological and mechanical properties of the rubber compounds were also measured. The effects of varying time and temperature on self-healing performance have been evaluated.

2. Experimental
2.1. Materials
ENR-50 (Epoxyprene), which has 50% (mol%) epoxy content and 80±5 MU Mooney viscosity, was purchased from Muang Mai Guthrie Public Company Ltd. (Thailand). Lignin alkali with 5% humidity and 6.5 of pH value was obtained from Sigma Aldrich. 1,3-bis(citraconimidomethyl)benzene was purchased from Lanxess Deutschland GmbH (Germany) with the commercial name of Perkalink 900. HAF N330 carbon black (CB, filler) was originated from OMSK (Russia). Zinc oxide (activator, White Seal, 325 mesh particle size) was rubber grade and purchased from Metal Oksit (Turkey). Stearic acid (activator, 52–62 °C of congealing point) was also standard rubber grade additive and was purchased from Zeta Kauçuk (Turkey). Antioxidants; polymerized 2,2,4-trimethyl-1,2-dihydroquinoline (TMQ), *N*-isopropyl-*N*′-phenyl-p-phenylenediamine (IPPD), and ozone wax were obtained from Zeta Kauçuk (Turkey). TMQ, with a softening point of 90 ±10 °C, whereas IPPD was of 70 °C. Curing system components; *N*-cyclohexyl-2-benzothiazole sulfenamide (CBS, accelerator) and insoluble sulfur (vulcanization agent, 80% purity), both contained 80% active substance and 20% elastomer binder; they were purchased from Zeta Kauçuk (Turkey). All additives were commercially available and used as received.

2.2. Preparation of compounds and test procedures
Rubber compounds were prepared by using a 2 l (gross volume) internal mixer (Met-Gur, Turkey) and sheeted out on a laboratory mill subsequently. Firstly, epoxidized natural rubber was masticated for 2 min at a rotor speed of 30 rpm to obtain desired flow properties. Carbon black, lignin, and process oil were then fed into the mixer and mixed for 1 min

at 25 rpm. The rotor speed was kept constant at 25 rpm during the rest of the mixing. In the next three steps, a 30 s interval was applied between activators (zinc oxide and stearic acid), stabilizers (TMQ, IPPD, and ozone wax), and the curing system, including CIMB (CBS, sulfur, and CIMB). The final compound was then mixed 1 min further and dumped from the mixer at approximately 60 °C. A 150 mm wide laboratory-type two-roll mill with a friction ratio of 1:1.1 was used for the final homogenization and shaping of the compound. 5 cycles of wound-up with a 3 mm nip thickness were performed on the mill to ensure a standard mixing process.

Compound formulations are given in Table 1. In Group 1, REF is the control compound, which does not comprise any of lignin and CIMB as the self-healing agent. LA3 and LA6 comprise 3 and 6 phr lignin alkali, respectively. Compounds comprising only CIMB are in Group 2, and various amounts of CIMB were used in these compounds. Group 3 and Group 4 comprise both agents in various amounts, where the amounts are also indicated by the compound codes.

Alpha Pioneer 2000 model moving die rheometer (MDR) was used to measure the optimum cure times of the rubber compounds according to ASTM D5289. Minimum torque (M_L), maximum torque (M_H), scorch time (t_{s2}), and optimum cure time (t_{90}) were measured; cure extent (*CE*) and cure rate index (*CRI*) parameters were calculated according to the

standard. Compounds were vulcanized on a hydraulic hot press under 150 bar pressure and for their respective optimum cure times (time corresponding to maximum torque) at 150 °C. Test samples were then cut from the vulcanized sheets by using standard sharp blades.

Mechanical properties of Die C dumb-bell shaped vulcanizates were measured by using a universal testing machine (Instron 3345) with 500 mm/min crosshead speed according to ASTM D412. Tensile strength, elongation at break, and tensile stress at 50% elongation (50% modulus) values were recorded. 5 samples for each compound were tested, and the average value was reported as a result.

A self-healing study was performed on tensile-fractured samples, which were manually re-attached to establish contact between two fractured surfaces in an ASTM D412 Die C-sized mold at selected healing temperatures (160, 170, 180 and 190 °C) for 5, 10 and 15 minutes in the air over operating at ambient pressure. The minimum healing temperature was selected as 160 °C after prior analysis for obtaining meaningful self-healing performance. After healing at the specified conditions, the self-healed specimens were subjected to tensile testing. 5 samples were tested and the average value was used to calculate and report the self-healing ratio. The self-healing performance of the samples was evaluated by means of their percentage retention in tensile strength values as well as by their visual inspection. Equation (1)

Table 1. Rubber compound formulations.

| | Group 1 | | | Group 2 | | | Group 3 | | | Group 4 | | |
---	REF	LA3	LA6	4 CIMB	10 CIMB	15 CIMB	LA3-4 CIMB	LA3-10 CIMB	LA3-15 CIMB	LA6-4 CIMB	LA6-10 CIMB	LA6-15 CIMB
	Content [phr]											
ENR	100	100	100	100	100	100	100	100	100	100	100	100
CB (N-330)	40	40	40	40	40	40	40	40	40	40	40	40
Lignin	–	**3**	**6**	–	–	–	**3**	**3**	**3**	**6**	**6**	**6**
CIMB	–	–	–	**4**	**10**	**15**	**4**	**10**	**15**	**4**	**10**	**15**
Process oil	10	10	10	10	10	10	10	10	10	10	10	10
Zinc oxide	5	5	5	5	5	5	5	5	5	5	5	5
Stearic acid	2	2	2	2	2	2	2	2	2	2	2	2
TMQ	2	2	2	2	2	2	2	2	2	2	2	2
IPPD	1	1	1	1	1	1	1	1	1	1	1	1
Ozone wax	2	2	2	2	2	2	2	2	2	2	2	2
CBS	2	2	2	2	2	2	2	2	2	2	2	2
Sulfur	2	2	2	2	2	2	2	2	2	2	2	2

was used to calculate self-healing performance, where σ_i represents the original mechanical property (tensile strength) of the sample, and σ_f is the value of the same property of the same sample after self-healing [53, 54]. Visual inspection of healed samples was performed by using a MicroDirect 1080p HD (Celestron LLC, USA) microscope (Equation (1)):

$$\text{Self-healing ratio [\%]} = \frac{\sigma_f}{\sigma_i} \cdot 100 \qquad (1)$$

The swelling ratio of the samples was measured according to ASTM D471-12. For each compound, 5 samples were taken from healing surfaces, they were first subjected to ambient acetone extraction for 24 h, and dried in an air oven for a further 24 h prior to measuring initial weight is recorded as W_s. Each sample was immersed in toluene at ambient temperature for 72 h and dried in an air oven for 24 h until a constant mass (final weight, W_{ds}) could be obtained. Swelling ratio (Q), cross-link density (V_e), and the molecular weight between the cross-links (M_c) were calculated by using Equation (2), Equation (3), and Equation (4), respectively according to Flory-Rehner approach [26, 55, 56]:

$$Q = \frac{W_s}{W_{ds}} - 1 \qquad (2)$$

$$V_e = \frac{-\left[\ln(1 - V_2) + V_2 + \chi V_2^2\right]}{V_s\left(V_2^{1/3} - \frac{V_2}{2}\right)} \qquad (3)$$

$$V_e = \frac{1}{2M_c} \qquad (4)$$

where W_s and W_{ds} are the weight fraction of the polymer respectively in swollen and de-swollen phases, V_2 is the volume fraction of the rubber in swollen phase, V_s is the molar volume of the solvent, which is 106.3 ml/mol for toluene, and χ is the solvent-rubber interaction parameter. χ was taken as 0.34 for the toluene-ENR system [57, 58].

A Fourier transform infrared spectrometer (FTIR, Perkin Elmer Spectrum 100, PerkinElmer Inc., USA) was used to investigate structural analysis. The selected spectral resolution and the scanning range were installed as 4 scans and from 650 to 4000 cm^{-1}, respectively.

Dynamic mechanical analyzer (DMA, DMA 50, Metravib Design, France) was used for measuring both storage and loss moduli of the samples for 40–180 °C temperature range at 1 Hz frequency and 0.1% strain

amplitude conditions to investigate Diels-Alder and retro-Diels-Alder reactions during the self-healing process. Samples were subjected to three temperature cycles. In each cycle, samples were first heated to 180 °C by 10 °C/min, held at 180 °C for 15 minutes, and then cooled down to 40 °C by 2 °C/min cooling rate. Here, 180 °C and 15 min parameters were used for representing the optimum self-healing conditions, which were mentioned in the following parts of the paper.

3. Results and discussions
3.1. Rheological properties
Rheometer curves of four compound groups were obtained at 150 °C, and they are all shown in Figure 1. Common rheological parameters are also given in Table 2. Cure extent (*CE*) values were calculated as the difference between the maximum and minimum torque values (M_H and M_L) in dNm. Cure rate index [min^{-1}] of the rubber compounds was calculated using Equation (5) [59, 60].

$$CRI = \frac{100}{t_{90} - t_{s2}} \qquad (5)$$

As seen from Figure 1 and Table 2, incorporating CIMB into the REF compound along with lignin resulted in a 35–40% lower M_L value. It is more pronounced in the case of high CIMB levels and attributed to the plasticizing effect of CIMB as a processing aid [61]. For Group 1 compounds in Figure 1a, a relatively higher amount (6 phr) of lignin could considerably improve the maximum torque value. In contrast to lignin, the incorporation of CIMB did not lead to an increase in M_H, and lower M_H values also were obtained with increasing CIMB content for Group 2 (Figure 1b) compounds. Anti-reversion effect of CIMB was obvious for all the compounds comprising CIMB, as expected [62, 63]. For Group 3 (Figure 1c) and Group 4 (Figure 1d) compounds, which contain both lignin and CIMB, overall curing characteristics were measured as between those of Group 1 and Group 2 compounds. A remarkable increase (up to 40%) was noticed in the cure rate index for the compounds that comprise both lignin and CIMB when compared to the reference compound. This finding is attributed to reactive functional groups of lignin and CIMB to promote the epoxy ring-opening reaction on the ENR matrix and so to ensure further cross-linking reactions [45, 64, 65].
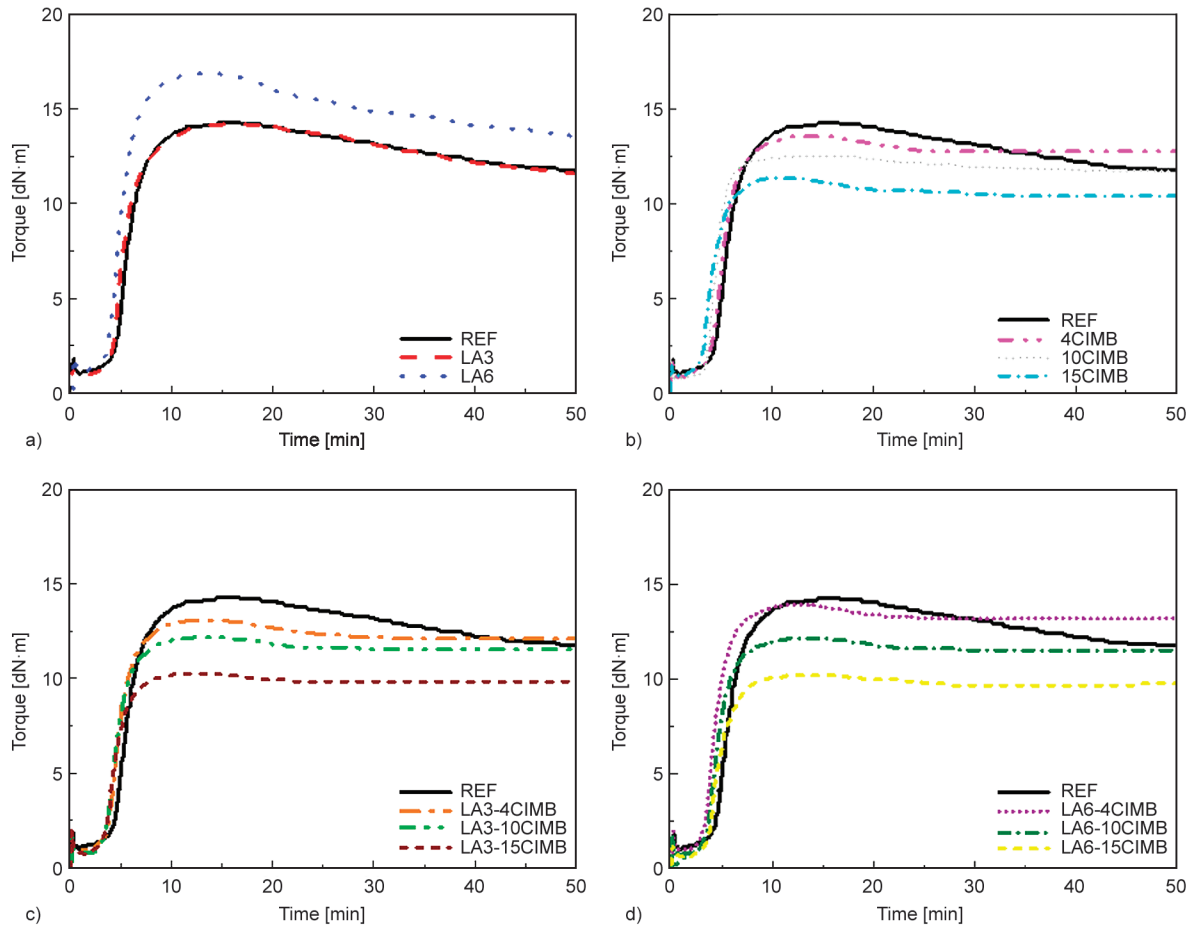
Figure 1. Rheometer curves obtained at 150 °C of a) Group 1, b) Group 2, c) Group 3 and d) Group 4.

Table 2. Rheological properties.

	M_L [dN·m]	M_H [dN·m]	t_{s2} [min]	t_{90} [min]	CE [dN·m]	CRI [min^{-1}]
REF	1.1	14.5	4.51	8.36	13.4	26.0
LA3	0.9	14.2	4.22	8.52	13.3	23.3
LA6	1.0	16.7	3.53	7.11	15.8	27.9
4CIMB	0.9	13.5	4.15	7.43	12.6	30.5
10CIMB	0.8	12.5	3.93	6.91	11.7	33.6
15CIMB	0.7	11.6	3.50	6.31	10.8	35.6
LA3-4CIMB	0.9	13.1	3.91	7.09	12.1	31.5
LA3-10CIMB	0.7	12.1	3.70	6.83	11.4	32.0
LA3-15CIMB	0.7	10.4	3.67	6.53	9.7	35.0
LA6-4CIMB	0.9	14.0	3.38	6.95	13.1	28.0
LA6-10CIMB	1.2	11.7	3.51	6.64	10.5	32.0
LA6-15CIMB	0.6	9.7	3.32	6.04	9.0	36.8

3.2. Tensile properties

The tensile test results of the original samples are given in Table 3. Although any enhancement in the mechanical performance of the REF compound was expected in this study, it would be helpful to figure out the overall effects of lignin and CIMB on ENR. It is seen from the table that both lignin and CIMB adversely affected the mechanical strength. However, most of the compositions still have acceptable material properties, and they can also be improved by various methods when the original material properties are of interest.

As can be clearly seen from Table 3, both additives resulted in lower tensile strength, elongation at break, and 50% modulus values. Indeed, blending lignin with most polymers is not straightforward because

Table 3. Original mechanical properties of the vulcanizates.

	Tensile strength [MPa]	Elongation at break [%]	50% Modulus [MPa]
REF	16.4±1.4	889±60	0.96±0.05
Group 1			
LA3	14.0±1.0	835±43	0.84±0.04
LA6	13.4±1.9	643±58	1.20±0.06
Group 2			
4CIMB	11.8±1.0	797±45	0.81±0.02
10CIMB	10.5±1.0	716±53	1.14±0.05
15CIMB	10.5±0.3	687±29	0.99±0.03
Group 3			
LA3-4CIMB	14.2±1.4	895±80	0.85±0.02
LA3-10CIMB	13.6±1.3	760±53	0.74±0.03
LA3-15CIMB	10.5±0.7	624±58	0.75±0.09
Group 4			
LA6-4CIMB	14.5±0.8	658±25	1.05±0.03
LA6-10CIMB	13.7±0.8	642±39	0.92±0.03
LA6-15CIMB	7.5±0.8	525±80	0.69±0.08

of its polar character and may result in a poor matrix interface [66]. CIMB has been found to have a higher impact on tensile properties compared to lignin due to its plasticizing effect [51]. However, particularly at lower (4 and 10 phr) CIMB levels, the presence of lignin could dampen the deteriorative effect of CIMB. Interactions between lignin and CIMB are most probably due to phenolic hydroxyl groups of lignin. The phenolic hydroxyl groups are the most reactive functional groups and can significantly affect the chemical reactivity of the material [43, 47, 67].

3.3. Self-healing study

Along with their visual inspection, the self-healing performance of the samples was evaluated by means of their retention in tensile strength values. Self-healing performance results at 180 °C and for 5, 10, and 15 min healing times are given for four different compound groups, separately in Figure 2.

It is seen in Figure 2 that ENR-based control compound (REF) exhibits 27–38% healing at elevated temperatures on its own. This was already an expected result due to the well-known limited self-crosslinking ability of ENR [14, 45]. As seen in Figure 2a, 3 phr lignin incorporation did not improve the self-healing performance of the reference compound except at relatively high healing temperatures. However, up to 47% healing could be obtained for the LA6 compound when sufficient healing time was allowed. Here, another interesting finding is that the maximum self-healing ratio for all compounds was measured at 15 min healing time. Although there is no proven temperature limit, lower self-healing performance at 190 °C has been attributed to competitive reactions in rubber matrix, in which one was healing, and the other one was chain scission resulting in lower tensile strength after self-healing.

As one can see in Figure 2b (Group 2), CIMB could improve self-healing performance from 27–38 to 35–55%. 55% self-healing ratio was measured for 15CIMB compound at 180 °C for 15 min healing time. However, it should be noted that there was
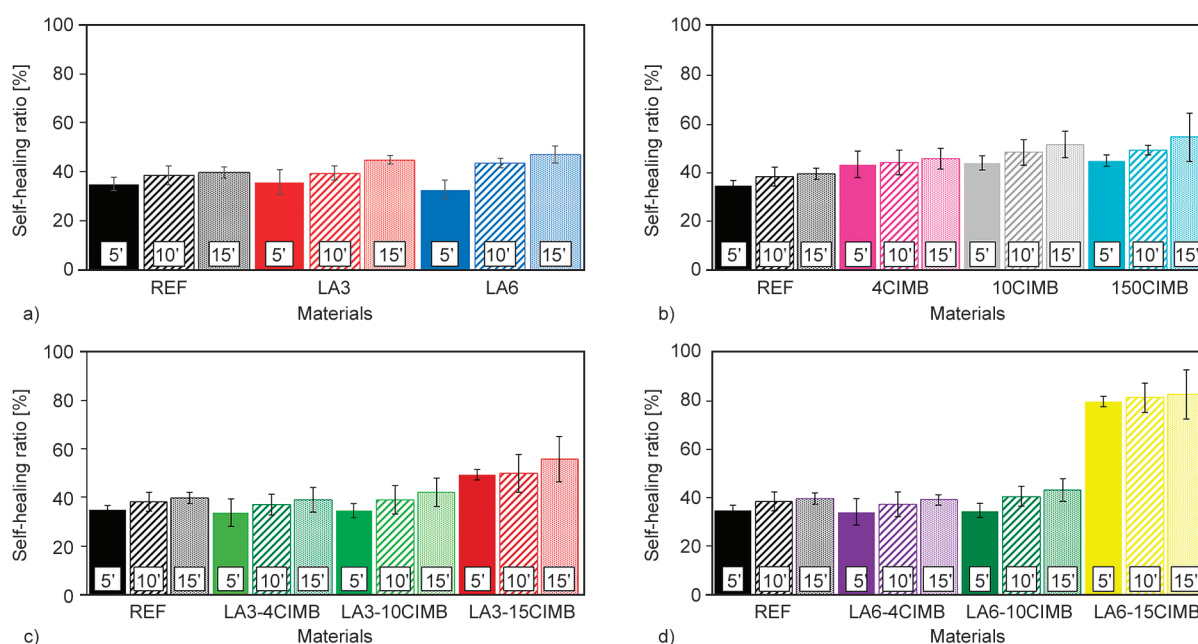
Figure 2. Self-healing ratio for various healing times at 180 °C; a) Group 1, b) Group 2, c) Group 3 and d) Group 4.

not a remarkable change in average self-healing performance when the amount of CIMB was increased from 10 to 15 phr in the compound.

Self-healing performance was also evaluated for the longest healing time (15 min), and the effect of healing temperature at 160, 170, 180, and 190 °C is shown in Figure 3. Contrary to Group 1 compounds, increasing the healing temperature of the 15CIMB compound did not cause a deterioration in self-healing performance. This was solely attributed to the anti-reversion effect of CIMB, which is also more pronounced at high temperatures.

Group 3 compounds comprise 3 phr lignin and CIMB ladder (Table 4). Here, any of the compounds did not exhibit an improvement in self-healing ratio when compared to Group 2 compounds, which comprise only CIMB in the same amounts as Group 3. The highest self-healing ratio for Group 3 was measured as 55%; this was of the LA3-15CIMB compound and measured at 180 °C – 15 min healing conditions (Figure 2d). When we compare Group 1 and Group 2 in each other, CIMB is still found to improve healing by balancing self-healing and reversion processes.

Using a relatively high amount (6 phr) of lignin with an increasing amount of CIMB (Group 4) was evaluated in Figure 2 and Figure 3. As seen in both figures, when the healing temperature was increased sufficiently, 6 phr lignin and 15 phr CIMB (LA6-15CIMB) could provide remarkable success in self-healing. This was also related to healing time. The
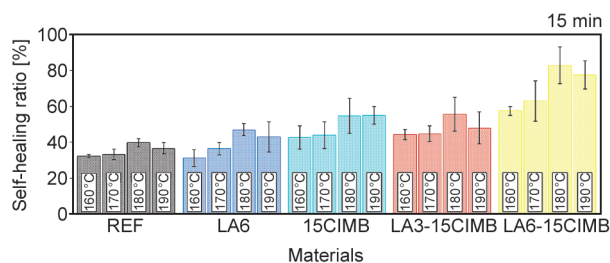

Figure 3. Self-healing ratio at various temperatures for 15 minutes healing time.

highest level of self-healing, which was 83%, again could be obtained at 180 °C. This impressive healing ratio was attributed to the best stoichiometric interaction between lignin and CIMB.

Structural mobility and localization are the key concepts for self-healing. Thus, high cross-link density is expected to reduce self-healing due to the fact that it restricts mobility in the polymeric matrix [68]. Indeed, there are some studies met in the literature indicating reciprocity between self-healing and cross-link density for ENR-based rubber compounds [1, 17, 69, 70] as well as for different polymeric structures [6, 71, 72]. In this study, the LA6-15CIMB compound exhibits not only the highest level of self-healing performance but also the lowest level of tensile modulus along with the lowest cure extent.

In other respects, better self-healing in the case of high temperatures and long healing periods can be attributed to sufficient inter-diffusion of polymer chains, which promotes epoxidation at the interphase [1, 19, 69]. Indeed, for Group 3 and Group 4 compounds comprising both lignin and CIMB, remarkably higher self-healing performance could be achieved at high temperatures when they are allowed to keep healing for sufficient healing time. However, it should be noted that healing efficiency tends to decrease at temperatures over 180 °C. The decrease in self-healing performance at 190 °C, can be associated with physical cross-links based on ionic interaction or hydrogen bonds [70].

3.4. Cross-link density

Cross-link densities of all the selected vulcanizates were calculated by using swelling results to understand better how self-healing performance is correlated to cross-link structure. Results are given in Table 5 for each compound, which was taken from the healing surfaces before and after self-healing. When evaluated, cross-link density values of the samples before self-healing are in a good correlation

Table 4. Self-healing ratio [%] in tensile strength of the vulcanizates for 15 min.

	at 160 °C	at 170 °C	at 180 °C	at 190 °C
REF	32±1	33±3	40±2	37±3
Group 1				
LA3	30±3	34±5	45±2	34±8
LA6	31±4	36±3	47±3	43±8
Group 2				
4CIMB	35±3	40±1	46±4	50±5
10CIMB	42±4	44±8	52±5	55±5
15CIMB	43±7	44±7	55±10	55±5
Group 3				
LA3-4CIMB	27±3	36±3	39±5	38±5
LA3-10CIMB	33±6	38±5	42±6	41±5
LA3-15CIMB	44±3	45±4	56±9	48±9
Group 4				
LA6-4CIMB	27±3	36±5	39±2	41±1
LA6-10CIMB	34±3	39±4	43±4	42±4
LA6-15CIMB	58±3	63±11	83±10	78±8

Table 5. Swelling ratio (Q), cross-link density (V_e) and molecular weight between cross-links (M_c) of the vulcanizates based on swelling measurements.

	Before self-healing [mol/m^3]			After self-healing [mol/m^3]		
	Q [%]	V_e [mol/m^3]	$M_c \cdot 10^3$ [g/mol]	Q [%]	V_e [mol/m^3]	$M_c \cdot 10^3$ [g/mol]
REF	1.7±0.3	585±26	2.2±0.1	2.2±0.1	397±26	2.9±0.1
LA6	1.8±0.1	594±68	1.9±0.1	1.9±0.2	522±78	2.3±0.1
15CIMB	1.9±0.5	517±65	2.3±0.1	1.8±0.0	563±21	2.0±0.0
LA6-15CIMB	2.0±0.2	453±86	2.4±0.1	1.7±0.0	635±19	1.8±0.0

with their cure extent values given in Table 2, which refers to cure data. For 15CIMB and LA6-15CIMB samples, cross-link density values were measured higher after self-healing.

It is much more remarkable for the LA6-15CIMB sample, which contains both lignin and CIMB in higher amounts. It is very well-known that extent of cross-linking reaction of ENR strictly depends on the ring-opening level of the epoxy groups. Besides, the amount of lignin has a significant impact on the reaction by promoting the interaction between epoxy groups and CIMB. Therefore, the higher cross-link density of the given sample after self-healing can readily be attributed to further cross-linking reactions, and this finding supports the fact that LA6-15CIMB composition exhibits the best self-healing performance, as indicated above. This is also an expected result of decreasing average molecular weight between the cross-links (M_c). Indeed, the elastic retention force is inversely proportional to the average distance between the cross-links on the polymer chain [55, 73].

When we correlate with the initial cross-link density, self-healing performance has been found to decrease with increasing cross-link density due to less polymer chain diffusion in the rubber matrix, as extensively explained in related studies in the literature [21,

74, 75]. However, when the fractured samples are subjected to the self-healing process for appropriate healing conditions (time and temperature), further cross-links are able to form if the rubber compound contains the required species promoting self-healing [19, 21, 26, 72]. LA6-15CIMB sample, which has the lowest initial cross-link density and the highest one after self-healing, represents this fact as a good example.

3.5. Optical micrographs of self-healed materials

For all the compound groups, 180 °C – 15 min has been found to be the best self-healing condition. Thus, representative pictures of the samples, which were healed at 180 °C were given below in Figure 4. Healed samples were also shown under ×100 magnification in Figure 5. Figures clearly show that all the parameters: composition, temperature, and healing time, are highly effective in self-healing performance. Samples, which self-healed at appropriate conditions, could exhibit excellent recovery that is almost the same as their initial appearance. The sample exhibiting the highest self-healing ratio, LA6-15CIMB, has also been depicted in Figure 6 to verify how high self-healing performance affects physical appearance.

Figure 4. Representative pictures – original tensile-fractured samples before self-healing and after self-healing at 180 °C for 15 min.
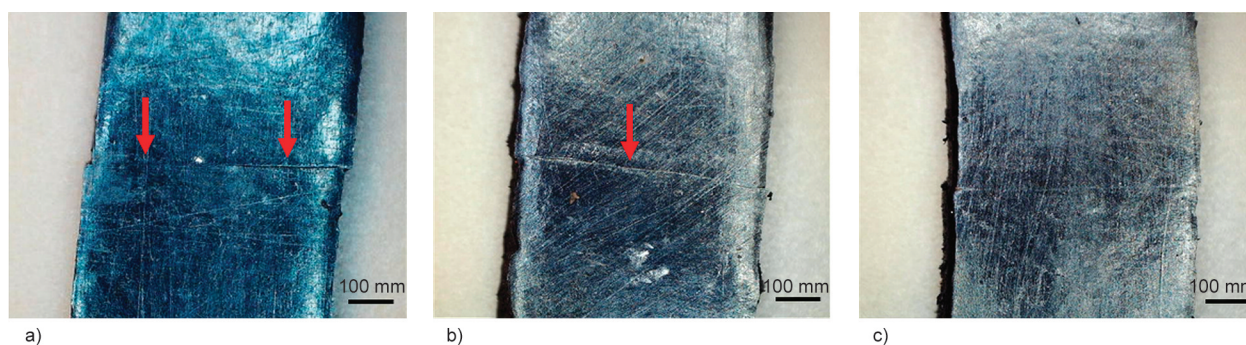
Figure 5. Optical micrographs of LA6-15CIMB samples after self-healing a) at 180 °C for 5 min, b) at 180 °C for 10 min, and c) at 180 °C for 15 min.
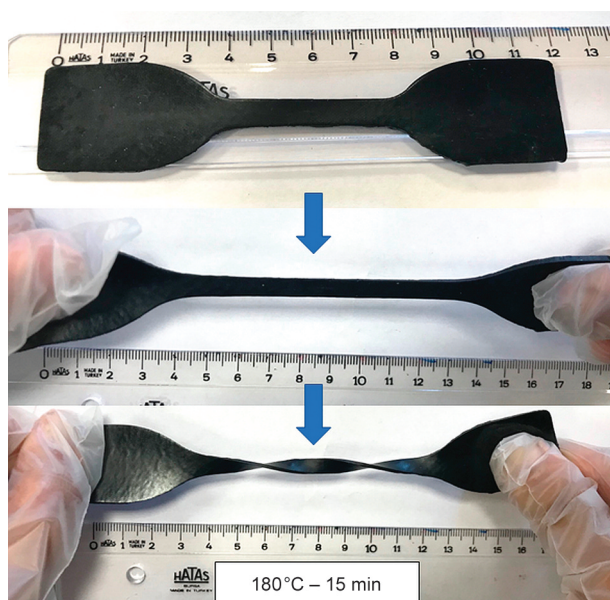

Figure 6. LA6-15CIMB sample after self-healing at 180 °C for 15 min.

Figure 7. ATR-FTIR spectra of selected vulcanizates.

3.6. FTIR analysis and proposed reaction mechanism

For verifying the potential chemical interactions between ENR, lignin, and CIMB, selected samples were analyzed by using an FTIR device. The attenuated total reflectance (ATR)-FTIR spectrum of the reference compound REF, LA6, 15CIMB, and LA6-15CIMB compounds are given in Figure 7 and Figure 8, respectively, before and after self-healing at 180 °C for 15 min healing conditions.

The peaks at 2959, 2917, and 2850 cm^{-1} in Figure 8, which are detected at all vulcanizate spectra, are characteristic peaks of ENR and represent –CH$_3$ stretching vibration, C–H stretching vibration, and –CH$_2$ symmetric and asymmetric stretching vibrations, respectively [76, 77]. Besides, the 875 cm^{-1} band refers to the presence of an epoxy ring (C–O–C) along with 1458 and 1377 cm^{-1} bands, which belong to C–H stretching and bending vibrations, respectively [1, 21, 56, 68, 77–81].

In Figure 7, the cyclic imide (–C=O) bending vibration peak, which is characteristic of CIMB, is seen for 15CIMB and LA6-15CIMB vulcanizates, as expected [61]. When comparing LA6 and REF samples, the peak intensity at 1175 cm^{-1} is lower for LA6 vulcanizates which refers to lignin to promote epoxy ring opening reaction in ENR [1, 82].

In Figure 8a and Figure 8b, for REF and LA6 compounds, the peaks around 1700 cm^{-1} (1737 and 1743 cm^{-1}) refer to non-conjugated C=O of carbonyl and carboxylic groups. These peaks are associated with the oxidation of cis-double bonds and/or the rearrangement of epoxy groups [1, 43, 78]. Higher peak intensity at 1097 and 1065 cm^{-1} bands in FTIR spectra of LA6 and LA6-15CIMB (Figure 8b and Figire 8d) indicates increasing C–O–C stretching vibrations. These peaks can be associated with the ENR backbone to interact with the other species present in the reaction media [6]. Besides, C=S and C=O groups come from epoxy ring opening reactions [80]. The
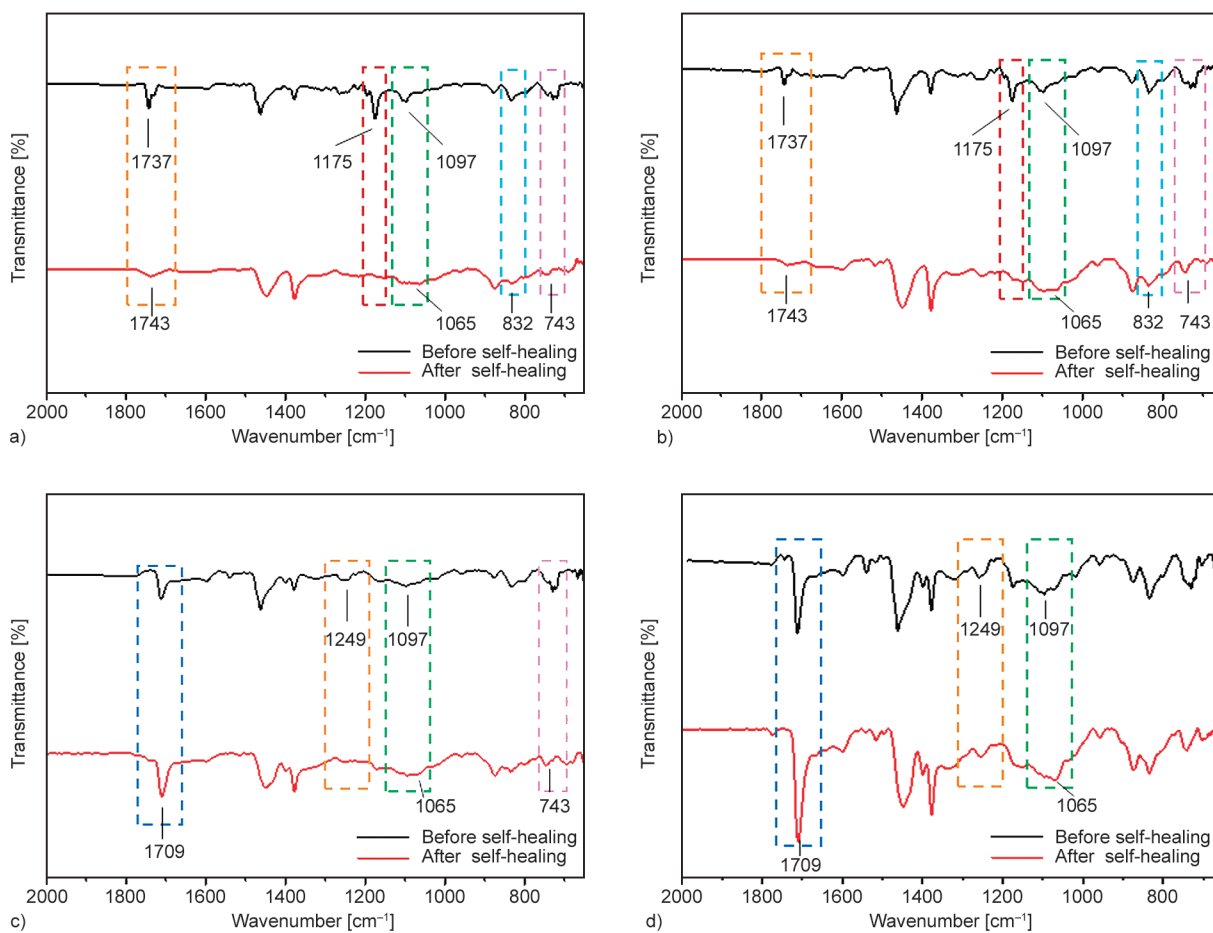
Figure 8. Extended ATR-FTIR spectra of a) REF, b) LA6, c) 15CIMB, and d) LA6-15CIMB vulcanizates before and after self-healing.

increasing peak intensity in the same absorption band also supports the presence of ether cross-links between lignin and epoxy groups of ENR as well as sulfonate ester cross-links [84]. Please note that the highest self-healing ratio of the LA6-15CIMB sample was also attributed to the possible chemical interactions between lignin, ENR, and CIMB. In Figure 8a and Figure 8b, the peak intensity of the 832 cm^{-1} band refers to C=C bonds after self-healing. For all the samples, 1249 and 743 cm^{-1} bands belong to C–O symmetric stretching vibration and ring stretching vibration, respectively [1, 77, 83]. Then, the sharp decrease in the peak intensities of the same bands is attributed to the epoxy ring opening reaction for LA6-15CIMB vulcanizate.

CIMB is known to attach to the polymer structure via the broken cross-links during reversion, whereas it is normally not active at the beginning of the vulcanization reaction [28, 84]. In Figure 7, cyclic imide (–C=O) stretching vibration peak (1709 cm^{-1}) is detected in the presence of CIMB. Cross-linking during self-healing is expected to occur via C=C bonds

on ENR for CIMB-containing vulcanizates [61]. This is also supported by the highly increasing 1709 cm^{-1} peak for LA6-15CIMB vulcanizate (Figure 8c and Figure 8d), which exhibits the best self-healing performance.

Evaluating all FTIR observations as well as the rheological and mechanical test results, the proposed reaction mechanism between ENR, lignin, and CIMB is summarized in Figures 9–11. Figure 9 depicts the traditional sulfur vulcanization of ENR and epoxy ring-opening reaction. During the vulcanization step at a sufficiently high vulcanization temperature, the active accelerator complex, which is able to react with sulfur, reacts with allylic sites of the polymer chain and readily initiates cross-linking reaction [85].

Also, the epoxy ring-opening reaction of ENR by the effect of lignin is given in Figure 9. Kraft lignin is a branched macromolecule and is able to give strong intra-molecular interactions thanks to its several functionalities. Phenolic hydroxyl groups have the highest concentration among these functionalities

[47]. Reactive –OH groups of lignin interact with the oxygen atom on the ENR epoxy ring to initiate the ring-opening reaction via the formation of hydrogen bonding [4]. Cross-linking reaction between ENR and lignin without using any curative has also been well-defined in literature [45].
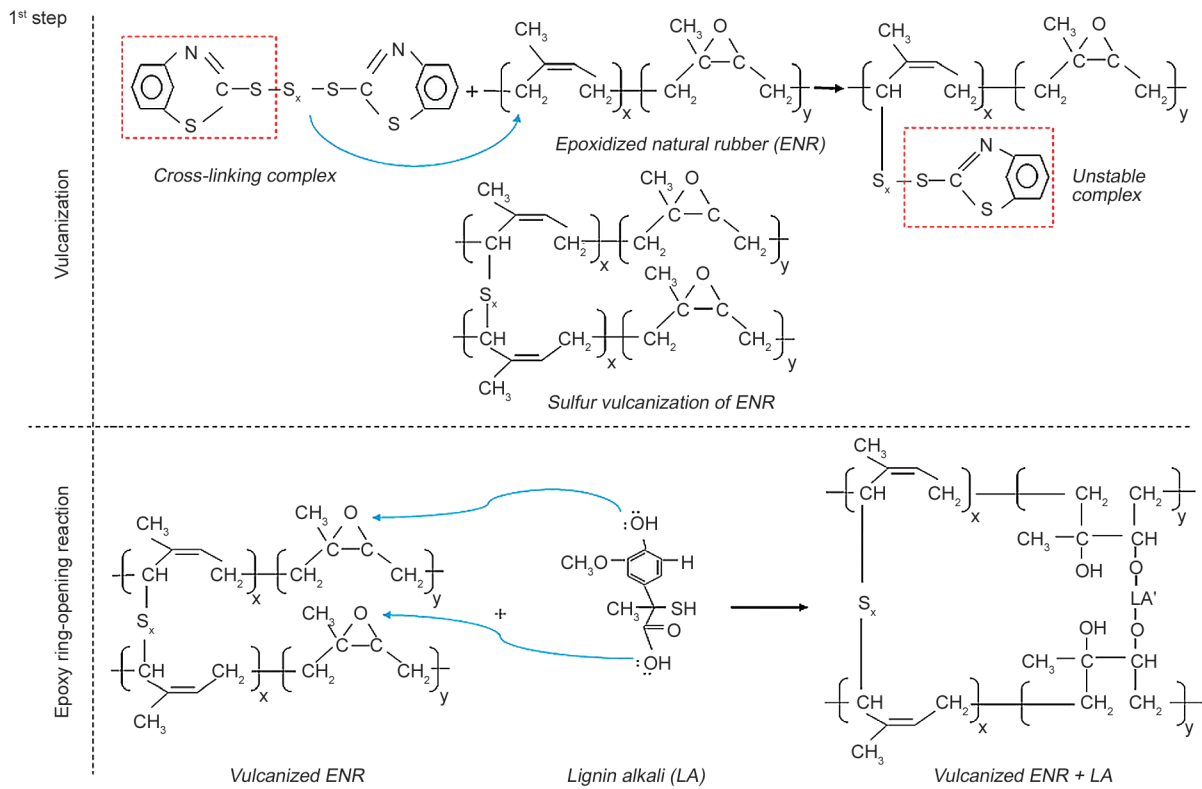

Figure 9. Traditional sulfur vulcanization mechanism and the epoxy ring-opening reaction of ENR in the presence of lignin.
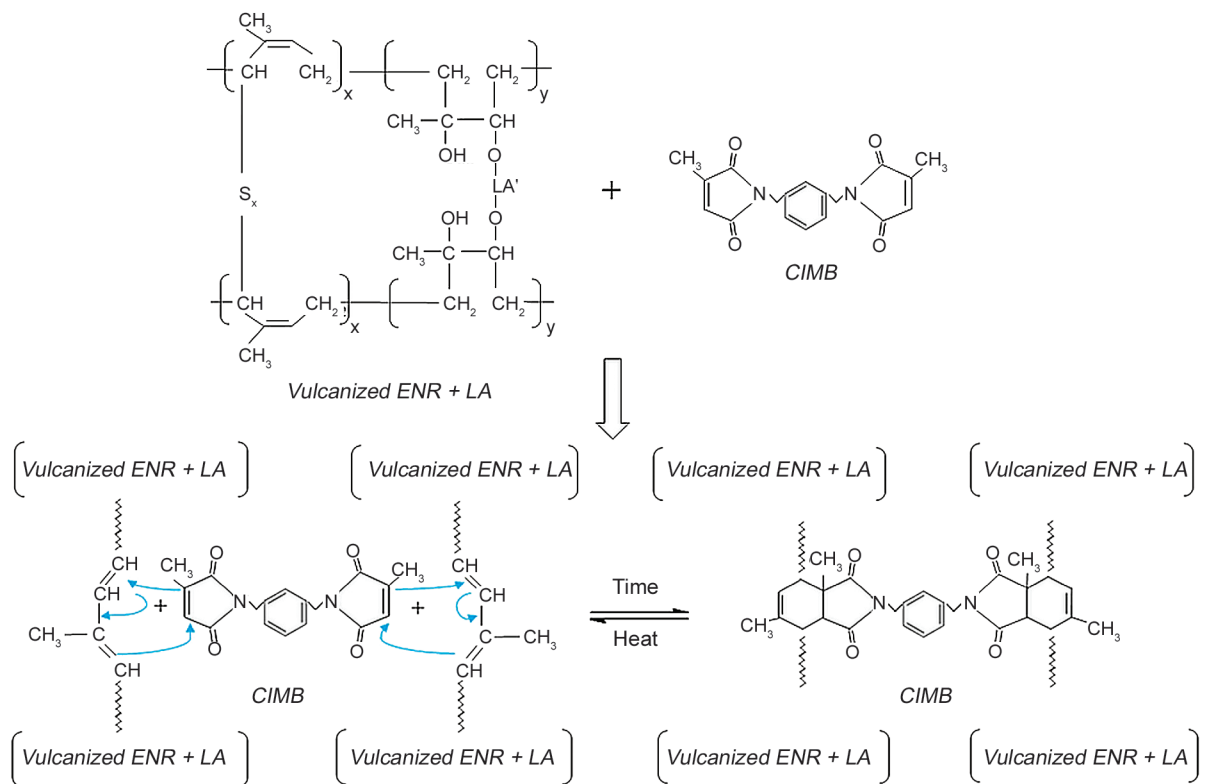
Figure 10. Proposed Diels-Alder and retro-Diels-Alder reaction mechanisms between ENR and CIMB.

3ʳᵈ step: Alder-ene reaction between ENR and CIM
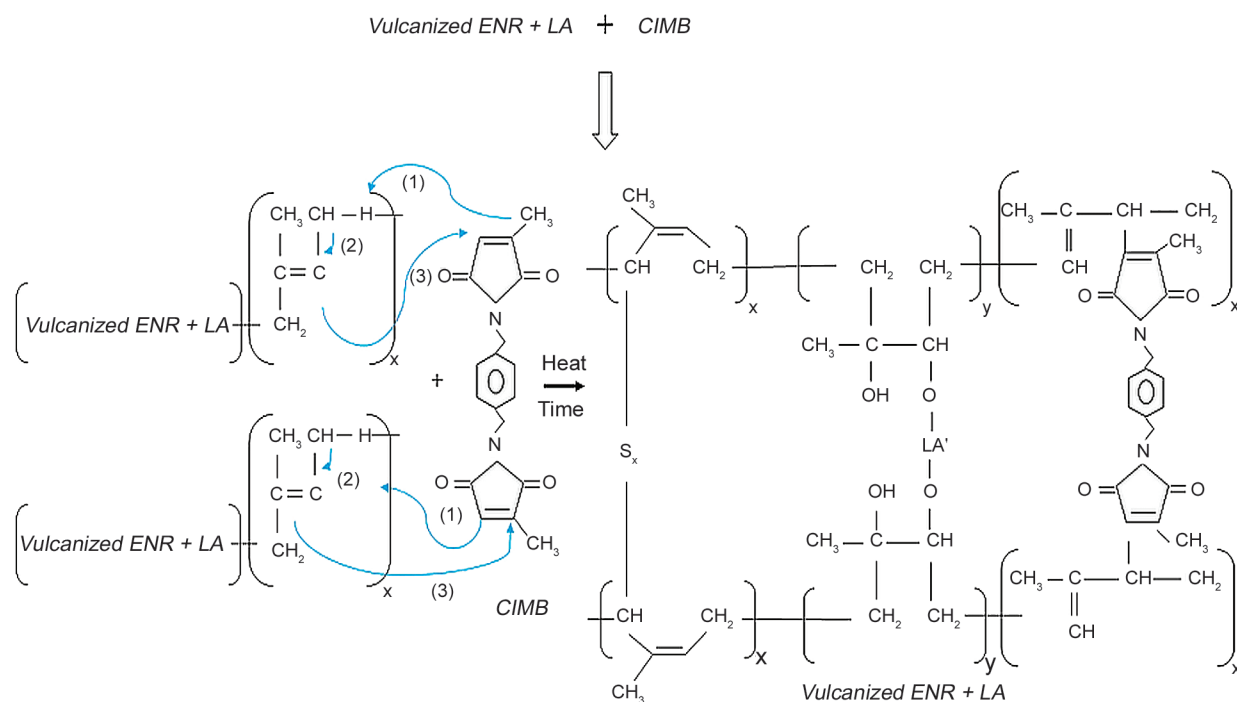
Figure 11. Proposed Alder-ene reaction between ENR and CIMB.

CIMB is a traditional anti-reversion agent, which is able to interact with double bonds on the polymer chain to provide reversible covalent bonds via a Diels-Alder reaction at relatively high vulcanization temperatures. Therefore, CIMB can be considered as a potential self-healing agent for sulfur-cured rubber materials [29, 60, 84]. The amount of reversible cross-links depends on double bond concentration on the polymer backbone, as expected. For ENR vulcanizates, along with the double bonds, epoxy rings have the potential to increase total reactivity for interacting with CIMB molecules.

In this study, the main function of lignin is believed to promote the epoxy ring-opening reaction to let ENR interact further with CIMB. The proposed Diels-Alder reaction mechanism of ENR in the presence of both lignin and CIMB is given in Figure 10. Carbonyl groups linked to maleimide terminations make the double bond on bismaleimide highly active to act as a dienophile for the Diels-Alder reaction with conjugated dienes [30]. Increasing cross-link density of LA6-15CIMB vulcanizate after self-healing also coincides with the diene-dienophile reaction (Diels-Alder) of CIMB and double bonds on fractured polymer chains [29, 37, 86, 87].

The proposed Alder-ene reaction mechanism between CIMB and isoprene units on ENR molecules is given in Figure 11 [30, 61, 62]. This reaction is thought to take place within the self-healing process. Higher cross-link density of CIMB containing vulcanizates after self-healing, as well as new chemical bonds detected in FTIR spectra of these samples, can be accepted as strong proof for this evaluation.

3.7. Dynamic mechanical analysis
The reversible character of the self-healing process was investigated by following the dynamic modulus of the four representative samples. The selected vulcanizates REF, LA6, 15CIMB, and LA6-15CIMB, which were already self-healed at 180 °C for 15 min, were subjected to customized dynamic heating-cooling cycles, and the obtained results are given in Figure 12. In each cycle of dynamic analysis, the retro-Diels-Alder reaction is expected to occur at high temperatures, whereas the ENR and CIMB give Diels-Alder reaction during cooling down to 40 °C. As seen in the figure, storage modulus, as well as loss modulus values, increase in the cooling period indicating the Diels-Alder reaction as well as the Alder-ene reaction in each cycle. Immediately after the heating period starts, the modulus values show a sharp drop. This behavior can be attributed to the retro-Diels-Alder reaction, which results in breaking down the cross-links formed by Diels-Alder and Alder-ene reactions in the previous cooling period, and the overall dynamic results show a good correlation with
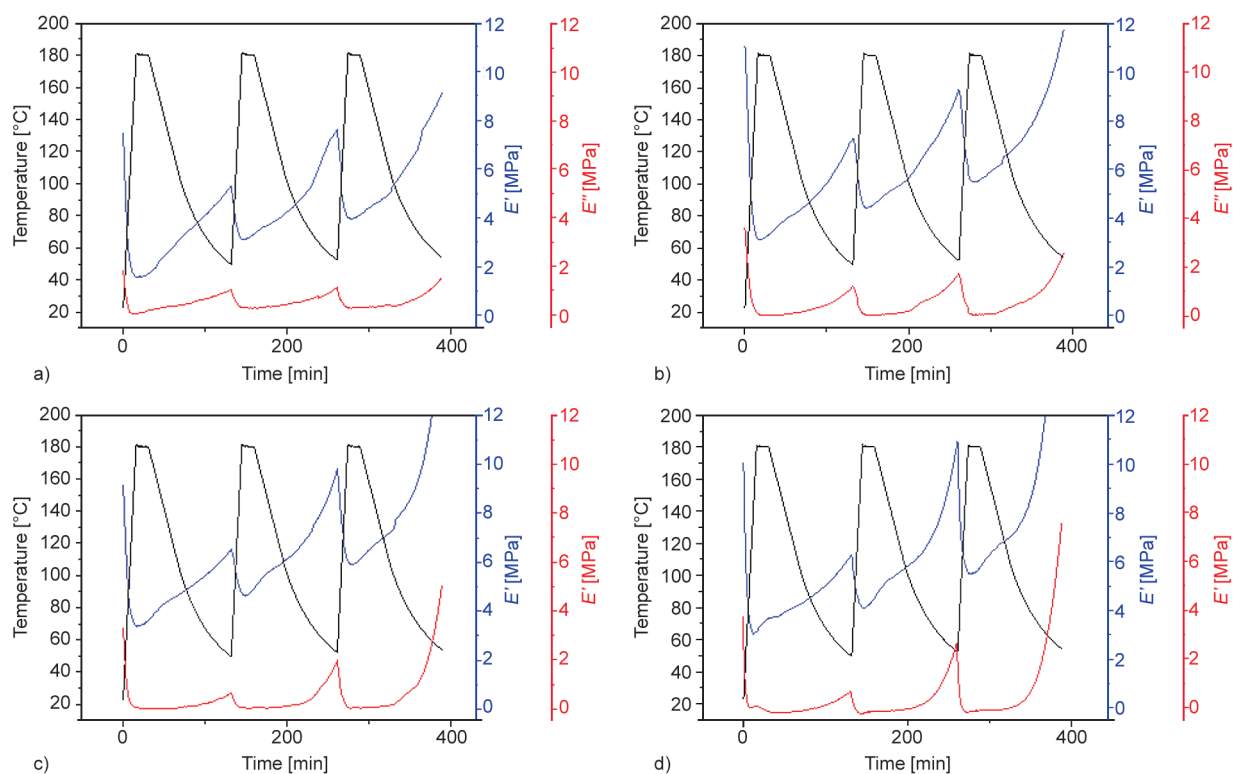
Figure 12. Dynamic moduli of the selected vulcanizates during repetitive heating-cooling cycles. a) REF, b) LA6, c) 15CIMB and d) LA6-15CIMB.

the recent literature [8, 26, 88]. When we compare the storage modulus of lignin and CIMB-containing samples with the reference one, significantly higher modulus values of these samples after each cooling period were also found to be related to their higher self-healing ratio. Besides, the LA6-15CIMB compound, which exhibited the highest level of healing, has the highest storage modulus values, especially after the second and third cycles. Indeed, the lower modulus of all CIMB-containing vulcanizates after the first cycle could easily be attributed to their lower initial mechanical strength.

4. Conclusions
In this study, the self-healing performance of an ENR-based rubber compound in the presence of lignin and CIMB has been investigated by means of retention in tensile strength as well as by visual inspection. Self-healing agents resulted in a higher cure rate due to reactive interactions of lignin and CIMB on the ENR matrix to promote further cross-linking reactions. Lignin could improve self-healing from 27 to 47% on its own, whereas CIMB, which was found to improve healing by balancing healing

and reversion processes, could do it up to 55% at specific healing conditions. Using 6 phr lignin and 15 phr CIMB in the same composition provided a remarkable increase in cross-link density by self-healing as well as the highest level of self-healing (83%) at 180 °C for 15 min healing time. This impressive healing ratio was attributed to the synergistic effect of lignin and CIMB at the best stoichiometric ratio. However, using any of lignin and CIMB may need further attention when the initial mechanical properties are of interest since both additives have an adverse effect on the mechanical strength of the ENR-based material.

The reaction mechanism comprising lignin-promoted epoxy ring-opening reaction on ENR backbone, Diels-Alder, and Alder-ene reactions between CIMB and isoprene units of ENR was proposed for the self-healing process. The reversible character of Diels-Alder and retro-Diels-Alder reactions could also be proved by dynamic analysis.

References

[1] Rahman M. A., Sartore L., Bignotti F., di Landro L.: Autonomic self-healing in epoxidized natural rubber. ACS Applied Materials and Interfaces, **5**, 1494–1502 (2013).
https://doi.org/10.1021/am303015e

[2] Khan A. A. P., Khan A., Ansari O., Shaban M., Rub M. A., Azum N., Jilani A., Asiri A. M.: Self-healing of polymer materials and their composites. in 'Self-healing composite materials' (eds.: Khan A., Jawaid M., Raveendran S. N., Asiri A. M. A.) 103–121 (2019).
https://doi.org/10.1016/B978-0-12-817354-1.00007-7

[3] Zhu M., Liu J., Gan L., Long M.: Research progress in bio-based self-healing materials. European Polymer Journal, **129**, 109651 (2020).
https://doi.org/10.1016/j.eurpolymj.2020.109651

[4] Behera P. K., Mohanty S., Gupta V. K.: Self-healing elastomers based on conjugated diolefins: A review. Polymer Chemistry, **12**, 1598–1621 (2021).
https://doi.org/10.1039/d0py01458c

[5] Terryn S., Langenbach J., Roels E., Brancart J., Bakkali-Hassani C., Poutrel Q., Georgopoulou A., Thuruthel T. G., Safaei A., Ferrentino P., Sebastian T., Norvez S., Iida F., Bosman A. W., Tournilhac F., Clemens F., van Assche G., Vanderborght B.: A review on self-healing polymers for soft robotics. Materials Today, **47**, 187–205 (2021).
https://doi.org/10.1016/j.mattod.2021.01.009

[6] Xu C., Nie J., Wu W., Fu L., Lin B.: Design of self-healable supramolecular hybrid network based on carboxylated styrene butadiene rubber and nano-chitosan. Carbohydrate Polymers, **205**, 410–419 (2019).
https://doi.org/10.1016/j.carbpol.2018.10.080

[7] Utrera-Barrios S., Verdejo R., López-Manchado M. A., Santana M. H.: Evolution of self-healing elastomers, from extrinsic to combined intrinsic mechanisms: A review. Materials Horizons, **7**, 2882–2902 (2020).
https://doi.org/10.1039/d0mh00535e

[8] Utrera-Barrios S., Verdejo R., López-Manchado M. Á., Santana M. H.: The final frontier of sustainable materials: Current developments in self-healing elastomers. International Journal of Molecular Sciences, **23**, 4757 (2022).
https://doi.org/10.3390/ijms23094757

[9] Ismail H.: Potential of rubberwood as a filler in epoxidized natural rubber compounds. Journal of Elastomers and Plastics, **33**, 34–46 (2001).
https://doi.org/10.1106/B04H-YKPD-H80B-KQ8N

[10] Mascia L., Clarke J., Ng K. S., Chua K. S., Russo P.: Cure efficiency of dodecyl succinic anhydride as a cross-linking agent for elastomer blends based on epoxidized natural rubber. Journal of Applied Polymer Science, **132**, 41448 (2015).
https://doi.org/10.1002/app.41448

[11] Tanjung F. A., Hassan A., Hasan M.: Use of epoxidized natural rubber as a toughening agent in plastics. Journal of Applied Polymer Science, **132**, 42270 (2015).
https://doi.org/10.1002/app.42270

[12] Luo Y. Y., Wang Y. Q., Zhong J. P., He C. Z., Li Y. Z., Peng Z.: Interaction between fumed-silica and epoxidized natural rubber. Journal of Inorganic and Organometallic Polymers and Materials, **21**, 777–783 (2011).
https://doi.org/10.1007/s10904-011-9539-x

[13] Poh B. T., Lim A. L.: Adhesion properties of pressure-sensitive adhesives prepared from SMR 10/ENR 25, SMR 10/ENR 50, and ENR 25/ENR 50 blends. Journal of Applied Polymer Science, **109**, 115–119 (2008).
https://doi.org/10.1002/app.27489

[14] Xu T., Jia Z., Wang S., Chen Y., Luo Y., Jia D., Peng Z.: Self-crosslinkable epoxidized natural rubber–silica hybrids. Journal of Applied Polymer Science, **134**, 44605 (2017).
https://doi.org/10.1002/app.44605

[15] Öter M., Karaağaç B.: Epoxidised natural rubber as adhesion promoter in natural rubber based compounds. Journal of Rubber Research, **23**, 333–341 (2020).
https://doi.org/10.1007/s42464-020-00061-9

[16] Roychoudhury A., De P. P., Bhowmick A. K., De S. K.: Self-crosslinkable ternary blend of chlorosulphonated polyethylene, epoxidized natural rubber and carboxylated nitrile rubber. Polymer, **33**, 4737–4740 (1992).
https://doi.org/10.1016/0032-3861(92)90686-Q

[17] Cheng B., Lu X., Zhou J., Qin R., Yang Y.: Dual crosslinked self-healing and recyclable epoxidized natural rubber based on multiple reversible effects. ACS Sustainable Chemistry and Engineering, **7**, 4443–4455 (2019).
https://doi.org/10.1021/acssuschemeng.8b06437

[18] Ünügül T., Karaağaç B.: Vulcanization of chlorinated polyethylene/chloroprene rubber compounds at lower temperatures in the presence of reactive silanes. Journal of Applied Polymer Science, **138**, 50544 (2021).
https://doi.org/10.1002/app.50544

[19] Imbernon L., Oikonomou E. K., Norvez S., Leibler L.: Chemically crosslinked yet reprocessable epoxidized natural rubber *via* thermo-activated disulfide rearrangements. Polymer Chemistry, **6**, 4271–4278 (2015).
https://doi.org/10.1039/c5py00459d

[20] Liu L., Zhu L., Zhang L.: A solvent-resistant and biocompatible self-healing supramolecular elastomer with tunable mechanical properties. Macromolecular Chemistry and Physics, **219**, 1700409 (2018).
https://doi.org/10.1002/macp.201700409

[21] Xu C., Nie J., Wu W., Zheng Z., Chen Y.: Self-healable, recyclable, and strengthened epoxidized natural rubber/carboxymethyl chitosan biobased composites with hydrogen bonding supramolecular hybrid networks. ACS Sustainable Chemistry and Engineering, **7**, 15778–15789 (2019).
https://doi.org/10.1021/acssuschemeng.9b04324

[22] Algaily B., Kaewsakul W., Sarkawi S. S., Kalkornsurapranee E.: A self-healing system based on ester crosslinks for carbon black-filled rubber compounds. Journal of Composites Science, **5**, 70 (2021).
https://doi.org/10.3390/jcs5030070

[23] Wu D. Y., Meure S., Solomon D.: Self-healing polymeric materials: A review of recent developments. Progress in Polymer Science, **33**, 479–522 (2008).
https://doi.org/10.1016/j.progpolymsci.2008.02.001

[24] Boden J., Bowen C. R., Buchard A., Davidson M. G., Norris C.: Understanding the effects of cross-linking density on the self-healing performance of epoxidized natural rubber and natural rubber. ACS Omega, **7**, 15098–15105 (2022).
https://doi.org/10.1021/acsomega.2c00971

[25] Gheneim R., Perez-Berumen C., Gandini A.: Diels–Alder reactions with novel polymeric dienes and dienophiles: Synthesis of reversibly cross-linked elastomer. Macromolecules, **35**, 7246–7253 (2002).
https://doi.org/10.1021/ma020343c

[26] Tanasi P., Santana M. H., Carretero-González J., Verdejo R., López-Manchado M. A.: Thermo-reversible cross-linked natural rubber: A Diels-Alder route for reuse and self-healing properties in elastomers. Polymer, **175**, 15–24 (2019).
https://doi.org/10.1016/j.polymer.2019.04.059

[27] Wemyss A. M., Bowen C., Plesse C., Vancaeyzeele C., Nguyen G. T. M., Vidal F., Wan C.: Dynamic crosslinked rubbers for a green future: A material perspective. Materials Science and Engineering R: Reports, **141**, 100561 (2020).
https://doi.org/10.1016/j.mser.2020.100561

[28] Sathi S. G., Jang J. Y., Jeong K-U., Nah C.: Thermally stable bromobutyl rubber with a high crosslinking density based on a 4,4′-bismaleimidodiphenylmethane curing agent. Journal of Applied Polymer Science, **133**, 44092 (2016).
https://doi.org/10.1002/app.44092

[29] Gopi Sathi S., Stoček R., Kratina O.: Reversion free high-temperature vulcanization of cis-polybutadiene rubber with the accelerated-sulfur system. Express Polymer Letters, **14**, 823–837 (2020).
https://doi.org/10.3144/expresspolymlett.2020.68

[30] Sathi G. S., Jeon J., Won J., Nah C.: Enhancing the efficiency of zinc oxide vulcanization in brominated poly (isobutylene-co-isoprene) rubber using structurally different bismaleimides. Journal of Polymer Research, **25**, 108 (2018).
https://doi.org/10.1007/s10965-018-1512-8

[31] Mishra S., Mohanty A. K., Drzal L. T., Misra M., Hinrichsen G.: A review on pineapple leaf fibers, sisal fibers and their biocomposites. Macromolecular Materials and Engineering, **289**, 955–974 (2004).
https://doi.org/10.1002/mame.200400132

[32] Aradoaei S., Darie R., Constantinescu G., Olariu M., Ciobanu R.: Modified lignin effectiveness as compatibilizer for PET/LDPE blends containing secondary materials. Journal of Non-Crystalline Solids, **356**, 768–771 (2010).
https://doi.org/10.1016/j.jnoncrysol.2009.11.046

[33] Asrul M., Othman M., Zakaria M., Fauzi M. S.: Lignin filled unvulcanised natural rubber latex: Effects of lignin on oil resistance, tensile strength and morphology of rubber films. International Journal of Engineering Science Invention, **2**, 38–43 (2013).

[34] Kakroodi A. R., Rodrigue D.: Degradation behavior of maleated polyethylene/ground tire rubber thermoplastic elastomers with and without stabilizers. Polymer Degradation and Stability, **98**, 2184–2192 (2013).
https://doi.org/10.1016/j.polymdegradstab.2013.08.017

[35] Thakur V. K., Thakur M. K., Raghavan P., Kessler M. R.: Progress in green polymer composites from lignin for multifunctional applications: A review. ACS Sustainable Chemistry and Engineering, **2**, 1072–1092 (2014).
https://doi.org/10.1021/sc500087z

[36] Phakkeeree T., Ikeda Y., Yokohama H., Phinyocheep P., Kitano R., Kato A.: Network-like structure of lignin in natural rubber matrix to form high performance elastomeric bio-composite. Journal of Fiber Science and Technology, **72**, 160–165 (2016).
https://doi.org/10.2115/fiberst.fiberst.2016-0023

[37] Zhou W., Zhang H., Chen F.: Modified lignin: Preparation and use in reversible gel *via* Diels-Alder reaction. International Journal of Biological Macromolecules, **107**, 790–795 (2018).
https://doi.org/10.1016/j.ijbiomac.2017.09.052

[38] Yu P., He H., Jia Y., Tian S., Chen J., Jia D., Luo Y.: A comprehensive study on lignin as a green alternative of silica in natural rubber composites. Polymer Testing, **54**, 176–185 (2016).
https://doi.org/10.1016/j.polymertesting.2016.07.014

[39] Doherty W. O. S., Mousavioun P., Fellows C. M.: Value-adding to cellulosic ethanol: Lignin polymers. Industrial Crops and Products, **33**, 259–276 (2011).
https://doi.org/10.1016/j.indcrop.2010.10.022

[40] Mili M., Hashmi S. A. R., Ather M., Hada V., Markandeya N., Kamble S., Mohapatra M., Rathore S. K. S., Srivastava A. K., Verma S.: Novel lignin as natural-biodegradable binder for various sectors – A review. Journal of Applied Polymer Science, **139**, 51951 (2021).
https://doi.org/10.1002/app.51951

[41] Frigerio P., Zoia L., Orlandi M., Hanel T., Castellani L.: Application of sulphur-free lignins as a filler for elastomers: Effect of hexamethylenetetramine treatment. BioResources, **9**, 1387–1400 (2021).

[42] Makhalema M., Hlangothi P., Motloung S. V., Koao L. F., Motaung T. E.: Influence of kraft lignin on the properties of rubber composites. Wood Research, **66**, 285–296 (2021).
https://doi.org/10.37763/wr.1336-4561/66.2.285296

[43] Barana D., Ali S. D., Salanti A., Orlandi M., Castellani L., Hanel T., Zoia L.: Influence of lignin features on thermal stability and mechanical properties of natural rubber compounds. ACS Sustainable Chemistry and Engineering, **4**, 5258–5267 (2016).
https://doi.org/10.1021/acssuschemeng.6b00774

[44] Moreno A., Sipponen M. H.: Lignin-based smart materials: A Roadmap to processing and synthesis for current and future applications. Materials Horizons, **7**, 2237–2257 (2020)
https://doi.org/10.1039/d0mh00798f

[45] Jiang C., He H., Yao X., Yu P., Zhou L., Jia D.: Self-crosslinkable lignin/epoxidized natural rubber composites. Journal of Applied Polymer Science, **131**, 41166 (2014).
https://doi.org/10.1002/app.41166

[46] Sakunkittiyut Y., Kunanopparat T., Menut P., Siriwattanayotin S.: Effect of kraft lignin on protein aggregation, functional, and rheological properties of fish protein-based material. Journal of Applied Polymer Science, **127**, 1703–1710 (2013).
https://doi.org/10.1002/app.37899

[47] Laurichesse S., Avérous L.: Chemical modification of lignins: Towards biobased polymers. Progress in Polymer Science, **39**, 1266–1290 (2014).
https://doi.org/10.1016/j.progpolymsci.2013.11.004

[48] Chung H., Washburn N. R.: Extraction and types of lignin. in 'Lignin in polymer composites' (eds.: Faruk O., Sain M.) Elsevier, Amsterdam, 13–25 (2016).
https://doi.org/10.1016/B978-0-323-35565-0.00002-3

[49] Mandlekar N., Cayla A., Rault F., Giraud S., Salaün F., Malucelli G., Guan J-P.: An overview on the use of lignin and its derivatives in fire retardant polymer systems. in 'Lignin – Trends and applications' (ed.: Poletto M.) 207–231 (2018).
https://doi.org/10.5772/intechopen.72963

[50] Gosselink R. J. A., Snijder M. H. B., Kranenbarg A., Keijsers E. R. P., de Jong E., Stigsson L. L.: Characterisation and application of NovaFiber lignin. Industrial Crops and Products, **20**, 191–203 (2004).
https://doi.org/10.1016/j.indcrop.2004.04.021

[51] Ikeda Y., Phakkeeree T., Junkong P., Yokohama H., Phinyocheep P., Kitano R., Kato A.: Reinforcing biofiller 'Lignin' for high performance green natural rubber nanocomposites. RSC Advances, **7**, 5222–5231 (2017).
https://doi.org/10.1039/c6ra26359c

[52] Duval A., Lange H., Lawoko M., Crestini C.: Reversible crosslinking of lignin *via* the furan-maleimide Diels-Alder reaction. Green Chemistry, **17**, 4991–5000 (2015).
https://doi.org/10.1039/c5gc01319d

[53] Hernández M., Grande A. M., Dierkes W., Bijleveld J., van der Zwaag S., García S. J.: Turning vulcanized natural rubber into a self-healing polymer: Effect of the disulfide/polysulfide ratio. ACS Sustainable Chemistry and Engineering, **4**, 5776–5784 (2016).
https://doi.org/10.1021/acssuschemeng.6b01760

[54] Khimi S., Syamsinar S. N., Najwa T. N. L.: Effect of carbon black on self-healing efficiency of natural rubber. Materials Today: Proceedings, **17**, 1064–1071 (2019).
https://doi.org/10.1016/j.matpr.2019.06.513

[55] Flory P. J., Rehner J.: Statistical mechanics of cross-linked polymer networks II. Swelling. The Journal of Chemical Physics, **11**, 521–526 (1943)
https://doi.org/10.1063/1.1723792

[56] Cao L., Fan J., Huang J., Chen Y.: A robust and stretchable cross-linked rubber network with recyclable and self-healable capabilities based on dynamic covalent bonds. Journal of Materials Chemistry A, **7**, 4922–4933 (2019).
https://doi.org/10.1039/c8ta11587g

[57] Jiang G., Zhang J., Ding J., Chen Y.: Design of PLA/ENR thermoplastic vulcanizates with balanced stiffness-toughness based on rubber reinforcement and selective distribution of modified silica. Polymers for Advanced Technologies, **32**, 2487–2498 (2021).
https://doi.org/10.1002/pat.5279

[58] Somseemee O., Saeoui P., Schevenels F. T., Siriwong C.: Enhanced interfacial interaction between modified cellulose nanocrystals and epoxidized natural rubber *via* ultraviolet irradiation. Scientific Reports, **12**, 6682 (2022).
https://doi.org/10.1038/s41598-022-10558-5

[59] Menon A. R. R., Pillai C. K. S., Nando G. B.: Vulcanization of natural rubber modified with cashew nut shell liquid and its phosphorylated derivative – A comparative study. Polymer, **39**, 4033–4036 (1998).
https://doi.org/10.1016/S0032-3861(97)00539-9

[60] Karaağaç B.: Use of ground pistachio shell as alternative filler in natural rubber/styrene–butadiene rubber-based rubber compounds. Polymer Composites, **35**, 245–252 (2014).
https://doi.org/10.1002/pc.22656

[61] Monsallier J. M.: Multifunctional acrylates as anti-reversion agents in sulfur cured systems. Kautschuk Gummi Kunststoffe, **62**, 442–447 (2009).

[62] Shibulal G. S., Jang J., Yu H. C., Huh Y. I., Nah C.: Cure characteristics and physico-mechanical properties of a conventional sulphur-cured natural rubber with a novel anti-reversion agent. Journal of Polymer Research, **23**, 237 (2016).
https://doi.org/10.1007/s10965-016-1128-9

[63] Gopi Sathi S., Harea E., Machů A., Stoček R.: Facilitating high-temperature curing of natural rubber with a conventional accelerated-sulfur system using a synergistic combination of bismaleimides. Express Polymer Letters, **15**, 16–27 (2021).
https://doi.org/10.3144/expresspolymlett.2021.3

[64] Hashim A. S., Kohjiya S.: Preparation and properties of epoxidized natural rubber network crosslinked by ring opening reaction. Polymer Gels and Networks, **2**, 219–227 (1994).
https://doi.org/10.1016/0966-7822(94)90006-X

[65] Zurina M., Ismail H., Ratnam C. T.: The effect of HVA-2 on properties of irradiated epoxidized natural rubber (ENR-50), ethylene vinyl acetate (EVA), and ENR-50/EVA blend. Polymer Testing, **27**, 480–490 (2008).
https://doi.org/10.1016/j.polymertesting.2008.02.001

[66] Aini N. A. M., Othman N., Hussin M. H., Sahakaro K., Hayeemasae N.: Lignin as alternative reinforcing filler in the rubber industry: A review. Frontiers in Materials, **6**, 329 (2020).
https://doi.org/10.3389/fmats.2019.00329

[67] Yang Z., Peng H., Wang W., Liu T.: Crystallization behavior of poly(ε-caprolactone)/layered double hydroxide nanocomposites. Journal of Applied Polymer Science, **116**, 2658–2667 (2010).
https://doi.org/10.1002/app.31787

[68] Utrera-Barrios S., Araujo-Morera J., de los Reyes L. P., Manzanares V. R., Verdejo R., López-Manchado M. Á., Santana M. H.: An effective and sustainable approach for achieving self-healing in nitrile rubber. European Polymer Journal, **139**, 110032 (2020).
https://doi.org/10.1016/j.eurpolymj.2020.110032

[69] Rahman M. A., Penco M., Peroni I., Ramorino G., Grande A. M., di Landro L.: Self-repairing systems based on ionomers and epoxidized natural rubber blends. ACS Applied Materials and Interfaces, **3**, 4865–4874 (2011).
https://doi.org/10.1021/am201417h

[70] Pire M., Norvez S., Iliopoulos I., le Rossignol B., Leibler L.: Epoxidized natural rubber/dicarboxylic acid self-vulcanized blends. Polymer, **51**, 5903–5909 (2010).
https://doi.org/10.1016/j.polymer.2010.10.023

[71] Araujo-Morera J., Santana M. H., Verdejo R., López-Manchado M. A.: Giving a second opportunity to tire waste: An alternative path for the development of sustainable self-healing styrene-butadiene rubber compounds overcoming the magic triangle of tires. Polymers, **11**, 2122 (2019).
https://doi.org/10.3390/polym11122122

[72] Surendran A., Thomas S.: Self-healing polymer-based systems. Elsevier, Amsterdam (2020).

[73] Moore C. G., Watson W. F.: Determination of degree of crosslinking in natural rubber vulcanizates. Part II. Journal of Polymer Science, **19**, 237–254 (1959).
https://doi.org/10.1002/pol.1956.120199202

[74] Peng Y., Hou Y., Wu Q., Ran Q., Huang G., Wu J.: Thermal and mechanical activation of dynamically stable ionic interaction toward self-healing strengthening elastomers. Materials Horizons, **8**, 2553–2561 (2021).
https://doi.org/10.1039/d1mh00638j

[75] Thajudin N. L. N., Zainol M. H., Shuib R. K.: Intrinsic room temperature self-healing natural rubber based on metal thiolate ionic network. Polymer Testing, **93**, 106975 (2021).
https://doi.org/10.1016/j.polymertesting.2020.106975

[76] Salehabadi A., Bakar M. A., Bakar N. H. H. A.: Effect of organo-modified nanoclay on the thermal and bulk structural properties of poly(3-hydroxybutyrate)-epoxidized natural rubber blends: Formation of multi-components biobased nanohybrids. Materials, **7**, 4508–4523 (2014).
https://doi.org/10.3390/ma7064508

[77] Tan W. L., Salehabadi A., Mohd Isa M. H., Abu Bakar M., Abu Bakar N. H. H.: Synthesis and physicochemical characterization of organomodified halloysite/epoxidized natural rubber nanocomposites: A potential flame-resistant adhesive. Journal of Materials Science, **51**, 1121–1132 (2016).
https://doi.org/10.1007/s10853-015-9443-9

[78] Ratnam C. T., Nasir M., Baharin A., Zaman K.: Electron beam irradiation of epoxidized natural rubber. Nuclear Instruments and Methods in Physics Research, Section B: Beam Interactions with Materials and Atoms, **171**, 455–464 (2000).
https://doi.org/10.1016/S0168-583X(00)00301-3

[79] Hamzah R., Bakar M. A., Khairuddean M., Mohammed I. A., Adnan R.: A structural study of epoxidized natural rubber (ENR-50) and its cyclic dithiocarbonate derivative using NMR spectroscopy techniques. Molecules, **17**, 10974–10993 (2012).
https://doi.org/10.3390/molecules170910974

[80] Nie J., Mou W., Ding J., Chen Y.: Bio-based epoxidized natural rubber/chitin nanocrystals composites: Self-healing and enhanced mechanical properties. Composites Part B, **172**, 152–160 (2019).
https://doi.org/10.1016/j.compositesb.2019.04.035

[81] Damampai K., Pichaiyut S., Mandal S., Wießner S., Das A., Nakason C.: Internal polymerization of epoxy group of epoxidized natural rubber by ferric chloride and formation of strong network structure. Polymers, **13**, 4145 (2021).
https://doi.org/10.3390/polym13234145

[82] Jiang C., He H., Jiang H., Ma L., Jia D. M.: Nano-lignin filled natural rubber composites: Preparation and characterization. Express Polymer Letters, **7**, 480–493 (2013).
https://doi.org/10.3144/expresspolymlett.2013.44

[83] Manoj N. R., De P. P., De S. K., Peiffer D. G.: Self-crosslinkable blend of zinc-sulfonated EPDM and epoxidized natural rubber. Journal of Applied Polymer Science, **53**, 361–370 (1994).
https://doi.org/10.1002/app.1994.070530314

[84] Datta R. N., Ingham F. A. A.: High temperature curing of passenger tires by using 1,3-bis-(citraconimidomethyl) benzene. Kautschuk und Gummi Kunststoffe, **52**, 758–762 (1999).

[85] Coran A. Y.: Vulcanization. in 'Science and technology of rubber' (eds.: Mark J. E., Erman B., Eirich F. R.) Academic Press, Cambridge, 321–366 (2005).
https://doi.org/10.1016/B978-012464786-2/50010-9

[86] Nicolaou K. C., Snyder S. A., Montagnon T., Vassilikogiannakis G.: The Diels-Alder reaction in total synthesis. Angewandte Chemie – International Edition, **41**, 1668–1698 (2002).
https://doi.org/10.1002/1521-3773(20020517)41:10<1668::AID-ANIE1668>3.0.CO;2-Z

[87] Karami Z., Zolghadr M., Zohuriaan-Mehr M. J.: Self-healing Diels–Alder engineered thermosets. in 'Self-healing polymer-based systems' (eds.: Thomas S., Surendran A.) Elsevier, Amsterdam, 209–233 (2020).

[88] Brancart J., Verhelle R., Mangialetto J., van Assche G.: Coupling the microscopic healing behaviour of coatings to the thermoreversible Diels-Alder network formation. Coatings, **9**, 13 (2019).
https://doi.org/10.3390/coatings9010013

express
polymer letters

Research article

Influence of molecular and crosslink network structure on vulcanizate properties of EPDM elastomers

Arshad Rahman Parathodika[1] , *Thiyyanthiruthy Kumbalaparambil Sreethu*[1] , *Purbasha Maji*[1], *Markus Susoff*[2], *Kinsuk Naskar*[1]*

[1]Rubber Technology Centre, Indian Institute of Technology, 721302 Kharagpur, West Bengal, India
[2]University of Applied Sciences, Osnabrück, Germany

Abstract. In elastomer science and technology, the advent of vulcanization led to a paradigm change. Despite ongoing research, vulcanization science and technology have a great deal of untapped potential. This article explores how the various vulcanization systems, such as sulfur-based, peroxide-based, and their hybrid systems, would reflect changes in the physiomechanical characteristics of ethylene-propylene-diene monomer (EPDM) rubber with various molecular configurations. This kind of analysis illuminates the characteristics of the crosslinking network established by each vulcanizing technology. Since solid viscoelastic rubbers include a large number of components, it is nearly impossible to evaluate the crosslinking network directly. If all components other than vulcanizing systems remained intact, stress relaxation behavior correlated directly with the crosslinking network inside the samples. In this work, temperature scanning stress relaxation (TSSR), a relatively new technique capable of creating the whole spectrum of stress relaxation, was effectively explored. The findings suggest that sulfur and carbon crosslinks coexist in hybrid systems regardless of the molecular structure of the elastomer, and their synergistic impact is evident. Furthermore, it is clear from the results that the molecular structure of the vulcanizates has an impact on the final properties, such as tensile, compression strength properties and thermal properties of the samples.

Keywords: polymer composites, rubber, mechanical properties, temperature scanning stress relaxation, hybrid crosslinking network

1. Introduction

Vulcanization, often known as curing, is the process by which a two-dimensional entangled polymer chain is crosslinked to form a three-dimensional network. In essence, vulcanization is a physical process that converts plastic polymer chains into an elastic polymer network. Several vulcanization processes have previously been identified and are extensively utilized in business and academics, the most popular of which are sulfur and peroxide-based procedures [1]. Vulcanization restricts the free flow of polymer chains through the formation of network junctions, which also entraps many entanglements. Overall, this results in an elastically active network in the elastomeric chains, which significantly enhances the material's mechanical performance. The type and nature of crosslinking networks developed and their cure sites have a significant role in the final vulcanizate properties of elastomers [2]. The dissociation energy, thermal stability and flexibility of the linkages are prime deciding factors when it comes to the application point of view.

Changes in curing systems are reflected in vulcanizate properties, which are directly related to the network produced in the elastomer if all other components remain the same. Consequently, a systematic examination of the mechanical properties of elastomeric samples in which only the curing systems

vary may provide a significant deal of information about the network produced and their characteristics; the same method is used in this research. Multiple researchers have shown the use of tensile and dynamic mechanical characteristics in elastomer crosslinking network characterization [3]. Although temperature scanning stress relaxation is a relatively recent technique for understanding the relaxation behavior of polymers, the effective use of this technique to comprehend crosslink network characteristics is one of the innovative aspects of our study. In addition, various traditional rubber tests were used to bolster the conclusions of this study.

Polymers subjected to constant strain display the well-known stress relaxation phenomena. Essentially, stress relaxation is a more or less pronounced reduction in stress as a function of time. Physical and/or chemical processes may be responsible for the microscopic factors that contribute to the macroscopic reduction in stress [4]. In thermoset rubbers, chemical processes occurring in the breakage of polymer chains and network junctions govern the thermal-mechanical behavior [5, 6]. Conventionally Maxwell model is used to represent the stress relaxation of viscoelastic solids, but the true behavior of materials is, unfortunately, more complex and cannot be captured by the basic Maxwell model [7]. According to the well-known theory of linear viscoelasticity, the complete relaxation process may be represented using the generalized Maxwell model, which is comprised of an unlimited number of spring-dashpot parts which provide an isothermal relaxation modulus as a function of time. In accordance with Alfrey's rule, the relaxation time constants are inversely proportional to temperature, *i.e.*, the higher the temperature, the lower the relaxation time constants, and vice versa [8–10]. Because the relaxation spectrum spans such a broad time scale, it is almost difficult to identify the complete function from a single measurement of stress relaxation. To generate a master curve based on the time-temperature superposition concept, typically, a series of observations at many temperatures must be performed. Therefore, a great deal of work is necessary to acquire comprehensive information about stress relaxation behavior. Recently, temperature scanning stress relaxation (TSSR) measurements have been used as an alternate method. In contrast to conventional isothermal experiments, the temperature is not held constant during TSSR measurements; rather, it climbs linearly

with a constant heating rate. Thus, the non-isothermal relaxation modulus ($E_{\text{non-iso}}$) is derived as a function of temperature. In a manner similar to observations of isothermal stress relaxation, the spectrum $H(T)$ may be approximated using Equation (1) [11–13]:

$$H(T) = -\Delta T \cdot \left(\frac{\mathrm{d}E_{\text{non-iso}}}{\mathrm{d}T} \right)_{\beta = \frac{\Delta T}{t} = \text{const}} \tag{1}$$

where the relaxation spectrum $H(T)$ is a function that is related to the system's population of relaxation mechanisms, and β is the heating rate of the temperature scan. Despite the fact that this function is not specified on a time scale, the relaxation processes shown by the polymer sample throughout the test may be easily recognized since the relaxation time constant decreases monotonically with rising temperature T. Due to its very high dependency on temperature, the relaxation time constant quickly decreases to negligible values within a short temperature range. Consequently, during the temperature scan of a TSSR test, the whole spectrum can be seen on a temperature scale within a very little time, which was successfully utilized in this study. In TSSR, in addition to stress relaxation, two further processes, namely heat expansion and rubber elasticity of the sample, are considered [14].

In addition to monomers, molecular level features of elastomers, such as molecular weight, monomer ratio, crystallinity, degree of unsaturation, type of branching, entanglement density, and viscosity, may significantly affect the final elastomer product attributes. How these features are represented in the final properties when various vulcanizing processes are used is very seldom addressed comprehensively. This research evaluated the vulcanizate qualities of two ethylene-propylene-diene monomer (EPDM) rubber types from opposite ends of the property spectrum by curing them with four distinct curing processes. EPDM was chosen as the basis matrix for this investigation because sulfur and peroxide-based curing processes have proven effective in commercial applications; another objective of this research is to analyze the behavior of hybrid curing systems. Consequently, the viability and uses of EPDM with both curing systems make it the ideal material for analyzing the features of a hybrid curing system based on sulfur and peroxide.

As previously mentioned, the most sought-after vulcanizing systems are sulfur and peroxide, but in this study, we are also incorporating the relatively new

idea of a hybrid system. In this instance, a hybrid system combines sulfur and peroxide system components, hoping to have a synergistic impact on the qualities of the vulcanizate. Carbon-sulfur-carbon linkages are created by sulfur vulcanization and are renowned for their excellent flexibility and higher tensile properties. In contrast, carbon-carbon crosslinks are created by peroxide and are renowned for their excellent thermal stability and low compression set properties [15, 16]. Both systems have flaws. Hence a hybrid system is anticipated to eliminate the flaws while combining the positive aspects of both systems. In general, sulfur systems are believed to form crosslinks at allylic positions of double bonds in unsaturated elastomers. In the case of EPDM, only the dimer molecule, Ethylidene norbornene (ENB), has double bonds. Peroxides may generate crosslinks in both the main chain and pendent dimer molecules, as seen in Figure 1. Thus, in a hybrid system, it is envisaged that such linkages would coexist, resulting in a number of alterations to the vulcanizate's characteristics. In addition, during the crosslinking with peroxide, peroxide creates macro radicals (radicals located in the EPDM main chain as a result of hydrogen abstraction). Sulfur is capable of attaching to these radicals and transferring the radical to them, resulting in sulfur crosslinks connecting the main chains of EPDM, which is anticipated to result in significant changes to vulcanizate properties [17].

Many authors discuss the impact of sulfur in the peroxide vulcanization system, with the same conclusion: adding a trace amount of sulfur enhanced the tensile capabilities with a compromise in compression set properties [18–20]. They concluded that the existence of labile sulfur crosslinks explained their findings. Similar research also notes that adding sulfur results in less crosslink density (XLD) due to an interaction between the sulfur and peroxide radicals. Yet it has also been documented that in hybrid curing systems, the high values of crosslink densities show up when stearic acid and zinc oxide are present. Brodsky [19] have found that hybrid systems had higher tensile strength than sulfur vulcanizates and tear strength that is on par with sulfur vulcanizates. The effect of two-stage curing was reported previously [21]. Engelbert [22] showed that the mechanical qualities of EPDM might be enhanced by curing it using a combination of sulfur-peroxide and sulfur-electron beams. In addition, Chakraborty *et al.* [23] comprehensively evaluated several investigations covering a wide range of mixed curing systems. Cumuloxy radical annihilation in a sulfur/peroxide hybrid crosslinking system was reported by Banerjee and coworkers [20, 24–26] Kruželák and coworkers [27, 28] investigated the effect of curing system composition on crosslinking and physical and mechanical properties of acrylonitrile butadiene rubber (NBR) samples. They found that samples
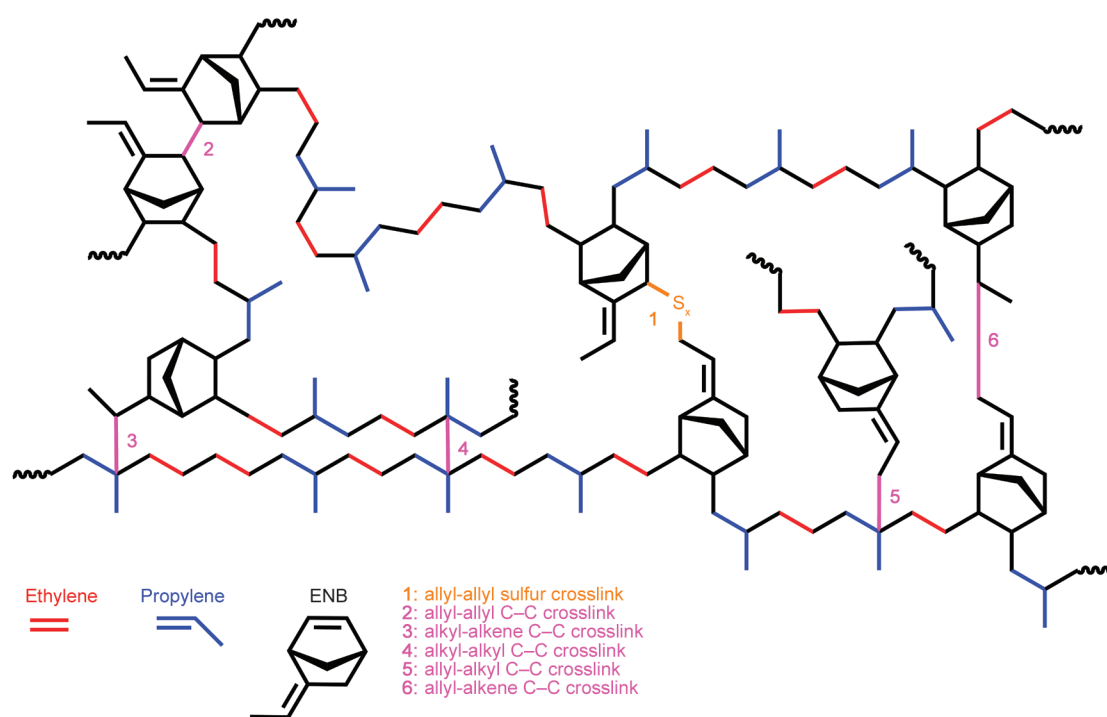

Figure 1. Schematic displaying various sulfur and carbon-carbon linkages observed in EPDM rubbers.

cured with an equivalent ratio of sulfur and peroxide had the highest tensile strength and elongation at break and that thermooxidative aging improved the physical-mechanical properties of vulcanizates based on NBR regardless of curing system composition. Nakason *et al.* [29] used the sulfur-peroxide hybrid cure technique to crosslink epoxidized natural rubber (ENR)/ polypropylene (PP) thermoplastic vulcanizates (TPVs). They reported that hybrid-cured TPVs showed greater mixing torques, shear stress, shear viscosity, tensile strength, and elongation at break than sulfur and peroxide-cured systems. Moreover, hybrid-cured TPVs had higher dispersed ENR particle sizes.

In essence, this research investigates the interrelationship between the molecular network structure of EPDM and the previously described vulcanizing systems (sulfur, peroxide, and hybrid systems) by comparing the physio-mechanical characteristics of vulcanizates. In detail, two grades of EPDM elastomers with entirely different molecular structures and attributes were selected to determine each cure system's disparate reactions to the distinct molecular structures of EPDM. In addition to two optimized hybrid systems, a commercially established sulfur system and a peroxide system were employed as vulcanizing systems in this investigation. Testing specimens of samples were produced based on both the EPDM grades using these four curing methods. A thorough analysis of the physio-mechanical responses of the samples derived the inter-relationship of the vulcanizate network and molecular structure in EPDM rubber.

2. Experimental
2.1. Materials
Two varieties of EPDM elastomers named Keltan 10675C DE and Keltan 4465 are procured from ARLANXEO Performance Elastomers, Changzhou City, China. Of which Keltan 10675C DE is a highly crystalline grade with 65 wt% ethylene content, 6.0 wt% ENB and a high Mooney viscosity of 67 MU(ML(1+8) 150 °C). In addition, this grade has controlled long-chain branching, which contributes to high performance and better processing properties. It also contains 50 phr of high-quality, colorless extender oil, making it an excellent grade for low-hardness rubber products that require excellent UV resistance. However, the Keltan 4465 is mostly amorphous

with an ethylene content of 56 wt%, ENB content of 4.1 wt%, and a Mooney of 48 Mooney unit (MU) (ML(1+4) 125 °C). This grade is of broad molecular weight distribution and 50 phr oil extension, which make it suitable for low hardness profiles. As per observed Mooney values, Keltan 10675C DE is predicted to have 1.5 times the molecular weight of Keltan 4465 and 10675C DE and 4465 grades have specific gravities of 0.86 and 0.87 kg/dm^3, respectively, as determined by the ASTM D 297–15 method. Perkadox 14-40B-PD-S (peroxide), a 40% active organic peroxide (Di[tert-butylperoxyisopropyl] benzene) from Nouryon, Amsterdam, The Netherlands, functions as a major vulcanization agent in this study. Zinc oxide (ZnO) and sulfur are obtained from Merck India Limited, Mumbai, India. All other rubber compounding ingredients say stearic acid, polymerized 2,2,4-trimethyl-1,2dihydroquinoline (TQ), and the vulcanization accelerators such as 2-mercaptobenzothiazole (MBT) and tetramethyl thiuram disulfide (TMTD) are procured from NOCIL India Limited, Mumbai, India. Merck India Limited (Mumbai, India), provided the cyclohexane solvent used in the swelling investigation. PCBL Limited's (Gujarat, India) N-550 grade fine extrusion furnace carbon black is also used in this investigation. Each component is used in its original form; those susceptible to absorbing moisture are dried in an oven before use.

2.2. Methodology
The experimental part of this study started with the preparation of masterbatches based on Keltan 10675C DE and Keltan 4465 according to the formulations shown in Table 1 at 145 °C and 60 rpm. Henceforth, they will be known as the HM series and LM series, respectively. After 24 hours of maturation, vulcanizing chemicals are integrated into the masterbatch using the same Haake™ Rheomix OS, a lab-sized internal mixer, at room temperature. The finished compound is sheeted in a two-roll mill, and its vulcanization time and other rheological characteristics are assessed using an MDR 2000 type moving die rheometer. Throughout the mixing process, ASTM D3182-21a is adhered to, and standard vulcanized sheets and test specimens are produced in a compression molding press from the final compound in line with the standards provided in the respective sections.

Table 1. Composition of samples present in this study in phr.

Ingredients	SHM-1	HHM-1	HHM-2	PHM-1	SLM-1	HLM-1	HLM-2	PLM-1
Keltan 10675 C DE[*]	150	150	150	150	–	–	–	–
Keltan 4465[*]	–	–	–	–	150	150	150	150
ZnO	3	3	3	–	3	3	3	–
Stearic acid	1	1	1	–	1	1	1	–
TQ	1	1	1	1	1	1	1	1
Carbon black (N 550)	70	70	70	70	70	70	70	70
MBT	0.5	0.5	0.5	–	0.5	0.5	0.5	–
TMTD	1	1	1	–	1	1	1	–
Sulfur	1.5	0.5	0.5	–	1.5	0.5	0.5	–
Perkadox 14-40 BPD	–	1.5	3	6	–	1.5	3	6

[*]50 phr oil extended elastomer

2.3. Characterization of samples

2.3.1. Mooney viscosity
The Mooney viscosity of raw rubbers was determined in accordance with ASTM D 1646 using a Mooneyline viscometer manufactured by Prescott Instruments (Tewkesbury, UK) with a big rotor at 125 °C. The results are analyzed to determine the type of basic elastomers.

2.3.2. Rheometeric studies
Disc-shaped specimens with a volume of approximately 5 cm^3 are cut from the final compound using a volumetric sample cutter. They are subjected to an isothermal cure study at 170 °C in Monsanto MDR 2000 (Akron, USA), with an oscillation arc of ±0.5° for 30 minutes. In addition to vulcanization features such as optimum cure time (TC_{90}), cure rate index (CRI), and delta torque, the rate constants of vulcanization are derived from this data.

2.3.3. Temperature scanning stress relaxation
The temperature-dependent stress relaxation behavior of samples was examined using a TSSR Meter (Brabender, Duisburg, Germany). The specimens are dumbbell-shaped (Type 5A, ISO 527) and were punched from a 2 mm thick compression-molded sheet. The specimens are kept in an electrically heated test chamber at 23 °C and a 50% strain is applied in the first stage. In the second phase, the sample is held at 50% strain for two hours to diminish short-term relaxation mechanisms. In the third phase, the non-isothermal test was conducted by gradually increasing the temperature at a rate of 2 °C/min until the stress relaxation was complete or the sample rupture. A schematic view of the test procedure is given in Figure 2.

A thermocouple near the specimen center detected its temperature in real-time. High-quality signal amplifiers and analog-to-digital (AD) converters were utilized to detect and digitize force transducer and thermocouple analog signals. All signals were transmitted to a computer, where software treated and evaluated the data and controlled the test operation. The results include force ratio, which is the quotient $F(T)/F(0)$. $F(T)$ and $F(0)$ indicate the force at temperature T and T_0, respectively. T_{10}, T_{50}, and T_{90} are determined from the normalized force-temperature curve, as shown in Figure 2. Here, the T_{90} could be used to measure the degree of thermo-oxidative chain breakdown of polymers. TSSR index (RI) is derived from the area under the normalized force-temperature curve, indicating the elastic behavior of the material (Equation (2)). The crosslink density of the samples can be obtained from TSSR(CLD-TSSR) based on the theory of rubber elasticity [30]:

$$RI = \frac{\displaystyle\int_{T_0}^{T_{90}} \frac{F(T)}{F_0}\,\mathrm{d}T}{T_{90} - T_0} \tag{2}$$

2.3.4. Mechanical properties
2 mm thick sheets are prepared from the final compound using compression molding. ASTM D 412-C type of dumbbell specimens are punched from the sheet, and tensile strength is measured at 25±2 °C in a Hioks-Hounsfield UTM (Test Equipment Ltd, Surrey, England) at a crosshead speed of 500 mm/min. The presented findings are the average of three specimens per sample. Furthermore, the hardness of all samples is measured from 6 mm thick disc specimens using a Shore A durometer.
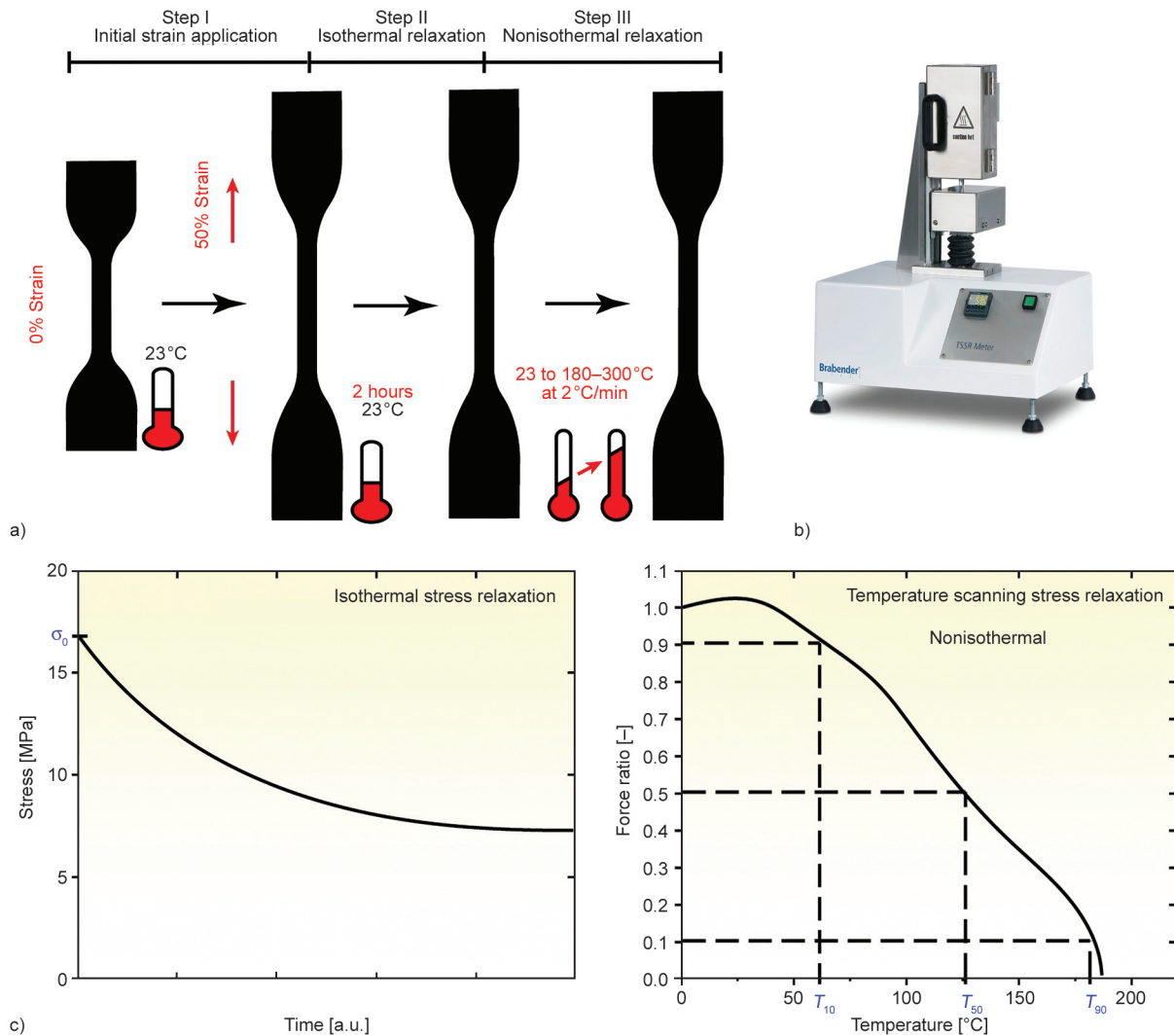
Figure 2. a) Schematic view of the test procedure, b) TSSR instrument, c) and conventional plots from TSSR.

2.3.5. Compression set

Method B under ASTM D 395 is used throughout the test. A cylindrical specimen with a thickness of 6 mm and a diameter of 13 mm is molded directly and used for the measurements. The cylindrical specimens were compression-molded using a vulcanization time of $TC_{90} + 5$ minutes to ensure that heat was evenly distributed throughout the thickness. The specimens are compressed in spacers that can maintain a constant deflection of 25% of the initial thickness for 70 hours at 100 °C. The initial and final thicknesses are measured using a thickness gauge, and the percentage compression set is computed using Equation (3). The stated results for the compression set are the mean of three specimens per sample:

$$Compression\ set\ [\%] = \frac{T_{Initial} - T_{Final}}{T_{Initial} - T_{Spacer}} \cdot 100 \quad (3)$$

where T is the thickness, $T_{Initial}$, T_{Final}, are the thickness of the sample before and after compression set experiments, also T_{Spacer} is the thickness of the spacer used for the experiment.

2.3.6. Heat aging

Vulcanized sheets of 2 mm thickness were heat-aged at 100 °C for 72 hours in a hot air oven.

Change in tensile properties

The tensile properties of the samples are tested before and after heat aging in accordance with ASTM D 412. The percentage change in properties is calculated from Equation (4):

$$\Delta P[\%] = \frac{P_{after\ ageing} - P_{before\ ageing}}{P_{before\ ageing}} \cdot 100 \quad (4)$$

where P refers to the tensile properties such as tensile strength, elongation at break, modulus.

Dynamic mechanical analysis (DMA)
In tensile mode, strain sweep measurements are conducted using 20×5 mm strips punched from a 2 mm thick vulcanized sheet. This test is used to analyze the aging behavior of the samples, strips from aged and unaged samples are tested, and the results are compared. The strain sweep is performed in the dynamic strain range of 0.01 to 20% at a frequency of 10 Hz in Metravib 50N France at 50 °C. Parameters such as storage modulus (E'), loss modulus (E''), and tan delta ($\tan\delta$) are obtained from this study.

2.3.7. Swelling studies
Using swelling tests in cyclohexane for 72 h at 25±2 °C, crosslink density was determined. The analysis uses 2 mm thick disk-shaped vulcanized specimens. Equation (5) was used to calculate the volume fraction of swollen rubber (V_r). Where m_1 and m_2 are the dry polymer and solvent swollen sample weights, while ρ_1 and ρ_2 are their densities. Test specimens were weighed before swelling, after swelling, and after drying and then using the Flory–Rehner equation (Equation (6)), crosslink density (ν) was calculated. V_s refers to cyclohexane's molar volume, which is 107.7 cm³/mol. Flory-Huggins polymer-solvent interaction parameter (χ) of EPDM-Cyclohexane used was 0.38 [31]. It can be noted that when comparing compounds with the same filler content, relative crosslink density values can be compared without Kraus adjustment [32, 33]:

$$V_r = \frac{Volume\ of\ rubber}{Volume\ of\ rubber + Volume\ of\ solvent} = \frac{\frac{m_1}{\rho_1}}{\frac{m_1}{\rho_1} + \frac{m_2}{\rho_2}} \quad (5)$$
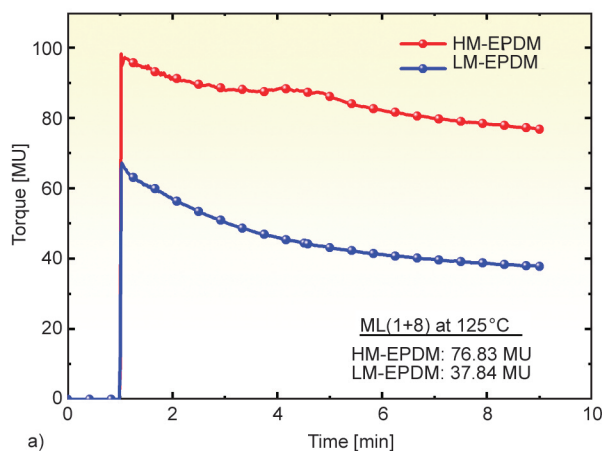
$$\nu = -\frac{1}{2V_s} \cdot \frac{\ln(1 - V_r) + V_r + \chi V_r^2}{V_r^{1/3} - \frac{V_r}{2}} \quad (6)$$

3. Results and discussion
3.1. Mooney viscosity
The sole difference between the two series of samples in this analysis is their base elastomers. Mooney viscosity is therefore utilized as a tool to investigate their fundamental differences in molecular structure [34]. Figure 3 depicts the Mooney viscosity plot of both base elastomers, revealing that the HM series base elastomer has a Mooney value of 76.8 MU, which is twice as large as the LM series base elastomer Mooney viscosity under similar test conditions. The Mooney value clearly shows that the HM series base elastomers have a larger molecular weight and a lower polydispersity index than the LM series base elastomer. Furthermore, it suggests the existence of more long-chain ethylene crystallites in HM series base elastomer. In all the performance properties of the vulcanizates in this study, the effect of this fundamental difference in molecular structure can be observed.

3.2. Rheometric studies
The curing behavior of samples was analyzed at 170 °C on a Monsanto moving die rheometer. Table 2 summarizes the critical cure parameters derived from the rheo curves (Figure 4), such as scorch time (TS_2), maximum torque (M_H), delta torque (ΔS: measured as the difference between maximum and minimum torque), cure time (TC_{90}: time taken to attain 90% maximum torque) and cure rate index [35].
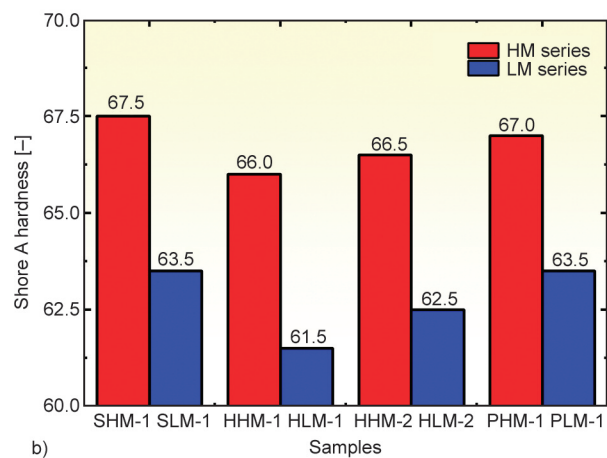

Figure 3. a) Mooney viscosity of two grades of EPDM used, b) Shore A hardness of the samples.

Table 2. Vulcanization parameters obtained from Monsanto moving die rheometer MDR 2000.

Sample	TS_2 [min]	M_H [dN·m]	Delta torque [dN·m]	TC_{90} [min]	CRI [–]
SHM-1	0.89	20.32	17.70	10.27	10.66
HHM-1	1.23	16.01	13.02	8.97	12.91
HHM-2	1.12	16.17	13.19	8.44	13.68
PHM-1	0.76	19.71	16.57	11.09	9.69
SLM-1	1.21	15.58	13.65	11.19	10.02
HLM-1	1.47	12.03	10.09	8.90	13.46
HLM-2	1.39	12.66	10.69	9.31	12.63
PLM-1	1.11	15.26	13.18	13.09	8.35

Figure 4 illustrates the difference between the HM and LM series' rheological behavior. The maximum torque value difference between the HM and LM series remains relatively consistent regardless of the curing technique (4.17±0.47 dN·m). This indicates that none of these curing systems induce significant scission or breakage in the main chain of the elastomers; instead, crosslinking is the predominant response that occurs here. It can also be noted that the elastomeric chain network structure and their branching type are different for both series. Aside from this, when comparing the HM and LM series, the other

curing metrics, such as TC_{90} and CRI, exhibit no noticeable change.

Within a series, the essential cure parameters of both hybrid systems in the HM and LM series are comparable, indicating that only a small proportion of peroxide is directly involved in the crosslinking process. However, the samples are also brought to the subsequent investigations in order to comprehend the function of this additional peroxide in determining the cure site and the impact of sulfur on peroxy radical destruction. Based on the comparable M_H and delta torque values of sulfur-based and peroxide-based samples in both series (SHM-1 *vs*. PHM-1 and SLM-1 *vs*. PLM-1), it can be inferred that both curing methods are capable of producing network structure at 170 °C. However, the hybrid systems exhibit lower M_H and delta values of around 3.5 units in both series. This difference is often linked to decreased network density and the degree of recovery. It is expected because the likelihood of peroxy radical destruction is high, and it restricts the availability of components for the vulcanization process. However, in the case of hybrid systems, this is not the case because, as seen in Table 1, unlike sulfur- or peroxide-based systems,
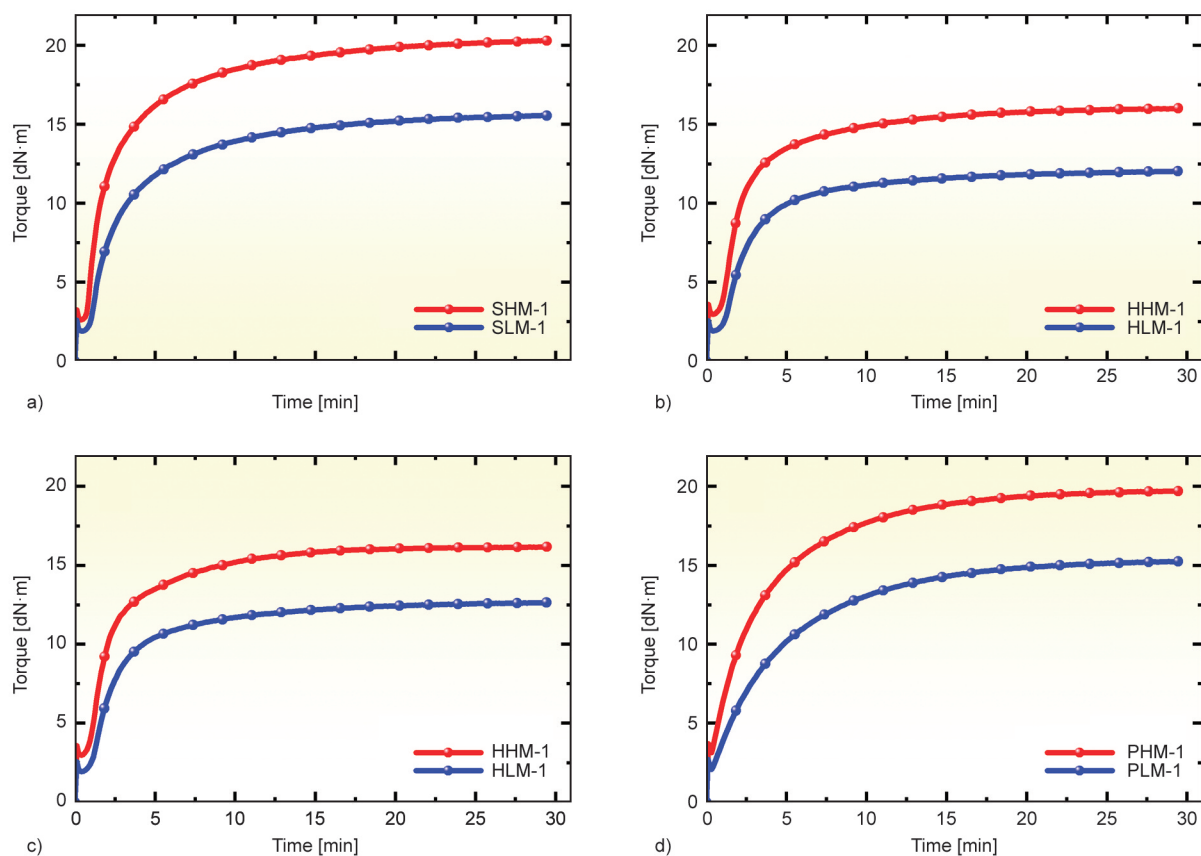
Figure 4. Vulcanization rheo plots of a) sulfur, b) and c) hybrid and d) peroxide-based systems at 170 °C.

hybrid systems use less vulcanization chemicals; these recipes are proved to perform best in our previous investigation [17]. In addition, it contradicts the notion that hybrid systems have better performance characteristics, as will be shown in the following sections.

3.3. Temperature scanning stress relaxation

Figures 5c and 5d, depict the stress-temperature curves from TSSR for the HM series and LM series, respectively. The normalized force temperature curves are shown in a similar fashion in Figures 5a and 5b. Normalized force versus temperature curves of HM series samples features a strong initial rise in force, which may be ascribed to the improved entropy effect of HM series base elastomer (EPDM-Keltan 10675 C DE) owing to regulated long chain branching. In turn, this improves their mechanical performance to levels equivalent to natural rubber. In addition, samples from the LM series also exhibit the first rise in the force-temperature curve, although it is gradual and similar to curves described by other au-

thors [36]. In TSSR plots, one of the most significant differences between the HM and LM series is that some of the LM series sample force values decay by more than 50% at higher temperatures, but the HM series decay is smaller. This is because the LM series base elastomer (EPDM-Keltan 4465) has a low molecular weight and a higher polydispersity index. Detail-wise, the low molecular weight and high polydispersity index of the LM series base elastomer indicate the presence of polymeric chains of varying lengths, of which shorter chains are typically not assumed to form elastically active entanglements; furthermore, they tend to slip over other chains and enhance the stress relaxation process. However, the presence of rigid carbon-carbon crosslinks, in essence, creates the effect of higher molecular weight, and the difference is evident in the case of the PLM-1 sample. In detail, Table 3 summarizes the key parameters from TSSR. In line with the classical theory of rubber elasticity for unfilled compounds, the Neo-Hookean rule (Equation (7)) holds, and the stress (σ)
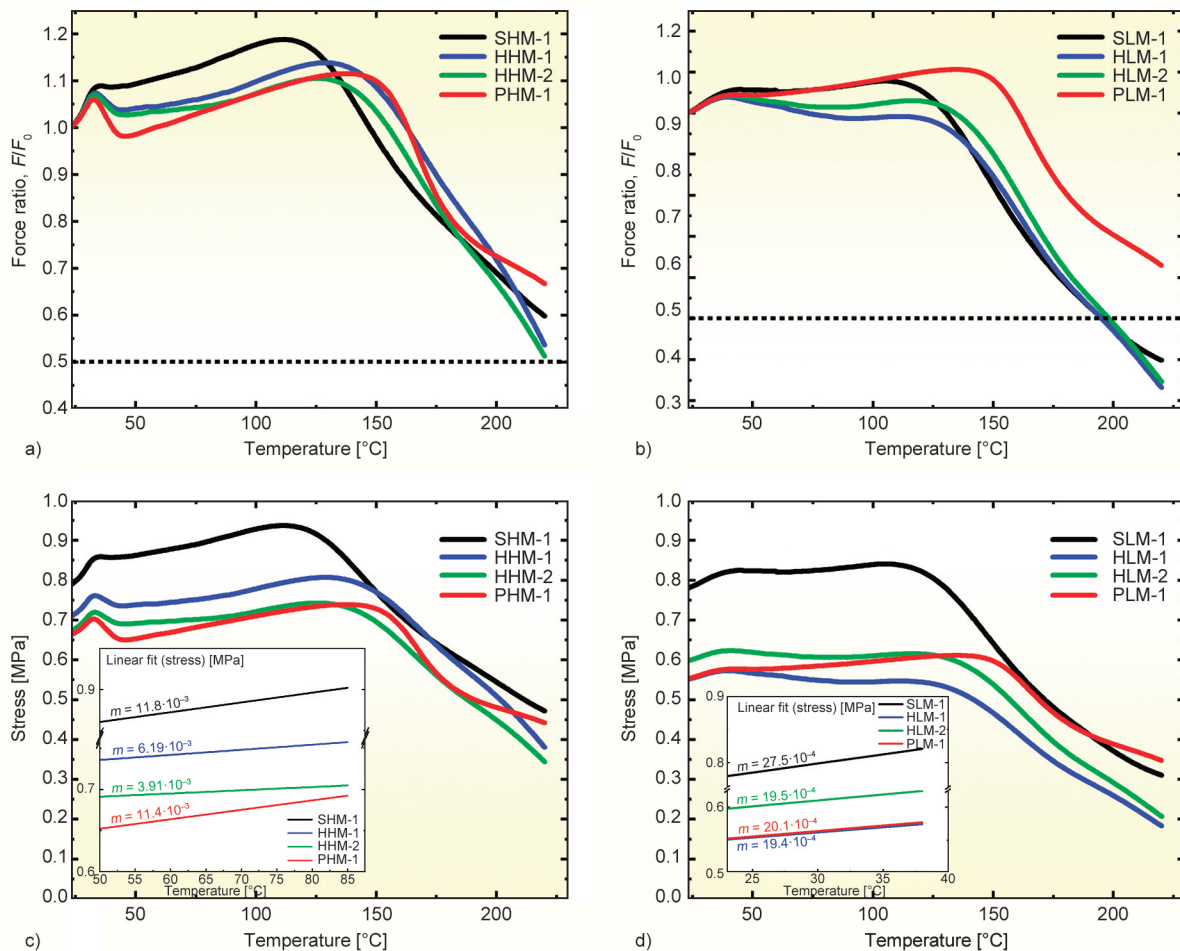

Figure 5. Normalised force ratio curve of a) HM series b) LM series stress *vs* temperature curve of c) HM series d) LM series, on insight the slope of stress vs temperature curve.

is proportional to the crosslink density of the network (ν):

$$\sigma = \nu \cdot R \cdot T \cdot (\lambda - \lambda^{-2}) \qquad (7)$$

where R is the universal gas constant, T is the temperature, and λ (strain ratio) = $l/l0$, where l is the sample length and $l0$ is the sample's initial length. The stress temperature coefficient K for a constant λ is provided by Equation (8):

$$K = \left(\frac{d\sigma}{dT}\right)_\lambda = \nu \cdot R \cdot (\lambda - \lambda^{-2}) \qquad (8)$$

From this crosslink density can be obtained using Equation (9):

$$\nu = \frac{K}{R \cdot (\lambda - \lambda^{-2})} \qquad (9)$$

To extend this model to filled rubber compounds, λ is substituted with Λ and the reinforcing component ϕ is added (Equation (10)):

$$\Lambda = \epsilon \cdot \phi + 1 \qquad (10)$$

where ϵ represents the relative strain and the factor of reinforcement (ϕ) is defined by $\phi = 1 + 2.5V_f + 14.1V_f^2$ (V_f: volume fraction of filler). It is evident from Equation (8) that the slope of the stress *versus* temperature curve is correlated to the crosslink density of samples [37]. Such plots can be produced using TSSR (see Figures 5c and 5d), and the slope at low temperatures is taken into account when estimating crosslink density since sulfur-based and carbon-carbon crosslinks are stable at these temperatures. In this work, the crosslink density of samples is determined using the stress-temperature plot from TSSR. In this way of examination, the crosslink density values of LM series samples are somewhat lower. It is due to the greater number of elastically active entanglements in the HM series due to its longer chain length.

When comparing samples within a series, it is fascinating to see their deconvoluted relaxation spectra (Figure 6). Monosulfidic and polysulfide connections are represented by two different peaks in sulfur-cured materials. In contrast, peroxide samples have a single signal, which corresponds to carbon-carbon bonds. In addition, the hybrid system exhibits three peaks, which indicates the co-existence of sulfidic and carbon-carbon bonds. The peak temperature correlates to the temperature stability of individual crosslink bonds. Therefore it can be shown that polysulfide linkages have a temperature resistance of 147 °C (Figure 6a Peak 1) and monosulfide linkages have a temperature resistance of 200 °C (Figure 6a Peak 2). In contrast, peroxide-induced carbon-carbon bonds have a temperature resistance

Table 3. Critical parameters from TSSR analysis.

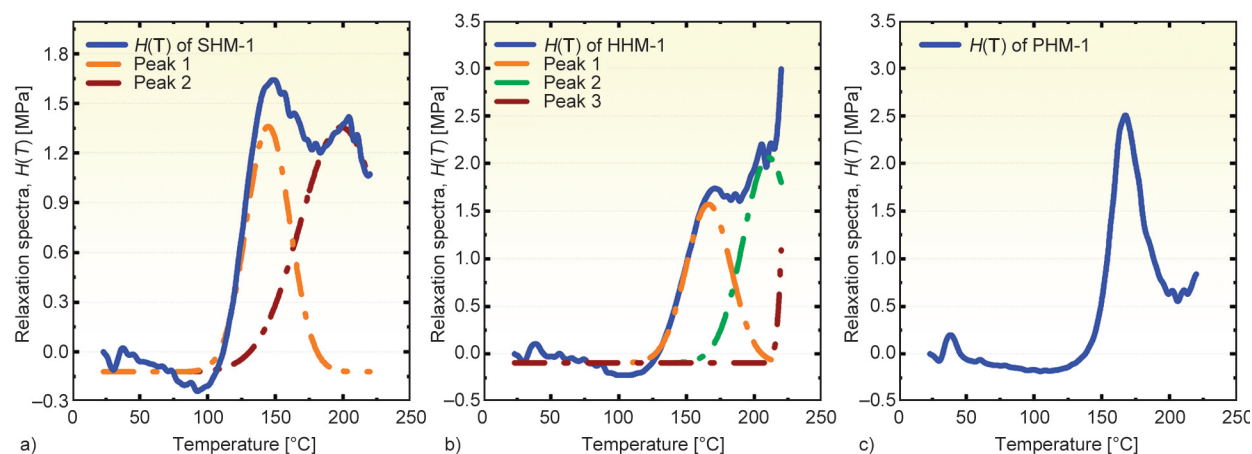| Sample	σ_0 [MPa]	T_{10} [°C]	T_{50} [°C]	TSSR index	Crosslink density* [mol/m³]
SHM-1	0.79	160.6	–	0.99	1180.0
HHM-1	0.71	175.1	–	0.99	619.0
HHM-2	0.67	167.4	–	0.96	391.8
PHM-1	0.66	171.1	–	0.98	1140.6
SLM-1	0.78	142.4	195.5	0.87	275.6
HLM-1	0.55	143.2	195.2	0.84	194.0
HLM-2	0.60	150.5	198.3	0.87	195.1
PLM-1	0.55	169.6	–	0.98	201.4

*These values are obtained from TSSR

Figure 6. Relaxation spectra from TSSR of a) sulfur cured (SHM-1) b) hybrid cured (HHM-1) and c) peroxide cured (PHM-1) samples.

of 170 °C. The deconvoluted relaxation spectrum of a hybrid treatment has three peaks at 164, 205, and 212 °C. The peak at 164 °C corresponds to polysulfide links, while the peaks at 205 and 212 °C relate to monosulfide and carbon-carbon connections; however, it is difficult to discriminate between them. The increased temperature resistance of polysulfide and monosulfide links may be attributable to the likelihood of sulfur linkage formation in the backbone of EPDM elastomer in hybrid systems as opposed to pure systems. Relaxation spectra of the LM series also follow the same trend. In addition, based on the T_{10} values, hybrid cure systems have better temperature stability. The T_{10} values for hybrid cure systems rise by 14.5 and 4 °C compared to sulfur and peroxide systems, respectively, indicating greater network formation and slower relaxation in hybrid systems.

The TSSR index may be used to examine the elasticity of samples; the greater the TSSR index, the greater the elasticity of the rubber network [6, 38]. Greater elasticity within a certain elastomer grade correlates to greater network density and/or strength, as well as a higher number of entrapped entanglements. The phrase 'entrapped entanglement' refers to entanglements that got imprisoned as a result of the creation of crosslinks. Detailing polymers composed of high molecular weight chains made of repeating units. Due to microscopic Brownian motions, polymer chains get entangled with one another. Models of random walking explain this occurrence. However, when strain is given to an uncrosslinked polymer, the chains flaw and tend to align, resulting in a decrease in entanglement. However, when a polymer undergoes crosslinking, the free movement of chains is constrained, many entanglements are protected or imprisoned, and they help the polymer to improve its elasticity, and they are called elastically active entrapped entanglements. The TSSR index values of samples indicate that all HM series samples have similar TSSR index values. With the exception of peroxide-cured samples, the same pattern reappears in the LM series as well. In comparing the TSSR index of both series, all samples in the HM series have a value close to one, indicating their high elasticity, whereas the LM series has a value of 0.86, indicating that the LM series has inferior elastic properties compared to the HM series, with the exception of the peroxide-cured LM sample.

3.4. Swelling studies

The crosslink densities of the samples were also determined using swelling, followed by the Flory Rehner equation (Equation (6)). Figure 7 crosslink density values derived from swelling experiments and TSSR. The fluctuation of vulcanizate characteristics with crosslink density has been the subject of several investigations [39]. In general, characteristics such as tensile, tear, and fatigue life improve with increasing crosslink density until they reach a maximum, at which point they tend to decrease with additional increases in crosslink density. In contrast, some characteristics, such as dynamic modulus and compression set, continue to improve as crosslink density increases. Several papers provide potential reasons for this phenomenon [40, 41]. There are many forms of intermolecular and intramolecular crosslinks as well as network defects, such as dangling chain ends and chain loops. However, only chemical crosslinks that are elastically active and entanglements that are trapped will contribute to the physical qualities.
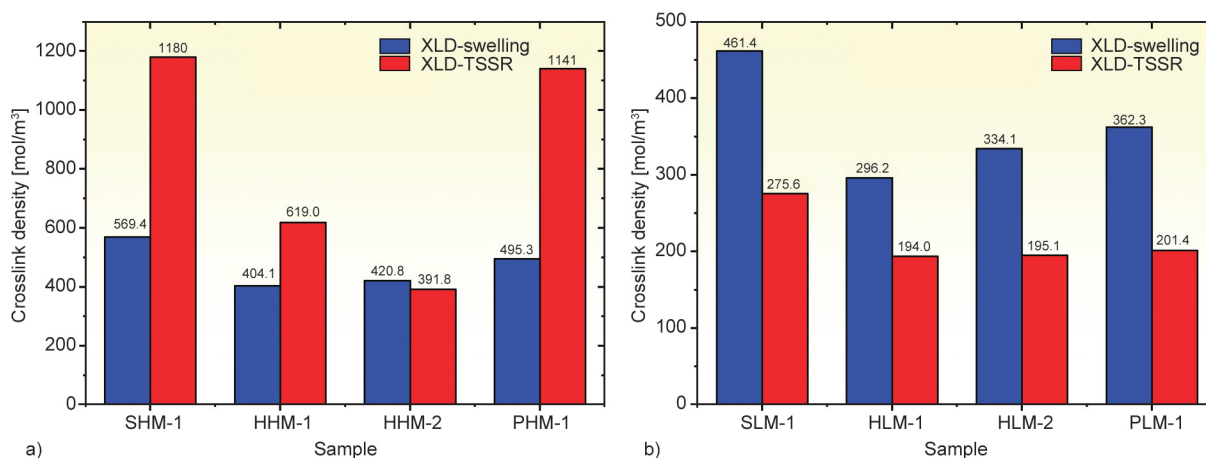

Figure 7. Crosslink densities from swelling study and TSSR meter for a) HM series b) LM series.

Consequently, it is not required that an increase in crosslink density would optimize all vulcanizate qualities in the same manner as delta torque. In both TSSR and swelling studies, the findings of this study indicate that the crosslink density of samples from the HM series is greater than that of samples from the LM series. It is due to the increased molecular weight and entanglement density of the HM series elastomer, in essence, both the measurement methods quantify the crosslink density based on the physical response. The second significant difference between the series is that, whereas in the HM series, TSSR measurement exhibits higher values than swelling, in the LM series, swelling experiments exhibit higher values than the TSSR. Comparing samples within a series reveals that both the HM and LM series exhibit a similar pattern of delta torque values, indicating that the majority of torque development during vulcanization is due to the generation of crosslinks in the rubber matrix. Both sulfur- and peroxide-based systems exhibit greater crosslink density values than hybrid systems in both series. However, the superior performance of hybrid systems could be attributed to their versatile options for cure sites. Comparing sulfur, hybrid, and peroxide systems, the crosslink density value trends from TSSR and swelling are in agreement. However, the crosslink density values of the two hybrid systems exhibit a little deviation from the trend between TSSR and swelling. Moreover, swelling experiments reveal a smaller variation in crosslink density between pure and hybrid systems, whereas TSSR demonstrates an approximately two-fold difference. In general, all of the crosslink density values presented are comparable to the crosslink density values of existing EPDM compounds of commercial interest, which are documented in a number of studies.

3.5. Mechanical properties

The vulcanizate qualities, such as tensile and dynamic capabilities, can provide a fair indication of the crosslinked network and its structure. Aside from that, it is generally accepted that a lower crosslink density, which is above a critical crosslink density, will be more effective at blunting the crack tips than a higher crosslink density. It is because a higher crosslink density restricts segmental motion, thereby reducing the ability of the chains to respond to the crack [42]. Figures 8 represents the tensile properties of the samples. Moreover, the HM series base elastomer (EPDM-Keltan 10675 C DE) is a growing alternative to natural rubber. Using hybrid vulcanization systems, the HHM-1 sample has a tensile strength of 25.9 MPa, which outperforms the standard-filled natural rubber compounds. Tensile strength data shows that all samples in the HM series are stronger than the LM series irrespective of the curing system used, which can be attributed to the high molecular weight of the base elastomer, their controlled long chain branching and their high crystalline nature due to the presence of ordered polyethylene chain segments. However, the LM series samples show higher elongation at break values than the HM series, which correlates to their high amorphous nature and low viscosity. Similar filler content is utilized throughout the samples; consequently, a similar reinforcement index is anticipated. Nearly all of the samples exhibit a similar reinforcement index, except for pure peroxide samples, which can be attributed to the higher concentration of rigid carbon-carbon crosslinking bonds in peroxide samples. Interestingly, both sulfur-cured and hybrid-cured samples have comparable values of 100 and 200% modulus values. On the other hand, both times, the peroxide samples have a higher modulus value for the HM series. However,
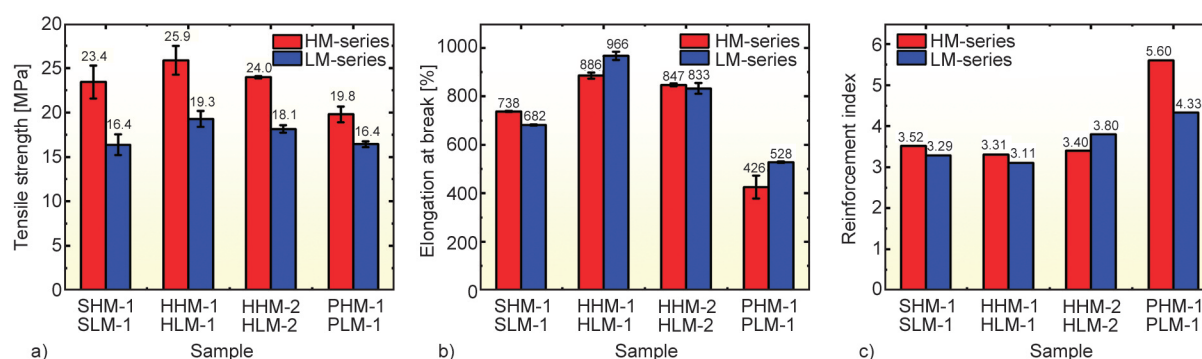

Figure 8. Bar plots of a) tensile strength, b) elongation at break, c) reinforcement index.

the 300% modulus values of both series differ greatly, and in most cases, the HM series shows a higher value. Regardless of the series, when comparing the tensile strength and elongation at break of samples within a series, both hybrid samples outperform pure sulfur and peroxide systems. This is a significant accomplishment of the study, which is anticipated to occur owing to the hybrid system's extra sulfur cure sites. As the hybrid system exhibits much greater tensile and elongation capabilities than the pure system, the modulus values of the hybrid system are somewhat smaller than those of the pure system, which is predicted owing to the hybrid system's high chain segmental motion. In contrast, peroxide samples have a greater reinforcement index and lower elongation at break than hybrid and pure sulfur systems. In essence, hybrid compounds have enhanced tensile qualities relative to their counterparts.

3.6. Compression set

Compression set at a lower temperature is exactly proportional to crosslinking density, regardless of the kind of crosslink, since at lower temperatures, almost crosslinks have the same impact, taking their thermal stability into account [43]. Comparing compression set values across series reveals that samples from the HM series had a lower compression set value for all curing processes, which is advantageous. As in the prior situation, it may be linked to their molecular

structure. Moreover, the trend of compression set values of samples in both series is the same, indicating that this feature is directly connected to the crosslinked network generated rather than elastomers' intrinsic properties. Compression set values of all samples are represented in Figure 9a. While comparing the compression set values of samples, it can be shown that the hybrid system shows a mediocre value between the sulfur and peroxide systems, which further indicates the presence of the co-existence of both sulfur and carbon-carbon linkages. To make a rough estimate based on the compression set values, it can be proven that a hybrid system creates around 65% sulfur crosslinks, and the rest are carbon-carbon linkages. As both series continue to show this pattern, the theory becomes more compelling.

3.7. Heat aging

The thermal stability of the network formed during vulcanization is evaluated during a heat aging test, which can then be used to predict how the material would function and deteriorate in a real application. Samples age when subjected to high temperatures over extended periods of time, and as a result, less thermally stable polysulfide crosslinks rearrange to mono or di-sulfidic connections. Even if there is an improvement in properties, a more significant shift from initial values has no positive effects, which causes alterations in the characteristics of the system
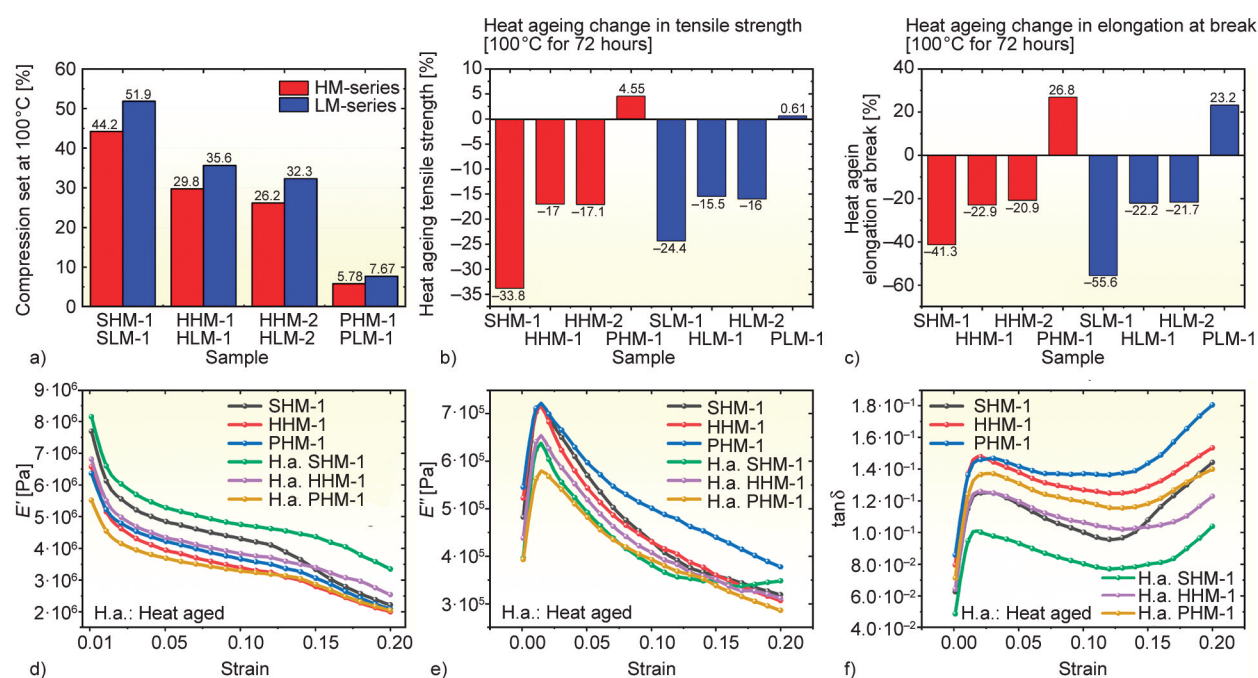

Figure 9. Bar plots of a) compression set, b) change in tensile strength, c) heat aging change in elongation at break, and d) strain sweep storage modulus plot e) strain sweep loss modulus plot f) tan δ from DMA.

in which the article functions. In this research, samples are examined for their tensile qualities and their strain sweep behavior under the dynamic circumstances specified in the characterization section. Then, they were aged at 100 °C for 72 hours, and their tensile characteristics and strain sweep behavior were examined again to determine the impact of aging on the crosslinked network. Figures 9b and 9c represents the variation of properties in tensile characteristics after heat aging, both series follow the same pattern, and the sulfur vulcanizates tensile properties degrade more, and the peroxide sample tensile properties increase little, as anticipated and described in the literature. In addition, when compared to sulfur vulcanizates, hybrid systems exhibit superior performance and 50% less degradation. This again confirms the presence of both carbon linkages and sulfur linkages in hybrid systems. Figure 9d–9f depicts the results of DMA strain sweep measurements. Three samples from the HM series are investigated in this study, and the findings indicate that sample SHM-1 exhibits a reduction in the Payne effect, which is connected with the rearrangement of polysulfide links to monosulfide linkages. However, the hybrid system (HHM-1) shows similarity to the peroxide system (PHM-1), which exhibits an increase in the Payne effect upon aging. As all samples have a comparable filler component, the variance in the Payne effect is mostly attributable to network structure and type.

4. Conclusions

The physio-mechanical characteristics of two grades of EPDM elastomers vulcanized using a sulfur cure system, a peroxide cure system, and two hybrid systems were evaluated. Responses from samples were correlated with the crosslink network in the samples, and the influence of the molecular structure of EPDM in various curing systems was apparent. Temperature-scanning stress relaxation is utilized as the primary instrument to comprehend the network structure of both elastomer grades. In the TSSR relaxation spectrum, it has been shown that sulfur, peroxide, and hybrid cures produce distinct kinds of networks. In essence, a hybrid cure shows the co-existence of both the carbon linkages and sulfur linkages. Similarly, the crosslink density values of samples from swelling studies validate the TSSR findings. In addition, it was intriguing to discover that, regardless

of the base elastomer grade, the trend of crosslink density values and the network type were identical, although the TSSR measurement and swelling studies in both grades exhibited distinct absolute values. The physical behavior of the samples in tensile mode and compression mode also validates the results of TSSR. The hybrid samples, in which multiple kinds of crosslinks coexist, overcome the deficiencies of each system and exhibit better behavior in terms of overall qualities. A heat aging test was conducted to confirm the thermal stability of the formed crosslinking bonds and determine the application potential of the hybrid system. All samples performed as expected in the heat aging test based on their constituent crosslink bonds, with the hybrid positioned between the best-performing peroxide-based samples and the worst-performing sulfur-based samples. Overall, the study demonstrates the utility and application potential of a hybrid system with the help of findings about various types of crosslink networks, the co-existence of dual networks, and their stable behavior regardless of the molecular structure of EPDM. In addition, it illuminates the newly developed high-molecular-weight EPDM grade and its exceptional performance characteristics.

References

[1] Akiba M., Hashim A. S.: Vulcanization and crosslinking in elastomers. Progress in Polymer Science, **22**, 475–521 (1997).
https://doi.org/10.1016/S0079-6700(96)00015-9

[2] Loo C. T.: High temperature vulcanization of elastomers: 2. Network structures in conventional sulphenamide-sulphur natural rubber vulcanizates. Polymer, **15**, 357–365 (1974).
https://doi.org/10.1016/0032-3861(74)90177-3

[3] Aprem A. S., Joseph K., Thomas S.: Recent developments in crosslinking of elastomers. Rubber Chemistry and Technology, **78**, 458–488 (2005).
https://doi.org/10.5254/1.3547892

[4] Meng F., Pritchard R. H., Terentjev E. M.: Stress relaxation, dynamics, and plasticity of transient polymer networks. Macromolecules, **49**, 2843–2852 (2016).
https://doi.org/10.1021/acs.macromol.5b02667

[5] Vennemann N.: Characterization of thermoplastic elastomers by means of temperature scanning stress relaxation measurements. in 'Thermoplastic elastomers' (eds.: El-Sonbati A. Z.), IntechOpen, Rijeka, Vol. 1, 347–370 (2012).
https://doi.org/10.5772/35976

[6] Chatterjee T., Vennemann N., Naskar K.: Temperature scanning stress relaxation measurements: A unique perspective for evaluation of the thermomechanical behavior of shape memory polymer blends. Journal of Applied Polymer Science, **135**, 45680 (2018).
https://doi.org/10.1002/app.45680

[7] Johnson A. R., Quigley C. J.: A viscohyperelastic maxwell model for rubber viscoelasticity. Rubber Chemistry and Technology, **65**, 137–153 (1992).
https://doi.org/10.5254/1.3538596

[8] Treloar L. R. G.: The physics of rubber elasticity. Clarendon Press, Oxford (1975).

[9] Flory P. J.: Statistical mechanics of swelling of network structures. The Journal of Chemical Physics, **18**, 108–111 (1950).
https://doi.org/10.1063/1.1747424

[10] Eichinger B. E.: Rubber elasticity: Solution of the James-Guth model. Physical Review E, **91**, 052601 (2015).
https://doi.org/10.1103/PhysRevE.91.052601

[11] Anagha M. G., Chatterjee T., Naskar K.: Assessing thermomechanical properties of a reactive maleic anhydride grafted styrene-ethylene-butylene-styrene/thermoplastic polyurethane blend with temperature scanning stress relaxation method. Journal of Applied Polymer Science, **137**, 49598 (2020).
https://doi.org/10.1002/app.49598

[12] Banerjee S. S., Natarajan T. S., Subramani B. E., Wießner S., Janke A., Heinrich G., Das A.: Temperature scanning stress relaxation behavior of water responsive and mechanically adaptive elastomer nanocomposites. Journal of Applied Polymer Science, **137**, 48344 (2020).
https://doi.org/10.1002/app.48344

[13] Barbe A., Bökamp K., Kummerlöwe C., Sollmann H., Vennemann N., Vinzelberg S.: Investigation of modified SEBS-based thermoplastic elastomers by temperature scanning stress relaxation measurements. Polymer Engineering and Science, **45**, 1498–1507 (2005).
https://doi.org/10.1002/pen.20427

[14] Vennemann N., Schwarze C., Kummerlöwe C.: Determination of crosslink density and network structure of NR vulcanizates by means of TSSR. Advanced Materials Research, **844**, 482–485 (2014).
https://doi.org/10.4028/www.scientific.net/AMR.844.482

[15] Loan L. D.: Mechanism of peroxide vulcanization of elastomers. Rubber Chemistry and Technology, **40**, 149–176 (1967).
https://doi.org/10.5254/1.3539040

[16] Naskar K., Noordermeer J. W. M.: Dynamically vulcanized PP/EPDM blends: Effects of different types of peroxides on the properties. Rubber Chemistry and Technology, **76**, 1001–1018 (2003).
https://doi.org/10.5254/1.3547766

[17] Parathodika A. R., Raju A. T., Das M., Bhattacharya A. B., Neethirajan J., Naskar K.: Exploring hybrid vulcanization system in high-molecular weight EPDM rubber composites: A statistical approach. Journal of Applied Polymer Science, **139**, e52721 (2022).
https://doi.org/10.1002/app.52721

[18] Das C. K., Banerjee S.: Studies on dicumyl peroxide vulcanization of styrene – butadiene rubber in presence of sulfur and 2-mercaptobenzothiazole. Rubber Chemistry and Technology, **47**, 266–281 (1974).
https://doi.org/10.5254/1.3540436

[19] Brodsky G. I.: Mixed peroxide-sulfur curing system for rubbers. in 'ACS Rubber Meeting, Orlando, USA' 1–28 (1993).

[20] Manik S. P., Banerjee S.: Sulfenamide accelerated sulfur vulcanization of natural rubber in presence and absence of dicumyl peroxide. Rubber Chemistry and Technology, **43**, 1311–1326 (1970).
https://doi.org/10.5254/1.3547331

[21] Roland C. M., Warzel M. L.: Orientation effects in rubber double networks. Rubber chemistry and technology, **63**, 285–297 (1990).
https://doi.org/10.5254/1.3538259

[22] Bevervoorde-Meilof E.W.E., Haeringen-Trifonova D., Vancso G., Does L., Bantjes A., Noordermeer J.: Cross-link clusters: Reality or fiction?. KGK-Kautschuk und Gummi Kunststoffe, **53**, 426–433 (2000).

[23] Chakraborty S. K., Bhowmick A. K., De S. K.: Mixed cross-link systems in elastomers. Journal of Macromolecular Science Part C, **21**, 313–332 (1981).
https://doi.org/10.1080/00222358108080020

[24] Manik S. P., Banerjee S.: Determination of chemical cross-links in rubbers. Die Angewandte Makromolekulare Chemie: Applied Macromolecular Chemistry and Physics, **6**, 171–178 (1969).
https://doi.org/10.1002/apmc.1969.050060117

[25] Manik S. P., Banerjee S.: Studies on dicumylperoxide vulcanization of natural rubber in presence of sulfur and accelerators. Rubber Chemistry and Technology, **42**, 744–758 (1969).
https://doi.org/10.5254/1.3539254

[26] Manik S. P., Banerjee S.: Studies on sulfur vulcanization of natural rubber accelerated with diphenylguanidine both in presence and absence of dicumyl peroxide. Journal of Applied Polymer Science, **15**, 1341–1355 (1971).
https://doi.org/10.1002/app.1971.070150605

[27] Kruželák J., Sýkora R., Hudec I.: Sulfur and peroxide curing of rubber compounds based on NR and NBR. Part I: cross-linking and physical-mechanical properties. Kautschuk Gummi Kunststoffe, **70**, 27–33 (2017).

[28] Kruželák J., Sýkora R., Hudec I.: Sulfur and peroxide curing of rubber compounds based on NR and NBR. Part II: Thermooxidative ageing. Kautschuk Gummi Kunststoffe, **70**, 41–47 (2017).

[29] Nakason C., Wannavilai P., Kaesaman A.: Effect of vulcanization system on properties of thermoplastic vulcanizates based on epoxidized natural rubber/polypropylene blends. Polymer Testing, **25**, 34–41 (2006).
https://doi.org/10.1016/j.polymertesting.2005.09.007

[30] Vennemann N., Bökamp K., Bröker D.: Crosslink density of peroxide cured TPV. Macromolecular Symposia, **245–246**, 641–650 (2006).
https://doi.org/10.1002/masy.200651391

[31] Zhao Q., Li X., Gao J.: Aging of ethylene–propylene–diene monomer (EPDM) in artificial weathering environment. Polymer Degradation and Stability, **92**, 1841–1846 (2007).
https://doi.org/10.1016/j.polymdegradstab.2007.07.001

[32] Dijkhuis K. A. J., Noordermeer J. W. M., Dierkes W. K.: The relationship between crosslink system, network structure and material properties of carbon black reinforced EPDM. European Polymer Journal, **45**, 3302–3312 (2009).
https://doi.org/10.1016/j.eurpolymj.2009.06.029

[33] Kraus G.: Swelling of filler-reinforced vulcanizates. Journal of Applied Polymer Science, **7**, 861–871 (1963).
https://doi.org/10.1002/app.1963.070070306

[34] Nakajima N., Harrell E. R.: Method of obtaining viscosity curves with mooney rheometer. Rubber Chemistry and Technology, **52**, 9–19 (1979).
https://doi.org/10.5254/1.3535212

[35] Babu R. R., Singha N. K., Naskar K.: Dynamically vulcanized blends of polypropylene and ethylene-octene copolymer: Comparison of different peroxides on mechanical, thermal, and morphological characteristics. Journal of Applied Polymer Science, **113**, 1836–1852 (2009).
https://doi.org/10.1002/app.30076

[36] Bhattacharya A. B., Gopalan A. M., Chatterjee T., Vennemann N., Naskar K.: Exploring the thermomechanical properties of peroxide/*co*-agent assisted thermoplastic vulcanizates through temperature scanning stress relaxation measurements. Polymer Engineering and Science, **61**, 2466–2476 (2021).
https://doi.org/10.1002/pen.25772

[37] Blume A., Kiesewetter J.: Determination of the crosslink density of tire tread compounds by different analytical methods. Kautschuk Gummi Kunststoffe, **72**, 33–42 (2019).

[38] Uthaipan N., Junhasavasdikul B., Vennemann N., Nakason C., Thitithammawong A.: Investigation of surface properties and elastomeric behaviors of EPDM/EOC/PP thermoplastic vulcanizates with different octene contents. Journal of Applied Polymer Science, **134**, 44857 (2017).
https://doi.org/10.1002/app.44857

[39] Blow C. M.: Rubber technology and manufacture. Butterworths for the Institution of the Rubber Industry, London (1971).

[40] Beek W., Willink D., Aa P., Nijhof L.: Hybrid cure systems for EPDM and EPM - based on organic peroxide-accelerated sulfur. Gummi Fasern Kunststoffe, **70**, 98–108 (2017).

[41] Maiti M., Patel J., Naskar K., Bhowmick A. K.: Influence of various crosslinking systems on the mechanical properties of gas phase EPDM/PP thermoplastic vulcanizates. Journal of Applied Polymer Science, **102**, 5463–5471 (2006).
https://doi.org/10.1002/app.25106

[42] Hamed G. R.: Effect of crosslink density on the critical flaw size of a simple elastomer. Rubber chemistry and technology, **56**, 244–251 (1983).
https://doi.org/10.5254/1.3538117

[43] Martin G., Barrès C., Cassagnau P., Sonntag P., Garois N.: Viscoelasticity of randomly crosslinked EPDM networks. Polymer, **49**, 1892–1901 (2008).
https://doi.org/10.1016/j.polymer.2008.02.003

express
polymer letters

Research article

The influence of entanglements of macromolecules on the mechanical and thermal properties of polylactide composites with carbon nanotubes

Hoorieh Barangizi [iD]*, Justyna Krajenta* [iD]*, Andrzej Pawlak*[*] [iD]

Centre of Molecular and Macromolecular Studies, Polish Academy of Sciences, Sienkiewicza 112, 90-363 Lodz, Poland

Abstract. The influence of the reduction of macromolecular entanglements on the thermal and mechanical properties of polylactide composites containing 0.1–1.0 wt% of carbon nanotubes was investigated. Partial disentangling of the macromolecules improved the dispersion of the filler during composite fabrication. Greater mobility of less entangled polylactide macromolecules affected the crystallization of nanocomposites, which occurred already during the cooling of the melt and not only as a cold crystallization. Isothermal crystallization studies showed a beneficial combination of matrix disentanglement and increased nanotube nucleation, leading to much faster crystallization. In the entangled composite, crystallization at 120 °C was completed after 14 min, while in the partially disentangled composite only after 9 min. The reduction of entanglements of macromolecules also affected the mechanical properties. The plastic deformation was more easily initiated, and stresses in the strain-hardening phase increased more slowly during the deformation of disentangled homopolymers. In composites, the strain-hardening effect depended not only on the content of nanotubes but also on their dispersion, which was better in the less entangled polylactide matrix.

Keywords: nanocomposites, mechanical properties, thermal properties, disentangling

1. Introduction

Polylactide (PLA) is an aliphatic polyester derived from renewable resources. It has been intensively explored because it is non-toxic to the human body, friendly to the environment, and compostable [1]. Polylactide can occur in the form of two stereoisomers, designated as L and D, but is usually a mixture of them. When the content of the minor enantiomer does not exceed a few percent, the polymer is capable of crystallization. Usually, it does not occur directly during cooling from the melt but during increasing the temperature in the solid state, as the so-called cold crystallization [2, 3]. Polylactide is brittle under typical exploitation conditions, *i.e.*, below a glass transition at 56–58 °C. However, at temperatures above 60 °C, it is possible to obtain large deformations.

One of the possible ways to improve the unsatisfactory properties of biopolymer is to make a composite. The effective fillers are multi-walled carbon nanotubes (MWCNT). The properties of PLA/MWCNT composites were studied by many authors [4, 5]. The research focused mainly on two issues: thermal properties, including crystallization, and mechanical properties.

Many studies have focused on the crystallization of composites [6–13]. Some of them are concerned with non-isothermal crystallization. The tested composites were able to crystallize when cooled, which resulted in cold crystallization observed in PLA but not in PLA/MWCNT [6]. Different were the observations by Park *et al*. [9], where only a decrease in the cold crystallization temperature (T_{cc}) and an increase

---

in the melt crystallization temperature were observed as a result of increasing carbon nanotubes (CNTs) content in the composite. Rizvi *et al*. [10] noted that a decrease in T_{cc} is observed for CNTs concentration below 2 wt% because highly concentrated MWCNTs inhibit the growth of PLA crystals and increase this temperature. Similar to changes in T_{cc}, the melting temperature of the composites changed. The glass transition temperature (T_g) usually was constant, although Wu and Liao [11] noticed an increase in T_g with the addition of CNTs.

According to Wu *et al*. [13], the presence of nanotubes has a nucleating effect on both the melt crystallization and the cold crystallization of PLA. However, the nanotubes also act as a physical barrier, hindering crystal growth [12]. As a result, the presence of nanotubes accelerated the melt crystallization while retarded the overall kinetics of the cold crystallization. The heat of melting of PLA in the composite regularly decreased with the CNTs content [11].

Xu *et al*. [7] noticed for MWCNTs with a modified surface that, if they have a smaller aspect ratio, the nucleation rate of PLA spherulites increases. It was attributed to fewer sidewall carboxyl groups on the surfaces of MWCNTs with smaller aspect ratios, which provides more nucleation sites for PLA crystallization. The increase in PLA crystallinity after modification of MWCNTs compared with the composite of unmodified MWCNTs and the double melting behavior for nanocomposites, while the pure PLA showed a single melting character, were the main observations of Mina *et al*. [8].

Isothermal crystallization studies showed that the insertion of CNT effectively increased the crystallization rate of PLA [9]. Also, for carboxyl-functionalized MWCNTs composite, the effect of nanotubes on the isothermal cold crystallization of PLA was observed [12].

The mechanical properties of PLA/MWCNT composites are essential for practical applications; therefore, they have been studied by several teams. Some of them observed an increase in tensile strength with an increase in the content of nanotubes [14], but other authors did not find such dependence [15]. It was also found that the flexural strength of the composite increased with MWCNTs content [14]. The mechanical properties of composites depended on the shape of the filler. Composites with a higher aspect ratio were characterized by a higher modulus

and higher tensile strength, which was related to the better dispersion of CNTs [16].

Studies of the properties of composites with chemically modified CNTs lead to the general conclusion that the modification of mechanical properties is most effective when the chemical treatment of CNTs improves their dispersion [11, 17–19]. It was found that the tensile strength of PLA/CNT composite was enhanced when a small number of modified MWCNTs was added to PLA [8, 9]. The observations of changes in the modulus of elasticity were contradictory. Ramontja *et al*. [17] noted that Young's modulus of the composite is lower than that of pure PLA, but Chiu *et al*. [20], Park *et al*. [9], and Mina *et al*. [8] reported the opposite tendency.

In all of the above studies, the mechanical properties were determined at 20–25 °C, which meant that PLA was rigid even after CNTs were applied, so only minimal tensile deformation of the composite was possible.

Since the properties of PLA composites depend on the dispersion of CNTs, it was investigated how the dispersion depends on extrusion parameters [21]. In processing, it is recommended to use masterbatches. The MWCNTs dispersion within the diluted composites was predominated by the filler dispersion in the masterbatches. The high rotational speed – in combination with a screw profile containing mainly mixing elements – was found to be very suitable for the dispersion and distribution of MWCNTs. The temperature profile applied showed less influence.

The polymers that make the composites have entangled macromolecules in the amorphous phase [22]. These macromolecular entanglements significantly affect the behavior of not only the deformed polymer but also its composite. It is assumed that in a typically synthesized polymer, macromolecular entanglements are at an equilibrium level characteristic of each polymer [23, 24]. The entanglement density of macromolecules is characterized by giving the average molecular mass between the entanglements. Values in the range of 4000–10 500 g/mol are given in the literature for polylactide [24, 25].

It is possible to reduce the density of entanglements, and appropriate methods have been developed [25]. The reduction of entanglements can be achieved by polymerization occurring together with crystallization. For commercially available polymers, entanglements can be reduced by dissolution. The more the polymer solution is diluted, the less contact there is

between macromolecules and their entanglement. A certain difficulty is to maintain limited entanglements when converting the polymer from solution to solid state. This is often achieved by freezing the solution and sublimating the solvent or precipitating it with a non-solvent. The ability of the polymer to crystallize when the solution is cooled may also be useful in maintaining disentanglement.

Disentangling polymers in solution is well suited for scientific purposes. However, in industrial applications where the environmental aspect must be taken into account, it would be better to achieve the disentanglement of macromolecules in a different way. Recently, attempts have been made to disentangle macromolecular chains using large-amplitude oscillatory shear flow [26]. It should be noted that a fully disentangled polymer is not of interest as a material because the entanglements ensure the continuity of the amorphous phase during deformation. At the same time, the partial reduction of the entanglement density is interesting because, as has been shown for many polymers, it significantly affects their properties [27, 28].

Attempts were made to partially disentangle polylactide macromolecules, similarly to a number of other polymers [24, 29–31]. The rheological experiments showed that polylactide obtained from 0.1 wt% methylene chloride solution has only 20% of the original entanglements. The crystallization studies under isothermal conditions have shown that crystal growth can be 10% faster in partially disentangled PLA. Shifts in temperatures defining crystallization regimes were also observed [31]. The role of chain entanglements in the crystallization of stereocomplex of partially disentangled PLA enantiomers was studied by Sun *et al*. [32]. It was observed that disentangling promoted not only a higher crystallization rate but also higher crystallinity of the complex in both the non-isothermal and isothermal conditions. The less-entangled samples crystallized exclusively as the highly crystalline stereocomplexes, in contrast to the predominant homo crystallization that occurred in the common entangled samples.

The tensile test of mechanical properties showed that plastic deformation is easier in the partially disentangled polymer. This was particularly evident as a decrease in strain hardening rate because, during the final strain phase the deformation is mostly controlled by entanglements in the amorphous phase [33].

Although there are already many reports on the properties of partially disentangled polymers, there are almost no such studies in the case of polymer composites. An exception is a recently published article by Barangizi and Pawlak [34] discussing the crystallization of polypropylene in a composite with 1 wt% dispersed nano Al_2O_3. It was found that isothermal and non-isothermal crystallization occurs faster or at a higher temperature, respectively, if the composite has fewer macromolecular entanglements. This was evident during the measurements of the spherulite growth rate as well as the rate of melt-crystal conversion. However, the crystallization in the nanocomposite was slower than in the homopolymer because the dispersed nanoparticles hindered the movement of macromolecules to the growing crystals.

Luo *et al*. [35] studied the recovery of entanglements in polypropylene with graphene nanoplates and noticed that the presence of graphene increases the rate of crystallization. Drakopoulos *et al*. [36] prepared from a solution a composite of gold nanoparticles dispersed in partially disentangled ultra-high molecular weight polyethylene (UHMWPE). The composite was then calendered and stretched to draw ratios ranging from 2–200. Thus, the processability of UHMWPE was shown. As a result of the deformation, an increase in UHMWPE crystallinity by 15% was found at high drawing ratios. It was also observed that the average size of the gold aggregates increased with the orientation of the composite. Studies of polyethylene with polyhedral oligomeric silsesquioxanes [37, 38] lead to the conclusion that sufficiently small nanoparticles (*e.g.*, 1.5 nm, smaller than the tube size of polyethylene (PE), equal to 3.6 nm) can result in higher free volume in the melt, less chain entanglement, and thus a lower complex viscosity of polymer matrix. The distribution of TiO_2 nanoparticles in waterborne acrylic copolymer coatings caused a chain disentanglement and an order of magnitude decrease of T_g [39].

As can be seen from the above review of the literature, there are no reports that would allow a complete assessment of how the reduced density of macromolecular entanglement affects the formation and properties of composites. Particularly interesting are composites with fillers having a high aspect ratio, well dispersing in the polymer matrix, and characterized by sufficient adhesion to the matrix polymer. To carry

out the relevant research on composite with partially disentangled macromolecules, we chose PLA/MWCNT composite, focusing on its most important properties, *i.e.* thermal and mechanical.

2. Experimental
2.1. Materials
Poly(L-lactide) NW 4032D by Nature Works was used in the research. It contained only 1.15% of D-lactide, so it was able to crystallize. Molecular weight measurements by gel permeation chromatography with multi-angle laser light scattering detection (GPC–MALLS) gave the following values: number average molecular weight, M_n = 72 000 g/mol, mass average molecular weight, M_w = 88 000 g/mol. Thin multi-walled carbon nanotubes were produced by Nanocyl S.A. (Belgium) using a catalytic chemical vapor deposition (CCVD) process. According to the manufacturer's data, NC 7000 nanotubes have an average diameter of 9.5 nm, length of 1.5 µm, and surface area of 250–300 m²/g.

2.2. Methods
The partial disentangling of PLA was done in solution using a procedure similar to that proposed by Liu *et al*. [30]. PLA – after drying for 4 hours at 70 °C – was dissolved in methylene chloride at a concentration of 0.5% by weight. Mixing of the polymer and solvent was carried out in a glass flask with a mechanical stirrer for 40 min at 25 °C. The homogeneous solution was slowly poured into a large volume of liquid nitrogen. In the next step, ethanol was added to the frozen solution in a volume five times the volume of the solution. This resulted in the precipitation of polylactide as a white powder. Finally, residual methylene chloride and ethanol were removed by drying for about 8 hours under a vacuum at room temperature. Previously performed rheological studies showed that by using this procedure, the molecular mass between entanglements increased from 10 500 g/mol for the original PLA to 32 800 g/mol for the solution-treated PLA. This means three times fewer entanglements in the polymer.

Both fully entangled and partially disentangled PLA was used to prepare composites with MWCNTs. The composites were produced using EHP-5CS mini extruder (Zamak-Mercator, Krakow, Poland). The plasticizing system of this extruder was composed of two screws with a variable profile and a return channel with a valve, enabling multiple passages of the material through the extruder. The components were mixed for 10 min at a temperature of 180 °C with screw rotation of 60 rpm. The composites of entangled or partially disentangled PLA, including 0.1 or 1.0 wt% of MWCNTs, were prepared. It is assumed that to obtain the desired properties of nanocomposites, the content of 1 wt% of the filler should be sufficient. On the other hand, it was difficult to predict whether effects related to the disentanglement of the composite matrix would be visible at a very low content of CNTs. Therefore, the contents of 0.1 and 1.0 wt% CNTs were selected for the study. We did not modify the surface of the filler. Although it could improve the dispersion of nanotubes, it would make it difficult to interpret the impact of reducing macromolecular entanglements on the morphology of the nanocomposite and its properties. Therefore, the modification of the filler-polymer interactions was abandoned, but we paid attention to whether a satisfactory dispersion of the filler was achieved in the mixing process.

The morphologies of the composites were observed with a polarized light microscope Nikon Eclipse 80i (Nikon Corp., Japan). The aim of the research was to analyze the filler dispersion. The samples for observation were prepared on a Linkam TAHMS 600 (Linkam Sci., Salfords, United Kingdom) hot stage. A small piece of the composite was placed between two thin microscopic glasses. Then, such a sandwich was put on the plate of the hot stage, melted for 1 min at 220 °C, and gently compressed into a layer with a thickness of 12–14 µm. The molten film was quickly cooled to room temperature, thereby limiting crystallization and making it transparent for observation. The samples prepared in this way were observed in the microscope in the light transmission mode. Fragments of samples with typical dispersion of filler were photographed. Each of the five photographs taken for each material covered an area of 0.6×0.9 mm. From these photographs, histograms that show the frequency of occurrence of agglomerates of a certain size in each composite were determined. Observations of the morphology of the composites at higher magnification were carried out using a scanning electron microscope (SEM) Jeol JSM 6010LA (JEOL Ltd., Japan). The samples for observation were first broken in liquid nitrogen, and then the exposed surfaces were sputtered with gold. DSC Q 20 (TA Instruments, New Castle, USA) apparatus was used to conduct thermal tests on samples

having a weight 7–8 mg. For the non-isothermal test, the sample was heated to 220 °C at a rate of 10 °C/min, cooled to 25 °C at the same rate, and then heated to 220 °C. In isothermal tests, the sample was heated to 220 °C, kept there for 3 min, and then cooled down at the rate of 10 °C/min to the final temperature of 120 or 125 °C. While maintaining this temperature, changes in heat flow were observed. The experiment was stopped when heat changes became invisible.

The thermogravimetric analyzer TGA 5500 (TA Instruments, New Castle, USA) was used to assess the thermal stability of the tested materials. Examined samples were heated at a rate of 10 °C/min under nitrogen flow from 20 to 600 °C, and weight changes were measured.

The samples for the mechanical test were prepared by hot pressing pieces of composites or polylactides at 180 °C for 6–8 min. Plates with a thickness of 1 mm were obtained, from which samples were cut. The specimens had a gauge length of 25 mm, a width of 10 mm, and a thickness of 1 mm. Five samples of each material were prepared for testing. The samples were tested in a tensile mode using the Instron 5582 (Instron, Norwood, USA) universal machine. The experiments were carried out in an environmental chamber, which enabled the tests to be conducted at temperatures of 20–70 °C. The stretching rate was 10%/min. Changes in the shape of the samples during deformation were recorded by photographs. Markers were drawn on the surface of the samples, which helped to determine local changes in dimensions. By measuring the sizes for a selected small volume between the markers, the volume strain ΔV as a function of the strain was calculated. The volume strain is defined as (Equation (1)):

$$\Delta V = \frac{V - V_0}{V_0} \qquad (1)$$

where V_0 is the initial volume of the analyzed fragment of the sample, and V is the actual volume of this fragment. The large value of ΔV is attributed to the occurrence of cavitation phenomena [40]. Micrometer-size cavities (voids) appear in the amorphous phase of the polymer. The intensity of the phenomenon decreases with temperature when the possibility of stress relaxation in the amorphous phase of the polymer increases. The tensile experiment was limited to the engineering strain of 400–500% due to the size of the environmental chamber.

Most of the samples tested at 70 °C did not break at these strains.

X-ray scattering, resulting from structural changes in deformed samples, was investigated in the small angle X-ray scattering (SAXS) experiment. The GeniX Xenocs (Xenocs, Grenoble, France) X-ray source operating at 50 kV and 1 mA was combined with a Kiessig-type SAXS camera of 1.2 m in length. The scattered radiation was recorded using a Pilatus 100 K detector. The investigated samples had similar thicknesses.

The formation of the crystalline phase due to the deformation of the stretched material was investigated by recording 2-dimensional wide-angle X-ray scattering (WAXS) patterns. The radiation source was a CuK$_\alpha$ lamp (sealed tube operating at 30 kV and 50 mA, by Philips). The deformed sample from the mechanical test was placed in the path of the X-ray beam at a distance of 39 mm from the Pilatus 100K detector, which recorded the scattering image.

The dynamic mechanical analyzer DMA Q800 (TA Instruments, New Castle, USA) was used to determine how the storage and loss moduli of the PLA sample change with temperature. The test specimens in the shape of strips had the following dimensions: length 10 mm, width 6 mm, and thickness 0.25 mm. The experiments were performed in the film tension mode. Measurements were carried out in the temperature range of 10–160 °C, at a frequency of 1 Hz and a scanning rate of 3 °C/min. The choice of the maximum temperature resulted from the expected melting of the samples above it.

Abbreviations of material names used in the text are presented in Table 1.

3. Results and discussion
3.1. Morphologies of composites

Before carrying out the thermal and mechanical tests, the dispersion of nanotubes in the polymer matrix was evaluated. It is almost impossible to avoid the presence of individual large agglomerates of filler in

Table 1. Abbreviations of material names used in the text.

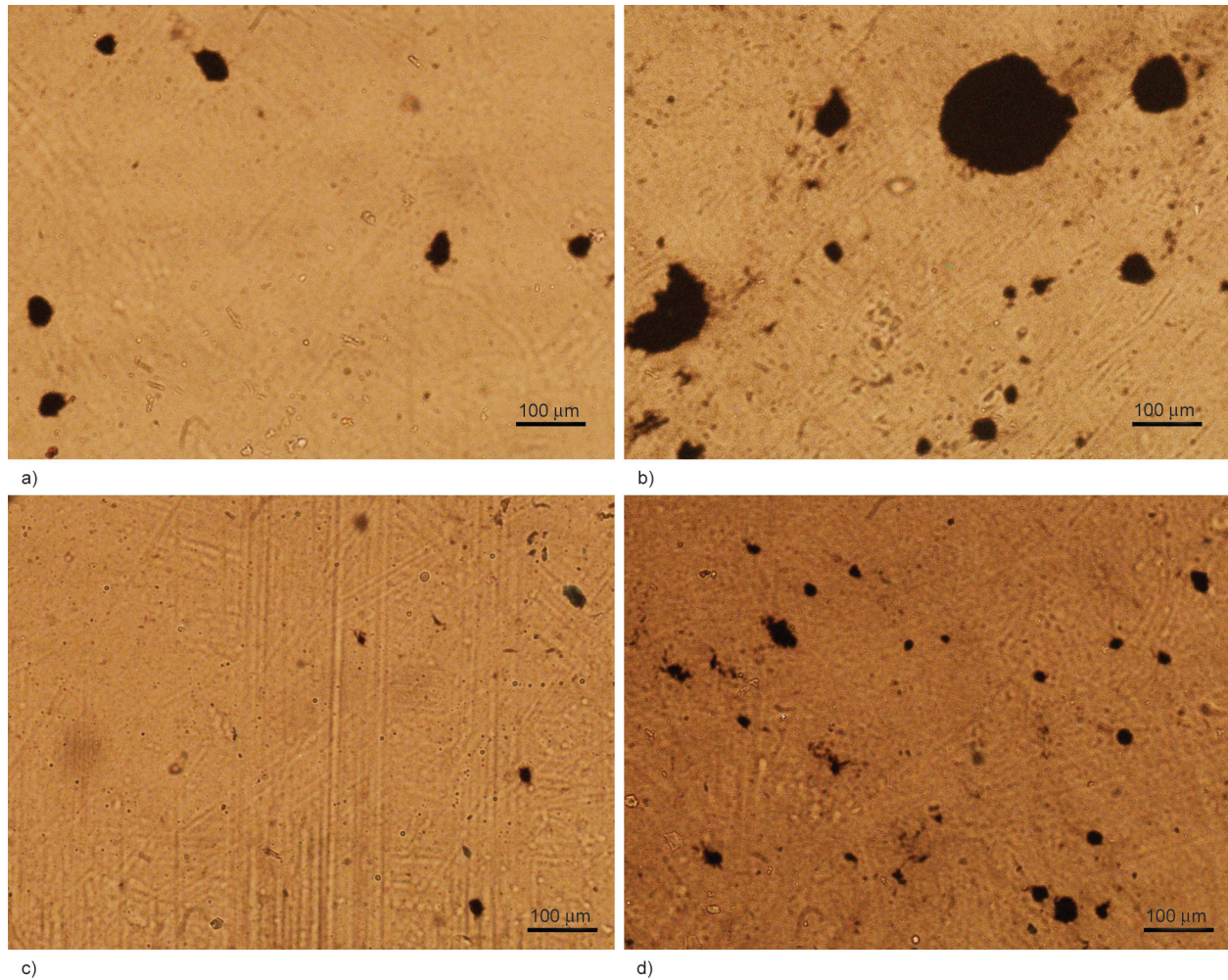| Material	PLA matrix	MWCNT contents [wt%]
PLAi	Initial PLA, fully entangled macromolecules	0
PLAi 0.1		0.1
PLAi 1.0		1.0
PLAd	Solution treated, partially disentangled macromolecules	0
PLAd 0.1		0.1
PLAd 1.0		1.0

Figure 1. Morphologies of thin films of composites: a) PLAi 0.1, b) PLAi 1.0, c) PLAd 0.1, d) PLAd 1.0.

composite, which become visible when analyzing a representative volume of the examined sample. Such information is provided by light microscopy in the transmission mode through a thin layer of the composite. Figure 1 shows typical photographs of the tested composites. Dark inclusions are agglomerates of carbon nanotubes. As expected, agglomerates of micrometer sizes were present in limited numbers, depending on the concentration of filler and type of matrix.

The largest agglomerates were visible in the photographs of the PLAi 1.0 composite, the smallest in the case of the PLAd 0.1 composite. Intermediate, similar sizes of inclusions were visible for PLAi 0.1 and PLAd 1.0 composites. The agglomerates visible in the pictures have been measured, and histograms have been prepared to show the frequency of occurrence of agglomerates of certain sizes. These histograms are shown in Figure 2. They cover the size range from 3 to 150 µm. The histograms confirm the observations that the reduction of macromolecular

entanglements has a positive effect on the distribution of carbon nanotubes inside the polymer. For example, in the PLAd 0.1 composite, almost 70% of the agglomerates had a size below 10 µm, while in the entangled PLAi 0.1 composite, the largest number of inclusions were 10–20 µm in size, and the size distribution was also much wider. An increase in filler content from 0.1 to 1.0 wt% increases the tendency to agglomerate. The number of large agglomerates with sizes above 50 µm is increasing. However, when comparing the PLAi 1.0 and PLAd 1.0 composites, it is clear that also, with higher nanotube contents, the reduction of macromolecular entanglements has a positive effect on their dispersion. Only single agglomerates larger than 50 µm were visible in the images for PLAd 1.0. It should be remembered that light microscopy images do not show inclusions below 3 micrometers, while SEM images (discussed later) showing such inclusions cover very small areas of samples and are of little use for calculating the proportion of inclusions of various sizes.
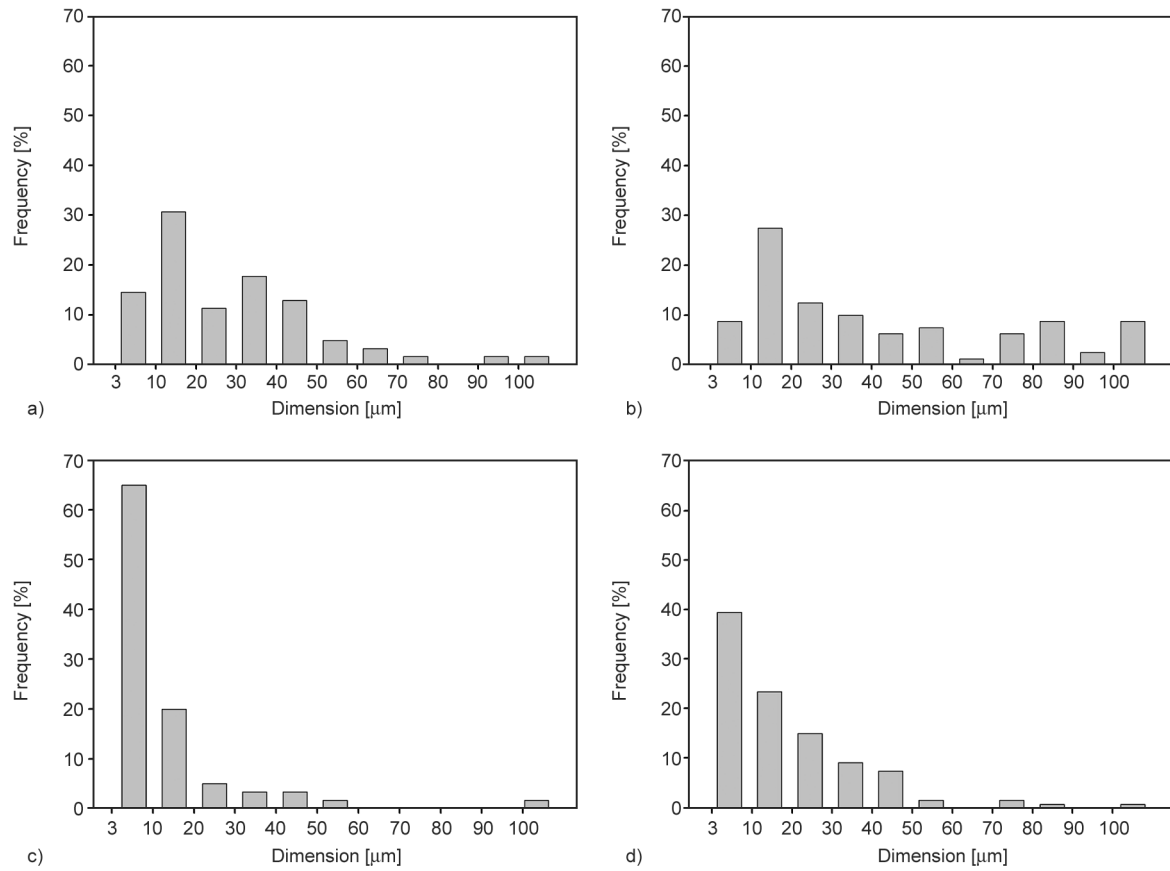
Figure 2. Histograms showing the frequency of occurrence of CNT agglomerates of various diameters: a) PLAi 0.1, b) PLAi 1.0, c) PLAd 0.1, d) PLAd 1.0.

It can be assumed that most of the MWCNTs used are finely dispersed and invisible in microscopic images. Although it is difficult to measure the contribution of the smallest particles to the total filler content, it can be roughly estimated from microscopic photographs. The ratio of the volume occupied by visible MWCNTs agglomerates, V_{CNT}, to the volume of the PLA, V_{PLA}, determined from photographs was: 0.78% for PLAi 0.1, 5.90% for PLAi 1.0, 0.38% for PLAd 0.1 and 1.84% for PLAd 1.0, respectively (see Table 2).

The ratio of the mass of visible MWCNTs, m_{CNT}, to the mass of PLA, m_{PLA}, may be calculated from the Equation (2):

$$\frac{m_{CNT}}{m_{PLA}} = \frac{V_{CNT}}{V_{PLA}} \cdot \frac{\rho_{CNT}}{\rho_{PLA}} \tag{2}$$

where ρ_{CNT} is the density of MWCNTs filler, and ρ_{PLA} is the density of PLA. According to the manufacturers, the bulk density of MWCNTs is equal to 0.075 g/cm³, and the density of PLA is equal to 1.24 g/cm³. During melt processing, mobile macromolecules penetrate the free space between the nanoparticles, applying moderate pressure on the nanotube assemblies. If we assume that there was no significant compression of nanotubes, the density of MWCNTs inside the polymer should be close to the bulk density of MWCNTs. According to this

Table 2. Volume (V_{CNT}/V_{PLA}) and mass (m_{CNT}/m_{PLA}) ratios of MWCNTs and PLA determined by optical microscopy (OM) and calculated fractions of MWCNTs invisible in the microscope.

Composite	V_{CNT}/V_{PLA} [%]	m_{CNT}/m_{PLA} [%]	Mass content of CNTs inserted into composite [%]	Mass content of nanoparticles not visible by OM [%]
PLAi 0.1	0.78	0.05	0.1	50
PLAi 1.0	5.90	0.35	1.0	65
PLAd 0.1	0.38	0.02	0.1	80
PLAd 1.0	1.84	0.11	1.0	89

assumption, it can be calculated from Equation (2) that the m_{CNT}/m_{PLA} ratios in examined composites were 0.05% for PLAi 0.1, 0.35% for PLAi 1.0, 0.02% for PLAd 0.1 and 0.11% for PLAd 1.0. Comparison of these values with the fact that the total content of MWCNTs in the composites was 0.1 or 1.0% means that most of the MWCNTs were dispersed to such an extent that they were not visible in the light microscope. The last column in Table 2 shows what percentage of the nanofiller was below 3 µm. For all composites, at least 50% of the nanotubes were dispersed at the nano level, *i.e.*, good dispersion was obtained. Comparing the composites with the same filler content but with less or more entangled macromolecules, it can be seen that better dispersion of the filler occurs in the partially disentangled PLA composite. The morphologies of the composites at higher magnifications, available in scanning electron microscopy, were also observed. The photographs in Figure 3. show that more agglomerates were present in composites with entangled macromolecules, especially

when the filler content increased from 0.1 to 1 wt%. For example, single agglomerates with a diameter of 3–5 µm are visible in Figure 3b, while in the PLAd matrix (Figure 3d), the size of the agglomerates does not exceed 2 µm. When only 0.1 wt% of MWCNTs was introduced into the matrix, smaller agglomerates can be seen in the photographs (Figure 3a), and in the PLAd 0.1 composite, they are even poorly visible (Figure 3c). As can be seen from the calculations in Table 2 and from the SEM observations, although there are agglomerates in the composites, most of the CNTs are dispersed at the nanometer level.

3.2. Non-isothermal crystallization

Non-isothermal crystallization was investigated by DSC. The typical heating-cooling-heating protocol was used. In the case of limiting the entanglement of macromolecules, a possible change in the value of the glass transition temperature (T_g) could be expected. In the published studies of PLA-MWCNTs composites, there were conflicting reports about the
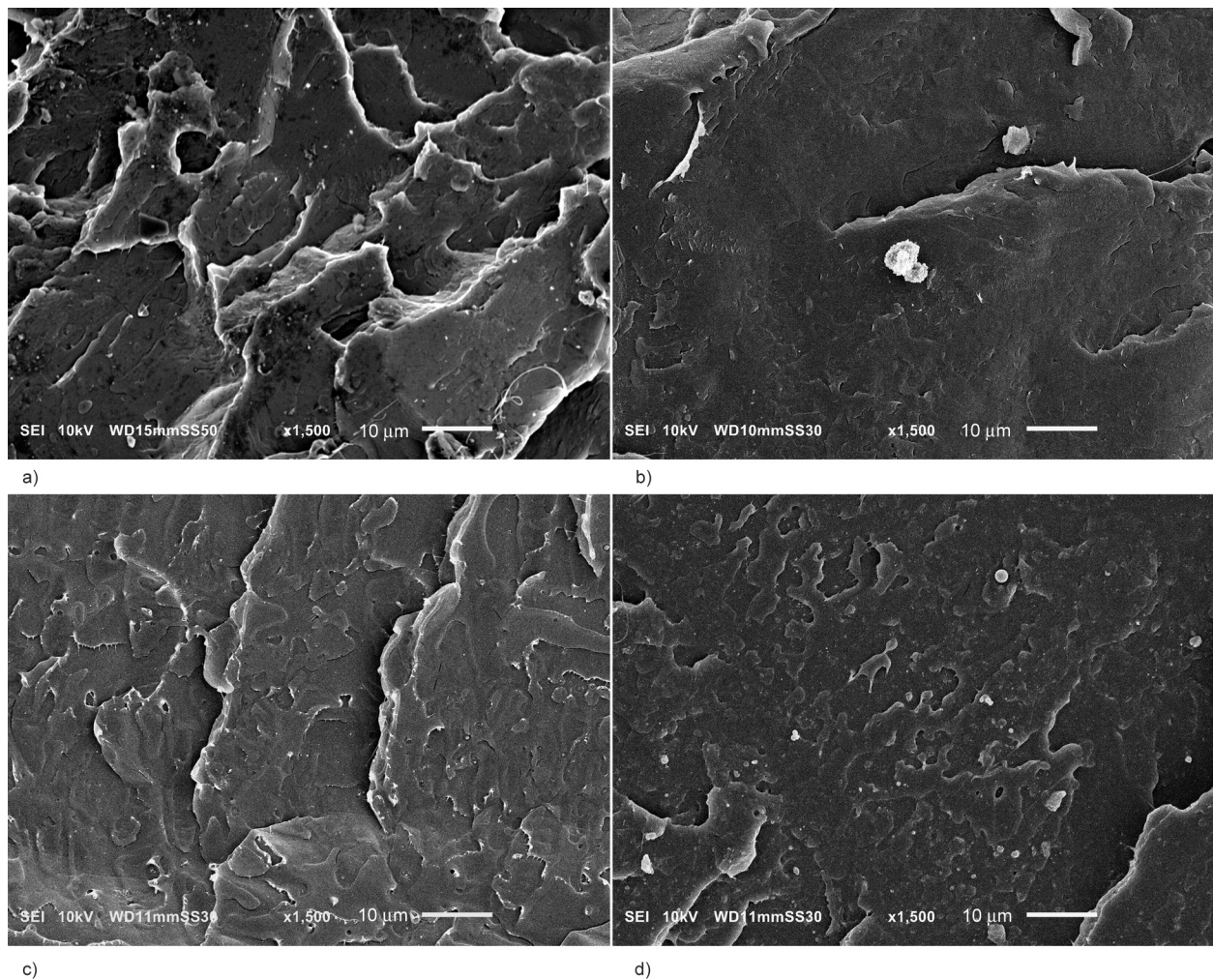

Figure 3. Morphology of the internal surface of composite: a) PLAi 0.1, b) PLAi 1.0, c) PLAd 0.1, d) PLAd 1.0.

Table 3. Glass transition temperatures measured in DSC non-isothermal experiment.

Sample	I. Heating [°C]	Cooling [°C]	II. Heating [°C]
PLAi	57.4	58.9	60.7
PLAi 0.1	54.6	59.5	62.1
PLAi 1.0	55.3	58.2	62.4
PLAd	57.1	58.8	62.1
PLAd 0.1	55.6	60.8	61.6
PLAd 1.0	56.6	61.0	62.2

change or no change in the glass transition in the presence of filler [10, 11]. Therefore, when analyzing the results of DSC, we first focused on the glass transition temperature. The results of T_g measurements are presented in Table 3. The determined glass transition temperatures depended somewhat on the phase of the temperature cycle in which they were measured. However, changes in T_g related to the disentangling of macromolecules or the presence of nanotubes were not systematic and were within the range of accuracy of temperature determination.

Table 4 presents the thermal transitions that were observed in non-isothermal DSC studies above the glass transition. When calculating the degree of crystallinity, it was taken into account that the heat of melting of 100% crystalline PLA is 93 J/g [41, 42] and that the mass fraction of PLA in the composites is less than 100%. The first heating reflects the state of the material created during its preparation. When the temperature of the sample increased to 98.4–105.1 °C, depending on the material, cold crystallization, *i.e.*, solid-state crystallization, was observed. Changes in the cold crystallization temperature (maximum of peak) were not large and it was difficult to

see regularity related to the composition of the sample or degree of entanglement of macromolecules. The measured heat of cold crystallization was high, and the calculated increase in crystallinity was 32–44%. Considering that for PLA, it is difficult to achieve crystallinity above 40% [43], this means that before the measurements, the tested composites had a low content of the crystalline phase. The crystallinity obtained by cold crystallization (X_{cc}) was lower for PLAd than for PLAi and regularly decreased with the content of nanotubes in the composite. The difference between the polylactides is probably due to the different polymer preparation procedures and the smaller amount of nuclei present in PLAd. On the other hand, the reduction of cold crystallization with the increase in the content of MWCNTs indicates their barrier role for this type of crystallization.

In all tested samples, with the exception of PLAd, a slight exothermic transformation was visible at 155–156 °C with the heat of 0.2–1.5 J/g. This transformation, just prior to the melting of the material, is attributed to the transformation of the α′ crystalline phase in PLA into the more stable α phase [44].

The melting process observed during the first heating reached its maximum at the temperature of 166.9–169.4 °C without a regular dependence on the composition of samples. The total crystallinity (X_m) determined from the heat of melting showed a similar tendency as the crystallinity of cold crystallization. It was higher for PLAi than for PLAd and regularly decreased with the addition of nanotubes. The difference between the X_m and X_{cc} values, characterizing the initial crystallinity and amounting to 1.3–5.7%,

Table 4. The results of non-isothermal crystallization experiment.

Sample	I. Heating				Cooling		II. Heating			
	T_{cc} [°C]	X_{cc} [%]	T_m [°C]	X_m [%]	T_c [°C]	X_c [%]	T_{cc} [°C]	X_{cc} [%]	T_m [°C]	X_m [%]
PLAi	99.5	43.5	166.9	48.3	93.1	5.9	100.4	34.7	166.8	45.8
PLAi 0.1	105.1	39.4	169.5	40.7	89.6	3.1	102.4	33.1	168.2	40.2
PLAi 1.0	102.2	34.6	168.9	40.3	89.4	4.7	99.1	28.3	168.3	38.2
PLAd	105.3	40.2	169.4	42.0	94.1	0.7	125.1	37.5	168.8	42.5
PLAd 0.1	100.3	36.1	168.4	40.4	98.5	23.1	96.6	9.8	167.9	40.5
PLAd 1.0	98.4	31.7	168.9	36.1	100.5	27.6	105.7	3.8	168.5	38.7

T_{cc} – cold crystallization temperature,
T_m – melting temperature,
T_c – crystallization temperature,
X_{cc} – crystallinity calculated from the heat of cold crystallization,
X_m – total crystallinity determined from the heat of melting,
X_c – crystallinity calculated from the heat of crystallization on cooling.

confirmed that the crystallinity of the samples before the DSC tests was low.

The interesting effects were observed when cooling the melt, during which crystallization of polylactide happened. Crystallization of PLAi and PLAi 0.1, PLAi 1.0 composites started at temperatures of 111–113 °C. The temperature of the beginning of crystallization in PLAd was similar, although it was difficult to determine it precisely due to the weakness of the effect. The temperatures of the beginning of crystallization in the PLAd 0.1 and PLAd 1.0 composites were much higher, at 122.4 and 121.1 °C, respectively. The maximum (peak) crystallization temperature was similar for both homopolymers, one degree higher for PLAd. However, as the filler content increased, the temperature representing the maximum changed differently for the entangled and disentangled PLA matrix composites. In the fully entangled PLAi composites, the maximum crystallization was shifted to lower temperatures after the addition of carbon nanotubes. It can be assumed that the presence of nanotubes limits the movement of macromolecules to growing crystals, not compensated by additional nucleation on MWCNTs. The crystallinity in PLAi and its composites is low (3–6%), and it decreases in the composite, which supports the assumption that nanotubes are more crystallization obstacles than promoters as crystallization nuclei.

Crystallization in PLAd composites proceeded differently. The PLAd homopolymer obtained very low crystallinity on cooling, but the PLAd 0.1 and PLAd 1.0 composites crystallized easily. After adding MWCNTs to PLAd, the maximum crystallization temperature (from 94.1 to 100.5 °C) and the degree of crystallinity (from 0.7 to 27.6%) significantly increased. Better dispersion of the filler in PLAd composites than in PLAi composites meant that a larger fraction of nanoparticles present in the polymer could cause nucleation of crystallization. With the greater mobility of the less entangled macromolecules, the combined effect of enhanced nucleation and easier transport outweighed the fact that the nanotubes were obstacles to the movement of macromolecules to crystallization sites. As a result, a significant increase in the degree of crystallinity was observed during the cooling of composites with disentangled macromolecules.

The behavior of materials observed during the second heating depended on the previous crystallization during cooling. The well-crystallizing PLAd 0.1 and PLAd 1.0 composites showed limited cold crystallization. PLAi, PLAd, PLAi 0.1, and PLAi 1.0, which crystallized poorly on cooling, showed effective cold crystallization. For PLAi composites, a certain reduction in the degree of crystallinity was visible with an increase in the CNT content. PLAi and PLAi composites began to cold crystallize at 81–83 °C, similarly to PLAd 0.1 (81.1 °C), while the cold crystallization in PLAd 1.0 started at 88.0 °C. The maximum of the cold crystallization peak was observed at the temperature of 96.6–105.7 °C. Considerably delayed, probably due to the limited number of nuclei, was the crystallization in PLAd. Its beginning was at 93.5 °C, maximum at 125 °C, and the crystallization peak smoothly turned into a melting peak.

During the second heating, in most materials, with the exception of PLAd and PLAd 1.0, there was a slight α′-α transition peak, visible at 153.5–154.6 °C, with the heat of transition of 1.1–3.1 J/g. At temperatures above 154 °C, the melting process began to be visible. The melting temperatures during the second heating were similar for all studied materials (166.8–168.8 °C). The total crystallinity of PLAi and PLAd composites was in the range of 38.7–45.8% and slightly decreased with the increase in the content of nanotubes. The measured total crystallinity resulted from previous normal and cold crystallization.

3.3. Isothermal crystallization

The crystallization properties of polymers and composites were also examined in isothermal conditions. Based on the results in non-isothermal conditions, knowing the temperatures of the beginning of crystallization during cooling, two temperatures were selected for isothermal tests: 120 and 125 °C. The time dependencies of the heat flow are shown in Figure 4, and the characteristic times of crystallization are shown in Table 5. In all examined materials, crystallization at 120 °C proceeded faster than at 125 °C. The dynamics of isothermal crystallization depend on two factors: nucleation and rate of crystal growth. We previously determined the lamella growth rate for this polymer, which was 2.15 μm/min at 120 °C and 2.25 μm/min at 125 °C for PLAi and 2.25 μm/min at 120 °C and 2.35 μm/min at 125 °C for PLAd [31]. Nucleation was not determined in these studies, but it is usually more intense in semi-crystalline polymers at lower crystallization temperatures. As a result of the interaction of both factors, it takes much longer to crystallize at 125 °C.
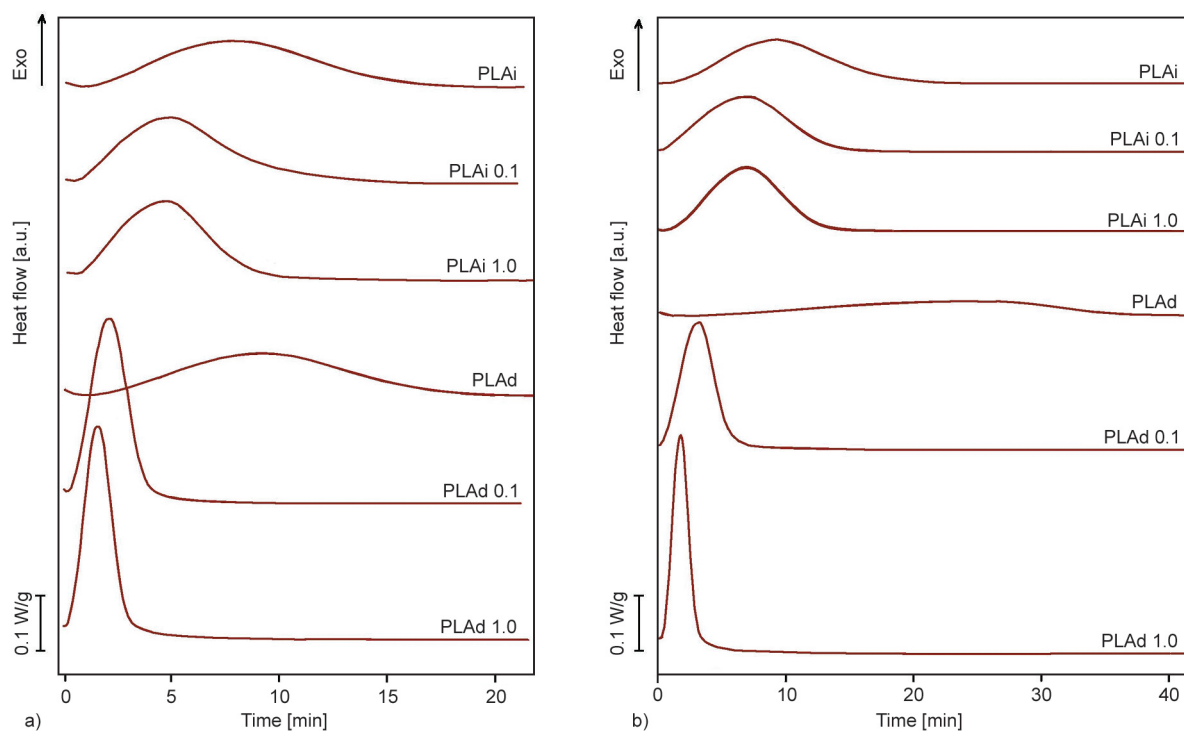
Figure 4. Changes of heat flow with time recorded during isothermal crystallization at 120 °C (a) and 125 °C (b).

Table 5. Times characterizing isothermal crystallization at 120 and 125 °C and heat of crystallization.

Material	$T = 120$ °C				$T = 125$ °C			
	t_{min} [min]	t_{max} [min]	t_{end} [min]	Heat [J/g]	t_{min} [min]	t_{max} [min]	t_{end} [min]	Heat [J/g]
PLAi	1.0	7.9	19.0	38	1.0	10.0	21.9	43
PLAi 0.1	0.7	5.0	15.9	40	0.3	8.1	20.0	43
PLAi 1.0	0.7	4.7	13.5	37	0.5	7.5	18.3	42
PLAd	1.3	9.2	21.0	40	1.6	24.0	39.0	43
PLAd 0.1	0.3	2.0	9.7	37	0.3	4.1	16.3	40
PLAd 1.0	0.0	1.6	8.5	37	0.3	3.0	14.5	41

t_{min} – start time of crystallization,
t_{max} – time when the maximum heat flow was observed,
t_{end} – end time of crystallization.

Comparing both homopolymers, *i.e.* PLAi and PLAd, the second one needed more time to crystallize. As discussed during the non-isothermal crystallization, some nuclei were removed from the PLAd during solvent treatment. The greater difference in crystallization time of both homopolymers observed at 125 °C, when the activity of the present nuclei decreases, confirms that there were fewer nuclei in PLAd. The slightly faster crystal growth rate in PLAd did not compensate for the lower nucleation.

For composites, the addition of nanotubes shortened the crystallization time. However, significantly more MWCNTs particles in 1.0 wt% of composites give only a slight shortening of crystallization compared to 0.1 wt% composites. Increasing the content of nanotubes provides additional nuclei, but only some of the nanotubes nucleate polylactide. On the other hand, almost all nanoparticles are an obstacle to the movement and crystallization of polymer chains and there are definitely more of them in the composite with 1.0 wt% MWCNTs by weight. Therefore, the crystallization time is only slightly shortened with the increase in the content of nanotubes.

Table 5 also shows that the crystallization process was faster in composites with partially disentangled chains than in their fully entangled counterparts. Better dispersion of MWCNTs, providing more active nuclei, and greater mobility of macromolecules are

the reasons for this faster crystallization, although improved dispersion also means more obstacles from nanotubes in the path of macromolecules.

The heat of crystallization for each material was higher at a temperature of 125 °C than at 120 °C because the total time of process was longer, and some annealing just formed crystals increased the total crystallinity. The heats of crystallization of composites were slightly lower than for homopolymers; however, the observed changes were not regular.

3.4. Thermogravimetry

In order to determine whether a less entangled matrix or the presence of nanotubes affects the thermal stability of the tested materials, thermogravimetric measurements were performed. The change in the mass of the tested sample as a function of temperature and the derivative of the change in this mass are shown in Figure 5. Thermal degradation of all samples occurred in the same temperature range of 270–400 °C. The dynamics of the process were very similar for both PLAs and their composites. The temperature at which the mass of the sample changed the fastest was slightly higher in the composites. It was 367 °C for PLAi and 369 °C for PLAi 1.0. In the case of partially disentangled materials, this temperature was 365 °C for PLAd and 368 °C for PLAd 1.0.

The slight decrease in temperature observed for the partially disentangled polymer can be attributed to easier access to the polymer volume. On the other hand, a slight increase in the temperature of the fastest degradation in composites is caused by the barrier effect resulting from the presence of fillers. Although a slight influence of the structure of the samples on

the thermal resistance is visible, it generally does not affect the good stability of the materials.

3.5. Mechanical properties

The conditions for mechanical testing were first established using PLAi samples subjected to tensile tests at different temperatures. The strain-stress curves of PLAi are shown in Figure 6a. It can be seen how quickly the yield stress decreases with increasing temperature. This stress was 73 MPa at 20 °C, 49 MPa at 40 °C, and 32 MPa at 50 °C. At a temperature of 20 °C, which is well below the glass transition, the possibilities of movement of 'frozen' PLA macromolecules were very limited, which led to the rapid breaking of the samples. From theoretical considerations, it is known that the influence of the degree of entanglement of the macromolecular network on the properties should be visible primarily at higher strains, where strain hardening occurs. Therefore, the tests of partially disentangled samples should be carried out at a temperature where large deformations are possible. As seen in Figure 6a, the deformability of PLAi significantly increases at higher temperatures.

Disentanglement of the polymer usually increases the probability of brittle failure due to the easier formation of voids inside the material, but this negative effect decreases with increasing temperature as the mobility of macromolecules increases. For the above reasons, it would not be a good idea to test our polymers and composites at ambient temperature, but good testing conditions could be expected above the glass transition temperature.

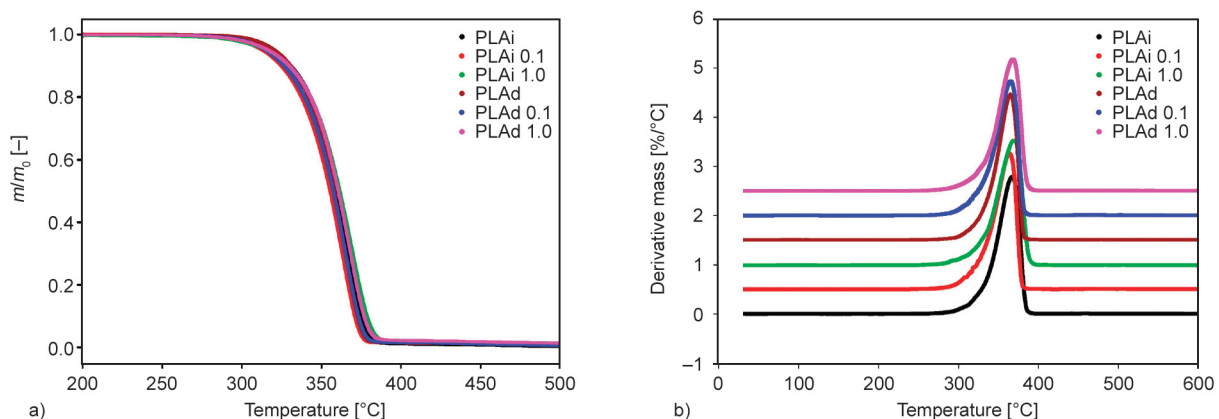Observations of the samples during and after the test showed that the mechanism of deformation changed

Figure 5. a) The ratio of the current, *m*, and initial mass of the sample, m_0, as a function of temperature during heating in nitrogen atmosphere; b) derivative of mass loss during heating. The black curve in Figure 5b is in its original positions, the other curves have been proportionally (0.5 each) shifted vertically for better visibility.
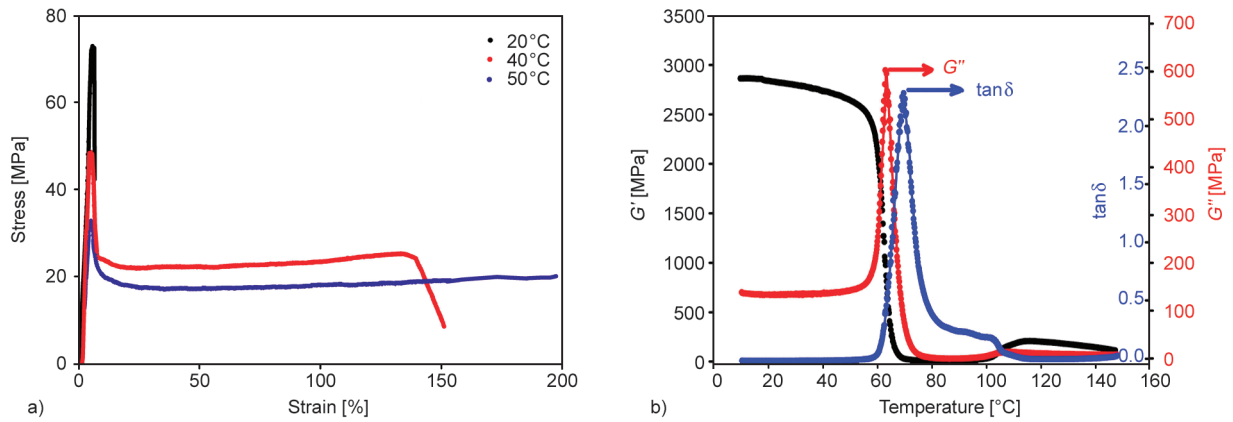
Figure 6. a) Mechanical properties of PLAi determined during tensile test at temperatures of 20, 40 and 50 °C; b) storage modulus (G'), loss modulus (G'') and tan δ measured for PLAi samples at temperatures of 10–160 °C.

as a function of temperature. It was a brittle fracture with signs of crazing before the break when tested at 20 °C, formation of a localized single shear band with necking at 40 °C and almost uniform deformation at 50 °C.

To determine the best temperature for tensile testing of our PLA, the DMTA, studies were conducted (Figure 6b). Experiments have shown that the glass transition occurs at a temperature range of 50 to 70 °C. The maximum of G'' was observed at 62.5 °C, and the maximum of tan δ was at 68.7 °C. The storage modulus remained constant from 70 °C. For these reasons, the tensile properties of our samples were examined at 70 °C, where a large deformation could be observed, including the strain-hardening phase. Similarly, other authors interested in PLA deformation mechanisms conducted research at temperatures of 70 °C and higher [2, 44].

The results of the tensile test of PLAs and composites at 70 °C are shown in Figure 7. The exemplary

strain-stress curves are shown. All tested materials were able to achieve high engineering strains of 350–500%. The yield point was reached at 50–55% strain for homopolymers, increasing to the strain of 65–70% for composites. However, no strong localization of deformation at the yield was observed in the form of a neck appearing in the tested sample. The yield stress values are shown in Table 6. As expected, the stress values at high test temperatures were low, less than 1 MPa. At the yield point, it is seen that less stress is needed to initiate the plastic deformation in the less entangled PLAd polylactide. For both polymers, the yield strength increased with the content of nanotubes, indicating some reinforcement of the matrix by MWCNTs, which is more effective in PLAd composites. The standard deviations for the tested samples were 4–8% of mean values (Table 6), which proves good repeatability of measurements.

At elongations beyond the yield point, the deformed sample entered the plateau stage, in which no significant changes in stress are usually observed. In the tested samples, this phase was relatively short and ended at a strain of about 150%.

Significant differences between the studied materials appeared at large deformations. After a short drop and a plateau in the curves, the next stage of deformation, called strain-hardening, began (at the strain

Figure 7. Representative strain-stress curves showing the mechanical properties of the samples in a tensile test at 70 °C.

Table 6. Yield stress (σ_y) measured at 70 °C.

Sample	σ_y [MPa]
PLAi	0.51±0.02
PLAi 0.1	0.55±0.04
PLAi 1.0	0.67±0.03
PLAd	0.48±0.02
PLAd 0.1	0.63±0.03
PLAd 1.0	0.84±0.03

of 200–250%). During strain-hardening, the stress measured in the tested samples increased quickly, and there were significant differences between the samples. One of the factors responsible for the rate of stress increase is the density of macromolecular entanglements, which determines the stronger or softer reaction of the deformed macromolecular network in the polymer. This is the reason for the slow increase in stress for partially entangled PLAd and greater for fully entangled PLAi. The second factor influencing the course of strain-hardening is the presence of nanofillers in the composites. In the case of both polylactide matrices, the increasing amount of dispersed filler accelerated the stress increase and shifted the beginning of the hardening phase to smaller strains. With the same content of nanotubes, a stronger reinforcement effect was seen in the composite with a less entangled amorphous phase. For example, in the PLAd 1.0 composite, at 350% strain, the stresses were 1.4 times higher than in the PLAi 1.0 composite (3.4 *vs*. 2.5 MPa) and 5 times higher than in the PLAd polymer. The differences

between the composites can be attributed to the previously discussed better dispersion of the filler. Thus, well-dispersed, numerous nanotubes have a stronger effect on the strain-hardening than the reduction of entanglements in the PLA macromolecules network.

In order to learn more about the changes taking place inside the composites during deformation, measurements of their shape (*i.e.*, length, width, and thickness) in the function of time were made. Knowing the changes in shape, it was possible to calculate the change in volume in a selected fragment of the sample. Such measurements are usually made for the first deforming part of the sample, where structural changes during plastic deformation occur fastest. However, in the case of the tested materials, the deformation of individual parts of the sample occurred similarly, so the selection of the right fragment was less important. Figure 8a shows how the width W and thickness D of the samples decreased during deformation in the example of the PLAd sample. Size changes were very similar for the other materials tested (not shown here). In the applied experimental
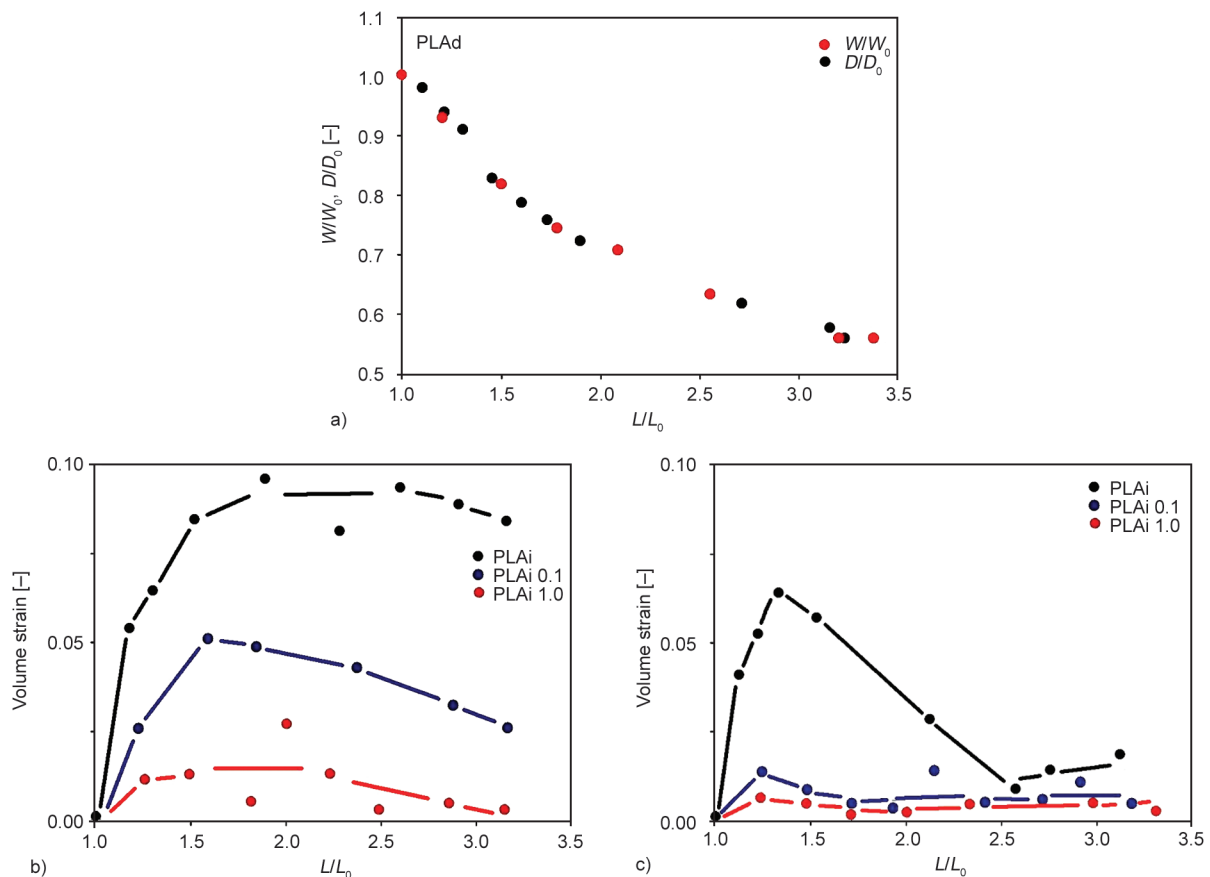

Figure 8. a) Changes in the dimensions of the sample during deformation measured for PLAd. L – actual length, L_0 – initial length, W – actual width, W_0 – initial width, D – actual thickness, D_0 – initial thickness; b) volume strain calculated for PLAi and its composites; c) volume strain calculated for PLAd and its composites. The lines connecting the points are intended to help the reader notice the trends of the results.

conditions, changes in thickness were very similar to changes in the width of the tested sample, which means that the shape of its cross-section did not change.

Figure 8b and Figure 8c show volume changes during the deformation of the tested materials, calculated according to Equation (1). The increase in volume in our polylactides was relatively low. The largest increase in volume was observed for PLAi (0.10 at $L/L_0 = 2.0$) and PLAd (0.07 at $L/L_0 = 1.4$). In the composites, with the increase of the MWCNTs content, the volume strain decreased to almost zero. This decrease was faster when the matrix was less entangled, most likely as a result of better nanoparticle dispersion. The very small volume strain of the composites supported the assumption that limited micro cavitation was present only in PLAi and PLAd. The scale of cavitation, and thus the increase in volume, depends on the possibility of relaxation of local stresses in the matrix. Both the greater mobility of less entangled macromolecules and the better MWCNTs dispersion prevent stronger stress concentration in the PLA matrix.

Analyzing the volume strain with the progress of deformation, it can be seen that the volume rapidly increased until the local deformation of 1.5–2.0. Since the samples deformed almost uniformly, this corresponded to engineering strain of 50–100%, *i.e.*, deformation just after yielding (see Figure 7), when the structure of the polymer is reorganized, and cavities

usually are initiated. For larger strains (*i.e.*, for $L/L_0 = 2.5$–3.0), a decrease in the volume strain is observed, usually explained by a change in the shape of the voids into more elongated but thinner, and therefore with a smaller volume of each void.

In order to better understand the structural changes that occurred in the tested materials, the samples after the tensile test were characterized by X-ray methods, and WAXS and SAXS tests were performed. X-ray experiments were conducted to clarify three issues: the occurrence of crystallization due to deformation, the orientation of structural elements, and the appearance of nanocavitation. The answer to the first question can be provided by the WAXS 2D experiment; the nanovoiding and orientation of the nanotubes should be visible in the SAXS patterns.

WAXS 2D scattering images from the tested samples before and after deformation up to 350% of strain are shown in Figure 9. For non-deformed homopolymers and composites, only scattering in the amorphous phase is visible, which confirms the absence of a crystalline phase and agrees with the previously discussed results of DSC studies on crystallization. The scattering images changed after the samples were deformed. In the case of both polylactides, a strong localization of signals is visible and the patterns resemble those observed for fibers. The scattering is mainly from the newly formed crystalline phase, although a weakened amorphous hallo is still visible. The ring fragments (arcs or blobs) represent
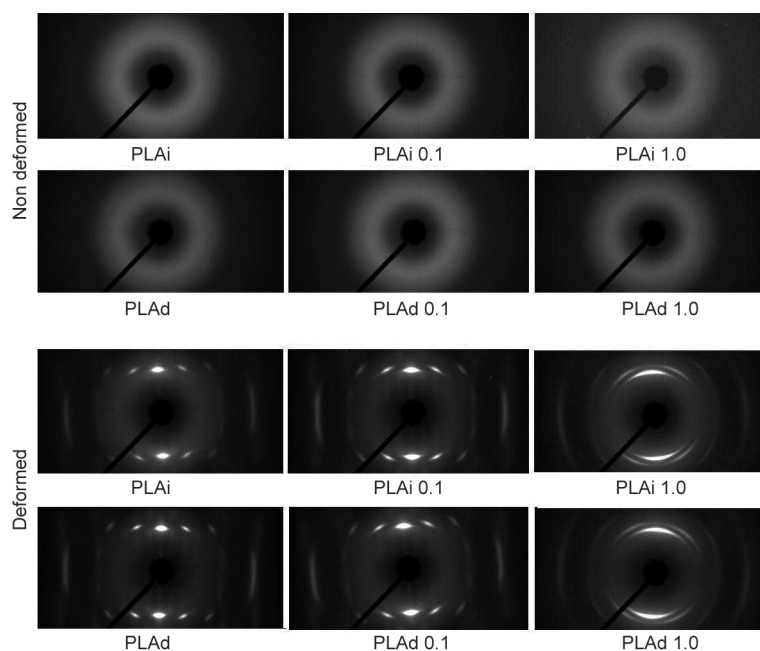

Figure 9. WAXS patterns registered for non-deformed samples and samples deformed to strain of 350%. The direction of stretching in the photographs was horizontal.

the scattering at 2θ angles of 16.7°, 19.1°, 24.9°, and 33.0°. The last two reflections are hardly visible. The most intensive reflection (*i.e.*16.7°) is visible in the vertical direction, and the last one (33.0°) is in the horizontal direction, *i.e.*, in the direction of stretching. The reflection at 2θ =16.4° is assigned to the (200) and (110) crystal planes and the reflection at 2θ = 18.7° represents the diffraction on the (203) crystal plane [3, 43]. The lack of reflections at 2θ = 14.8° and 22.2° indicates that the less ordered α′ form rather than the α form was formed in the sample [2]. The location of reflections (200) and (110) indicates a strong orientation of the macromolecules forming crystals in the direction of deformation.

A very similar evolution of polylactide WAXS patterns was observed with the progress of deformation by Stoclet *et al*. [2] and Zhang *et al*. [45]. They noticed that patterns indicating crystallization in the sample were first seen shortly before or at the beginning of the strain-hardening phase. Stoclet *et al*. [2] have seen much weaker crystalline scattering at 70 °C than is visible in Figure 9; however, it may be explained much faster deformation rate in their case, limiting the time available to crystallization during the experiment. On the other hand, Zhang *et al*. [45] observed that an increase in strain rate tends to favor crystallization. In Zhang's work, it was also shown that annealing for the time corresponding to the tensile experiment did not lead to the formation of a crystalline phase. This agrees with our supplementary observations. Thus, the patterns of PLAs in Figure 9 are the result of strain-induced crystallization, not annealing during deformation.

Scattering images after deformation for PLAi 0.1 and PLAd 0.1 composites are very similar to those recorded for polylactide. A thorough analysis, however, shows slightly less concentration of reflections, *e.g.*, from the (200)/(110) planes. The change in the shape of the reflections, which take the form of arcs, increases with the content of MWCNTs in the composites. This can be clearly seen in the scattering images on PLAd 1.0 and PLAi 1.0 composites. The presence of nanotubes makes it difficult to orientate macromolecules and the resulting crystals are therefore less oriented with the increase in the content of the nanofiller.

It required clarification on whether the composition of the material affected the intensity of crystallization caused by deformation and whether, for example, crystals of different thicknesses grew. Information on these topics was provided by DSC studies of deformed samples, carried out by heating to the melt state. The measurement results are presented in Table 7. Compared to the data in Table 3, an increase in the glass transition temperature of about 2 °C is noticeable.

The tested materials, apart from PLAd 1.0, showed limited cold crystallization, occurring at temperatures 15–20 °C lower than the temperatures measured previously for non-oriented samples (see Table 4). Melting took place at temperatures of 165.8–166.4 °C, and their small dispersion indicates a similar thickness of crystals present in different samples. Differences between the heat of melting and the heat of cold crystallization show the crystallinity of the deformed samples. The degree of crystallinity determined after deformation was at the level of 40–45%, similar for all tested materials.

Figure 10a shows small-angle scattering images recorded for non-deformed samples. There is a visible lack of orientation and an increase in the intensity of scattering with the increase in the content of

Table 7. Temperatures and heats of crystallization and melting measured for samples stretched to 350% strain.

Sample	T_g [°C]	T_{cc} [°C]	H_{cc} [J/g]	T_m [°C]	H_m [J/g]	$H_m - H_{cc}$ [J/g]	X [%]
PLAi	60.2	79.1	9.8	166.1	47.5	37.7	40.5
PLAi 0.1	60.1	88.9	2.7	165.8	44.5	41.8	44.9
PLAi 1.0	59.6	88.9	2.7	166.4	42.0	39.3	42.3
PLAd	65.8	89.0	2.7	165.8	43.1	40.4	43.4
PLAd 0.1	58.1	89.9	3.6	166.1	43.5	39.9	42.9
PLAd 1.0	57.3	–	–	166.2	42.0	42.0	45.2

T_g – glass transition temperature,
T_{cc} – cold crystallization temperature,
T_m – melting temperature,
H_{cc} – heat of cold crystallization,
H_m – heat of melting,
X – crystallinity of samples before the cold crystallization.
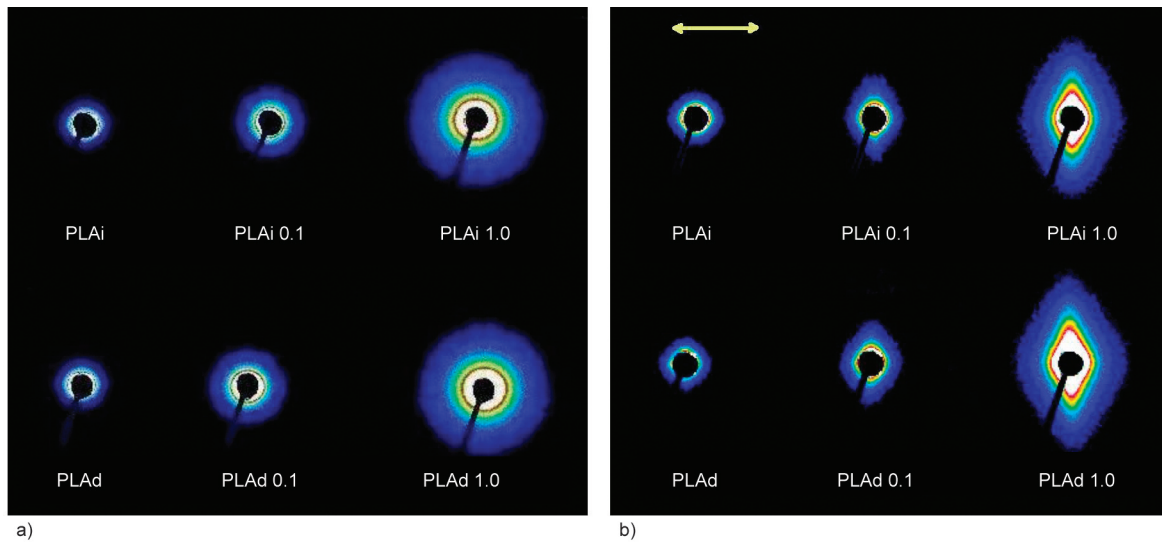
Figure 10. Small-angle X-ray scattering on the tested materials: a) non-oriented samples, b) samples after deformation in the tensile test up to 350%. The yellow arrow shows the direction of stretching.

MWCNTs in the composites. The scattering of X-ray on polylactide only comes from the amorphous phase and is, therefore weak. In composites, it is accompanied by intense scattering on nanotubes. Scattering images recorded for samples deformed to 350% of strain are shown in Figure 10b. Patterns for PLAi and PLAd have not changed significantly, and

the orientation of the polymers is not visible on them. Also, the intensity of scattering was similar for homopolymers before and after deformation. The studied samples had the same thickness, so it was possible to compare intensity and scattering profiles. Profiles taken in the vertical direction in Figure 10 are shown in Figure 11a, and Figure 11b. Figure 11c
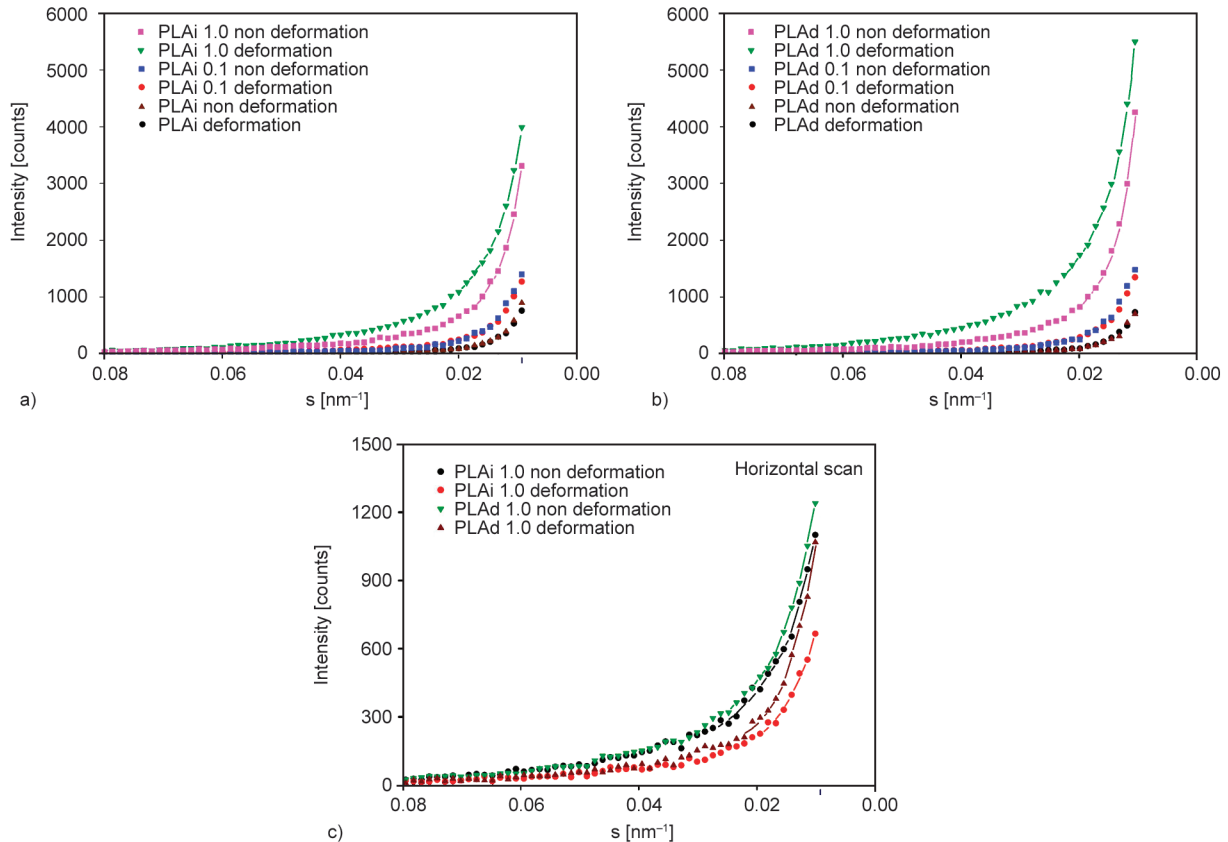
Figure 11. Scattering intensity profiles taken from the SAXS patterns in Figure 10 in the vertical PLAi (a), and PLAd (b) and horizontal (c) directions. On the horizontal axis is the wave vector, s.

shows profiles in the horizontal (stretching) direction for selected samples.

The important issue is whether there are changes in scattering that indicate crystallization or cavitation. From the results of WAXS studies, it was expected that the formation of the periodic crystal structure should be visible in the SAXS patterns, mainly in the horizontal direction. In the case of crystallization, parameters such as long period and lamella thickness can usually be specified based on SAXS. However, for deformed, semi-crystalline PLAi and PLAd samples, the additional scattering is small, which makes it very difficult to determine the above parameters. This is explained by the fact that the density of the amorphous phase is close to the density of the imperfect α′ crystalline phase, which makes the scattering intensity on the periodic structure low [44, 46]. Similarly to microvoids also nanovoids can be generated during polylactide deformation, which should be seen as a rapid increase in scattering intensity. Such additional scattering is not visible when comparing intensity profiles for deformed and non-deformed polylactides. This means that the formation of nanovoids did not occur in homopolymers. Zhang *et al.* [45] observed nanocavitation during the deformation of amorphous polylactide at a temperature of 75 °C, but this phenomenon occurred for higher strain rates, with large strains. The minimum rate used in their experiment was 0.01 s^{-1}, which was one order of magnitude higher compared to our experiments performed at 0.0017 s^{-1}.

For composites after deformation, the orientation of the scattering signal perpendicularly to the stretching direction was visible. The effect was more pronounced when the nanotube concentration was higher. Looking at the vertical scattering profiles for the non-deformed and deformed the same composite, can be seen the difference. Scattering after deformation is greater. However, when analyzing horizontal profiles, scattering from deformed samples in this direction is smaller. When the scattering was integrated for the whole image, the differences in the total scattering intensity before and after deformation did not exceed 5%, which is not significant. This means that scattering for composites was mainly from the nanotubes, so the shapes of the patterns indicate the orientation of the nanotubes in the direction of deformation. The contribution to the scattering of that coming from the crystalline phase was small. Scattering on nanovoids was not observed.

4. Conclusions

As a result of the conducted research, it was found that the reduction of entanglements of macromolecules in the polylactide-MWCNTs composite affects: filler dispersion during processing, ability to crystallize, and mechanical properties. In the composites in which PLA macromolecules were less entangled, better dispersion of nanoparticles was obtained. This can be attributed to easier penetration of macromolecules into the agglomerated CNTs, as well as lower viscosity in the melt, altering the processing conditions.

Large differences between composites with entangled and less entangled macromolecules were observed during non-isothermal crystallization studies. PLAd prepared from solution had fewer nuclei than PLAi, which limited the normal and cold crystallization in this polymer. The presence of nanotubes in the entangled polymer hindered their crystallization. The potential effect of nucleation on the nanotubes did not outweigh the fact that the nanotubes were an obstacle to crystal growth. The addition of nanoparticles to PLAd, better dispersed than in PLAi, gave a sufficient number of nuclei, which, combined with greater mobility of macromolecules and easier obstacle avoidance, resulted in intensive crystallization already during cooling, not only during cold crystallization.

The isothermal crystallization confirmed the observations from the non-isothermal crystallization that there were fewer nuclei in PLAd, which increased the crystallization time. In composites, the process was faster for those with less entangled macromolecules due to easier migration of macromolecules into the growing crystals.

The influence of macromolecular entanglements as well as the content and dispersion of nanotubes, was visible when examining the mechanical properties. Partial disentanglement of macromolecules in the polylactide matrix resulted in lower stresses during the initiation of the plastic deformation. Although the strain-hardening phase for homopolymers was more pronounced for more entangled PLAi, in composites the stress increased faster in those with more and better-dispersed MWCNTs. The better dispersion of the fillers had a greater effect on the stresses than the degree of entanglement of the macromolecules. The slight increase in volume observed during the deformation of homopolymers was attributed to the formation of a small number of microvoids. WAXS studies confirmed the occurrence of the intensive

strain-induced crystallization of polylactide. The crystals were strongly oriented, especially when the number of nanotubes was limited. The MWCNTs themselves also became oriented during the deformation of the composites.

Acknowledgements

References
[1] Garlotta D.: A literature review of poly(lactic acid). Journal of Polymers and the Environment, **9**, 63–84 (2001).
https://doi.org/10.1023/A:1020200822435

[2] Stoclet G., Seguela R., Lefebvre J. M., Elkoun S., Vanmansart C.: Strain-induced molecular ordering in polylactide upon uniaxial stretching. Macromolecules, **43**, 1488–1498 (2010).
https://doi.org/10.1021/ma9024366

[3] Zhang J., Tashiro K., Tsuji H., Domb A. J.: Disorder-to-order phase transition and multiple melting behavior of poly(L-lactide) investigated by simultaneous measurements of WAXD and DSC. Macromolecules, **41**, 1352–1357 (2008).
https://doi.org/10.1021/ma0706071

[4] Kaseem M., Hamad K., Deri F., Ko Y. G.: A review on recent researches on polylactic acid/carbon nanotube composites. Polymer Bulletin, **74**, 2921–2937 (2017).
https://doi.org/10.1007/s00289-016-1861-6

[5] Gonçalves C., Gonçalves I. C., Magalhães F. D., Pinto A. M.: Poly(lactic acid) composites containing carbon-based nanomaterials: A review. Polymers, **9**, 269 (2017).
https://doi.org/10.3390/polym9070269

[6] Kim S. Y., Shin K. S., Lee S. H., Kim K. W., Youn J. R.: Unique crystallization behavior of multi-walled carbon nanotube filled poly(lactic acid). Fibers and Polymers, **11**, 1018–1023 (2010).
https://doi.org/10.1007/s12221-010-1018-4

[7] Xu Z., Niu Y., Wang Z., Li H., Yang L., Qiu J., Wang H.: Enhanced nucleation rate of polylactide in composites assisted by surface acid oxidized carbon nanotubes of different aspect ratios. ACS Applied Materials Interfaces, **3**, 3744–3753 (2011).
https://doi.org/10.1021/am200932q

[8] Mina M. F., Beg M. D. H., Islam M. R., Nizam A., Alam A. K. M. M., Yunus R. M.: Structures and properties of injection-molded biodegradable poly(lactic acid) nanocomposites prepared with untreated and treated multiwalled carbon nanotubes. Polymer Engineering and Science, **54**, 317–326 (2014).
https://doi.org/10.1002/pen.23564

[9] Park S. H., Lee S. G., Kim S. H.: Isothermal crystallization behavior and mechanical properties of polylactide/carbon nanotube nanocomposites. Composites Part A: Applied Science and Manufacturing, **46**, 11–18 (2013).
https://doi.org/10.1016/j.compositesa.2012.10.011

[10] Rizvi R., Khan O., Naguib H. E.: Development and characterization of solid and porous polylactide-multi-wall carbon nanotube composites. Polymer Engineering and Science, **51**, 43–53 (2011).
https://doi.org/10.1002/pen.21792

[11] Wu C-S., Liao H-T.: Study on the preparation and characterization of biodegradable polylactide/multi-walled carbon nanotubes nanocomposites. Polymer, **48**, 4449–4458 (2007)
https://doi.org/10.1016/j.polymer.2007.06.004

[12] Zhao Y., Qiu Z., Yan S., Yang W.: Crystallization behavior of biodegradable poly(L-lactide)/multiwalled carbon nanotubes nanocomposites from the amorphous state. Polymer Engineering and Science, **51**, 1564–1573 (2011).
https://doi.org/10.1002/pen.21933

[13] Wu D., Wu L., Zhou W., Zhang M., Yang T.: Crystallization and biodegradation of polylactide/carbon nanotube composites. Polymer Engineering and Science, **50**, 1721–1733 (2010).
https://doi.org/10.1002/pen.21695

[14] Kuan C-F., Kuan H-C., Ma C-C. M., Chen C-H.: Mechanical and electrical properties of multi-wall carbon nanotube/poly(lactic acid) composites. Journal of Physics and Chemistry of Solids, **69**, 1395–1398 (2008).
https://doi.org/10.1016/j.jpcs.2007.10.060

[15] Szatkowski P., Czechowski L., Gralewski J., Szatkowska M.: Mechanical properties of polylactide admixed with carbon nanotubes or graphene nanopowder. Materials, **14**, 5955 (2021).
https://doi.org/10.3390/ma14205955

[16] Wu D., Wu L., Zhou W., Sun Y., Zhang M.: Relations between the aspect ratio of carbon nanotubes and the formation of percolation networks in biodegradable polylactide/carbon nanotube composites. Journal of Polymer Science Part B: Polymer Physics, **48**, 479–489 (2010).
https://doi.org/10.1002/polb.21909

[17] Ramontja J., Ray S. S., Pillai S. K., Luyt A. S.: High-performance carbon nanotube-reinforced bioplastic. Macromolecular Materials and Engineering, **294**, 839–846 (2009).
https://doi.org/10.1002/mame.200900197

[18] Yoon J. T., Jeong Y. G., Lee S. C., Min B. G.: Influences of poly(lactic acid)-grafted carbon nanotube on thermal, mechanical, and electrical properties of poly(lactic acid). Polymers Advanced Technologies, **20**, 631–638 (2009).
https://doi.org/10.1002/pat.1312

[19] Mat Desa M. S. Z., Hassan A., Arsad A., Mohammad N. N. B.: Mechanical properties of poly(lactic acid)/multiwalled carbon nanotubes nanocomposites. Materials Research Innovations, **18**, S6-14–S6-17 (2014).
https://doi.org/10.1179/1432891714Z.000000000924

[20] Chiu W-M., Chang Y-A., Kuo H-Y., Lin M-H., Wen H-C.: A study of carbon nanotubes/biodegradable plastic polylactic acid composites. Journal of Applied Polymer Science, **108**, 3024–3030 (2008).
https://doi.org/10.1002/app.27796

[21] Villmow T., Pötschke P., Pegel S., Häussler L., Kretzschmar B.: Influence of twin-screw extrusion conditions on the dispersion of multi-walled carbon nanotubes in a poly(lactic acid) matrix. Polymer, **49**, 3500–3509 (2008).
https://doi.org/10.1016/j.polymer.2008.06.010

[22] Wool R. P.: Polymer entanglements. Macromolecules, **26**, 1564–1569 (1993).
https://doi.org/10.1021/ma00059a012

[23] Eckstein A., Suhm J., Friedrich C., Maier R-D., Sassmannshausen J., Bochmann M., Mülhaupt R.: Determination of plateau moduli and entanglement molecular weights of isotactic, syndiotactic, and atactic polypropylenes synthesized with metallocene catalysts. Macromolecules, **31**, 1335–1340 (1998).
https://doi.org/10.1021/ma971270d

[24] Fetters L. J., Lohse D. J., Colby R. H.: Chain dimensions and entanglement spacings. in 'Physical properties of polymers handbook' (ed: Mark J. E.) Springer, New York, 447–454 (2007).

[25] Pawlak A.: The entanglements of macromolecules and their influence on the properties of polymers. Macromolecular Chemistry and Physics, **220**, 1900043 (2019).
https://doi.org/10.1002/macp.201900043

[26] Wang B., Cavallo D., Zhang X., Zhang B., Chen J.: Evolution of chain entanglements under large amplitude oscillatory shear flow and its effect on crystallization of isotactic polypropylene. Polymer, **186**, 121899 (2020).
https://doi.org/10.1016/j.polymer.2019.121899

[27] Kong D-C., Yang M-H., Zhang X-S., Du Z-C., Fu Q., Gao X-Q., Gong J-W.: Control of polymer properties by entanglement: A review. Macromolecular Materials and Engineering, **306**, 2100536 (2021).
https://doi.org/10.1002/mame.202100536

[28] Wang X., Liu R., Wu M., Wang Z., Huang Y.: Effect of chain disentanglement on melt crystallization behavior of isotactic polypropylene. Polymer, **50**, 5824–5827 (2009).
https://doi.org/10.1016/j.polymer.2009.10.002

[29] Sasaki T., Morino D., Tabata N.: Origin of enhanced cold crystallization rate for freeze-dried poly(L-lactide) from solutions. Polymer Engineering and Science, **51**, 1858–1865 (2011).
https://doi.org/10.1002/pen.21977

[30] Liu X-T., Bao R-Y., Li Y-M., Yang W., Xie B-H., Yang M-B.: Effect of chain entanglement on the melt-crystallization behavior of poly(L-lactide) acid. Polymer Research, **23**, 164 (2016).
https://doi.org/10.1007/s10965-016-1060-z

[31] Krajenta J., Safandowska M., Pawlak A., Galeski A.: All-polymer composites – A new approach with the use of disentangled semi-crystalline polymers. Part I. Disentangling and properties of disentangled polylactide. Polimery, **65**, 167–173 (2020).
https://doi.org/10.14314/polimery.2020.3.1

[32] Sun C., Zheng Y., Xu S., Ni L., Li X., Shan G., Bao Y., Pan P.: Role of chain entanglements in the stereocomplex crystallization between poly(lactic acid) enantiomers. ACS Macro Letters, **10**, 1023–1028 (2021).
https://doi.org/10.1021/acsmacrolett.1c00394

[33] Krajenta J., Pawlak A., Galeski A.: All-polymer composites – A new approach with the use of disentangled semi-crystalline polymers. Part II. Preparation of composites from partially disentangled polylactide. Polimery, **65**, 261–267 (2020).
https://doi.org/10.14314/polimery.2020.4.1

[34] Barangizi H., Pawlak A.: Crystallization of partially disentangled polypropylene in nanocomposites with aluminum oxide. Polymer, **254**, 125049 (2022).
https://doi.org/10.1016/j.polymer.2022.125049

[35] Luo J., Liu M., Chen J., Min J., Fu Q., Zhang J.: Effectively maintaining the disentangled state of isotactic polypropylene in the presence of graphene nanoplatelet. Polymer, **226**, 123806 (2021).
https://doi.org/10.1016/j.polymer.2021.123806

[36] Drakopoulos S. X., Tarallo O., Guan L., Martin-Fabiani I., Ronca S.: Nanocomposites of Au/disentangled UHMWPE: A combined optical and structural study. Molecules, **25**, 3225 (2020).
https://doi.org/10.3390/molecules25143225

[37] Zhang X., Zhao S., Xin Z.: The chain dis-entanglement effect of polyhedral oligomeric silsesquioxanes (POSS) on ultra-high molecular weight polyethylene (UHMWPE). Polymer, **202**, 122631 (2020).
https://doi.org/10.1016/j.polymer.2020.122631

[38] Romo-Uribe A., Reyes-Mayer A., Paredes-Pérez M., Lichtenhan J., Yañez-Lino M., Sarmiento-Bustos E.: POSS driven chain disentanglements, decreased the melt viscosity and reduced O_2 transmission in polyethylene. Polymer, **165**, 61–71 (2019).
https://doi.org/10.1016/j.polymer.2019.01.024

[39] Romo-Uribe A.: Dispersion at single unit TiO_2 nanoparticles reduced T_g, induced chain disentanglement and reduced tensile modulus in waterborne acrylic coatings. Macromolecular Materials and Engineering, **306**, 2000591 (2021).
https://doi.org/10.1002/mame.202000591

[40] Pawlak A., Galeski A., Rozanski A.: Cavitation during deformation of semicrystalline polymers. Progress in Polymer Science, **39**, 921–958 (2014).
https://doi.org/10.1016/j.progpolymsci.2013.10.007

[41] Fischer E. W., Sterzel H. J., Wegner G. K. Z. Z.: Investigation of the structure of solution grown crystals of lactide copolymers by means of chemical reactions. Kolloid-Zeitschrift und Zeitschrift für Polymere, **251**, 980–990 (1973).
https://doi.org/10.1007/BF01498927

[42] Saeidlou S., Huneault M. A., Li H., Park C. B.: Poly(lactic acid) crystallization. Progress in Polymer Science, **37**, 1657–1677 (2012).
https://doi.org/10.1016/j.progpolymsci.2012.07.005

[43] Barrau S., Vanmansart C., Moreau M., Addad A., Stoclet G., Lefebvre J-M., Seguela R.: Crystallization behavior of carbon nanotube−polylactide nanocomposites. Macromolecules, **44**, 6496–6502 (2011).
https://doi.org/10.1021/ma200842n

[44] Zhou C., Li H., Zhang W., Li J., Huang S., Meng Y., deClaville Christiansen J., Yu Z., Wu Z., Jiang S.: Direct investigations on strain-induced cold crystallization behavior and structure evolutions in amorphous poly(lactic acid) with SAXS and WAXS measurements. Polymer, **90**, 111–121 (2016).
https://doi.org/10.1016/j.polymer.2016.03.014

[45] Zhang X., Schneider K., Liu G., Chen J., Brüning K., Wang D., Stamm M.: Structure variation of tensile-deformed amorphous poly(L-lactic acid): Effects of deformation rate and strain. Polymer, **52**, 4141–4149 (2011).
https://doi.org/10.1016/j.polymer.2011.07.003

[46] Mahendrasingam A., Blundell D. J., Parton M., Wright A. K., Rasburn J., Narayanan T., Fuller W.: Time resolved study of oriented crystallisation of poly(lactic acid) during rapid tensile deformation. Polymer, **46**, 6009–6015 (2005).
https://doi.org/10.1016/j.polymer.2005.05.081

express
polymer letters

Research article

Application of polydimethylsiloxane (PDMS) as a flexible substrate for wireless body and local area network antenna with CSRR integration

Praveen Kumar Sharma[1]*⬦ iD, Jae-Young Chung*[2]

[1]Research Center for Electrical and Information Technology, Seoul National University of Science and Technology, 01811 Seoul, Republic of Korea
[2]Department of Electrical and Information Engineering, Seoul National University of Science and Technology, 01811 Seoul, Republic of Korea

Abstract. This research illustrates the application of PDMS (polydimethylsiloxane), a silicon-based polymer with loss tangent ($\tan\delta_{\varepsilon_r}$) and dielectric constant (ε_r) values of 0.02 and 2.65, as a flexible substrate for antenna (PDMS substrate based flexible antenna – PSFA). In this paper, two flexible antennas having a size of 50.2×40.1×1 mm are presented for wireless body and local area networks. A split ring resonator (CSRR) structure with circular geometry is integrated on the patch in the second proposed antenna as compared to the first antenna with the same dimensions. As a result, this antenna has multiband notched frequency characteristics at 5.12, 5.80, and 6.66 GHz, respectively, with improved performance. It also helped to reduce SAR and backward radiation. Both of the proposed antennas behave well and exhibit significant concordance between simulation and measurement findings when tested in various operational situations, including wet and conformal conditions and demonstrate the suitability of PDMS as a flexible substrate for antenna applications.

Keywords: adhesion, conformal analysis, flexible antenna, modeling and simulation, material testing, PDMS

1. Introduction

Compared to conventional electronic devices with rigid substrates, flexible substrate-based electronics have many benefits. These flexible devices can withstand unusual operating environments like twisting, bending, and stretching. As a result of additional atypical performance requirements brought on by the rising demand for novel wireless communication systems in recent years, antenna designers have had to overcome a number of technological impediments. For such applications, it is preferable to have a flexible, compact, lightweight, easily integrable, and inexpensive antenna. These qualities are also desired in wearable antennas [1] for body-worn applications because they mitigate potential health risks

for the user. As a result, flexible antennas designed utilizing flexible substrates are preferred over traditional antennas using rigid substrates to satisfy such requirements.

Materials for conductive portions like patch, ground, and feed, as well as substrate materials, should be carefully chosen when designing a flexible antenna. This decision will largely depend on the desired applications taken into account. Fabric, polymers, and paper-based substrates are the three basic categories of flexible substrates that may be utilized to develop flexible antennas. The vulnerability of fabric substrates to external factors like temperature variations and hydrophilicity is higher. They perform only partially when conditions are flexible, stretchable, and

conformal [2]. Similar restrictions apply to paper-based substrates; hence polymer-based substrate polydimethylsiloxane (PDMS) is favored in this research.

Researchers are always experimenting with new approaches and materials to enhance the performance of flexible and wearable antennas. One is the use of metamaterial loading in flexible and wearable antennas. Flexible antennas' performance can be further enhanced by various metamaterial structures, such as split-ring resonators (SRRs), by downsizing their size, boosting their bandwidth, efficiency, and directivity, and enhancing their radiation patterns [3, 4]. These features facilitate wave polarization, wave absorption, and surface wave reduction. For lowering the specific absorption rate (SAR) of flexible/wearable antennas, metamaterial surfaces have also gained popularity. By reducing the energy the body absorbs, metamaterials are frequently employed to protect the human body from dangerous radiation [5]. They are unquestionably helpful in antenna design. Still, a great deal of research is to be done in this field, particularly their implementation in flexible and wearable antennas using polymer substrates like PDMS. This encouraged us to design and analyze a PDMS substrate-based flexible antenna-2 (PSFA-2) for wireless body and local area networks that is inspired by a split ring resonator (CSRR) structure and compare it to a flexible antenna having the same dimensions (PSFA-1) that is not loaded with CSRR to assess its advantages. There are several pieces of research available in the literature that employs SRRs in the antenna design to create frequency notches and broadband behavior and to improve the antenna performance. Still, there are very few on the design of flexible/ wearable antennas with CSRR loading, particularly using the polymer substrates like polydimethylsiloxane (PDMS) for the targeted wireless local area network (WLAN) and wireless body area network (WBAN) applications as presented in this paper. Furthermore, many researchers have employed a variety of CSRRs and their arrays, but here only one CSRR employed in PSFA-2 is performing the same task, thus reducing the design complexity. The employed substrate PDMS in both of the presented antennas is fabricated and characterized to improve the design accuracy and both of the presented antennas are tested under varying operating conditions. Simple antenna structures, even with the CSRR incorporation, stable and enhanced performance with

flexibility, easy and cost-effective development process make the proposed antennas employable, and PDMS a good candidate as a flexible substrate for the targeted applications; these are some of the major contributions of the presented research as compared to the previous works.

Both of the proposed antennas show a multiband behavior and operate at the 5.0 GHz band (Institute of Electrical and Electronics Engineers, IEEE 802.11ac) to resolve the 2.45 GHz band's issues relating to traffic and the 6.0 GHz (IEEE 802.11ax) band, which was just debuted in 2020 for fast wireless local area network applications. To address fast wireless body area network applications, an additional band of 5.8 GHz (IEEE 802.16d) is attained in the PSFA-2 by a single CSRR loading. The presented paper is divided into five sections. After a brief introduction in section 1, section 2 provides an overview of the PDMS development and characterization techniques. Antenna designs and fabricated prototypes are presented in section 3. In section 4, the performance of both the presented PSFAs is compared with SAR, conformal, and wet condition analysis. Finally, the paper is concluded in section 5 by summarizing all the results obtained.

2. PDMS Fabrication and dielectric characterization

The choice of substrate is a crucial component of antenna design since its physical and dielectric qualities have a direct impact on the antenna's radiating properties. Polydimethylsiloxane (PDMS), which is a silicone-based elastomer belonging to silicon-organic compounds, is used as a flexible substrate in both of the proposed antennas. PDMS has gained popularity in recent years not only as a substrate for antenna applications but also as a coating for antenna hydrophobics [6], wearable sensors [7], membranes [8], *etc.* It possesses qualities that make it an appropriate substrate for flexible antennas – it is highly flexible (Young's modulus <3 MPa) and transparent, has less effect of environmental variations like absorption of moisture, is thermally and chemically stable, and has nearly isotropic dielectric properties [9]. The flexible substrate PDMS is developed using the conventional process, as summarized in Figure 1.

After the substrate has been chosen and successfully developed in accordance with the specifications, its characterization is carried out utilizing our prior research [10–12]. Since PDMS is anisotropic, the values
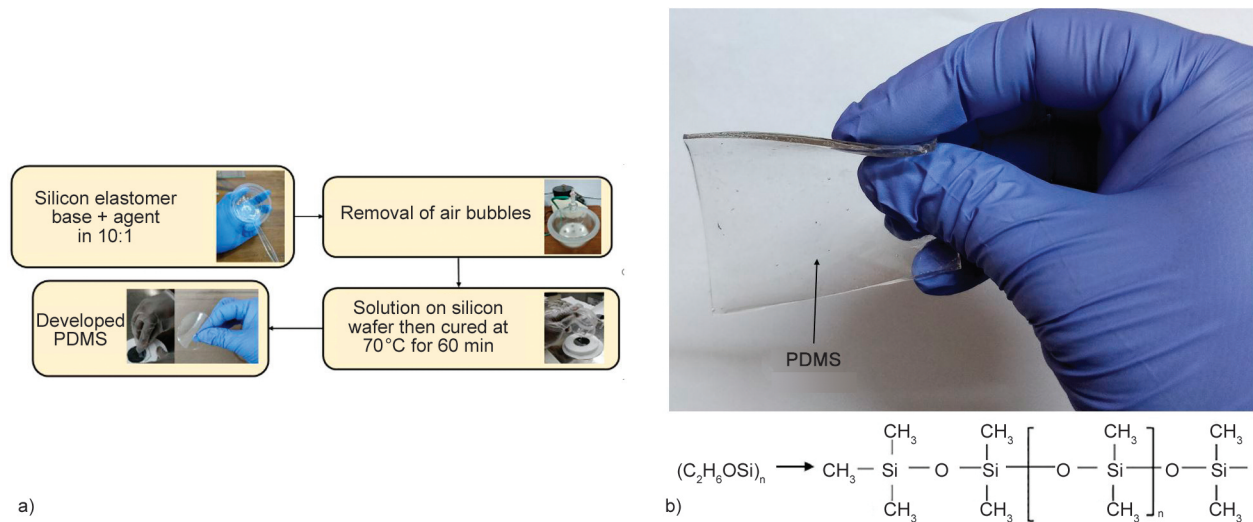
Figure 1. a) PDMS development process, and b) developed PDMS.

for the dielectric properties vary in different directions. The characterization of the PDMS as a flexible substrate is crucial since it has been noted from the literature that various researchers have employed different values of the dielectric characteristics for various applications [13–15]. This variation in the values of the dielectric parameters is mainly because of the applied characterization methods like, for example, conventional methods like Kent, free-space, Courtney, *etc.*, methods evaluate the dielectric parameters in a parallel direction [16–18]. Whereas the methods like transverse magnetic (TM) mode, re-entrant cavity, substrate integrated waveguide (SIW), *etc.* methods investigate the dielectric parameters in a perpendicular direction [19–21]. All of these methods are not appropriate for the characterization of polymers and may result in variable outcomes for anisotropic substrates.

Resonance and planar structure techniques based on our past works are employed here to investigate the PDMS dielectric characteristics [9, 10]. As shown in Figure 2a, two distinct resonators, R1 (for parallel values) and R2 (for perpendicular values), were

designed exclusively for resonance measurements of PDMS's dielectric characteristics in both directions. The measurements show that the dielectric constants were 2.7 and 2.5, and the loss tangents were 0.03 and 0.02 in parallel and perpendicular directions, respectively. Therefore, it should be underlined that the perpendicular dielectric constant is approximately 5.1% smaller than the parallel one, demonstrating the low anisotropy of this material.

This method is also applied to other similar materials to validate the acquired values, and when their resulting values are compared with the values provided by the manufacturer, a reasonable correlation is found, as shown in Table 1. The covered ring resonator, shown in Figure 2b, has been used in planar structure measurements to assess the isotropic counterparts to PDMS's anisotropic dielectric characteristics and help to minimize simulation problems with the anisotropic substrates in antenna applications. The loss tangent is calculated to be 0.02, and the dielectric constant to be 2.65. The isotropic equivalent values of the PDMS lie between the parallel-perpendicular values, as illustrated in Figure 3.
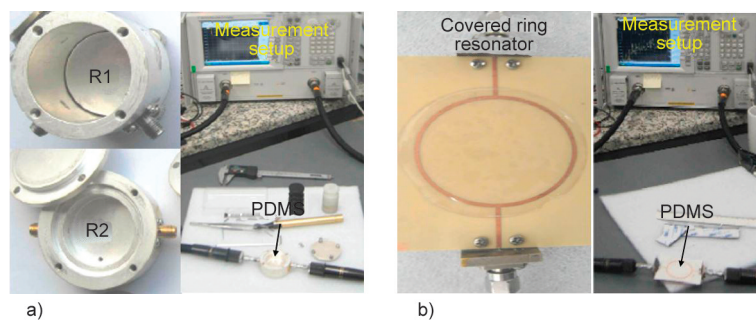

Figure 2. Measurement setups for a) Resonance measurement, and b) planar structure measurement method.

Table 1. Dielectric values of different materials by the resonance measurements (approximates).

Material	Perpendicular value, $\dfrac{\tan\delta_{\varepsilon_{r_{perpendicular}}}}{\varepsilon_{r_{perpendicular}}}$ (~)	Parallel value, $\dfrac{\tan\delta_{\varepsilon_{r_{parallel}}}}{\varepsilon_{r_{parallel}}}$ (~)
Polydimethylsiloxane (PDMS)	0.0200/2.5	0.0300/2.7
Cyclic olefin copolymer (COP)	0.0003/2.3	0.0005/2.3
Polytetrafluoroethylene (PTFE)	0.0002/2.0	0.0003/2.1
Polycarbonate (PC)	0.0050/2.7	0.0060/2.7
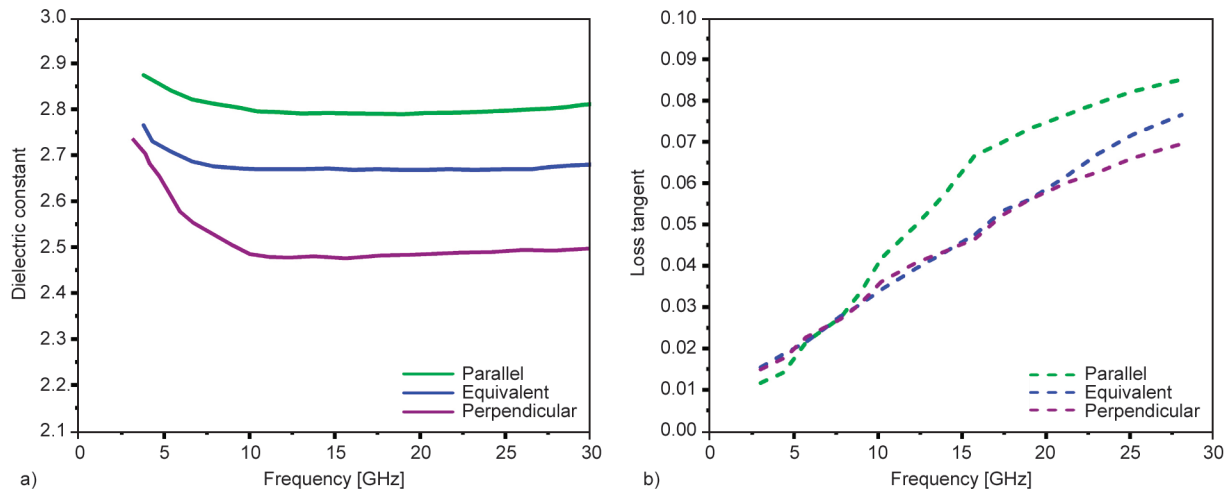
Figure 3. Obtained dielectric values by resonance and planar measurements: a) dielectric constant values and b) loss tangent values.

3. Antenna design

Two flexible antennas (PSFA-1 and 2) for wireless body and local area networks are presented in this paper. The PSFA-2 incorporates a CSRR structure to exemplify the advantages of employing it in flexible antenna designs with PDMS substrate; however, both antennas have the same physical dimensions.

3.1. Antenna geometry

Both of the proposed flexible antennas of size 50.2×40.1×1 mm having a circular patch are designed using PDMS as a flexible substrate with ε_r of 2.65 and $\tan\delta_{\varepsilon_r}$ of 0.02. The antenna geometries are depicted in Figure 4 and listed in Table 2 with their precise dimensions. In order to examine the effects

Table 2. Antenna physical parameters.

Parameter	l	w	r	f_l	f_w	g_l	g_w	l_g	w_g	l_s	w_s
	[mm]										
Value	50.2	40.1	15.0	17.0	18.0	19.0	3.0	50.2	40.1	12.0	0.5
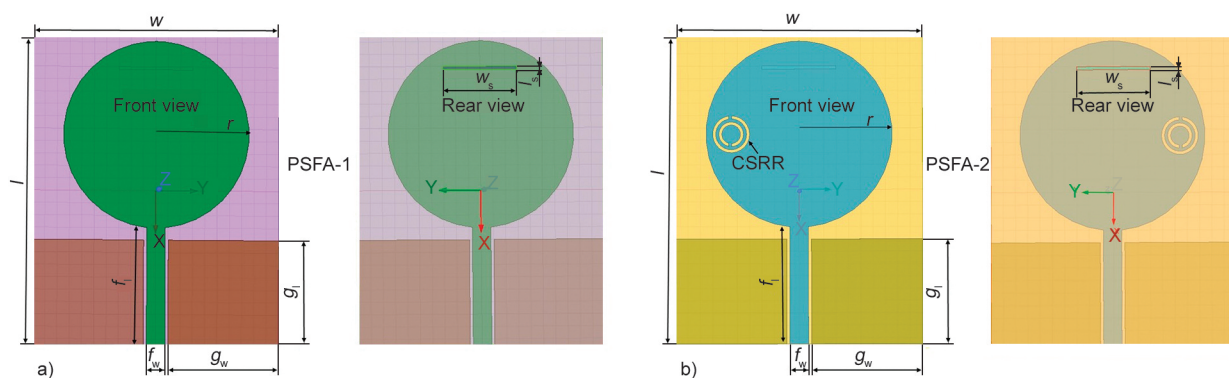
Figure 4. Antenna geometries: a) PSFA-1, and b) PSFA-2.

on the radiation performance, which are detailed in later portions of this paper, a CSRR structure is inserted in the PSFA-2 on the same side of the patch. Prior to being used in the antenna design, the CSRR is additionally examined and optimized for its behavior [22] using Ansys HFSS software.

The incorporation of the CSRR in the antenna design is quite advantageous since it makes the design more compact while acting as a magnetic resonator, increases bandwidth by limiting standing waves, and enhances the antenna's radiation characteristics. These benefits are experimentally confirmed in the later sections of this paper in the design and analysis of PSFA-2.

The circular SRR's resonant frequency (f_{res}) is (Equation (1)):

$$f_{res-CSRR} = \frac{1}{2\pi}\sqrt{\frac{1}{L_{total}C_{total}}} =$$
$$= \frac{1}{2\pi\sqrt{L_{total}\left[\frac{(\pi r_{avg}-s_{gap})C_{pul}}{2} + \frac{\varepsilon_0 \omega t}{2s_{gap}}\right]}} \quad (1)$$

where L_{total} and C_{total} are the total inductance and total capacitance of the unit cell structure, r_{avg} is the

ring's average radius, s_{gap} is the gap in split, C_{pul} is the per unit length capacitance. The total inductance of the unit cell is (Equation (2)):

$$L_{total} = 0.0002l_w\left(2.303\log_{10}\frac{4l_w}{t} - c\right)\mu H \quad (2)$$

where l_w is the wire's cross-section length for a single loop, c is the wire loop geometry constant, and is equal to 2.4.

The CSRR unit cell geometry is shown in Figure 5a, and the equivalent circuits of both PSFAs are depicted in Figure 5b and Figure 5c, respectively. Its response as an SRR structure is confirmed by Figure 6, which shows that the SRR has a negative permeability and permittivity in the required region of operation. The CSRR interacts dynamically with electromagnetic waves when these parameters are negative, as it produces a negative refractive index, which lessens standing waves and enhances the antenna's performance.

3.2. Fabrication of prototypes

The prototypes of the presented antennas are developed and measured using the vector network analyzer
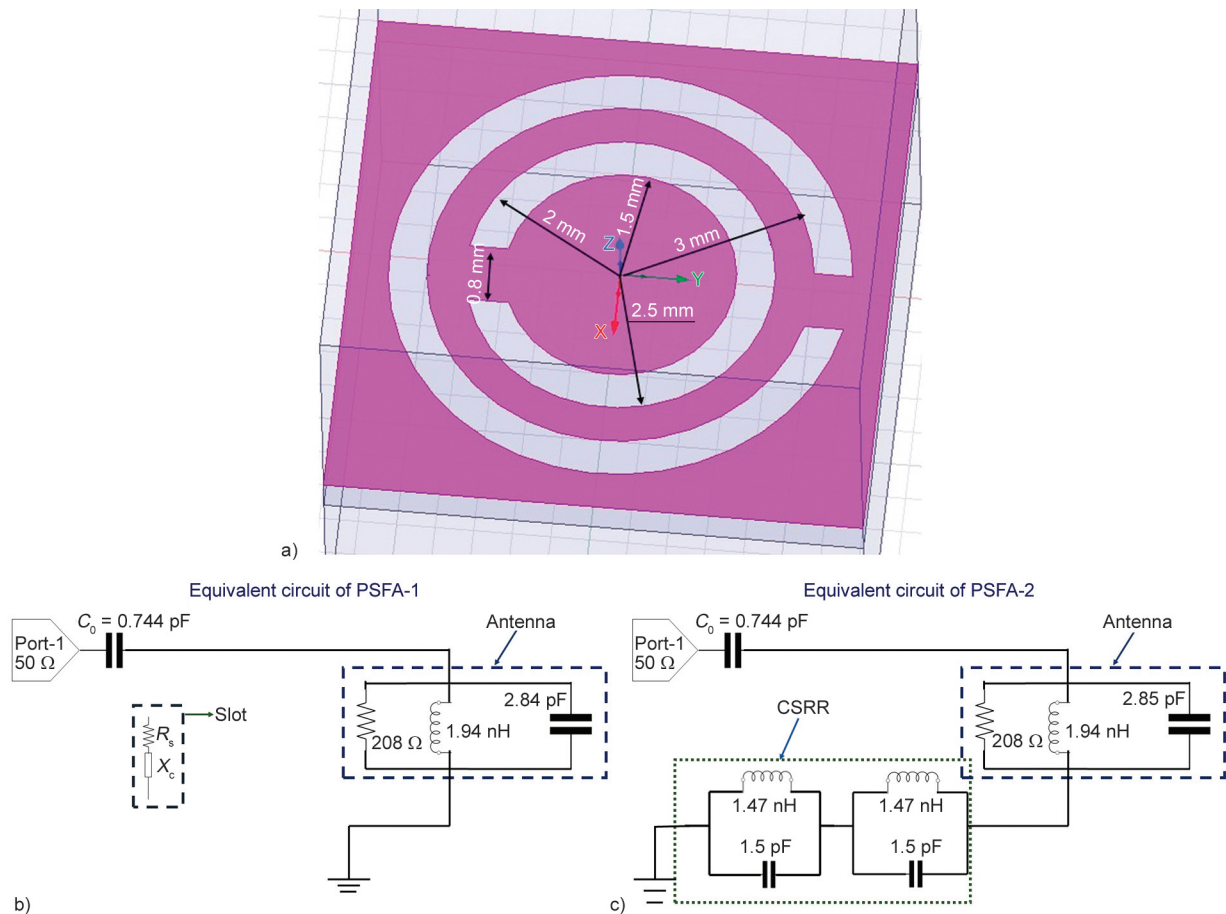

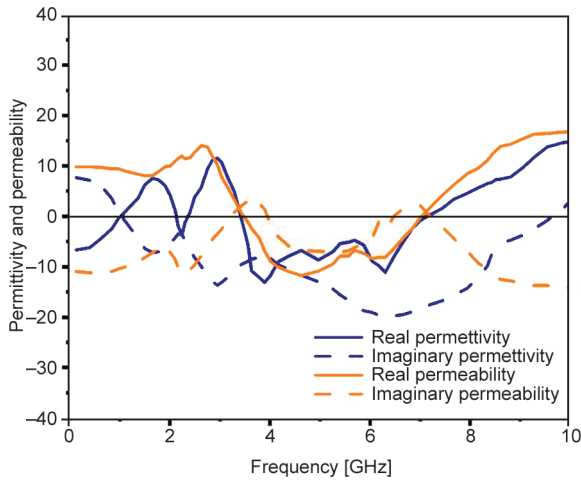**Figure 5.** a) Circular SRR dimensions; equivalent circuits: b) PSFA-1, and c) PSFA-2.

Figure 6. Circular SRR response.

(VNA) Figure 7, to validate the simulation results. In order to fabricate the antennas, first of all, the PDMS is developed as mentioned in section 2 with the required thickness of 1 mm, then it is cut as per the antenna dimensions of 50.2×40.1 mm. The copper tape 0.059 mm thick is used for the metallic parts of the antenna. Due to its superior adhesive qualities, the flexible substrate PDMS makes it simple for the copper tape to adhere. Both fabricated antennas exhibit steady performance even under variable working conditions, as described in the following sections of this article.

4. Performance analysis
The evaluation of the obtained results from the simulation and measurement of the two designed PSFAs is carried out in this section. Both antennas are compared while operating under varying operating situations like conformal and wet conditions with SAR analysis.

4.1. Radiation parameters
Both of the presented antennas show notched frequency behavior for the target applications, as shown in Figure 8. The PSFA-1 with dual-band behavior has impedance bandwidths of 0.75 GHz (4.60–5.35 GHz) at 5.03 and 0.51 GHz (6.39–6.90 GHz) at 6.53 GHz; 0.698 GHz (5.00–5.69 GHz) at 5.40 and 0.5 GHz (6.10–6.60 GHz) at 6.70 GHz in the simulation and experimental results respectively. While the PSFA-2 shows a triple band behavior having impedance bandwidths of 0.83 GHz (4.50–5.33 GHz) at 5.12 GHz, 0.64 GHz (5.60–6.24 GHz) at 5.80 GHz, and 0.53 GHz (6.35–6.88 GHz) at 6.66 GHz in simulation and 0.8 GHz (4.80–5.60 GHz) at 5.24, 0.61 GHz (5.62–6.23 GHz) at 5.72 and 0.518 GHz (6.48–6.99 GHz) at 6.81 GHz in measured results respectively. Figure 9 illustrates the voltage standing wave ration (*VSWR*) of both the presented antennas with both simulation and measurement results having values less than 2. The close correlation between the simulation and measured radiation patterns at resonating frequencies across different planes is illustrated in the Figure 10 and Figure 11. Both of the proposed PSFAs exhibit nearly omnidirectional radiation patterns and show a conventional monopole behavior. The total gain of the PSFA-1 and PSFA-2 is 4.8 and 6.3 dBi, respectively (Figure 12). The third frequency band at 5.8 GHz, a decrease in the reflection coeficient (S_{11}) and *VSWR*, and an enhancement in antenna gain can all be vividly viewed from the discussions above as benefits of implementing a single CSRR in the PSFA-2 with polymer substrate PDMS as summarized in Table 3. *E*-field distribution of both PSFAs are shown in Figure 13.
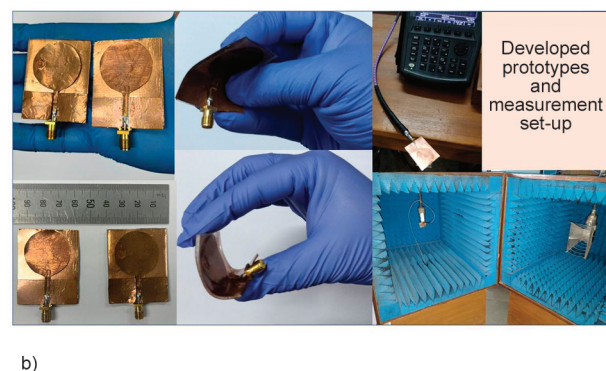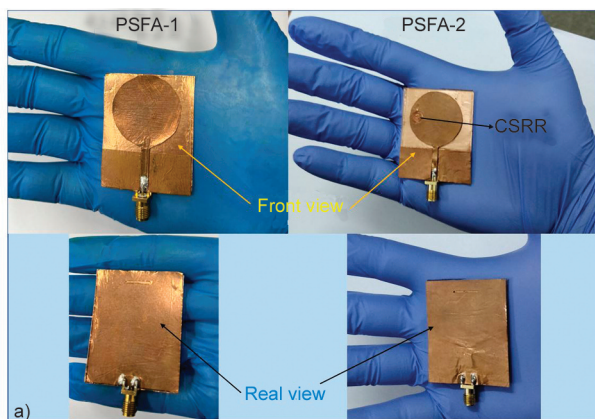

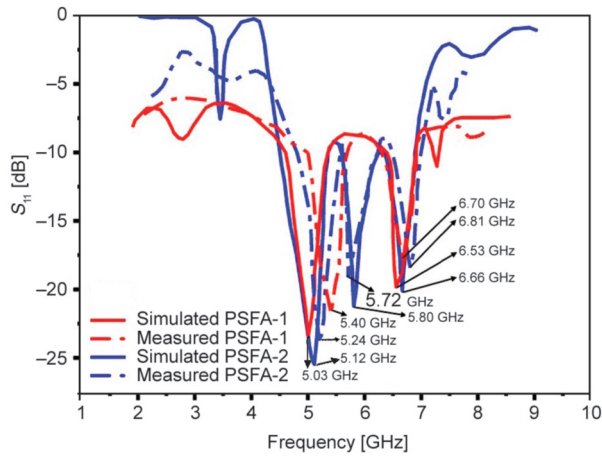**Figure 7.** Fabricated prototypes: a) PSFA-1 and PSFA-2, and b) prototypes and measurements.
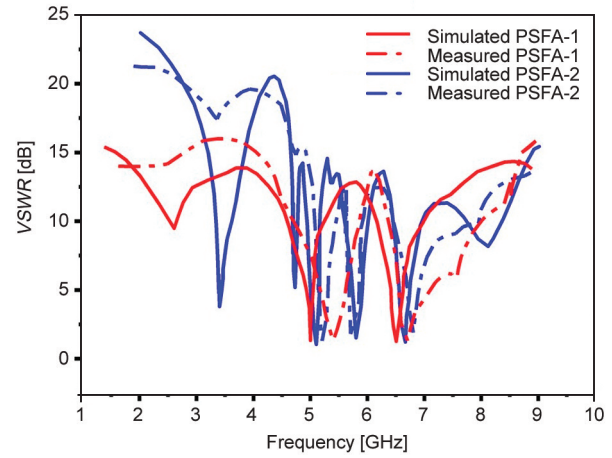
Figure 8. S_{11} values for the PSFAs (1 and 2).

Figure 9. *VSWR* values for the PSFAs (1 and 2).
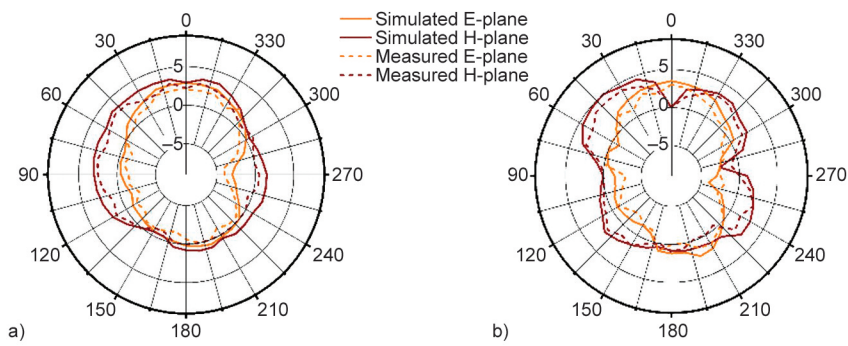

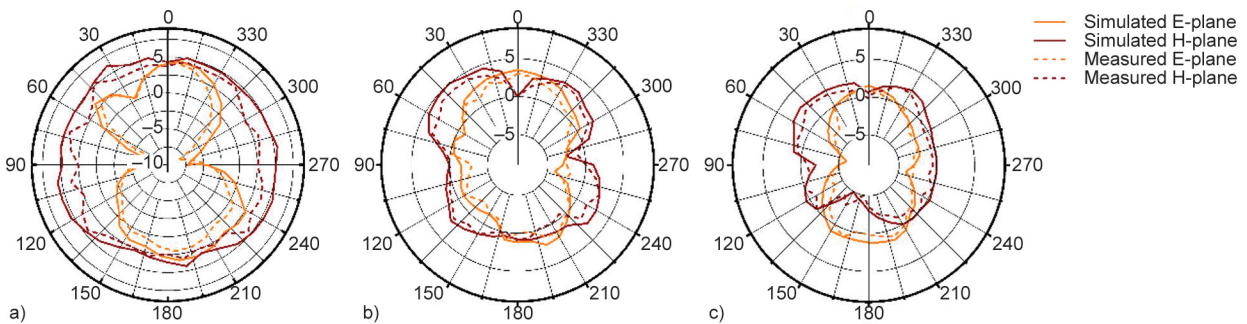**Figure 10.** PSFA-1 radiation patterns, a) 5.0 GHz, b) 6.5 GHz.

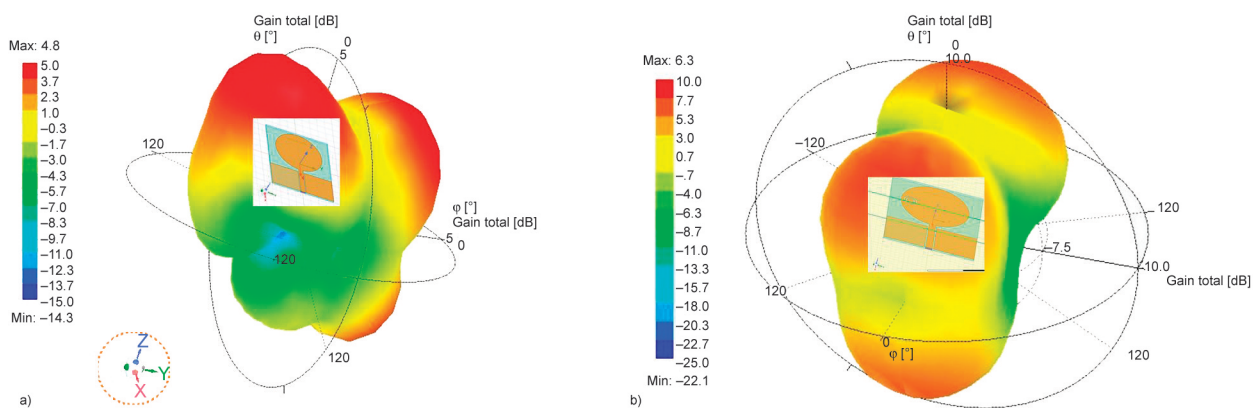**Figure 11.** PSFA-2 radiation patterns, a) 5.10 GHz, b) 5.80 GHz, c) 6.60 GHz.

Figure 12. 3D gain plot: a) PSFA-1, and b) PSFA-2.

Table 3. Comparison of PSFAs.

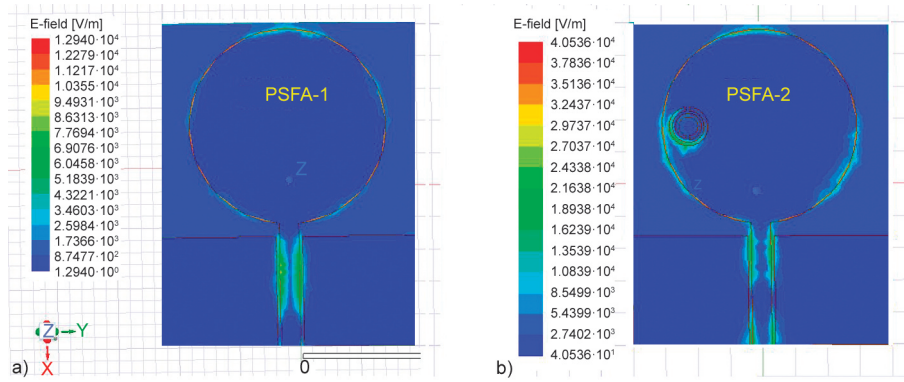| Parameters	PSFA-1				PSFA-2					
	Simulation results		Experimental results		Simulation results			Experimental results		
Frequency [GHz]	5.03	6.53	5.40	6.70	5.12	5.80	6.66	5.24	5.72	6.81
S_{11}/$VSWR$ [dB]	−23.4/1.32	−19.8/1.26	−21.8/1.56	−18.1/1.32	−25.6/1.02	−21.2/1.50	−20.1/1.20	−24.0/1.30	−19.1/1.80	−18.4/1.92
−10 dB BW [GHz]	0.75	0.51	0.69	0.50	0.83	0.64	0.53	0.80	0.61	0.51
Gain [dBi]	4.0	1.8	3.8	1.5	6.2	4.1	2.4	6.0	4.2	2.2

Figure 13. E-field distribution for the a) PSFA-1 and b) PSFA-2.

4.2. Estimation of SAR using simulation model

Employing a multi-layered model in simulation (Figure 14a), the specific absorption rate (SAR) analysis is carried out to examine how the proposed antennas affect the human body. The bottom layer of the SAR analysis model represents muscle, the mesoderm layer is fat, and the top is the skin [5, 23]. The obtained SAR values (averaged) by this model for PSFA-1 (5.03 GHz) and PSFA-2 (5.12 GHz) using an input power of 100 mW are shown in Figure 14b and Figure 14c. The measured values are 1.9 and 1.6 W/kg, respectively, which satisfy the European standard (<2 W/kg). Thus, in the second proposed antenna, the CSRR with PDMS substrate aided in reducing the SAR also.
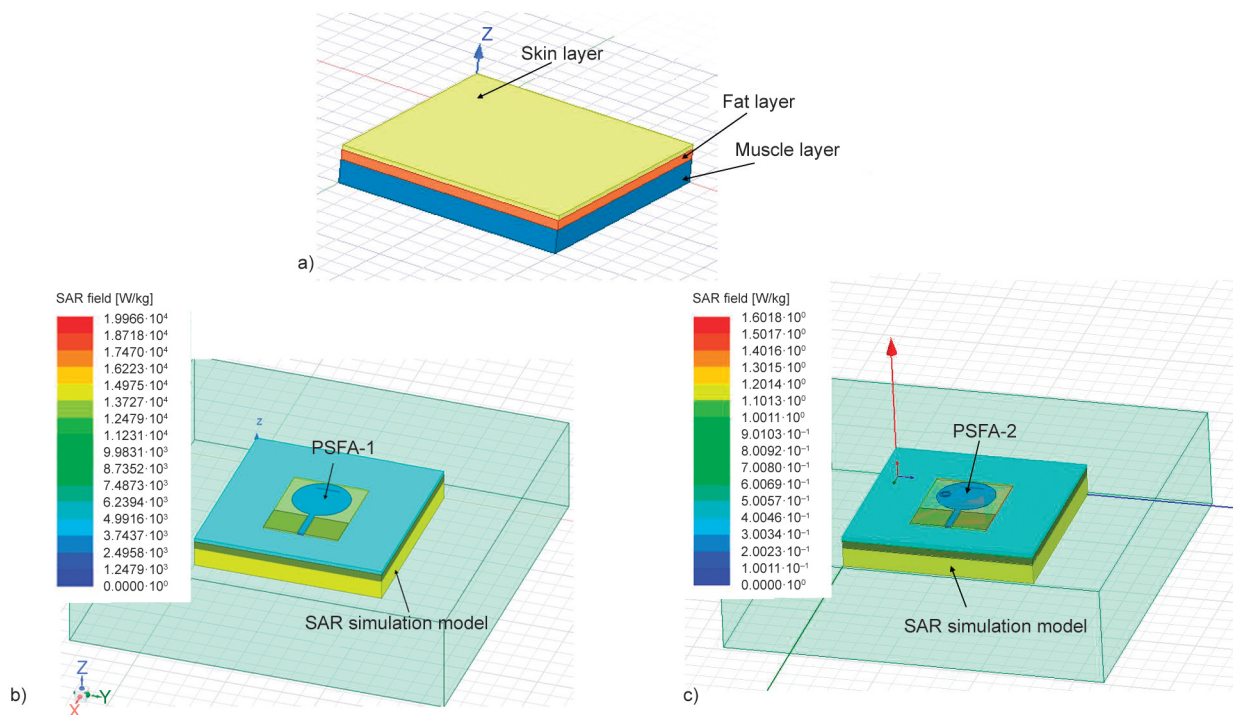

Figure 14. SAR Estimation: a) simulation model, b) for PSFA-1, and c) for PSFA-2.

4.3. Conformal condition analysis

The adoption of PDMS as a substrate has offered proposed antennas considerable flexibility so that they can be employed in conformal environments. Therefore in this sub-section, the developed antennas are evaluated under conformal conditions to assess their effects on the performance. Two different scenarios are chosen to observe its effects: firstly, the performance of both the antennas is tested on a hand at a ~10° bent, and in the second, measurements are made using two different cylinders with radii of 3 and 4 cm. When adopted for wearable applications, one of the essential considerations of the flexible antenna should function effectively while mounted on the body, in contrast to the constraint of stiff substrate antennas. Due to the presence of biological tissues that might drain some power, it behaves as a lossy medium. This drives the S-parameters of the presented antennas to fluctuate (Figure 15a), and changes in the resonating frequencies can also be noticed. It is noteworthy that the given antennas retain operation in the relevant frequency bands and possesses multiband capabilities. The dielectric characteristics of the substrate are crucial in this situation. Considering that PDMS has a comparatively low dielectric constant, it aids in suppressing surface waves and helps in achieving good impedance matching.

Both antennas are placed on cylinders with radii of 4.0 and 3.0 cm to investigate further the impact of bending on the antennas' radiating properties. Resonant frequencies and associated S_{11} values demonstrate a minor shift. However, as seen in Figure 15b and Figure 15c, the antennas still work in the needed multi-frequency bands while offering the notched features. Since PDMS is a substantially anisotropic substrate [9–12], it has been demonstrated experimentally and analytically that anisotropy and bending have opposing effects on the antenna's resonant properties [24, 25]. The results of the experimental investigation carried out here, and earlier studies are in satisfactory correlation with one another.
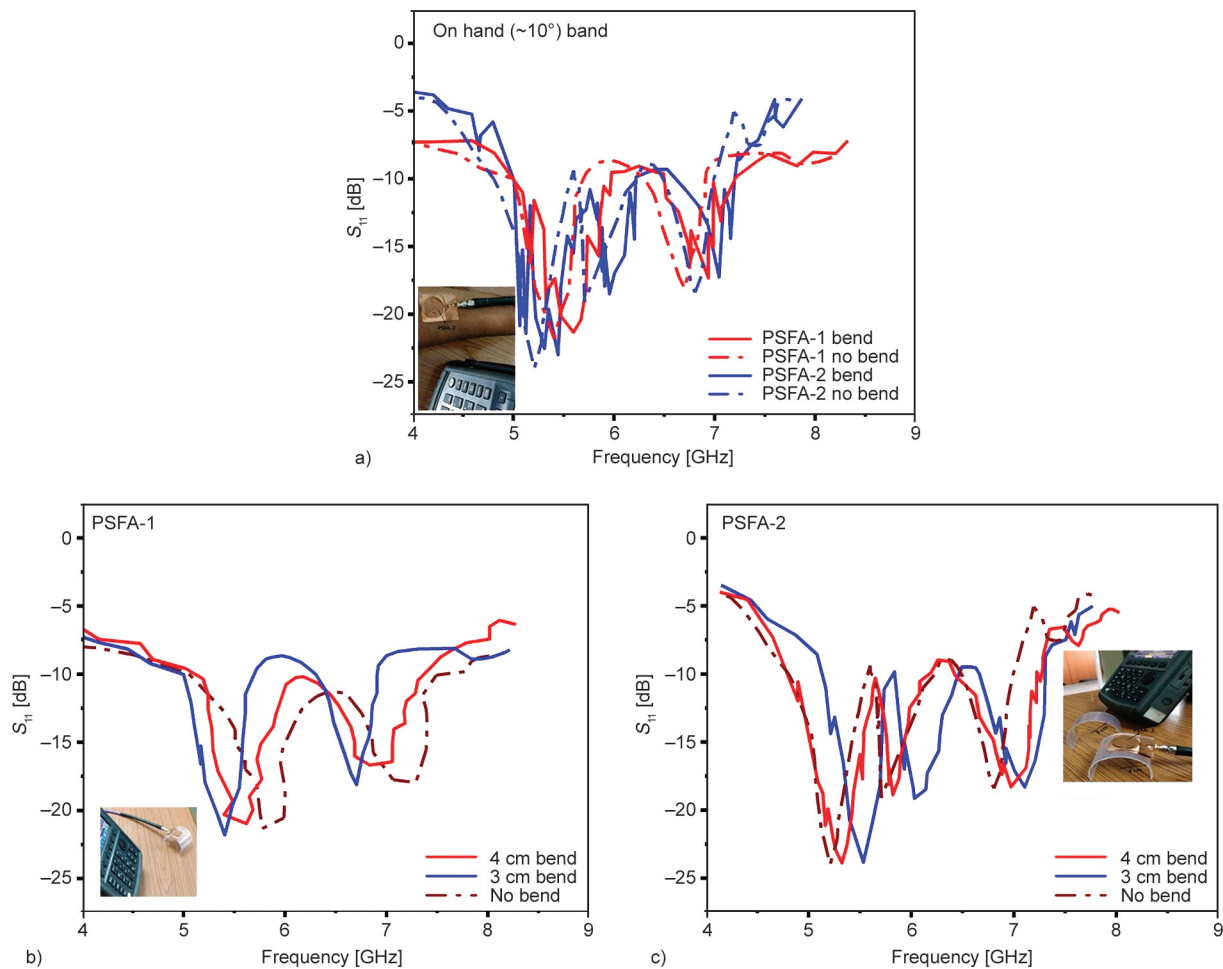

Figure 15. S_{11} *vs.* frequency curve: a) on hand; on cylinders of 4.0 and 3.0 cm, b) for PSFA-1, and c) for PSFA-2.

4.4. Wet condition analysis

In the literature, there are several choices for substrates that can be employed to design flexible and wearable antennas. Fabric substrates are the most frequently used substrates for wearable antenna designs. Despite having a variety of benefits, these materials are susceptible to operational environment changes like absorption of moisture and temperature fluctuations that can either directly or indirectly impact the radiation characteristics of the antenna [2]. These constraints have indeed been alleviated by using polymer-based substrates like PDMS, which has been used in this research. This has been demonstrated by evaluating the designed antennas under wet circumstances by submerging them in water, drying them after ten minutes, and evaluating their performance. The analysis presented here demonstrates that flexible antennas built of polymer substrates, such as PDMS, have very little effect from moisture since these materials do not absorb moisture as fabric substrates do. In our earlier study, we compared PDMS with denim substrate [2], where it was shown experimentally that denim is more susceptible to moisture and affects antenna performance more. The measurement setup for the wet condition evaluation and the fluctuation of the S_{11} parameters in the wet condition is shown in Figure 16. For the proposed antennas using polymer substrate PDMS, very little variation in the resonating frequencies and related S_{11} parameters is observed. This demonstrates the
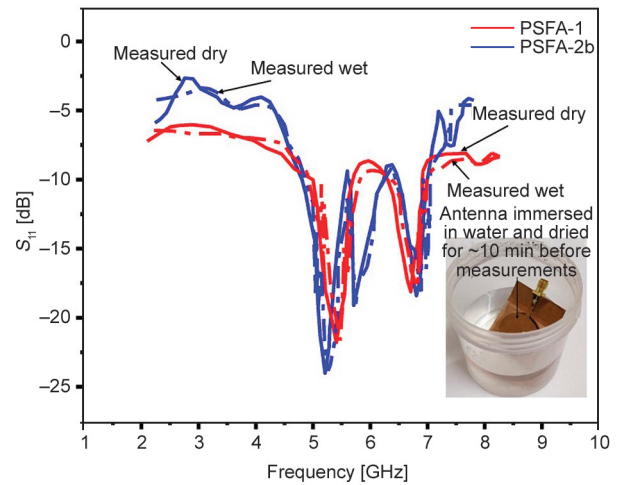

Figure 16. Measured S_{11} *vs.* frequency curve for both PSFAs in dry and wet conditions.

PDMS' appropriateness for the design of flexible antennas with steady performance under a range of operational situations.

5. Conclusions

In this paper, flexible substrate PDMS is employed to design flexible antennas for wireless body and local area network applications. The development and dielectric evaluation of PDMS as per the antenna requirements are also performed here. In order to demonstrate that SRR structures can be employed in flexible antennas with polymer substrates (PSFA) and to experimentally validate the merits of including them in antenna designs, a single CSRR structure is

Table 4. Comparison of PSFA with previous works.

Substrate material	Size [mm²]	Gain [dBi]	Applications	Type of metamaterial loading	Performance analysis in varying operating situations: bending analysis (BA); SAR analysis (SA); on body analysis (OB); wet condition analysis (WA)	References
Polyester	55×46	4.2/5.78	3.63 GHz/4.95 GHz (5G) applications	Not implemented	not performed	[26]
Liquid crystal polymer (LCP)	38×32	2	3.5 GHz (WiMAX)/5.8 GHz (WLAN), applications	Circular SRR (two)	BA	[27]
Polyamide	24×19	2.3/3.3/3.9	2.4 GHz/5.6 GHz (bluetooth), 3.8 GHz (5G NR) applications	Not Implemented	BA; SA; OB	[28]
Polydimethylsiloxane (PDMS)	80×67	4.53	5 GHz/7 GHz (UWB) applications	Not implemented	BA; SA; OB	[29]
Polydimethylsiloxane (PDMS)	70	4.16/4.34	2.45 GHz /5.8 GHz (ISM band) applications	Not implemented	BA; SA; OB	[30]
Polydimethylsiloxane (PDMS)	67×44	6.7	UWB applications	Not implemented	BA; SA; OB	[31]
Polydimethylsiloxane (PDMS)	50.2×40.1	6.2/4.1/2.4	5.12/5.80/6.66 GHz WLAN/WBAN applications	CSRR (single)	BA; SA; OB; WA	Proposed

integrated into the second antenna. It has helped in improving the performance of the PSFA-2, such as an increase in gain from 4.8 to 6.3dBi with better *VSWR* and S_{11} values; the additional frequency band of 5.80 GHz is achieved with 5.12 and 6.66 GHz band in the second antenna for fast wireless body area network applications (Table 4). Reduced SAR and stable performance under different operating situations like bending and wet conditions are the add-on advantages of using CSRR with PDMS. Both of the PSFAs are successfully analyzed for their operability for the target applications due to their simple structure, flexibility, cost-effective development process, and consistent performance under varied operating situations. Prototypes are also fabricated to verify the simulated results that show a good correlation with each other.

Acknowledgements

References

[1] Nguyen T. M., Chung J-Y.: Analysis and fabrication of a wearable antenna using conductive fibers. Journal of the Korea Academia-Industrial cooperation Society, **16**, 2770–2776 (2015).
https://doi.org/10.5762/KAIS.2015.16.4.2770

[2] Sharma P. K., Gupta N.: Design and analysis of polydimethylsiloxane (PDMS) and Jean substrate based flexible antenna for ultra-wideband applications. in 'Proceeding of 2021 IEEE MTT-S International Microwave and RF Conference (IMARC) Kanpur, India' 1–4 (2021).
https://doi.org/10.1109/IMaRC49196.2021.9714626

[3] Zhang K., Soh P. J., Yan S.: Design of a compact dual-band textile antenna based on metasurface. IEEE Transactions on Biomedical Circuits and Systems, **16**, 211–221 (2022).
https://doi.org/10.1109/TBCAS.2022.3151243

[4] Li R., Wu C., Sun X., Zhao Y., Luo W.: An EBG-based triple-band wearable antenna for WBAN applications. Micromachines, **13**, 1938 (2022).
https://doi.org/10.3390/mi13111938

[5] Keshwani V. R., Bhavarthe P. P., Rathod S. S.: Compact embedded dual band EBG structure with low SAR for wearable antenna application. Progress in Electromagnetics Research M, **113**, 199–211 (2022).
https://doi.org/10.2528/PIERM22071704

[6] Sayem A. S. M., Simorangkir R. B. V. B., Esselle K. P., Buckley J. L.: A conformal and transparent frequency reconfigurable water antenna. in 'Proceedings of 16th European Conference on Antennas and Propagation (EuCAP) Madrid, Spain' 1–4 (2022).
https://doi.org/10.23919/EuCAP53622.2022.9769462

[7] Shan H., Zhang Y., Gao J., Nag A., Rahaman A.: Integration of different graphene nanostructures with PDMS to form wearable sensors. Nanomaterials, **12**, 950 (2022).
https://doi.org/10.3390/nano12060950

[8] Rojas-Alva U., Møller-Poulsen F., Man S-L., Creamer C., Hanna D., Jomaas G.: Flame spread behaviour of Polydimethylsiloxane (PDMS) membranes in 1 g and μg environments. Combustion and Flame, **240**, 112009 (2022).
https://doi.org/10.1016/j.combustflame.2022.112009

[9] Sharma P. K., Gupta N., Dankov P. I.: Analysis of dielectric properties of polydimethylsiloxane (PDMS) as a flexible substrate for sensors and antenna applications. IEEE Sensors Journal, **21**, 19492–19504 (2021).
https://doi.org/10.1109/JSEN.2021.3089827

[10] Sharma P. K., Gupta N., Dankov P. I.: Characterization of polydimethylsiloxane (PDMS) as a wearable antenna substrate using resonance and planar structure methods. AEU-International Journal of Electronics and Communications, **127**, 153455 (2020).
https://doi.org/10.1016/j.aeue.2020.153455

[11] Sharma P. K., Gupta N., Dankov P. I.: Wideband transmission line characterization of polydimethylsiloxane (PDMS) as a wearable antenna substrate. in 'Proceeding of IEEE International Conference on Electronics, Computing and Communication Technologies (CONECCT) Bangalore, India', 1–4 (2020).
https://doi.org/10.1109/CONECCT50063.2020.9198526

[12] Sharma P. K., Chung J-Y.: Evaluation of polydimethylsiloxane (PDMS) as a substrate for the realization of flexible/wearable antennas and sensors. Micromachines, **14**, 735 (2023).
https://doi.org/10.3390/mi14040735

[13] Gao G-P., Dou Z-H., Yu Z-Q., Zhang B-K., Dong J-H., Hu B.: Dual-mode patch antenna with capacitive coupling structure for on-/off-body applications. IEEE Antennas and Wireless Propagation Letters, **21**, 1512–1516 (2022).
https://doi.org/10.1109/LAWP.2022.3170555

[14] Janapala D. K., Nesasudha M.: A highly miniaturized antenna with wider band for biomedical applications. Electromagnetic Biology and Medicine, **41**, 35–43 (2022).
https://doi.org/10.1080/15368378.2021.1993892

[15] Mukesh A. N., Sharma P. K., Yadav V. P., Payal P. O., Solanki L.: Design and analysis of an edge truncated flexible antenna for wi-fi applications. in 'Procceding of International Conference on Electronics and Renewable Systems (ICEARS) Tuticorin, India' 1861–1864 (2022).
https://doi.org/10.1109/ICEARS53579.2022.9752032

[16] Kent G.: Nondestructive permittivity measurement of substrates. IEEE Transactions on Instrumentation and Measurement, **45**, 102–106 (1996).
https://doi.org/10.1109/19.481319

[17] Hasar U. C., Kaya Y., Ozturk H., Izginli M., Ertugrul M., Barroso J. J., Ramahi O. M.: Improved method for permittivity determination of dielectric samples by free-space measurements. IEEE Transactions on Instrumentation and Measurement, **71**, 6002108 (2022).
https://doi.org/10.1109/TIM.2022.3153991

[18] Courtney W. E.: Analysis and evaluation of a method of measuring the complex permittivity and permeability microwave insulators. IEEE Transactions on Microwave Theory and Techniques, **18**, 476–-485 (1970).
https://doi.org/10.1109/TMTT.1970.1127271

[19] Kato Y., Horibe M.: Broadband permittivity measurements using a frequency-variable balanced-type circular-disk resonator. in 'Proceeding of 2018 Conference on Precision Electromagnetic Measurements (CPEM 2018) Paris, France' 1–2 (2018).
https://doi.org/10.1109/CPEM.2018.8501132

[20] Mohammed A. M., Wang Y., Salek M.: Dielectric measurement of substrate materials using 3D printed re-entrant cavity resonator. in 'Proceeding of 51st European Microwave Conference (EuMC) London, United Kingdom' 793–796 (2022).
https://doi.org/10.23919/EuMC50147.2022.9784354

[21] Tiwari N. K., Jha A. K., Singh S. P., Akhter Z., Varshney P. K., Akhtar M. J.: Generalized multimode SIW cavity-based sensor for retrieval of complex permittivity of materials. IEEE Transactions on Microwave Theory and Techniques, **66**, 3063–3072 (2018).
https://doi.org/10.1109/TMTT.2018.2830332

[22] Sharma P. K., Gupta N.: Design and analysis of a compact CSRR loaded defected ground plane antenna for ultra-wideband applications. in 'Proceeding of 2nd International Conference on Communication, Computing and Industry 4.0 (C2I4) Bangalore, India' 1–4 (2021).
https://doi.org/10.1109/C2I454156.2021.9689449

[23] Ali U., Ullah S., Khan J., Kamal B., Basir A., Flint J. A., Seager R. D.: Design and SAR analysis of wearable antenna on various parts of human body, using conventional and artificial ground planes. Journal of Electrical Engineering and Technology, **12**, 317–328 (2017).
https://doi.org/10.5370/JEET.2017.12.1.317

[24] Dankov P. I., Sharma P. K., Gupta N.: Numerical and experimental investigation of the opposite influence of dielectric anisotropy and substrate bending on planar radiators and sensors. Sensors, **21**, 16 (2020).
https://doi.org/10.3390/s21010016

[25] Dankov P. I., Levcheva V. P., Sharma P. K.: Influence of dielectric anisotropy and bending on wearable textile antenna properties. in 'Proceeding of International Workshop on Antenna Technology (iWAT) Bucharest, Romania' 1–4 (2020).
https://doi.org/10.1109/iWAT48004.2020.1570606843

[26] Afroz S., Al-Hadi A. A., Azemi S. N., Hoon W. F., Padmanathan S., Isa C. M. N. C., Sahoo B. C., Loh Y. S., Suhaimi M. I., Lim L. M., Samsudin Z., Mansor I., Soh P. J.: Dual band circular patch flexible wearable antenna design for sub-6 GHz 5G applications. in 'Proceeding of 2022 IEEE International RF and Microwave Conference (RFM)' Kuala Lumpur, Malaysia, 1–4 (2022).
https://doi.org/10.1109/RFM56185.2022.10065238

[27] Rao V., Madhav B. T. P., Anilkumar T., Prudhvinadh B.: Circularly polarized flexible antenna on liquid crystal polymer substrate material with metamaterial loading. Microwave and Optical Technology Letters, **62**, 866–874 (2020).
https://doi.org/10.1002/mop.32088

[28] Sreelakshmi K., Rao G. S., Kumar M. N. V. S. S.: A compact grounded asymmetric coplanar strip-fed flexible multiband reconfigurable antenna for wireless applications. IEEE Access, **8**, 194497–194507 (2020).
https://doi.org/10.1109/ACCESS.2020.3033502

[29] Simorangkir R. B. V. B., Kiourti A., Esselle K. P.: UWB wearable antenna with a full ground plane based on PDMS-embedded conductive fabric. IEEE Antennas and Wireless Propagation Letters, **17**, 493–496 (2018).
https://doi.org/10.1109/LAWP.2018.2797251

[30] Simorangkir R. B. V. B., Yang Y., Matekovits L., Esselle K. P.: Dual-band dual-mode textile antenna on PDMS substrate for body-centric communications. IEEE Antennas and Wireless Propagation Letters, **16**, 677–680 (2016).
https://doi.org/10.1109/LAWP.2016.2598729

[31] Janapala D. K., Nesasudha M., Neebha T. M., Kumar R.: Design and development of flexible PDMS antenna for UWB-WBAN applications. Wireless Personal Communications, **122**, 3467–3483 (2022).
https://doi.org/10.1007/s11277-021-09095-7